Nonlinear optical response of triple-mode silicon photonic crystal microcavities coupled to single channel input and output waveguides

by

Ellen N. Schelew

B.A.Sc., Queen's University, 2009
M.A.Sc., The University of British Columbia, 2011

A THESIS SUBMITTED IN PARTIAL FULFILLMENT OF
THE REQUIREMENTS FOR THE DEGREE OF

DOCTOR OF PHILOSOPHY

in

The Faculty of Graduate and Postdoctoral Studies

(Physics)

THE UNIVERSITY OF BRITISH COLUMBIA

(Vancouver)

October 2017

Abstract

Optical and opto-electronic components play important roles in both classical and quantum information processing technologies. Despite fundamental differences in these technologies, both stand to benefit greatly from moving away from bulky, individually packaged components, toward a scalable platform that supports dense integration of low power consumption devices. Planar photonic circuits, composed of devices etched in a thin slab of high refractive index material, are considered an excellent candidate, and have been used to realize many key components, including low-loss waveguides, light sources, detectors, modulators, and spectral filters. In this dissertation, a novel triple-microcavity structure was designed, externally fabricated, and its linear and nonlinear optical properties were thoroughly characterized. The best of the structures exhibited both high four-wave mixing conversion efficiencies and low threshold optical bistability, which are relevant to frequency conversion and all-optical switching applications.

The device consisted of three coupled photonic crystal (PC) microcavities with three nearly equally spaced resonant frequencies near telecommunication wavelengths ($\lambda \sim 1.5$ μm), with high quality factors ($\sim 10^5, 10^4$ and 10^3). The microcavity system was coupled to independent input and output PC waveguides, and the cavity-waveguide coupling strengths were engineered to maximize the coupling of the input waveguide to the central mode, and the output waveguide to the two modes on either side.

A novel and sophisticated measurement and analysis protocol was developed to characterize the devices. This involved measuring and modelling the linear and nonlinear transmission characteristics of each of the modes separately with a single tunable laser, as well as the frequency conversion efficiency (via stimulated four-wave mixing) when two tunable lasers pumped two of the modes, and the power generated in the third mode was monitored.

Comparisons of the entire set of model and experimental results led to the conclusion that this structure can be used to achieve both low-power-threshold optical switching and high efficiency four-wave-mixing-based frequency conversion. The advantages of this structure over others in the literature are its small footprint, multi-mode functionality and independent input and output channels. The main disadvantage that requires further refinement, has to do with its sensitivity to fabrication imperfections.

Lay Summary

The transmission infrastructure of the Internet consists of a global network of glass optical fibres that carry light signals, encoded with information, between data centers. In modern data centres, information processing is performed in microelectronic chips, and relatively bulky equipment is used to interface the optical and electronic signals. In the field of "integrated optics", research and development is aimed towards realizing compact and efficient interfacing components, integrated in light-based "photonic" microchips, much like their electronic counterparts, to help meet the growing demands of the ever-expanding Internet. One class of photonic technologies aims to achieve all-optical information processing functionalities by *controlling light with light* in the microchip. In this dissertation, a compact and efficient microchip device of this class is presented that exhibits a number of potentially useful functionalities. In order to understand and predict its performance, a complex analysis protocol is developed, that uses a novel combination of complimentary experimental probes, to characterize the device behaviour.

Preface

Identification and design of the research program was a collaborative effort between myself and my research supervisor, Dr. Jeff Young. I was the primary contributor to the device design, measurements and analysis. The device fabrication was facilitated by Dr. Lukas Chrostowski, and conducted at the University of Washington Microfabrication/Nanotechnology User Facility, by Dr. Richard Bojko and Shane Patrick.

One conference publication has arisen from this work:

- E. N. Schelew and J. F. Young, "Stimulated Four-Wave Mixing in a Heterostructure Photonic Crystal Triple Microcavity," in Advanced Photonics 2016 (IPR, NOMA, Sensors, Networks, SPPCom, SOF), OSA technical Digest (online) (Optical Society of America, 2016), paper IW2B.5.

The work presented in this publication overlaps with the content of this thesis, namely Chapters 3, 4 and 5, however it is not directly reproduced in this dissertation. My contributions to this work are the same as those described above.

The nonlinear coefficients in Table 5.3 were calculated based on microcavity mode profiles simulated numerically using Lumerical FDTD Solutions. All other calculations associated with the least-squares analysis in Chapter 5 were completed using MATLAB code that I wrote.

Table of Contents

List of Tables

List of Figures

List of Abbreviations

CW	Continuous wave
EBL	Electron beam lithography
FCD	Free-carrier dispersion
FDTD	Finite-difference time-domain
FWHM	Full width at half maximum
FWM	Four-wave mixing
G2G	Grating to grating reference device
M1	Cavity mode 1 (with lowest resonant wavelength)
M2	Cavity mode 2 (with center resonant wavelength)
M3	Cavity mode 3 (with highest resonant wavelength)
NLC	Nonlinear characterization
PC	Photonic crystal
PCWG	Photonic crystal waveguide reference device
PIC	Photonic integrated circuit
Q	Quality factor
QI	Quantum information
SEM	Scanning electron microscope
TCMT	Temporal coupled mode theory
TIR	Total internal reflection
TMC	Triple microcavity device
TPA	Two-photon absorption

List of Symbols

β_{FWM}	Four-wave mixing conversion coefficient
β_{TPA}	Two-photon absorption coefficient
$\Delta\lambda_m^{\mathrm{NL}}$	Resonant wavelength shift of mode m
$\Delta\omega_m^{\mathrm{NL}}$	Resonant frequency shift of mode m
ζ_{FCD}	Free-carrier dispersion nonlinear parameter
$\eta_{\mathrm{FWM}}^{\mathrm{P}}$	Four-wave mixing conversion efficiency
η_m^{wg}	Waveguide coupling ratio of mode m, $\tau_m^{\mathrm{out}}/\tau_m^{\mathrm{in}}$
λ_m	Resonant wavelength of mode m
σ_{FCA}	Free-carrier absorption cross-section
τ_m	Total microcavity lifetime of mode m
τ_{abs}	Linear material absorption lifetime
τ_{carrier}	Effective free-carrier lifetime
τ_m^{in}	Input waveguide coupling lifetime of mode m
τ_m^{lin}	Total linear microcavity lifetime of mode m
τ_m^{out}	Output waveguide coupling lifetime of mode m
τ_m^{scatt}	Scattering lifetime of mode m
τ_m^{FCA}	Free carrier absorption lifetime of mode m
τ_m^{TPA}	Two-photon absorption lifetime of mode m
ϕ_{in}	Fabry-Perot phase shift of input port
ϕ_{out}	Fabry-Perot phase shift of output port
$\boldsymbol{\chi}^{(3)}$	Third order nonlinear susceptibility
X^2	Sum of the squared differences
ω_m	Resonant frequency of mode m

dn/dT	Refractive index temperature dependence
n_{Si}	Refractive index of silicon
$n_{2,\mathrm{Si}}$	Nonlinear index coefficient
N	Free-carrier density
p_m^{out}	Probably that cavity photon in mode m couples to output waveguide
P_{th}	Kerr effect input power threshold
Q_m	Total quality factor of mode m
Q_{abs}	Linear material absorption quality factor
Q_m^{in}	Input waveguide coupling quality factor
Q_m^{out}	Output waveguide coupling quality factor
R_{th}	Thermal resistance
$\overline{T}_m^{\mathrm{lin}}$	Linear peak relative transmission
$\overline{T}_m^{\mathrm{NL}}$	Noninear peak relative transmission
v_g	Group velocity

Acknowledgements

First and foremost, I would like to sincerely thank Dr. Jeff Young for his guidance and support during my graduate studies. I thank him for sharing his vast knowledge, for challenging me, and for providing a wide variety of learning opportunities. I leave this lab knowing that no piece of lab equipment is too old to resurrect.

Thanks to the members of the Nanolab for creating a friendly and supportive environment. A special thanks to fellow graduate students Jonathan Massey-Allard, Dr. Hamed Mirsadeghi, Dr. Charles Foell and Xiruo Yan, it's been a pleasure learning and laughing with them over the years, and I thank them for all the stimulating discussions and for all their help. Thanks to Jingda Wu, Megan Nantel, and Lisa Rudolph for being great lab-mates during the end of my time in the Nanolab.

Thanks to Dr. Moshen Akhlaghi for his mentorship and for sharing with me his systematic problem solving techniques. Thanks to Dr. Mario Beaudoin and Dr. Alina Kulpa for their help in the cleanroom, and to Dr. Lukas Chrostowski, Dr. Richard Bojko and Shane Patrick for their help with device fabrication. Thanks to Dr. Ovidiu Toader, I don't think there is any computer related problem he can't solve.

I also thank Dr. James Day, Andrew Macdonald, Nathan Evetts, and the rest of the AMPEL building lunch crew for the light-hearted discussions about science and well beyond.

I am also very grateful for the support I received from the Natural Sciences and Engineering Research Council (NSERC), the Silicon Electronic-Photonic Integrated Circuits (Si-EPIC) Program and the Quantum Electronic Science and Technology (QuEST) Program, as well as the meaningful experiences they have afforded me. I'd like to thank the people at Lumerical for the opportunity to do an internship, and specifically Dr. James Pond and Dylan McGuire for sharing their expertise and for patiently teaching me.

Thanks to my family and friends for all their love and support during this journey. Finally, an immeasurable thank you to my partner Dan, for his unwavering support and encouragement through it all.

Chapter 1

Introduction

1.1 Context

Over the last two decades, the rapid growth of the Internet has lead to increasing demands for high bandwidth information processing and transmission. Large amounts of information are processed and stored in data centers using microelectronic chips. For long-haul transmission, the information is encoded in light, and launched into glass optical fibres that form a global network. The electronic and optical information is interfaced using optical and electro-optical components including lasers, photodetectors, modulators, and spectral multiplexers and demultiplexers, as illustrated in Fig. 1.1. On the transmission end, electronic signals are encoded in laser light using modulators, meanwhile on the receiving end, optical signals are converted to electronic signals using photodetectors. In transmission, multiple signals are transmitted in a single optical fibre by multiplexing (and demultiplexing) optical signals with different carrier frequencies. In modern day data centers, many of these interfacing components are bulky individual units, with high power consumption, that are installed in racks. This is in stark contrast to the microelectronic chips, where millions of compact electronic components are densely integrated.

One vision in "integrated optics" is to replace these racks of optical components with compact and efficient photonic integrated circuits (PICs) [48, 49, 83, 87] that support the same functionalities. This PIC approach has the potential to revolutionize data centers, and substantial progress has been made, by both academic and industry parties, toward developing the necessary integrated components. In PICs, the "wires" that transport light through the circuit are waveguides defined in planar 2D geometries, where total internal reflection confines the light to the high refractive index guiding channels, as shown in Fig. 1.2(a). Optical components like beam-splitters [54] and spectral filters [12, 100] are realized in compact geometries, as shown in Fig. 1.2(b) and (c). A

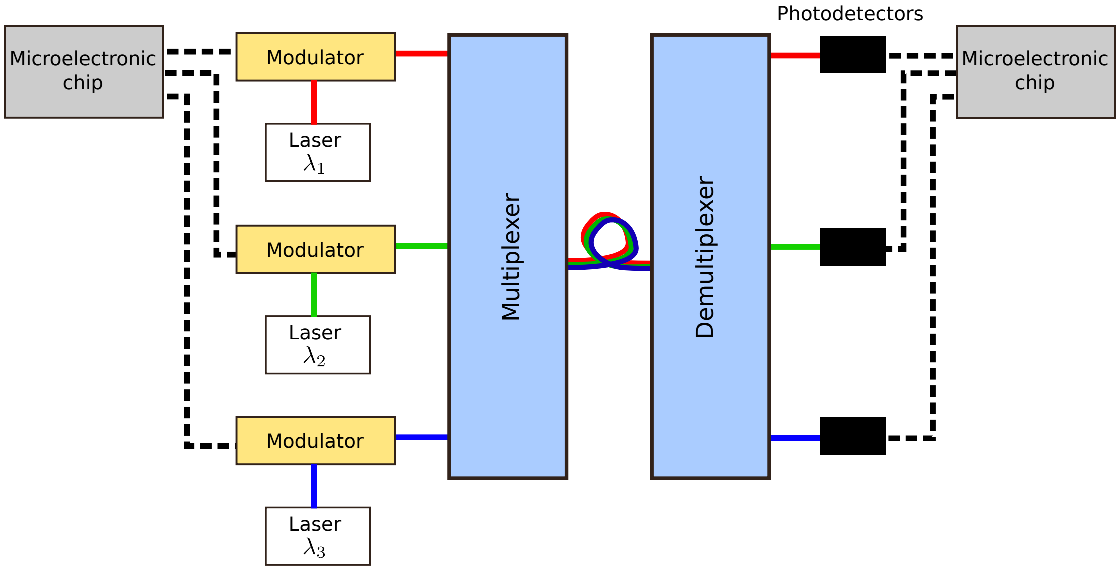

Figure 1.1: Schematic example of information sending and receiving. Three electronic signals, produced in one microelectronic chip, are transmitted to a remote microelectronic chip via a single optical fibre. The electronic signals (black dashed lines) are applied to modulators that encode the information in light arriving from continuous wave (CW) lasers via optical fibres (solid coloured lines). Each laser has a different optical frequency, and the three optical signals leaving the modulators are directed into a single optical fibre using a spectral multiplexer. The optical fibre carries the multiplexed signal to a remote destination, where it is separated into the three optical frequencies using a demultiplexer. The individual optical signals then arrive at photodetectors, that translate them into electronic signals, which are then directed to a second microelectronic chip.

long-standing goal has been to greatly reduce conversions between optical and electric signals by performing processing tasks like switching and routing in PICs, where *light is controlled with light* [2, 47, 60–62]. This will require devices that operate in the nonlinear optical regime, where one light signal perturbs the optical material through a nonlinear interaction, thus affecting the response of other light signals as they pass through the device.

In parallel, quite independently, while this PIC research and development has been evolving, so has the field of quantum information (QI). In one of the most application-ready areas of QI, namely quantum communication, manipulation of light at the single photon level is essential [28]. In addition, one of the many schemes being considered for realizing a full quantum computer involves launching and routing single photons through complex paths of beam-splitters, phase-shifters and detectors [36, 45, 57]. Just as with the Internet example above, current demonstrations have relied mostly on bulky components [77, 90, 108], but the potential advantages of using PICs for QI applications, chiefly scalability and manufacturability, are driving the development of integrated

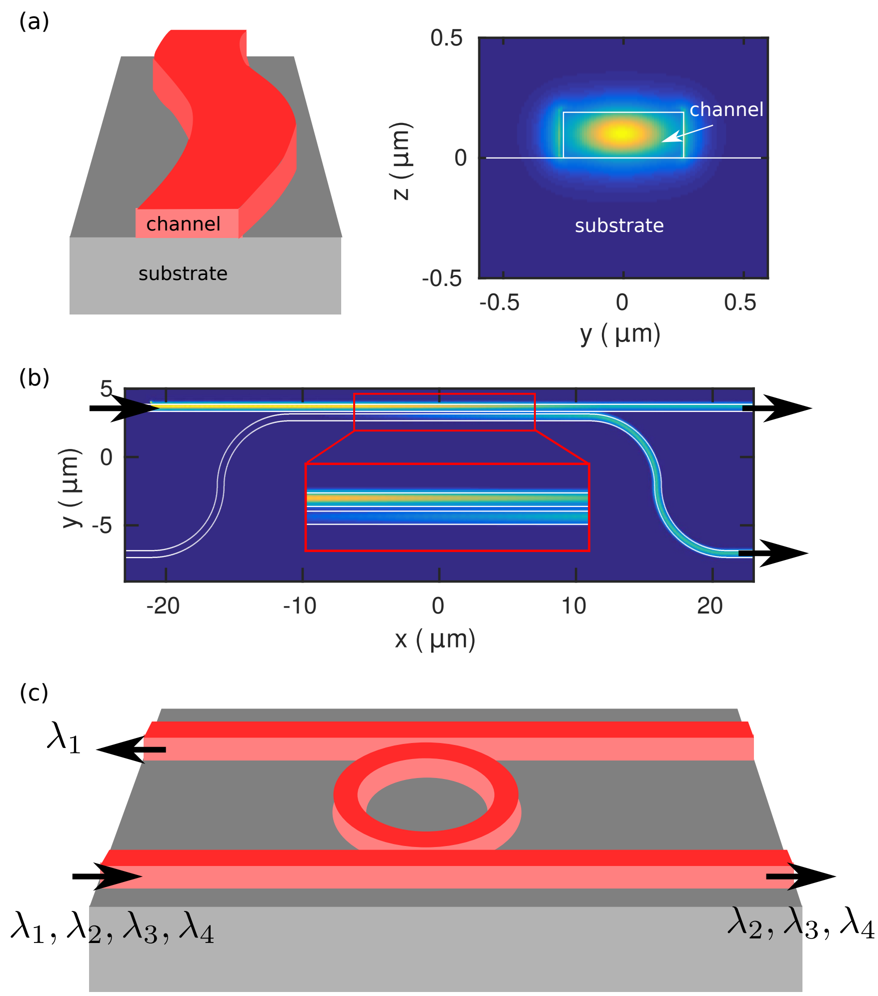

Figure 1.2: Schematic of PIC components. (a) An example waveguide that is composed of a high index channel that confines light by total internal reflection. The waveguide sits on a low index substrate, and is otherwise surrounded by air. An example of the cross-sectional mode profile for a PIC waveguide is shown on the right, where the white lines contour the channel and substrate. (b) A beam-splitter (directional coupler), that transfers light between two waveguides by evanescent coupling. (c) A compact spectral filter formed by a ring resonator coupled to two waveguides. In this example, the input excitation at λ_1, is resonant with the ring and is transmitted through to the top waveguide, while the other wavelengths are non-resonant and are directly transmitted.

waveguide circuits that incorporate single photon sources and detectors [1, 17, 29, 36, 57, 64, 68, 78, 98].

1.1.1 Photonic integrated circuit basics

In PICs, optical components are linked by channel waveguides that are interfaced with optical fibres to bring light in and out of the photonic circuit, as is schematically shown in Fig. 1.3. An ideal host-material for PICs supports low-loss passive components, like waveguides, beam-splitters and spectral filters, as well as active components like light sources (lasers, single-photon), detectors, and modulators, in which the material's optical properties are controlled electrically or optically.

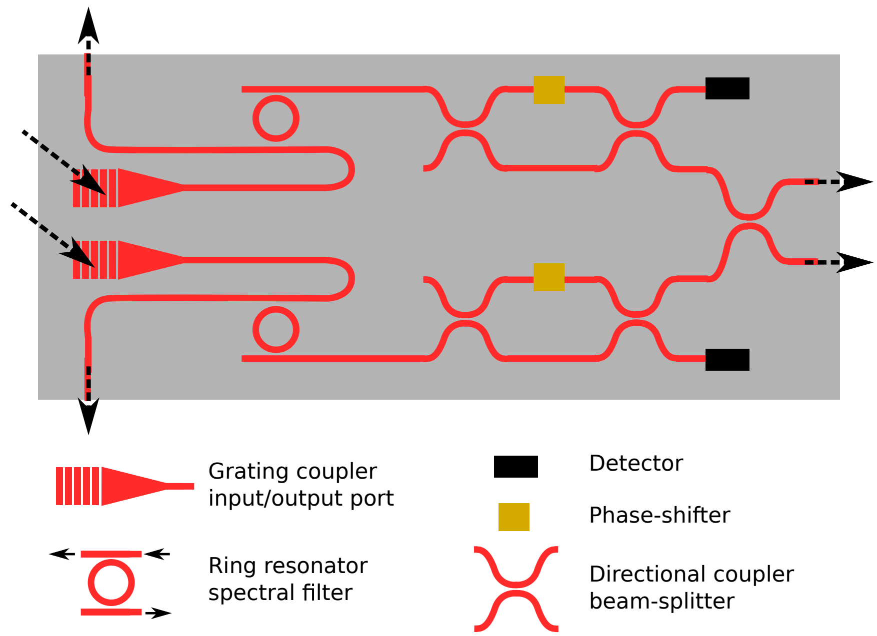

Figure 1.3: Schematic of a photonic integrated circuit, where optical components are defined in a high refractive index material, that sits on a slab of lower index index material (gray). Passive components including grating couplers, beam-splitters and spectral filters are shown, in addition to active components including phase-shifters and detectors. The dotted arrows show that light is routed elsewhere in the photonic circuit.

There are a number of different host-materials that have been explored for classical and quantum PICs, including most-significantly, silica-on-silicon, compound III-V semiconductors and silicon-on-insulator. Silica-on-silicon PICs have been widely employed, particularly for passive devices like waveguides and spectral filters (multiplexers and demultiplexers) [43], and to date, most PIC demonstrations of QI-relevant circuits have been in this platform [36, 69]. In this material system, silica is thermally grown on a silicon base and optical components are defined by doping the silica to change the refractive index. The most-significant advantage of this host-material is the small propagation loss that can be achieved with its relatively large cross section waveguides, that also affords efficient coupling to optical fibres. One primary disadvantage is that because the refractive index contrast is small, the critical angle for total internal reflection (TIR) is also small, which limits the bending radius of the waveguides, resulting in large device footprints (chip sizes on the order of several cm^2). In addition, these devices have limited active functionality. Index of refraction tuning, essential for phase-shifters in QI-related circuits, has been realized by integrating heating elements, however this process is inefficient and slow, due to the low thermo-optic coefficient of silica [36, 57]. Light sources and detectors are not viable in this platform without hybrid integration of more suitable active materials [33].

Compound III-V semiconductors, like InP, GaAs, GaInP, AlGaAs and InAs, are used to form compact devices with a number of active and passive functionalities. Many different types of devices have been successfully realized in this platform including lasers, detectors, modulators, single photon sources, photon pair sources, and optical switches [22, 35, 49, 62]. These semiconductor materials have direct electronic bandgaps, that make them excellent candidates for both classical and single-photon sources, as well as detectors [15, 42, 99]. The semiconductor crystal symmetry also supports a second order nonlinear susceptibility such that relatively efficient high speed electro-optic modulators are achievable. Many third order nonlinear processes, like four-wave mixing, have also been demonstrated, with relatively low nonlinear losses. These III-V PICs are in many ways the most versatile and successful to date, but in the context of high-volume manufacturing, of sophisticated opto-electronic circuits, they suffer from high material costs and a lack of well-developed foundries for mass manufacturing. The latter issue is related to another practical disadvantage, that large-scale microelectronic circuits are not manufactured in this platform, thus direct integration of optical and electronic components is not simple.

In contrast, silicon-on-insulator is highly attractive due to the central role that silicon plays in the semiconductor industry [37, 86, 87, 91], and the advanced complementary metal-oxide-semiconductor (CMOS) fabrication technologies that now exist for large scale manufacturing for both microelectronic and photonic circuits. Silicon-on-insulator (SOI) wafers contain a silicon device layer where optical components are defined by lithography and etching, that is supported by an oxide layer that is supported by a silicon base. Owing to the strong index contrast between silicon and the surrounding materials (oxide and air), TIR is strong, and compact silicon photonic devices are realized. There is a large academic and industrial research effort toward developing silicon PIC components, and a wide range of passive and active components have been realized [12, 78, 91, 97, 104]. However, the main drawback of working with silicon is its indirect bandgap, which makes it challenging to realize good sources and detectors. In addition, the centrosymmetry of the silicon prohibits second order nonlinear effects that are typically used for fast electro-optic switching in other host-materials. Alternative approaches are explored to overcome these issues. Silicon has a relatively strong third order nonlinear susceptibility, and third order nonlinear processes have been employed for all-optical signal processing devices and photon sources. Hybrid integration with other semiconductor materials has also seen some success, where laser sources and detectors made from III-V direct bandgap materials are wafer bonded to the silicon [91]. Ultra-sensitive detectors have also been realized by depositing and patterning superconducting materials on the silicon surface [1, 68].

1.2 Thesis motivation

The original motivation behind this work was to develop a photon source for quantum information processing in silicon photonic microchips. In quantum photonic technologies, a source that generates single photons either on demand, or at known times, is critical for photon state preparation and processing. One avenue for realizing an on-demand single photon source involves the deposition of quantum emitters, like quantum dots (semiconductor crystals with ~ 5 nm dimensions), on the silicon surface. A quantum dot acts like an "artificial atom" that emits a single photon when optically or electrically excited with a pulse [15]. This type of source is considered to be "deterministic", as there is control over when the photons are emitted. There are a number of technical challenges associated with ensuring the quantum emitter efficiently emits into the silicon microchip, often requiring a combination sophisticated device engineering and/or complex chemistry.

An alternative approach, the one taken in this thesis, takes advantage of the strong third order nonlinearity of silicon to spontaneously generate pairs of photons through a process called spontaneous four-wave mixing [17]. When the silicon device is excited with a single continuous-wave (CW) pump laser, signal and idler pairs of photons are spontaneously generated at two different frequencies, equally spaced above and below the pump frequency such that energy is conserved, as illustrated in Fig. 1.4(a). This process is proposed to realize "heralded" single photon sources, where the detection of one of the photons from a pair signals (or "heralds") the presence of the

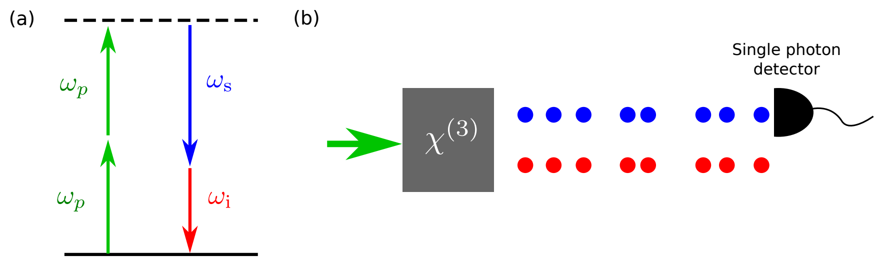

Figure 1.4: (a) Schematic of spontaneous four-wave mixing. Two "pump" photons with frequency ω_p are converted to a pair of "signal" and "idler" photons with frequencies ω_s and ω_i, respectively. Energy conservation requires that $2\omega_p = \omega_s + \omega_i$. (b) Spontaneous photon pair generation is implemented a heralded single photon source, when pumped with light at ω_p. The detection of a signal photon, by a single photon detector, heralds the presence of the idler photon.

other, as shown in Fig. 1.4(b). This source is non-determinstic, in that there is no control over when the pairs are generated. However, proposals have been suggested for achieving near-deterministic operation by multiplexing multiple sources and incorporating routing components like optical delays and switches [19, 101, 102]. The photon pair sources have also been used to realize quantum mechanically entangled photons, which also have applications in quantum information processing [29, 78, 97].

A silicon PIC was designed and fabricated for this purpose. In the process of characterizing its performance, specifically in comparing its nonlinear behaviour to model predictions, it was realized that owing to slight differences in the fabricated devices, as compared to the corresponding designs, many of the key model parameters had to be extracted from a non-trivial set of linear and nonlinear experiments, none directly associated with spontaneous pair generation. Some of these ancillary experiments are pertinent to other all-optical signal processing functions (alluded to above). In the end, the novel and sophisticated characterization scheme developed for this generic nonlinear structure became the main theme of the thesis.

1.3 Nonlinear processes in silicon

The nonlinear processes of interest to this thesis are first presented in the context of bulk silicon in Section 1.3.1. Applications based on these nonlinear processes are then discussed in Section 1.3.2, and examples of photonic structures that can be used to reduce the operating power and the footprint of nonlinear optical devices are reviewed in Section 1.3.3. The photonic structure pursued in this work is presented in Section 1.3.4.

1.3.1 Bulk silicon

Stimulated and spontaneous four-wave mixing (generating light at frequencies other than the driving frequency(s))

The nonlinear device presented in this thesis is specifically designed to promote pair generation through spontaneous four-wave mixing. Spontaneous four-wave mixing is a quantum mechanical nonlinear process, which is closely related to its classical counterpart, stimulated four-wave mixing. To help explain these third order nonlinear processes, classical nonlinear frequency mixing is first considered, using a simplified picture of nonlinear interactions (a more rigorous derivation for stimulated FWM is presented in Chapter 5).

In classical nonlinear frequency mixing, excitations at two or more different optical frequencies induce a nonlinear polarization density in the material that generates light at one or more new frequencies. For example, when excitations at optical frequencies ω_1 and ω_2 are present in material with a second order nonlinearity, the induced second order polarization density is $P^{(2)}(t) = \epsilon_0 \chi^{(2)} E(t)^2$, where $E(t)$ is the total electric field present and is approximately equal to $E_1 \cos(\omega_1 t) + E_2 \cos(\omega_2 t)$ (ignoring nonlinear field contributions) [14]. The polarization density in the medium thus contains contributions that go as $\sim \cos(\omega_1 t) \cos(\omega_2 t)$, that acts as a source that generates new electromagnetic fields at mixing frequencies $|\omega_1 \pm \omega_2|$.

In third order nonlinear materials, the polarization density depends on the field through $P^{(3)}(t) = \epsilon_0 \chi^{(3)} E(t)^3$. When excitations at two optical frequencies (derived from incident laser fields at ω_1 and ω_2) are present, the polarization density has contributions with $|\omega_x \pm \omega_y \pm \omega_z|$, where $\omega_x, \omega_y, \omega_z = \omega_1$ or ω_2. In stimulated four-wave mixing, light is generated at the new frequency $\omega_3 = |\pm\omega_2 \pm \omega_2 \mp \omega_1|$ through the third order nonlinear polarization density, where ω_1, ω_2 and ω_3 are commonly called the signal, pump and idler frequencies, respectively. In this process, two pump photons at the center frequency (ω_2) are mixed with one signal photon (at the other excitation frequency, ω_1) to generate an idler photon at the mixing frequency ω_3, where energy conservation requires $\omega_2 = (\omega_1 + \omega_3)/2$ (i.e. the three optical frequencies are equally spaced). The photon generation rate (i.e. power) at the idler frequency has a quadratic dependence on the pump power, and a linear dependence on the signal power.

When two continuous-wave lasers tuned to ω_1 and ω_2 are launched along the same axis into the bulk nonlinear material, the idler power depends on the degree to which the propagating optical modes involved in the conversion process (at ω_1, ω_2 and ω_3) are phase-matched.[1] This can be satisfied fairly naturally for FWM, by choosing $|\omega_2 - \omega_1|$ such that $|\omega_2 - \omega_1| << \omega_2$ and such that the bandwidth for the FWM process is narrow enough that the linear material dispersion is minimal.

In the spontaneous version of this process, only the pump excitation is present (ω_2), and vacuum fluctuations facilitate the conversion of two ω_2 pump photons to a pair of photons with frequencies ω_1 and ω_3. Alternatively, when two excitations are present at frequencies ω_1 and ω_3, two single photons at each of these frequencies are spontaneously converted to two photons at ω_2.

Kerr effect and two-photon absorption (modifying propagation properties at the driving frequency)

The Kerr nonlinearity is a classical third order nonlinear process which causes changes to both the real and imaginary parts of the refractive index of silicon, dependent on the field intensity. In contrast to the stimulated frequency mixing processes described above, where the third order polarization density oscillates at a new frequency, the Kerr nonlinearity arises due to polarization density contributions that oscillate at the excitation frequencies, through mixing processes like $|\pm\omega_1 \mp \omega_1 \pm \omega_1| = \omega_1$. In the linear limit, the refractive index is $n_0 = \sqrt{1+\chi^{(1)}}$, where $P^{(1)} = \epsilon_0 \chi^{(1)} E(t)$. When excitation at a single frequency is injected in the silicon, with electric field $E(t) = E_1 \cos(\omega_1 t)$, the Kerr nonlinearity introduces a third order polarization contribution that is proportional to both $E(t)$ and the field intensity I, such that the total polarization density is $P(t) \sim \epsilon_0 \left[\chi^{(1)} + \frac{3\chi^{(3)}}{2\epsilon_0 c n_0} I\right] E(t)$, and the nonlinear refractive index is $n_{\mathrm{NL}} \simeq n_0 + \frac{3\chi^{(3)}}{4n_0^2 \epsilon_0 c} I$.

In silicon, the real part of the $\chi^{(3)}$, at the frequencies of interest, is positive such that the real

[1] Phase matching means that the polarization density with oscillation frequency ω_3, which in general has a spatial dependence of $\exp(ik_3^{\mathrm{P}} z)$, where z is the propagation direction, will only efficiently generate electromagnetic fields at ω_3 if k_3^{P} matches the wavevector that light with frequency ω_3 propagates in the medium, $k_3 = \omega_3 n(\omega_3)/c$, where $n(\omega_3)$ is the refractive index at ω_3. The polarization density that arises from FWM is $k_3^{\mathrm{P}} = 2k_2 - k_1$, where $k_1 = \omega_1 n(\omega_1)/c$ and $k_2 = \omega_2 n(\omega_2)/c$, such that phase matching requires $\omega_3 n(\omega_3) = 2\omega_2 n(\omega_2) - \omega_1 n(\omega_1)$.

part of n_{NL} increases with intensity, thus introducing nonlinear dispersion. The imaginary part of the silicon $\chi^{(3)}$ is associated with two-photon absorption, a process in which two photons, with total energy $\omega_{\mathrm{tot}} \sim 2.4 \times 10^{15}$ rad/s (in units of $\hbar$), are absorbed to excite a free-carrier above the silicon electronic bandgap ($\Delta\omega_{\mathrm{Si}} = 1.68 \times 10^{15}$ rad/s). The absorption process is mediated by phonons to achieve momentum conservation across the indirect bandgap. Two-photon absorption has implications beyond directly introducing loss through the $\chi^{(3)}$-dependent refractive index. The free-carriers generated cause dispersion by lowering the real part of the refractive, and they also introduce further loss by absorbing radiation, thus adding yet another nonlinear contribution to the imaginary part of the refractive index. Furthermore, the power absorbed in both of these nonlinear processes result in thermal dispersion, such that the real part of the refractive index increases with heating. These "knock-on" effects can be described in terms of their contributions to an effective degenerate $\chi^{(3)}$.

In the discussions above, the $\chi^{(3)}$ is assumed to be a scalar, while in practice, it is a tensor that depends on the frequencies involved in the mixing processes. As such, the non-degenerate frequency mixing $\chi^{(3)}$ tensor, is different from degenerate nonlinear propagation $\chi^{(3)}$ tensor. However, for the cases considered in this thesis, the differences in the non-degenerate frequencies are so small that the $\chi^{(3)}$ tensor is effectively the same as that for degenerate mixing.

1.3.2 Applications of nonlinear processes in silicon

Frequency mixing

The original motivation of this work was to use spontaneous FWM in silicon to generate photon pairs for QI-related applications, including non-deterministic heralded single photon sources. It is interesting to note that second order nonlinear photon pair sources are currently the workhorses of bulk optical QI implementations, and also widely used for testing QI-related photonic circuits. These sources efficiently generate photon pairs through a second order process called "spontaneous parametric down-conversion" (SPDC), where a single pump photon is converted to two lower energy signal and idler photons [41]. Spontaneous FWM sources cannot, in general, serve as direct replacements for these sources, as SPDC sources can be operated in configurations where they generate photon pairs in quantum mechanically entangled states, which are of great interest in QI applications. It is not possible for spontaneous FWM sources to directly produce entangled photon pairs, however entangled states can be achieved by passing the photons through networks of beam-splitters and other optical components [29, 78, 97].

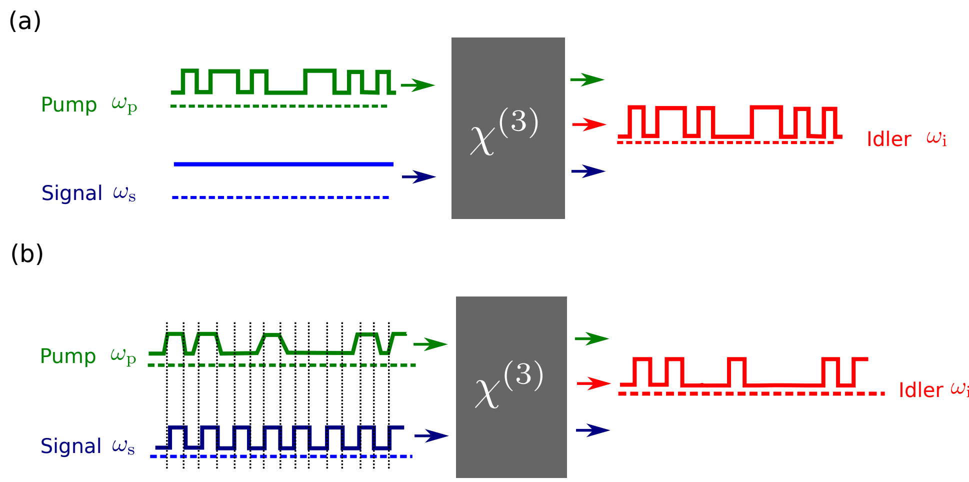

Figure 1.5: Schematic of stimulated four-wave mixing (FWM) signal processing applications. The signal, pump and idler frequencies are ω_s, ω_p and ω_i, where $2\omega_p = \omega_s + \omega_i$. (a) The signal-to-noise ratio (SNR) in a modulated amplitude signal (high and low amplitudes represent 1's and 0's, respectively) is reduced through the FWM process by translating the data signal from the pump light to idler light. The SNR is improved in the idler amplitude owing to the quadratic dependence of the idler power on the pump power. The schematic shows that the amplitude-modulated pump light undergoes frequency mixing with the unmodulated signal (ω_s) light, to produce modulated light at the idler frequency ω_i. Here the solid lines show the modulated signals, that sit above the no-power baselines (dashed-lines). (b) The timing jitter in a return-to-zero data stream (each bit is separated by a low amplitude time interval) is reduced by modulating the signal on the same clock, such that idler power can only be generated when the signal excitation is on.

Stimulated four-wave mixing has applications in classical quantum information processing, for various all-optical signal processing tasks [25, 74]. For example, this process can be used to distribute information over multiple frequency channels for parallel processing, as illustrated in Fig. 1.5(a). Information encoded in the modulated amplitude of an optical signal with carrier frequency ω_p (the pump), is translated to another frequency, ω_i (the idler), by activating a signal laser at $\omega_s = 2\omega_p - \omega_i$ which stimulates the four-wave mixing conversion process. Four-wave mixing is also used for improving the quality of optical signals by increasing the signal-to-noise and reducing the timing jitter, as illustrated in Fig. 1.5(a) and (b), respectively. In Fig. 1.5(a), when stimulated FWM is performed with an amplitude modulated pump excitation, and an unmodulated signal excitation, the idler light generated has a higher signal-to-noise than the pump due to the quadratic dependence on the pump power. The timing jitter is reduced when the signal is modulated on a clock that coincides with that of the pump, such that idler power can only be generated over the durations of time when the signal is active, as shown in Fig. 1.5(b). This approach is appropriate for "return-to-zero" data streams where there are time intervals between each bit when the signal is held in a low state.

The spontaneous and stimulated four-wave mixing applications are adversely affected by nonlinear absorption introduced by the Kerr nonlinearity. Input powers are raised to compensate for losses in the pump/signal excitations. In addition, absorption reduces the idler power in stimulated FWM applications and reduces pair generation rates in spontaneous four-wave mixing applications. In the context of heralded photon sources, the latter problem is two-fold, as the absorption of a single photon in a pair leads to a greater number of occurrences when the heralding photon triggers the detector in the absence of a partner photon [35].

Nonlinear dispersion

Nonlinear dispersion effects are employed to realize all-optical signal processing components like all-optical switches, all-optical bit memories and optical logic functions [3, 60, 63]. One basic approach taken involves using strong "pump" and weak "probe" excitations. The transmission response of the weak probe through the silicon device depends on the strength of the pump excitation that nonlinearly modifies the real part of the refractive index. When the transmission response function has a very strong dependence on the refractive index, low pump powers can achieve the desired control of the probe transmission. Optical resonators that contain nonlinear optical materials are commonly employed for this reason, as the resonant transmission frequencies are very sensitive to the refractive index.

In a high finesse optical resonator that contains a nonlinear optical material, high intensities of light build up inside the resonator when it is resonantly excited, such that nonlinear interactions can be achieved even with relatively low excitation powers. At very low incident powers the resonator effectively acts like a spectral filter, such that it only transmits light (and correspondingly only allows light within the resonator) with optical frequencies lying within the narrow-bandwidths of the resonant modes it supports. A probe excitation tuned to a resonant frequency is transmitted through the device, however its transmission is affected when a pump excitation, tuned near a different resonant mode frequency, is activated. The nonlinear change of the refractive index within the resonator induced by the pump causes the resonator mode frequencies to shift, such that the probe becomes non-resonant and its transmission significantly drops. This is the basic premise of all-optical switching.

There is also an "optical bistability" phenomenon that arises due to nonlinear dispersion in resonator structures, and plays an important role in a number of all-optical processing devices. Optical bistability is effectively a hysteresis in the resonator response function. In other words, the resonator response depends on the history of how it was probed. For example, when the transmission of light through the resonator is measured as a function of the excitation frequency, the resulting spectrum is different when the frequency is swept from low-to-high, as compared to when its swept high-to-low, and the nature of this altered spectrum depends on the incident power.

1.3.3 Efficient and compact nonlinear devices

For the bulk silicon nonlinear processes described above, the third order nonlinear polarization density is large when the local excitation intensity is high. A strong third order nonlinear response is achieved in bulk silicon when high excitation intensities are maintained over large volumes. Consider the case where the excitation is derived from laser light launched into the bulk silicon. A trivial way to increase the excitation intensity in the bulk silicon, is to simply increase the laser power. Alternatively, the laser can be tightly focused, such that a strong localized intensity is achieved. The highest intensity reached in a Gaussian beam is inversely proportional to the beam waist radius (at the narrowest point) squared. Away from the waist, the beam width diverges due to diffraction. The length over which the width is maintained below a factor of $\sqrt{2}$ of the waist radius, called the Raleigh length, is proportional to the beam waist squared. As a result, for focused lasers in bulk silicon, there is a trade-off between peak intensity and the volume over which a high intensity is maintained, that ultimately limits the achievable total nonlinear response for a given laser power. This means that in practice, nonlinear experiments in bulk silicon are almost always done with pulsed laser sources that have much higher peak power than CW sources.

The waveguides used to route light in PICs offer a simple and very effective means of avoiding this diffraction limit. Their cross-sectional areas are on the order of a squared wavelength, close to the diffraction limited area of a focused laser beam, but their Raleigh length is effectively the length of the waveguide itself. The effective distance of propagation over which the nonlinear interactions occur is thus increased over the bulk case by roughly the ratio of the waveguide length to the Raleigh length associated with a diffraction limited beam waist: this ratio can be huge. In four-wave mixing applications in silicon, CW pump powers of < 10 mW are launched into 1.0 cm long waveguides, and signal to idler conversion efficiencies of ~ -35 dB are observed [26]. As in the bulk case, it is critical that the three waveguide modes involved in the nonlinear process (at the pump, signal and idler frequencies) have propagation phases compatible with phase-matching. In the waveguides, the related mode dispersion is due to a combination of material dispersion and so called "waveguide dispersion" associated with the index contrast and waveguide dimensions.

The footprint of such a device can be dramatically reduced by turning a short segment of waveguide into a circular loop (radius $\sim 5 - 10$ μm), such that light circulates many times before eventually coupling out into a connecting waveguide. The structure described here is a ring resonator, that supports travelling wave resonant modes, such that only excitations with optical frequencies near the resonant mode frequencies are allowed to propagate in the ring. Over the phase-matching bandwidth of the waveguide, the modes frequencies are nearly equally spaced and, the mode profiles are spatially overlapping. This resonator structure is suitable for four-wave mixing applications, where the signal, pump and idler frequencies coincide with resonant modes. It is also suitable for the all-optical switching applications described above, as it supports multiple modes, and has a resonant response that is sensitive to nonlinear dispersion promoted in the ring.

Other types of travelling wave resonators are also considered for four-wave mixing applications, including pedestal microdisks and microtoroidal resonators [44, 72]. Light travels along the inner rim of the circular structure, which is suspended in air by a pedestal at its center, and is evanescently coupled to a tapered optical fibre for excitation and extraction. Silica microtoroidal whispering gallery mode resonators support very high quality factor modes ($Q > 10^8$) and demonstrate efficient frequency conversion spanning large bandwidths (cascaded over many modes), to create frequency combs [44]. However, these structures are not easily integrated into photonic circuits.

In general, resonator structures have the drawback of being narrowband (they only work if the excitation wavelengths correspond to the resonant mode frequencies). An alternative way to enhance the effective nonlinear interaction strength in a non-resonant manner is by engineering the dispersion of a straight waveguide to greatly reduce the group velocity of the relevant modes. By *slowing* the propagation speed of light, the relevant interaction *time* can be achieved over a much shorter propagation distance [9]. A common way to achieve "slow-light" is using photonic crystal waveguide structures [19, 56, 103]. In these structures, coherent scattering of submicron features etched in the silicon results in net propagation speeds of ~ 30 times smaller than the speed of light [9]. Photonic crystal waveguides $\sim$ several 100 μm long have been found to yield spontaneous four-wave mixing pair generation efficiencies ~ 20 times higher than centimeter long wire waveguides [35]. These compact structures are less amenable to the nonlinear dispersion applications discussed above as they are non-resonant.

The ultimate limit for reducing the footprint of nonlinear devices is reached by *stopping* light propagation. This is achieved with resonator structures that confine light for thousands or millions of optical cycles in cavities with dimensions on the order of a cubic wavelength. Section 1.4 explains how such resonators can be fabricated in silicon PICs using photonic crystal-based microcavities. These types of ultra-compact resonators have a footprint on the order 100 squared wavelengths, compared to a ring resonator, which typically occupies 1000 squared wavelengths. For optical switching applications, the smaller mode volume of these PC microcavities compared to ring resonators allow them to perform optical switching functions at reduced power levels. However, for FWM applications, a single PC microcavity can't be used since it typically supports only a single high Q mode.

One way to take advantage of these compact microresonators for FWM applications is to fabricate three copies in close enough proximity so that their nearly degenerate modes couple and form three distinct modes of a triple-cavity structure. A triple microcavity structure, was found to have spontaneous four-wave mixing photon generation rates 100 times greater than a ring resonator [8].

To realize efficient, low power, nonlinear devices based on optical resonators, like ring resonators and PC microcavities, it is critical that light is efficiently loaded in the microcavity, and unloaded into PIC waveguides. This requires careful engineering of the waveguide coupling. Single ring resonator structures are evanescently side coupled channel waveguides, with limited flexibility. In contrast, 2D PC microcavities offer a platform for flexible waveguide coupling, which adds to the the benefits of realizing nonlinear devices in this platform [58].

1.3.4 Nonlinear device design and performance

A photonic structure is proposed in this thesis, originally for use as an efficient photon pair source, but it is also well-suited for all-optical frequency conversion, and all-optical switching applications. A scanning electron microscope (SEM) image of the structure is shown in Fig. 1.6(a). It incorporates three coupled PC microcavities and two waveguides, and has a device area of $\sim 50\ \mu\mathrm{m}^2$. The structure is defined in an SOI wafer with a 220 nm device layer of silicon, that sits on 3 μm thick layer of $\mathrm{SiO_2}$ that lies on the silicon base.

Schematics of the excitation schemes used to measure the structure's nonlinear functionalities are shown in Figs. 1.6(b)-(d). Figure 1.6(b) illustrates that spontaneous four-wave mixing measurements involve resonantly coupling pump light from a single laser into the PC microcavity via the input waveguide, resulting in the generation of signal and idler photons in separate microcavity modes. These photons, along with pump microcavity photons, are coupled into the output waveguide, and directed off-chip for detection. Photons also leave the microcavity through other mechanisms, including coupling back into the input waveguide, scattering, and absorption in the silicon. The major challenge that the proposed design sought to overcome was to achieve preferential coupling of the signal and idler photons to the output waveguide, and preferential coupling of the pump photons to the input waveguide. In this work, attempted measurements of spontaneous FWM did not yield clear indications of photon pair generation, and future studies are required to understand the results from these measurements.

The frequency conversion is observed by resonantly exciting two modes of the microcavity using light from two lasers, such that idler photons are generated in a third resonant mode through stimulated four-wave mixing, as shown in Fig. 1.6(c). Across the four devices measured, the best frequency conversion efficiency (idler power divided by the product of the signal power and the squared pump power) is found to be $\eta^{\mathrm{P}}_{\mathrm{FWM}} = 1.4 \times 10^{-8}\ \mu\mathrm{W}^{-2}$, which is an order or magnitude higher than a comparable triple nanobeam photonic crystal microcavity [8] and ring resonator structures [5, 7, 92, 109].

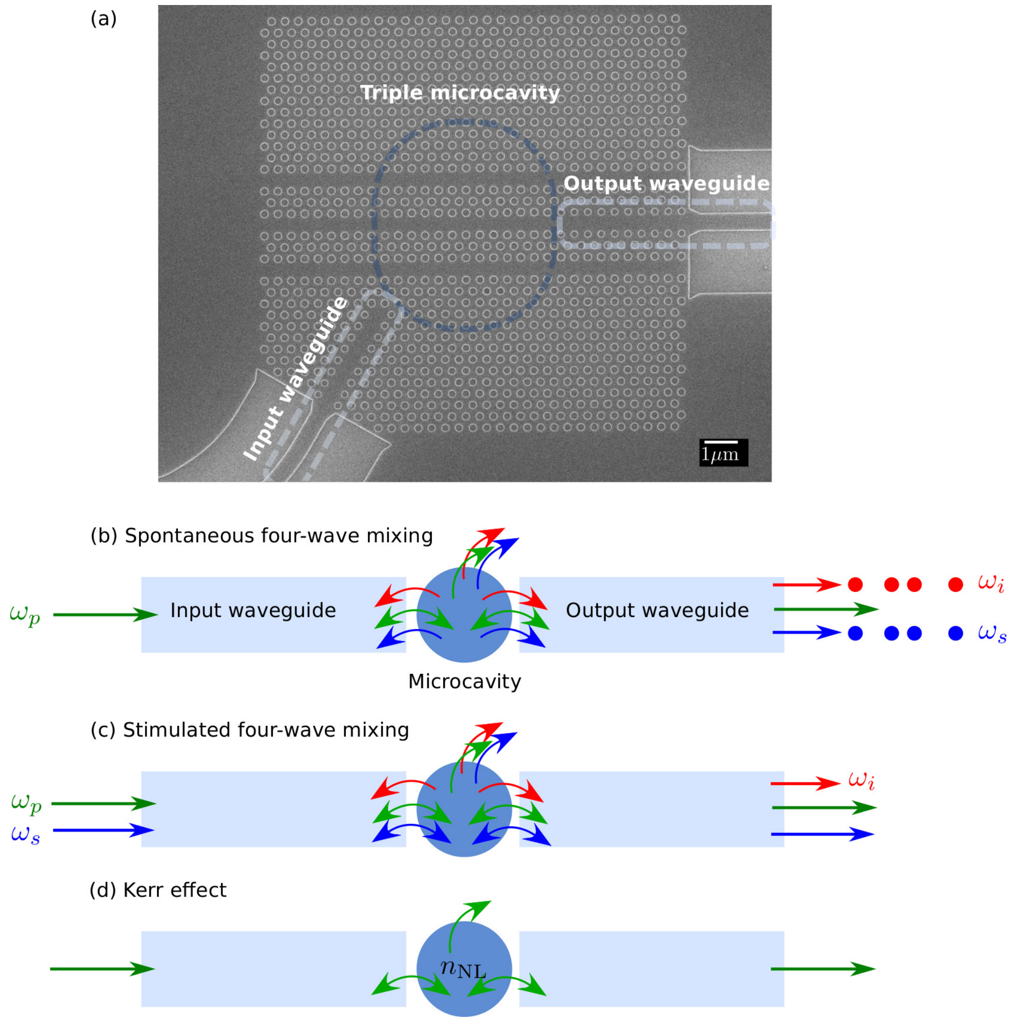

Figure 1.6: Proposed photonic crystal structure that supports multiple nonlinear functionalities. (a) Scanning electron microcavity image of a fabricated structure. The microcavity and waveguide regions are indicated. (b)-(d) Schematics of the microcavity (circle) coupled to input and output waveguides (rectangles) under different excitation schemes. The red, green and blue arrows show the passage of light at three different frequencies. (b) Spontaneous four-wave mixing. Pump light at ω_p (green) enters the input waveguide and resonantly excites a mode of the microcavity. Photon pairs are generated at signal and idler frequencies ω_s (blue) and ω_i (red), respectively, through spontaneous four-wave mixing. Energy conservation requires $2\omega_\mathrm{p} = \omega_\mathrm{s} + \omega_\mathrm{i}$, and the conversion process is only efficient where ω_s and ω_i pairs coincide with microcavity resonant modes. Photons leave the microcavity through coupling to the output waveguide, the input waveguide, and radiation, as indicated by the arrows. The microcavity photons are also absorbed by the silicon. (c) Stimulated four-wave mixing. Pump and signal excitations at ω_p (green) and ω_s (blue), respectively, resonantly excite two modes of the microcavity and photons are generated at the idler frequency ω_i (red). (c) Kerr effect. One mode of the microcavity is resonant probed with a single laser and the induced nonlinear changes to the microcavity refractive index affect transmission spectrum lineshape through resonant frequency shifts and decreased peak transmission.

The nonlinear Kerr effect, which is critical to all-optical switching applications, is demonstrated by exciting the microcavity with a single laser and measuring the transmission spectrum as a function of the laser power, as illustrated in Fig. 1.6(d). When probed at sufficiently high power, the nonlinear Kerr effect causes changes to the real and imaginary parts of the refractive index that results in shifts of the resonant wavelength and reduced transmission, such that the transmission lineshape becomes distinctly different from the Lorentzian lineshape observed at low powers. Based on the transmission spectra, it is possible to extract the minimum power threshold figure-of-merit, above which the Kerr effect is strong enough for the structure to be considered for all-optical processing applications. For the structures presented in this thesis, power thresholds as low as 17 μW are measured which compares well with those reported in the literature for 2D PC structures, which range from $\sim 10 - 200$ μW [11, 63, 84, 94].

1.4 Photonic crystal structures

A photonic crystal (PC) is a periodic arrangement of dielectric materials, and a planar two-dimensional (2D) PC is commonly realized by etching a periodic array of holes in a dielectric slab[61], as shown in Figs. 1.7(a) and (b). Planar photonic crystals are designed so that there is a range of frequencies over which light bound to the slab is prohibited from propagating in the crystal, called the photonic bandgap, which is analogous to the electronic band gap for an electron in an atomic lattice. The photonic bandgap plays important roles in common PC-based devices, slow-light waveguides and compact microcavities that strongly promote light-matter interactions.

Figure 1.7(c) shows the photonic bandstructure of a planar 2D PC, consisting of a high-index slab perforated by an hexagonal array of holes and surrounded by a uniform low-index region above and below. The bandstructure describes the electromagnetic modes supported by the PC at frequency ω, which obey Bloch's theorem, $\mathbf{E_k}(\mathbf{r}, \omega) = \exp(i\mathbf{k} \cdot \mathbf{r})\mathbf{u_k}(\mathbf{r}, \omega)$, where $\mathbf{u_k}(\mathbf{r}, \omega)$ is a periodic function, with lattice vector $\mathbf{a}$ in the plane of the slab, such that $\mathbf{u_k}(\mathbf{r} + \mathbf{a}, \omega) = \mathbf{u_k}(\mathbf{r}, \omega)$. This is alternatively stated as, $\mathbf{E_k}(\mathbf{r}+\mathbf{a}, \omega) = \exp(i\mathbf{k}\cdot\mathbf{a})\mathbf{E_k}(\mathbf{r}, \omega)$ [38]. Here modes are plotted for the three different axes of symmetry of the hexagonal PC structures. The $\mathbf{k}$ labels an electromagnetic mode that satisfies the Bloch equation with that $\mathbf{k}$ vector. There are two types of modes in this symmetrically clad slab, which appear in the bandstructure: transverse electric (TE) and transverse magnetic (TM). Transverse electric and magnetic modes have electric and magnetic

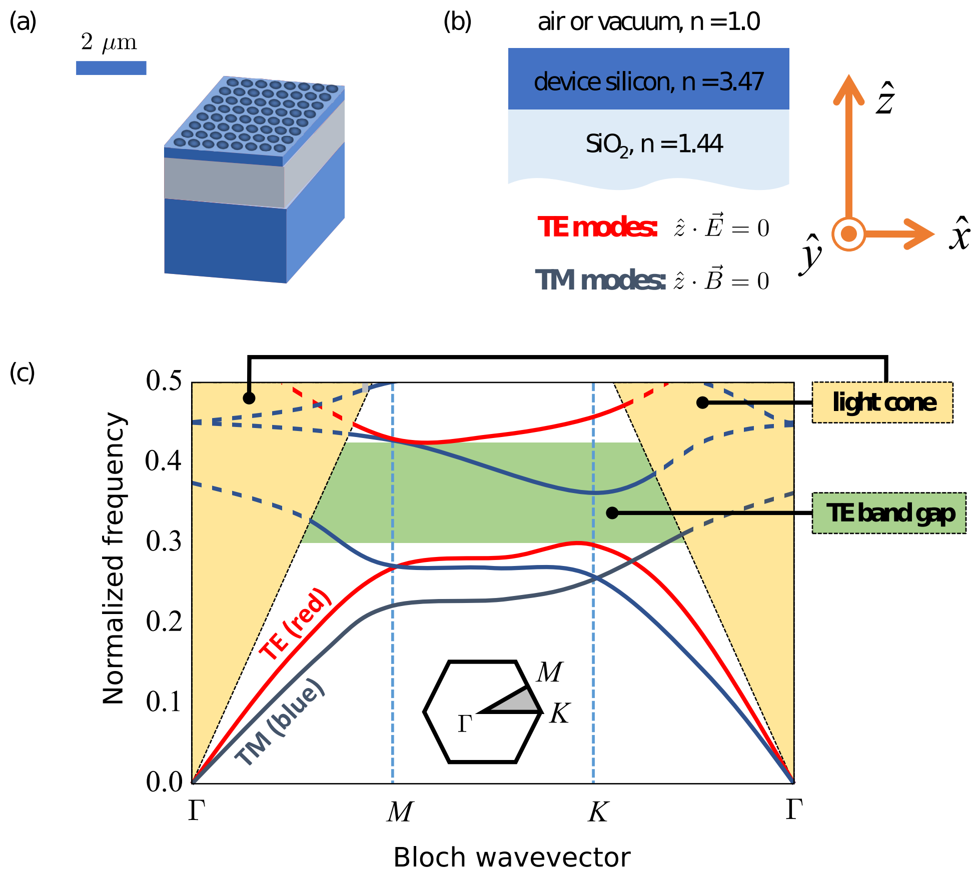

Figure 1.7: Planar photonic crystal defined in a silicon-on-insulator (SOI) wafer. (a) A hexagonal periodic lattice of holes is etched in the top silicon slab of the SOI, called the device silicon, which sits on an oxide layer and a silicon base. (b) Light is contained in the device silicon with respect to the $\hat{z}$ direction by total internal reflection (TIR) occuring at the air and SiO_2 oxide interfaces. The planar photonic crystal supports transverse-electric (TE) and transverse-magnetic (TM) modes. (c) Bandstructure of a PC, plotted as a function of the three reciprocal lattice vectors, in the first Brillouin zone. The TE and TM modes are shown as red and blue lines, respectively. The TE bandgap is indicated (shaded green), and the light cone is also indicated (shaded yellow). Modes that fall below of the light cone (solid lines) are bound to the device silicon through TIR, while those falling within the light cone are partially unbound (dashed lines). This figure is reproduced and modified, with permission, from Ref. [24].

field components that lie completely in the plane of the slab at its midpoint, respectively.

The bandstructure in Fig. 1.7(c) shows that the TE modes have a large photonic bandgap in thin slabs containing a periodic array of etched holes, which makes them ideal for device engineering. It is important to note that for 2D planar PCs, the bandgap is never a *full* bandgap, as there are always radiation modes that exist where $\omega \geq c|k|/n_s$, with n_s being the index of the material surrounding the slab (typically air and/or SiO_2). The presence of radiation modes goes hand in hand with the limitations of TIR in confining light to the slab. It is common to indicate the presence of the radiation modes in the bandstructure by including a "light-line" or "light-cone", as shown in Fig. 1.7(c). Modes that fall within the light cone (above the light-line) are called "quasi-bound" modes, while those that fall below the light-line are called "bound modes" as they are rigorously confined to the slab.

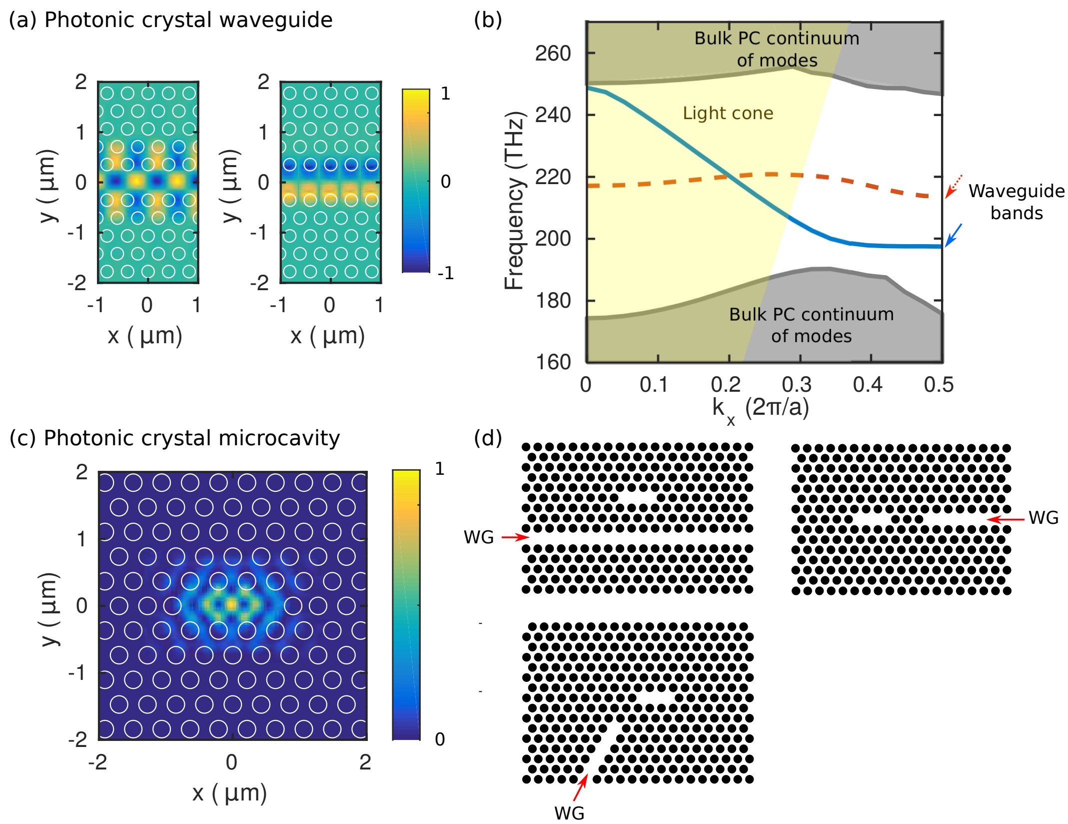

Figure 1.8: Photonic crystal (PC) defect structures defined in silicon-on-insulator. (a) Photonic crystal waveguide introduced to the PC by omitting a row of holes. The E_y field profiles in the center slab of the silicon for two different transverse electric waveguide modes are plotted, and the PC holes are outlined in white. (b) Bandstructure diagram for the line defect, plotted as a function of the wavevector along the waveguide axis, k_x, in units of $2\pi/a$, where a is the lattice spacing of the PC. The continuum of bulk PC modes are shown in gray. Two waveguide modes that exist in the bandgap are plotted as the solid blue and dashed red lines. The light cone is shown in pale yellow. The field profiles of the two modes at $k_x = \pi/a$ edge, indicated by solid and dotted arrows, are shown in (a), as the left and right plots, respectively. (c) Photonic crystal microcavity introduced to the PC by omitting three holes in a row, called an "L3" microcavity. The field intensity of the fundamental mode supported by the defect is plotted, and the holes are outlined in white. (d) Examples of coupling geometries between PC waveguides (WG) marked with red arrows and an L3 microcavity.

When a defect is introduced to the uniform photonic crystal structure, quasi-bound and bound modes can be introduced within the PC bandgap. A PC waveguide is created in a two-dimensional

(2D) planar PC by a omitting a line of holes [9, 53], as shown in Fig. 1.8(a). An example of the bandstructure along the waveguide axis is shown Fig. 1.8(b). In PC waveguides, light is transversely confined to the waveguide due to the absence of modes supported in the bulk photonic crystal. The guided light coherently scatters off the crystal as it propagates, making it possible to engineer very low group velocities, as exemplified by the flat dispersion curve. Photonic crystal waveguides are routinely used to achieve propagation speeds of $\sim c/30$, for applications requiring strong light-matter interactions.

Photonic crystal structures are not only used to slow light, but also to *stop* light. Microcavity resonators supporting standing-wave modes are realized in photonic crystals by perturbing the photonic crystal in a localized volume, like the example shown in Fig. 1.8(c). The microcavities provide a means to confine light to small volumes [$\sim (\lambda/n)$] for many optical cycles, creating an ideal environment for enhancing light-matter interactions. PC microcavities are considered for applications in a number of different fields included nonlinear optics, cavity quantum electrodynamics, optical trapping and optomechanics. Various designs have been proposed including linear hole defect structures [like the "L3" cavity in Fig. 1.8(c)] where one or more holes are omitted, heterostructure structures where the lattice spacing is perturbed, and mode gap structures where holes are shifted to create a defect region.

The oxide layer beneath the planar 2D PC microcavities is typically removed, in a process called "undercutting", to increase the photon cavity lifetime (and quality factor). The removal of SiO_2 increases the index contrast at the boundary ($n_{\mathrm{Si}} = 3.47, n_{\mathrm{SiO_2}} = 1.44, n_{\mathrm{air}} = 1$), resulting in a stronger TIR condition (or equivalently, making the light-cone smaller), such that radiation losses are reduced. This process has been found to improve quality factors by over an order of magnitude.

Light is coupled into and out of PC microcavities using PC waveguides that are brought in close enough proximity that their mode fields overlap. This is achieved using a variety of waveguide coupling schemes, like those shown for an L3 cavity in Fig. 1.8(d).

Ring resonators and nanobeam microcavities are two alternative compact microresonators considered for similar applications as 2D PC microcavities. Ring resonators typically have radii of $\sim 5-10\ \mu$m and $Q \sim 10^4$, and they support multiple modes separated by a free-spectral range, much like Fabry-Perot cavities. The free-spectral range is dependent on the waveguide mode/material dispersion. While the mode volumes of ring resonators are larger than 2D PC structures, they are competitive candidates for nonlinear applications owing to the multiple modes supported and the relative ease of fabrication. Nanobeam microcavities are another strong candidate. These are structures formed by patterning a one dimensional PC along a channel waveguide. These microcavities also benefit strongly from undercutting, and high Q undercut cavities with small mode volumes have been observed, comparable to those found for 2D PC structures. Two disadvantages of the nanobeam structure compared to the 2D PC structures is that they are less structurally stable after undercutting, and they offer less flexibility for waveguide coupling.

1.5 Dissertation overview

This thesis describes an efficient nonlinear integrated optical device structure that is thoroughly characterized using a novel combination of complementary experimental probes and associated nonlinear models. The device exhibits optical bistable behaviour at low excitation powers, and high efficiency frequency conversion (via stimulated four-wave mixing).

The primary focus of this work is on the device characterization, which is nontrivial in this structure primarily due to the presence of the two distinct waveguides coupled to the microcavity. The waveguide coupling strengths play important roles in controlling how much energy is coupled into the microcavity, and thus affect the magnitude of the nonlinear response. For a microcavity coupled to a single waveguide, the waveguide coupling strength is the same for both directions (assuming perfect fabrication), and so can be found from a straight-forward measurement, taken in the linear regime. As a result, the linear behaviour of the microcavity is reasonably well characterized, and the nonlinear behaviour can be studied directly [11, 94]. When a second microcavity-coupled waveguide is introduced, as is done here, it becomes impossible to determine both waveguide coupling strengths from the same, relatively simple, linear measurement. Numerical simulations provide good estimates for waveguide coupling strengths, so long as fabrication imperfections do not strongly affect them. Unfortunately, the current state of the art for SOI PC device fabrication does not satisfy this condition. As a result, it was necessary to develop a complex analysis protocol that takes into account, and relies on, a complete set of linear and nonlinear transmission, and stimulated FWM data.

Chapter 2 contains a basic overview of the linear transmission, nonlinear transmission (Kerr effect/bistability), and stimulated four-wave mixing spectroscopy measurement used in this work.

The device design and fabrication considerations are described in Chapter 3. The systematic procedure followed to design the photonic crystal structure, for spontaneous four-wave mixing, is outlined, and the numerical simulations that guide the design process are described. The design of the other circuit components, namely the input and output ports is also presented. An overview is also given of the fabrication layout, where critical device parameters are varied across the layout in an effort to ensure that at least a subset of the *actual* fabricated devices are similar to the *designed* devices. The "reference devices" included in the layout, which ultimately make it possible to estimate the contribution of the input and output ports to the total device response, are also described. Finally, the post-fabrication procedure used to undercut the fabricated devices is presented.

In Chapter 4, the initial measurements used to characterize the basic properties of the microcavity devices and lay the groundwork for the nonlinear measurements and characterization are presented. For example, to identify "good" microcavity candidates for four-wave mixing, which support three nearly equally spaced modes, the linear transmission spectra are surveyed for 56 devices across two microchips. The basic measurement scheme and results for stimulated four-wave mixing are presented for a good candidate device.

The main results of this work are presented in Chapter 5. Here the linear and nonlinear transmission results are reported, along with the four-wave mixing results, for four different triple-mode microcavity devices. The analysis procedure used to characterize the devices, and find the 15 microcavity parameters for each device that ultimately determine the device behaviour in the regimes of interest, is described. The best fit parameters are presented, and experimental data is compared to the model functions that contain these parameters.

In Chapter 6, the results presented in the previous chapter are discussed. The best fit parameters resulting from the analysis are compared to the literature and to numerical simulations. Two performance metrics for the nonlinear device are also compared to those in the literature: the stimulated four-wave mixing efficiency and the Kerr effect threshold power.

Finally, the conclusions of this work are presented in Chapter 7. The impact of this work is summarized here, and future work is proposed.

There are a number of appendices that are referenced within the body of the work. These appendices provide supplementary information on a range of different components of this work, including design, theory and analysis.

Chapter 2

General overview of linear and nonlinear measurements

Measurements of the linear and nonlinear functionalities of fabricated triple microcavity photonic crystal structures are central to this thesis. The measurements results not only help quantify the structure's suitability for frequency conversion and all-optical processing applications, but they are actually *required* in the characterization protocol used to extract the optical parameters necessary for creating a model that describes all nonlinear functionalities.

There are 15 unknown parameters that are sought after, which are summarized in Table 2.1. In the "linear" regime, when the microcavity is probed at low enough power that nonlinear effects are negligible, the parameters that dictate the response include the resonant wavelengths of the three resonant modes of interest, λ_m, and the lifetimes of different scattering and absorption processes that determine how light couples into and out of the microcavity, shown schematically in Fig. 2.1(a). The circle represents cavity mode m which has a standing wave pattern, and the rectangles represent the input and output PC waveguides. The black arrows show that light couples between the microcavity mode and the input and output waveguide modes with coupling lifetimes $\tau_{\mathrm{m}}^{\mathrm{in}}$ and $\tau_{\mathrm{m}}^{\mathrm{out}}$, respectively. The coupling strengths depend on the overlap between the cavity mode and the waveguide modes supported at the mode resonant frequency. Each mode has different coupling strengths to the input/output waveguides due to their distinct mode profiles, as shown in Figs. 2.1(b)-(d). The gray arrow shows that light can also couple out of the cavity through other mechanisms, like out-of-plane scattering and material absorption, with lifetimes $\tau_{\mathrm{m}}^{\mathrm{scatt}}$ and τ_{abs}, respectively. The absorption lifetime is not taken to be mode-dependent in this study, as it is expected to be very similar for each of the three modes, owing to the similar surface to volume ratios. Throughout this thesis, modes $m = 1, 2, 3$ refer to the lowest, middle and highest resonant wavelengths, respectively, and are also referred to as M1, M2 and M3.

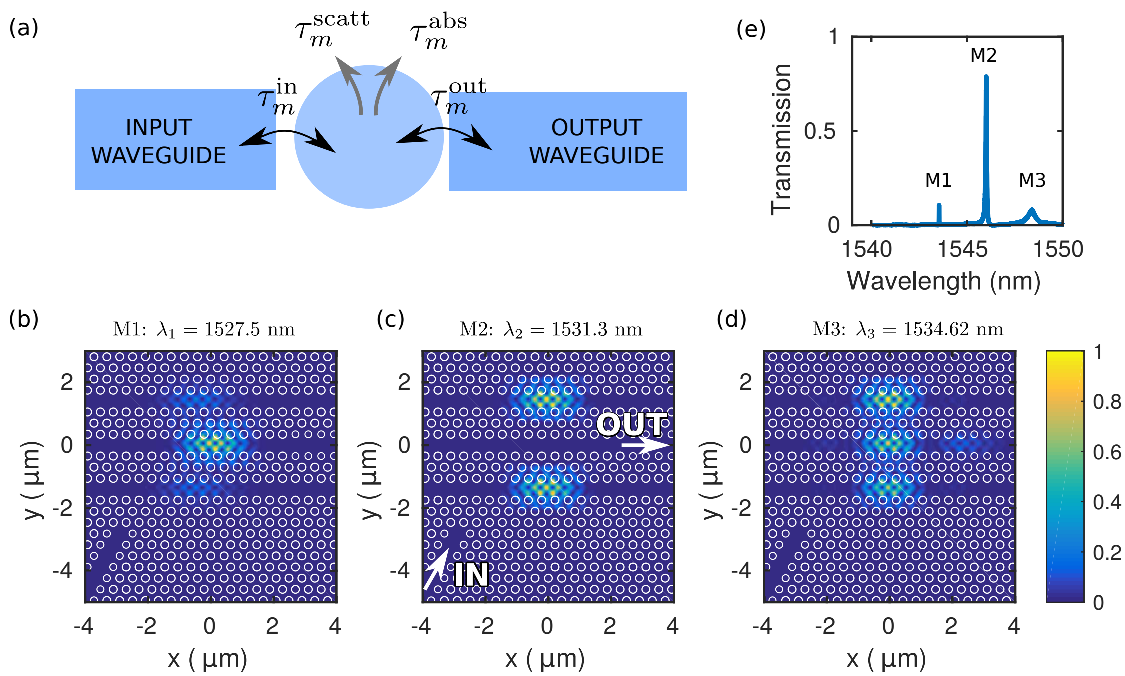

Figure 2.1: Triple photonic crystal (PC) microcavity coupled to input and ouput waveguides studied in this thesis. (a) Schematic diagram of the cavity modes coupling to various channels. The cavity is represented by the circle, while the waveguides are represented by rectangles. The coupling lifetimes for mode m are labelled, where $\tau_m^{\rm in}$ and $\tau_m^{\rm out}$ are the coupling lifetimes to the input and output waveguides, respectively, while $\tau_m^{\rm scatt}$ is the scattering lifetime and $\tau_m^{\rm abs}$ is the linear absorption lifetime. (b)-(d) Electric field intensity plots of modes M1, M2 and M3 (in that order). The PC holes are shown with white contours. The input and output waveguides are labelled is "IN" and "OUT". (e) Example of an experimental transmission spectrum measured in the linear regime for a triple microcavity device.

In the "nonlinear" regime, the optical Kerr effect leads to changes in both the real and imaginary parts of the refractive index, that impact the resonator response. The effective free-carrier lifetime, $\tau_{\rm carrier}$, and the thermal resistance, $R_{\rm th}$, are two microcavity parameters that determine the change in free carrier density and sample temperature as a function of excitation power. Excitation-power-depedent free-carrier density and microcavity temperature contribute to the nonlinear shifts of the cavity resonant frequency and Q value. There are other important parameters related directly or indirectly to the nonlinear response that are known for bulk silicon, and therefore do not have to be found in the characterization process. They include: the two-photon absorption coefficient, $\beta_{\rm TPA}$, the free-carrier absorption cross-section, $\sigma_{\rm FCA}$, the electron and hole free-carrier dispersion

Table 2.1: Summary of the linear and nonlinear microcavity parameters. The subscript m labels the microcavity modes, of which there are three. The number of unknown parameters of each type are listed in the "Unknown" column. The nonlinear parameters that are known for bulk silicon have no entry in this column. The number of unknown parameters that enter the model functions for the linear transmission (LT), nonlinear transmission (NLT), and stimulated four-wave mixing (FWM) measurements are indicated, and check marks indicate which of the known parameters are also included. The NLT model contains parameters for $m = 1$ and 2 only, as only these two modes are measured.

Parameter	Description	Unknown	LT	NLT	FWM
λ_m	Resonant wavelength	3	3	2	3
τ_m^{in}	Input waveguide coupling lifetime	3	3	2	3
τ_m^{out}	Output waveguide coupling lifetime	3	3	2	3
τ_m^{scatt}	Scattering lifetime	3	3	2	3
τ_{abs}	Linear material absorption lifetime	1	1	1	1
R_{th}	Thermal resistance	1		1	
τ_{carrier}	Effective free-carrier lifetime	1		1	1
β_{TPA}	Two-photon absorption coefficient			✓	✓
σ_{FCA}	Free-carrier absorption cross-section			✓	✓
ζ_{FCD}	Free-carrier dispersion nonlinear parameter			✓	
dn/dT	Refractive index temperature dependence			✓	
β_{FWM}	† FWM conversion coefficient				✓
	Total unknown parameters	15	13	11	14

† Calculated using $\chi^{(3)}$ for silicon (known) and numerical simulations.

parameter, $\zeta_{\text{FCD}}^{\text{e,h}}$, and temperature dependent index change of bulk silicon, dn/dT. Four-wave mixing also depends on the conversion coefficient β_{FWM}, which captures the strength of the third order susceptibility, $\chi^{(3)}$, and the overlap between the three modes involved in the process, and is well-estimated using numerical simulations.

Linear transmission spectra, measured at low power, directly and almost trivially provide nine pieces of information about the linear microcavity response: the resonant wavelength, λ_m, the peak relative transmission (normalized to the input power), $\overline{T}_m^{\text{lin}}$, and the total lifetime, τ_m^{lin}, for all three modes. However, the linear transmission model depends on 13 linear parameters [see the "LT" (linear transmission) column of Table 2.1]. So while the three λ_m are directly extracted from the linear transmission spectra, there are only 6 pieces of information about the unknown 10 lifetimes.

It is evident that this measurement alone is not sufficient for extracting all unknown microcavity parameters. Supplemental measurements in the nonlinear regime are required to provide necessary additional information on the linear parameters, and to extract the effective free carrier lifetime and thermal resistance parameters.

Measurements of the optical Kerr effect and stimulated frequency conversion together provide enough supplemental information about the optical response to reliably extract all unknown parameters. The optical Kerr effect is observed by measuring the transmission spectrum as a function of the input laser power. Specifically, in the nonlinear regime, the resonant wavelength undergoes a shift, $\Delta\lambda_m^{\mathrm{NL}}$, and the peak transmission, $\overline{T}_m^{\mathrm{NL}}$, decreases. For the structures studied in this thesis, two of the three modes have sufficiently high Qs that enough energy is loaded in the modes to induce observable nonlinear effects (for the laser powers accessible). The nonlinear transmission $\Delta\lambda_m^{\mathrm{NL}}$ and $\overline{T}_m^{\mathrm{NL}}$ for the two modes involved in the analysis are modelled using 11 unknown parameters, as shown in the "NLT" (nonlinear transmission) column of Table 2.1.

Frequency conversion is measured by resonantly exciting two modes of the microcavity using two lasers, and the power generated in the third mode through stimulated four-wave mixing is recorded as a function of one of the input powers, while the other is held fixed. There are two different excitation configurations (excite M1 and M2, or excite M2 and M3), resulting in a total of four data sets. The model that simultaneously describes both excitation configurations involves 14 unknown parameters, as shown in the "FWM" column of Table 2.1.

Conceptually, and in practice, the data obtained from the linear transmission spectra of each of the three modes, the nonlinear transmission of the two high Q modes, and the stimulated FWM power-dependent conversion efficiencies can be, and are, all combined into a single, least-squares analysis, where the squared differences between the experimental results and their respective model functions are globally minimized to extract a unique set of device parameters that adequately explain all linear and nonlinear behaviours. This approach was in fact only used after following a slightly different way of separately and iteratively applying a least-squares analysis to the nonlinear transmission and stimulated FWM data. While both approaches yield the same final result, the latter was used originally because it was more intuitive, and helped reveal useful information about correlations that exist between various parameters when focused on just one or the other of these nonlinear datasets.

2.1 Transmission in linear regime

In linear transmission measurements, light from a single laser is coupled into the microcavity, and out-coupled light is studied as a function of the laser wavelength. This is in many ways similar to the transmission measurement of a conventional macroscopic Fabry-Perot cavity, which is first reviewed here, before considering a more complex microcavity system.

2.1.1 Fabry-Perot cavity transmission

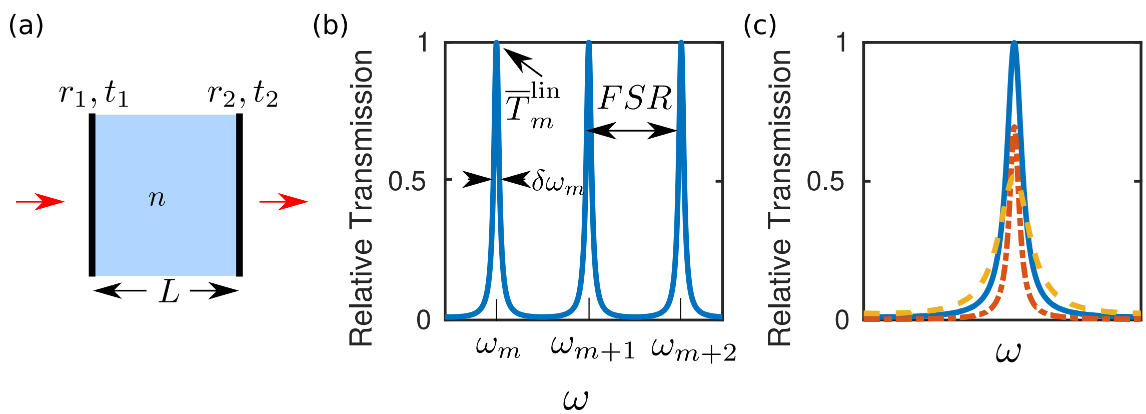

Figure 2.2: Fabry-Perot cavity. (a) Schematic of a Fabry-Perot cavity with two mirrors separated by a distance L, containing a medium with refractive index n. The mirrors have field transmission and reflection coefficients r_i and t_i. (b) Example relative transmission spectrum of a lossless Fabry-Perot cavity with identical mirrors. The resonant frequencies, ω_m are labelled, along with the linewidth $\delta\omega_m$ and maximum transmission $\overline{T}_m^{\text{lin}}$ for mode m. The free spectral range (FSR) is also labelled. (c) Relative transmission spectra for lossless cavity with identical mirrors (solid line), a cavity with loss and identical mirrors (dashed line), and a losses cavity with non-identical mirrors (dash-dotted line).

The simple Fabry-Perot cavity consists of two parallel flat mirrors with field reflectance r and transmittance t, as shown in Fig. 2.2(a), separated by distance L, containing a dielectric medium with refractive index n. In the transmission measurement, the light from single a continuous-wave (CW) laser is incident through one of the cavity mirrors and the light transmitted through the second mirror at the output of the cavity is measured. An example transmission spectrum is plotted as the solid line in Figs. 2.2(b) and (c), for the case where two mirrors are identical and there is no loss inside the cavity. This is a *relative* transmission spectrum, calculated by dividing the transmitted power after the second mirror by the power incident on the first mirror.

The peaks in the spectrum correspond to the resonant modes characteristic of the cavity, where the round-trip phase of light circulating the cavity is an integer multiple of 2π. The resonant modes are separated by the free spectral range,

$$\mathrm{FSR} = \frac{\pi c}{n_g L} \tag{2.1}$$

where c is the speed of light in vacuum, n_g is the group velocity of light the cavity dielectric medium, and L is the length of the cavity. In the following, dispersion is ignored such that $n_g = n =$ constant, and $\omega_m = m\mathrm{FSR}$, where m is the mode number.

Each resonant peak has three important features, which are labelled in Fig. 2.2(b): the resonant frequency, ω_m, the linewidth $\delta\omega_m$, and the maximum relative transmission, $\overline{T}_m^{\mathrm{lin}}$. These parameters contain information about the cavity geometry, material, and mirrors.

The linewidth, $\delta\omega_m$, is the full-width at half-maximum (FWHM) of the resonant transmission peak, and is given by,

$$\delta\omega_m = \frac{\mathrm{FSR}}{\mathscr{F}} \tag{2.2}$$

where $\mathscr{F} = \pi/(1-\sqrt{R_1 R_2})$ is the cavity finesse, and $R_1 = |r_1|^2$ and $R_2 = |r_2|^2$ are the intensity reflection coefficients for the first and second mirrors, respectively [2]. When the mirror reflectivities are high, such that $\mathscr{F}$ is large, the linewidth is small because light trapped in the cavity undergoes many optical cycles before leaking out, so only a small detuning of the laser frequency off-resonance leads to a large amount of destructive interference within the cavity, resulting in a low steady-state energy in the cavity and a drop in the transmission. The linewidth is related to the lifetime of photons in the cavity, τ_{m}, by,

$$\tau_m = \frac{2\mathscr{F}}{\mathrm{FSR}} = \frac{2}{\delta\omega_m}, \tag{2.3}$$

The photon lifetime is also expressed in units of the oscillation period using the quality factor, Q,

$$Q_{\mathrm{m}} = \tau_m \omega_{\mathrm{m}}/2 = \frac{\delta\omega_m}{\omega_m} = m\mathscr{F}. \tag{2.4}$$

[2]Here the cavity is assumed to be a "good" resonator with $R_1 R_2 \simeq 1$, such that it is appropriate to express the finesse $\mathscr{F} = \pi(R_1 R_2)^{1/4}/(1-\sqrt{R_1 R_2})$ to the lowest order of $(1-\sqrt{R_1 R_2})$.

Both $\mathscr{F}$ and Q are useful dimensionless parameters used to describe the strength of a resonator. For macroscopic cavities, it is sometimes more practical to work with $\mathscr{F}$ because m can be very large for the resonant modes in the laser wavelength range ($m \sim 10^5$).

For the transmission spectrum in Fig. 2.2(c), the maximum transmission relative to the input power outside of the first mirror, $\overline{T}_m^{\text{lin}}$, is unity. This is a signature of a lossless cavity with equal mirror reflectivities. When losses are introduced in the cavity, due to material absorption, scattering and other effects, $\overline{T}_m^{\text{lin}}$ is reduced along with τ_m, Q_m and $\mathscr{F}_m$, resulting in a broadening of the resonant linewidth, $\delta\omega_{\text{m}}$, as shown in the dashed line in Fig. 2.2(c). The transmission peak also falls below unity when the mirrors have different reflectivities, as is shown by the dash-dotted line in Fig. 2.2(c). This can be qualitatively understood by considering that when the reflectivities are equal, light resonantly reflected from the cavity completely destructively interferes with the non-resonantly (directly) reflected light off the first mirror, resulting in no reflected light. When the mirror reflectivities are unbalanced, this destructive interference condition is no longer met due to an imbalance in the resonantly and non-resonantly reflected light, resulting in some net reflection on resonance.

While the intensity of the output wave can never exceed the intensity of the input wave (i.e. $\overline{T}_m^{\text{lin}} \leq 1$), the intensity of light circulating in the cavity when excited on resonance can be significantly larger than the input intensity. For example, consider a lossless cavity with equal mirror reflectivities, probed on resonance. Given that the cavity transmission is unity, the right-ward travelling wave *inside* the microcavity has intensity $I_{\text{right}} = I_{\text{out}}/T = I_{\text{in}}/T$, where I_{in} and I_{out} are the input and output wave intensities (outside of the cavity), and $T = |t|^2$ is the transmission of the mirror. When T is very small, as true for a high finesse cavity, $I_{\text{right}} >> I_{\text{in}}$, and in the limit of high finesse, $I_{\text{right}} \simeq (\mathscr{F}_m/2\pi)I_{\text{in}}$ [85]. In a high finesse cavity, there are both right-ward and left-ward travelling waves with close to equal amplitudes, such that a sinusoidal standing-wave pattern is formed, and the total intracavity intensity as a function of position z is,

$$I_{\text{cav}}(z) \simeq \left|\sqrt{I}\exp(ikz) - \sqrt{I}\exp(-ikz)\right|^2 = 4I\sin^2(kz) \tag{2.5}$$

where $I = I_{\text{right}} \simeq I_{\text{left}}$, and $k = \omega n/c$ is the propagation wavevector inside the cavity. This results

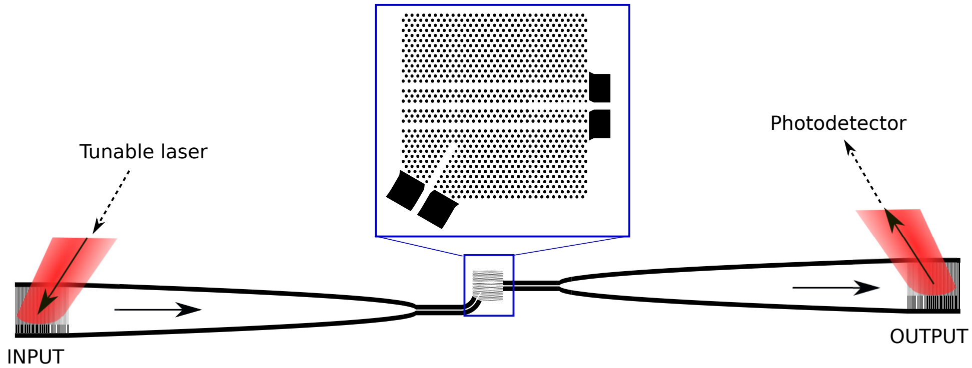

Figure 2.3: Simplified schematic of transmission measurement of photonic crystal (PC) triple microcavity device. Light from a tunable laser is focused on the input grating coupler and diffracted into a parabolic waveguide that narrows to a single-mode channel waveguide. This waveguide is interfaced with the input PC waveguide, which couples the microcavity. Light is extracted from the microcavity through the ouput PC waveguide, which is coupled to channel and parabolic waveguides terminated by the output grating coupler. The extract light is measured by a photodetector.

in a maximum cavity intensity of $\simeq (2\mathscr{F}_m/\pi)I_{\text{in}}$. The cavity enhancement of the field intensity plays an important role in promoting light-matter interactions for the nonlinear processes explored in this thesis.

Despite some major physical differences between a planar three-dimensional photonic crystal microcavity and the macroscopic Fabry-Perot cavity, both transmission spectra have the same three main features discussed above (ω_m, $\delta\omega_m$, and $\overline{T}_m^{\text{lin}}$).

2.1.2 Microcavity transmission

A simplified schematic of the measurement scheme used to study the transmission through microcavities is illustrated in Fig. 2.3. A more detailed schematic and description is given later, with other technical considerations in Section 2.1.3. The PC waveguides adjacent to the microcavity are coupled to channel waveguides that are expanded parabolically and terminated by grating couplers, which play the role of input/output ports. In transmission measurements, light from a single tunable CW laser is focused on the input grating coupler to launch light into the waveguides, while light leaving the output grating coupler is collected and sent to a photodetector.

The transmission spectrum for the single PC microcavity structure in Fig. 2.4(a), shown in Fig. 2.4(b), has a Lorentzian lineshape, and λ_m, $\delta\lambda_m$, and $T_{\text{m}}^{\text{lin}}$ are labelled. The transmission spectrum is obtained by dividing the spectrum at the output PC waveguide (the point labelled A in Fig.

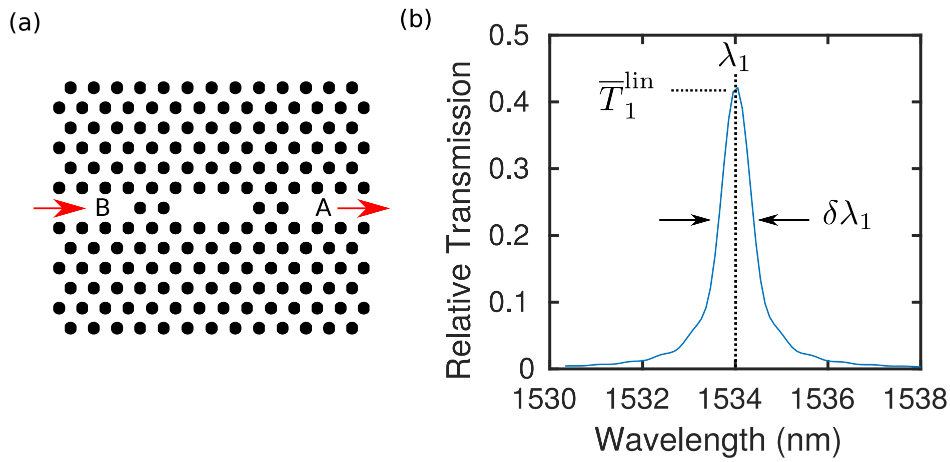

Figure 2.4: Single photonic crystal linear three hole defect (L3) microcavity with input and output waveguides. (a) Schematic of the microcavity, where black circles indicate holes etched in the silicon. The red arrows show the passage of light through the device for transmission measurements. (b) Transmission spectrum for the fundamental mode of an L3 cavity simulated with a finite-difference time-domain simulation. The resonant wavelength, λ_1, linewidth, $\delta\lambda_1$ and maximum transmission $\overline{T}_1^{\rm lin}$ are labelled.

2.4(a)) by the spectrum at the input PC waveguide (the point labelled B in Fig. 2.4(a)), such that the effects of all other optical and device components are excluded. The way in which these two spectra are determined is described in Section 2.1.3.

When contrasting the microcavity linear transmission spectrum in Fig. 2.4(a) with the Fabry-Perot transmission spectrum in Fig. 2.2(b), one superficial difference is that the microcavity transmission spectrum is plotted as a function of wavelength λ, as opposed to frequency, ω, in order to be consistent with the majority of the literature considered in this thesis. As such, the linewidth is labelled as $\delta\lambda$, and the Q is well approximated by $Q_m = \delta\lambda_m/\lambda_m$, so long as $\delta\lambda_m << \lambda_m$, which is true for the microcavities studied here.

One *important* difference between the microcavity and Fabry-Perot spectra is that the former contains only a single mode of interest. While multiple modes can be supported by these microcavities, the free spectral range is enormous compared to typical macroscopic resonator cavities, owing to the short microcavity "length" that is on the order of λ. As a result, one typically works with a microcavity mode with mode number $m = 1$, instead of $m \sim 10^5$ for macroscopic cavities. Given the low order of the modes considered for microcavities, it is common practice to quote the Q, instead of the finesse $\mathscr{F}$. When $m = 1$, Q serves as a good estimate of the cavity enhancement, where $\max(I_{\rm cav}) \simeq (2\mathscr{F}/\pi)I_{\rm in} \simeq QI_{\rm in}$.

The large free-spectral range of this single wavelength-scale microcavity makes this resonator structure a poor candidate of four-wave mixing processes, which involve frequency mixing between light simultaneously in three resonant modes separated by a tiny fraction of the centre frequency. Ideally, all three modes are close to $\lambda = 1545$ nm, nearly equally spaced in wavelength, and within the laser tuning range. This can be achieved using these low-order microcavity modes by including three such cavities in close proximity, as shown in Fig. 2.1. In this structure, three nearly identical cavities are fabricated in close proximity to form a coupled-resonator system. The coupled cavity system modes in Fig. 2.1 are a result of degenerate mode splitting. Transmission spectra of coupled-cavity devices show peaks associated with each of the three modes, with an example shown in Fig. 2.1(e). Each mode has a distinct set of λ_m, $\delta\lambda$ and $\overline{T}_m^{\text{lin}}$, as determined by the various rates at which energy in the three distinct modes dissipates to the environment.

2.1.3 Technical considerations

Transmission set-up

The transmission set-up used to measure the triple cavity devices is illustrated in Fig. 2.5. Light from a Venturi TLB 6600 Swept-Wavelength Tunable Laser is coupled into a single mode fibre (mode-field diameter 10.4 μm), and light exiting the fibre passes through a $\hat{\mathbf{y}}$-polarized linear polarizer (consistent with transverse electric excitation of the grating coupler) then is focused on the silicon chip surface using a pair of aspherical lenses (Thorlabs AL2550-C: focal length 50 mm, diameter 25 mm, numerical aperture 0.230). The focusing optics are arranged to produce one-to-one imaging, such that the spot on the sample (chip) is approximately 10 μm (verified using a knife edge measurement [10]). Light is collected off the chip surface using an elliptical mirror (numerical aperture ~ 0.06) placed 15 cm away from the sample that focuses light scattering from the chip surface at 1.5 m from the mirror, resulting in a 10$\times$ magnification factor. The collected light is reflected off Mirror 1, and is then sent through a linear polarizer (also $\hat{\mathbf{y}}$-polarized) and an iris before it's incident the Newport 818-G photodetector. Mirror 1 is adjusted to direct only the light from output grating coupler through the iris. While the elliptical mirror remains fixed, both the excitation optics (lenses and input polarizer) and the sample are mounted on x, y, z translation

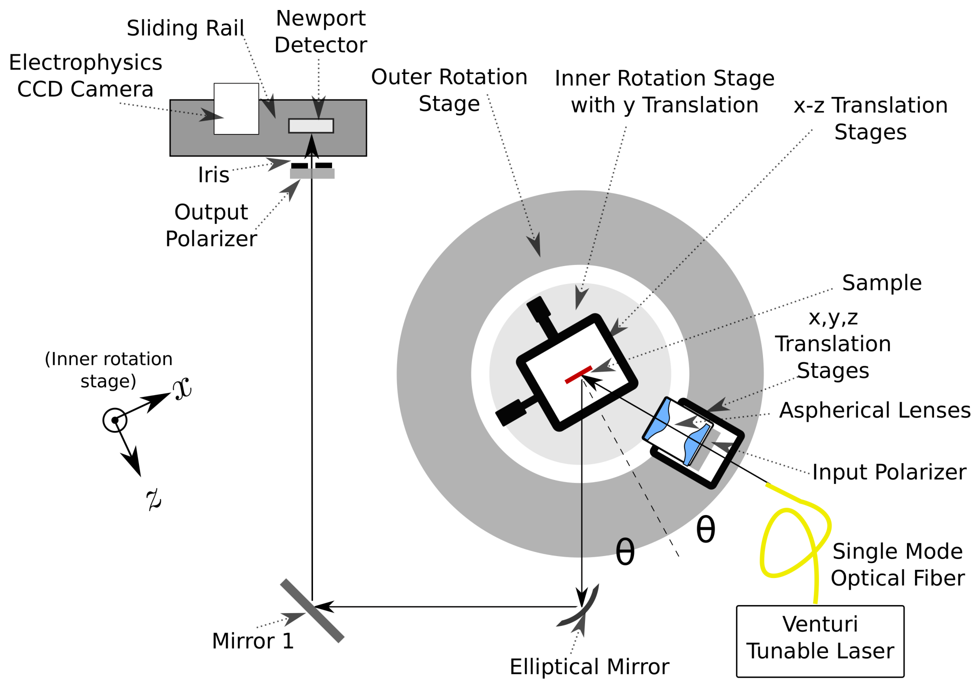

Figure 2.5: Transmission set-up. Light from a tunable laser is coupled into an optical fibre, and the out-coupled light passes through a polarizer ($\hat{\mathbf{y}}$-polarized) then is focused by two aspherical lenses onto the input grating coupler of a device on the sample (see Fig. 2.3), at an angle θ. Light leaving the output grating coupler is collected by an elliptical mirror (also at angle θ) that directs light through the output polarizer also $\hat{\mathbf{y}}$-polarized) and focuses it in a plane of an iris, and only the output grating light is passed onto a photodetector. Alternatively, the iris is left open and the sample is imaged on the CCD Camera.

stages to facilitate alignment. They are also mounted on separate rotation stages, making it possible to send/collect light over a range of angles, θ. This angular flexibility is important for grating coupling, as discussed in Section 3.2.2. In the initial alignment stages, the photodetector is replaced by an Electrophysics CCD camera (model 7290), such that the sample image is viewed.

Provided that each mode is spaced at least a couple linewidths away from neighbouring modes, it is possible to identify the three main spectral features distinct for each mode. The measurement apparatus and device components are typically optimized to work within a range of wavelengths, so ideally the modes also are spaced close enough together such that they all can be probed using only one measurement configuration.

Transmission normalization

One of the key pieces of information extracted from the relative transmission spectra is the absolute value at resonance. This quantity requires knowledge of the power in the input and output waveguides directly before and after the microcavity, respectively, which are not directly accessible. In typical transmission measurements, power measurements occur outside of the device, either in free-space or using optical fibers. There are often a number of optical elements between where the input/output powers are measured and the input/output waveguides. Some of these elements belong to the optical set-up (e.g. mirrors, lenses, polarizers), others are in the device itself (grating couplers, waveguides, impedance matching waveguide couplers that interface PC and channel waveguides, etc), as shown in Fig. 2.5. These components cause losses in the system that need to be accounted for to properly determine the power at the input/output PC waveguides. Some of these components also have spectral dependences that need to be carefully measured, and included in the normalization of the transmission spectrum.

It is possible to characterize the optical components that lie outside of the device on an individual basis. It is typically very difficult or impossible to characterize the intermediate components within the actual device of interest, so it is common practice to use *reference* devices, that contain isolated (or grouped) *identical* components that are studied separately. Of course, this method is only suitable so long as fabrication inconsistencies are minimal, and the reference components represent the actual device components well. This is generally true for the devices studied in this thesis, with the exception of one issue. Fabry-Perot interference between different circuit elements leads to parasitic sinusoidal modulations of the transmitted light intensity, which are phase-shifted from device to device. To deal with this issue, two unknown phase shift parameters, ϕ_{in} and ϕ_{out}, enter the least-squares analysis and are extracted as fit parameters, for each device. The transmission normalization procedure is described in greater detail in Appendix D.

2.2 Nonlinear transmission

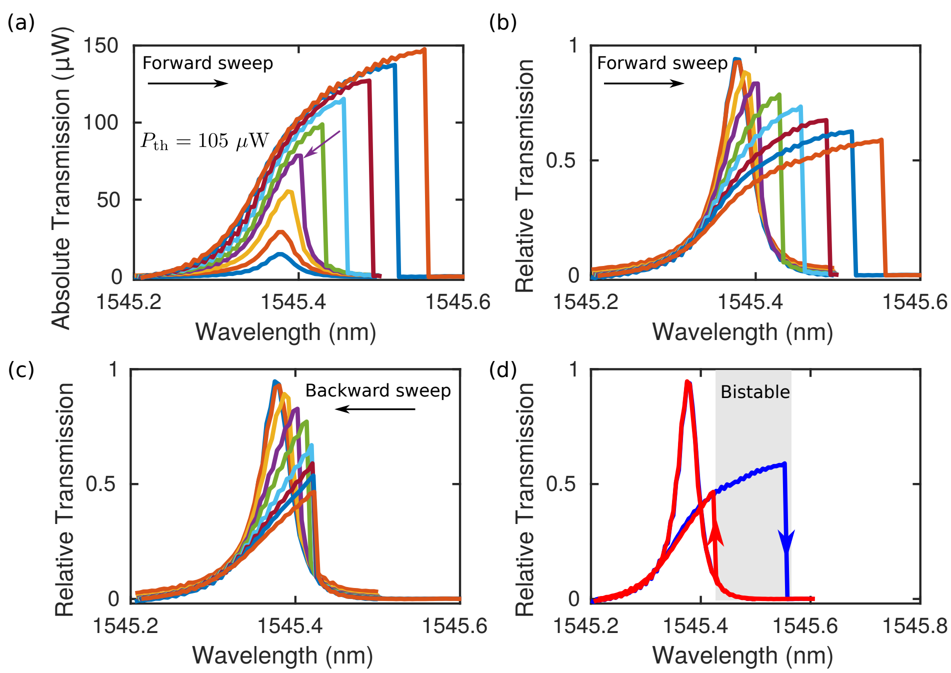

Figure 2.6: Nonlinear transmission spectra measured for the center mode of a photonic crystal (PC) triple cavity, where the transmission is relative to the input/output PC waveguides. (a) The absolute nonlinear transmission spectra measured with a forward sweep (wavelength swept from low to high) are plotted for input powers ranging from 16 to 250 μW. The arrow indicates the minimum threshold power, P_{th}, where the sharp drop in the transmission spectrum begins to appear. (b) Same as in (a) but for the relative transmission. (c) Same as in (b) but for a backward sweep (wavelength swept from high to low). (d) Example forward (blue) and backward (red) spectra taken at two 16 and 250 μW. The bistability is present in the higher power spectra, as the forward and backward sweep have a range of wavelengths where the spectra are non-overlapping.

Transmission spectra are measured in the nonlinear regime where the laser power is sufficiently high that changes to the silicon refractive index are induced through the Kerr effect. In this regime, the transmission lineshape become distinctly non-Lorentzian, as shown in Figure 2.6 where examples of the absolute and relative transmission are plotted as a function of probe power. Changes induced in the real part of the refractive index result in a shift in the resonant wavelength of the microcavity mode, and changes in the imaginary part of the index result in losses, which lower the total cavity lifetime and reduce the transmission. These effects result in complex spectral behaviour that is dependent on the sweep direction as well as the input power level, and contains information about waveguide coupling, and the nonlinear properties of the material and cavity structure.

The transmission spectra are also used to quantify the strength of the Kerr effect using a power threshold figure-of-merit. This is the minimum power where the sharp drop in the transmission spectrum begins to appear (see the spectrum labelled the arrow in Fig. 2.6(a)), which signifies that the structure can be considered for all-optical processing applications like all-optical switching [31, 63].

2.2.1 Nonlinear transmission lineshape

Each spectrum in Fig. 2.6 reflects the steady-state transmission for each individual wavelength, which means that each time the sweep wavelength is adjusted, there is a delay before the measurement is taken, to allow any transients in the temperature, free-carrier distribution and cavity energy to pass. To understand the transmission lineshape, it is useful to first consider what is happening to the resonant wavelength of the microcavity as a function of sweep wavelength and how that affects the transmission. In this example microcavity, it is assumed that the resonant wavelength shift is dominated by thermal effects, resulting in a red-shift as a function of energy loaded in the cavity. Figures 2.7(a) and (b) show the energy loaded in the microcavity and resonant wavelength as a function of the sweep wavelength, respectively.

For the *forward* wavelength sweep shown here, the laser wavelength starts blue-detuned off resonance, such that little energy is loaded into the cavity and the resonant wavelength is essentially equal to the *cold* cavity (linear) λ_m. As the wavelength is increased toward λ_m, more energy is loaded into the cavity and the resonant wavelength begins red-shift. As the sweep wavelength increases, more energy continues to be loaded into the cavity and the resonant wavelength continues to red-shift, until the sweep wavelength eventually catches the resonant wavelength. Just beyond this point is where the steady-state transmission undergoes a sudden drop due to an unstable cycle:

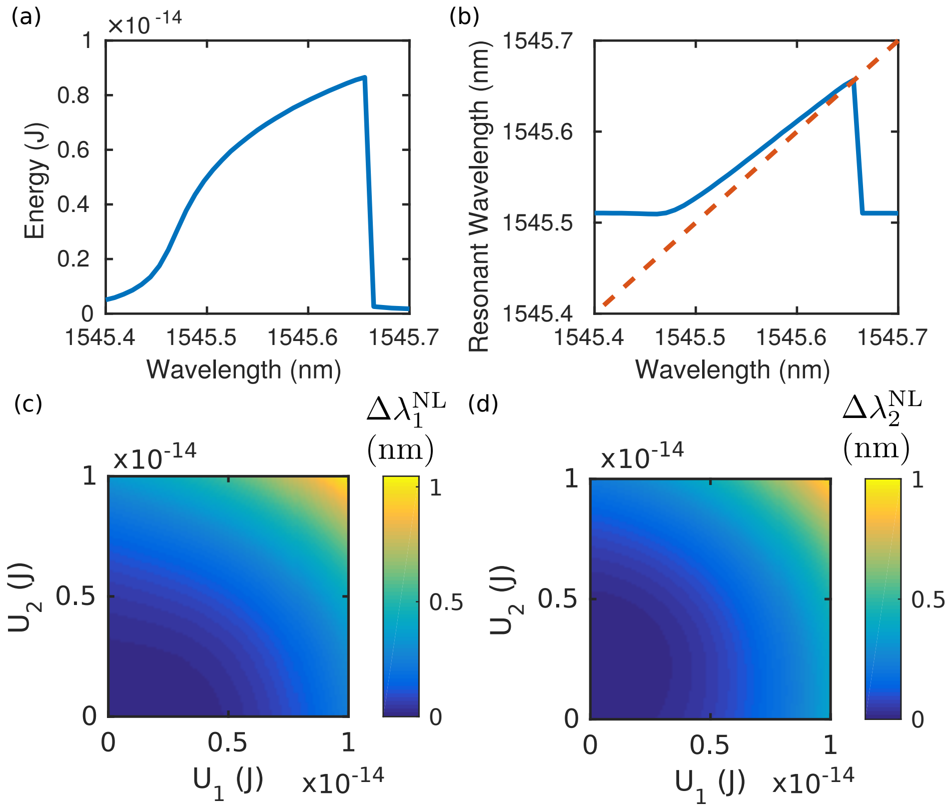

Figure 2.7: Nonlinear behaviour a triple microcavity under (a)-(b) single frequency excitation, and (c)-(d) dual frequency excitation when cross-coupling of nonlinear effects between modes is present. (a) Energy loaded in mode M2 as a function of sweep wavelength for an input power of $P_{\mathrm{in}} = 300\ \mu$W. (b) Resonant wavelength of the cavity mode as a function of sweep wavelength (solid line). The dashed line shows the sweep wavelength, for reference. (c) Nonlinear resonant wavelength shift of mode M1, $\Delta\lambda_1^{\mathrm{NL}}$, as a function of the energies U_1 and U_2 loaded in modes M1 and M2, respectively, for the same microcavity device in (a) and (b). The color scale is in units of nanometer. (d) Same as (c) but the resonant wavelength shift of M2, $\Delta\lambda_2^{\mathrm{NL}}$, is plotted.

the microcavity energy decreases due to the excitation being off-resonance, causing the resonant wavelength to blue-shift as the heating reduces, such that the excitation is increasingly further off-resonance. Beyond the drop, the relative transmission follows the low power spectral lineshape.

The transmission lineshape for the backward wavelength sweep (laser starts red-detuned from λ_m and ends blue-detuned) is different from the forward sweep and is illustrated in Fig. 2.6(c). For the backward sweep, as the wavelength is swept toward λ_m, energy is loaded into the cavity and the resonant wavelength is red-shifted *toward* the sweep wavelength. The sharp increase in the steady-state transmission occurs when an unstable cycle is initiated: the cavity energy is increasing, causing the resonant wavelength to approach the sweep wavelength, causing more energy to be loaded. Beyond this point, the wavelength is tuned increasingly off resonance and the energy in the cavity reduced. The wavelength where the transmission jumps is generally not at the same point where the power drops in a forward sweep 2.6(d), due to how energy gets loaded as a function of wavelength. The microcavity is in a *bistable* state for the range of wavelengths where the forward and backward sweeps yield different transmission, as labelled in Fig. 2.6(d).

Nonlinear losses also play a role in defining the nonlinear transmission lineshape. For both forward and backward sweeps, the transmission is reduced due to free-carrier nonlinear losses when the energy loaded in the cavity is high, as seen in Figs. 2.6(b) and (c), respectively. This results in a decrease in the maximum relative transmission as a function of sweep power.

2.2.2 Nonlinear transmission data analysis

All of this detailed spectral information obtained at a number of input power settings (see Fig. 2.6) can be reduced, for the purposes of modelling and parameter extraction, to two data sets: the peak transmission, $\overline{T}_m^{\mathrm{NL}}$, and peak resonant wavelength shift, $\Delta\lambda_m^{\mathrm{NL}}$, versus input power, both obtained in the forward sweep direction, like the example shown in Fig. 2.8. These data sets are obtained for the two high Q modes, M1 and M2, while the low Q mode (M3) is not studied, as insufficient energy is loaded into the cavity to induce significant nonlinear effects, even when the laser is at its maximum power.

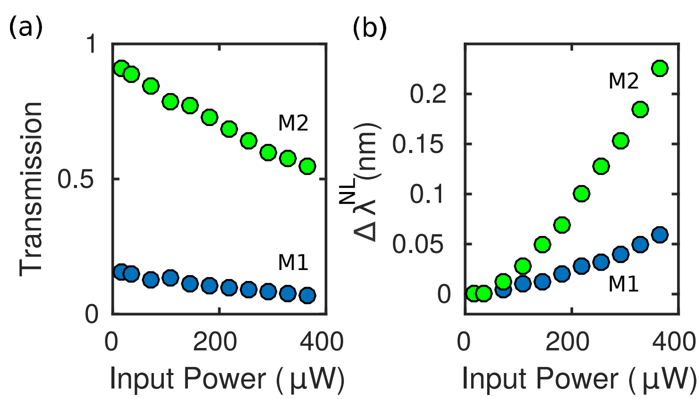

Figure 2.8: Example experimental data extracted from nonlinear transmission spectra taken as a function of input power for Modes M1 and M2. (a) Peak transmission. (b) Resonant wavelength shift.

The model used to predict the wavelength shifts and transmission maximum values for M1 and M2 includes 11 unknown microcavity parameters: $\lambda_1, \lambda_2, \tau_1^{\mathrm{in}}, \tau_2^{\mathrm{in}}, \tau_1^{\mathrm{out}}, \tau_2^{\mathrm{out}}, \tau_1^{\mathrm{scatt}}, \tau_2^{\mathrm{scatt}}, \tau_{\mathrm{abs}}, \tau_{\mathrm{carrier}}$, and R_{th}. In the least-squares approach taken in this work, there are six fit parameters that are directly extracted ($\eta_1^{\text{wg}} = \tau_1^{\text{out}}/\tau_1^{\text{in}}, \tau_{\text{abs}}, \tau_{\text{carrier}}, R_{\text{th}}, \phi_{\text{in}}, \phi_{\text{out}}$), while the rest of the parameters are informed from the linear transmission and four-wave mixing analysis results.

2.2.3 Technical consideration: time scales

Transmission spectra considered in this thesis are composed of sequences of steady-state measurements. This requires that all transient effects have passed when each step measurement is taken. There are a number of different processes at play during nonlinear transmission measurements, each with their own time scales. The time scales most relevant to the device operation are: the effective free-carrier lifetime, the effective thermal relaxation lifetime and the optical cavity lifetime.

The effective free-carrier lifetime, τ_{carrier}, depends on a number of different factors, including the carrier density and the microcavity structure. Single microcavities comparable to the those involved in the triple cavity have been found to have saturated effective carrier lifetimes around $0.5 - 1.8$ ns [11, 95, 105], and unsaturated lifetimes on the order of 10's of nanoseconds[11]. The saturated lifetime is expected to be limited by surface recombination effects [89, 95]. The thermal relaxation rate is related to the thermal resistance. A higher thermal resistance results in slower diffusion of heat from the microcavity. The time scale for single photonic crystal microcavities has been found to be around 100 ns [63]. The time scale for light loading and unloading from the microcavity depends on the total lifetime of the mode. For the triple cavity, the total lifetimes are different for each of the modes. The lowest Q modes have lifetimes ~ 3 ps ($Q \sim 2000$), while the highest Q modes have lifetimes ~ 300 ps, ($Q \sim 2 \times 10^5$).

The overall time scale required for the microcavity to reach steady-state is therefore limited by the thermal relaxation, to $\sim$ 100 ns. In nonlinear transmission measurements, a delay of microseconds between the wavelength step and the measurement is sufficient for ensuring that the system has reached steady-state. A relatively large delay of 50 ms was employed in the experiments in this thesis, to safely allow time for the necessary electronic communications to occur, and for the laser to change the wavelength.

2.3 Stimulated four-wave mixing

In four-wave mixing frequency conversion measurements, the microcavity is excited by pump and signal lasers, at wavelengths λ_{pump} and λ_{signal}, respectively, and photons are generated at the idler wavelength λ_{idler}, as illustrated in the simplified schematic in Fig. 2.9(a). The full measurement set-up is described in Section 2.3.1. The microcavity idler photons are coupled into the output PC waveguide, along with unconverted signal and pump photons, and are sent off-chip where spectral filters are used to transmit only the idler photons to a single photon detector. The idler, pump and signal microcavity photons also couple to the other possible waveguide and loss channels.

Conservation of energy requires that the signal and idler frequencies are equally spaced from the pump frequency. For photons with wavelengths near 1550 nm, the *wavelength* spacing is also essentially equal $[(\lambda_{\text{pump}} - \lambda_{\text{signal/idler}}) << \lambda_{\text{pump}}]$. Ideally the pump, signal and idler wavelengths coincide with resonant wavelengths of the microcavity. The triple PC cavities considered in this thesis are generally not perfectly equally spaced, and support two relatively high Q neighbouring modes ($Q >\sim 30,000$), and a low Q mode ($Q \sim 3000$), as in the example given in Fig. 2.9(b). For the devices measured in this thesis, the pump wavelength coincides with the central high Q mode, and one of the signal/idler wavelengths coincides with the outer high Q mode, while the third wavelength (idler/signal) falls within a linewidth of the low Q mode peak. The details regarding how the laser and filter wavelengths are chosen for optimal generation rates are discussed more thoroughly in Appendix A.

The idler power is generally reported with respect to the output waveguide, and is found by dividing the photon count rate measured by the single photon detector by the losses between the output waveguide and the detector, and multiplying by the energy of an idler photon, $\hbar\omega_{\text{idler}}$. This calculation includes the same optical and device components considered in the relative transmission normalization, as well as additional sources of loss like the spectral filter and the detector efficiency. The normalization procedure is described in Appendix D. The idler steady-state photon generation rate is measured as a function of the pump or signal power, while the other input power is kept fixed. This is done for both signal/idler mode excitation configurations.

When the pump and signal powers are relatively low such that nonlinear losses are negligible,

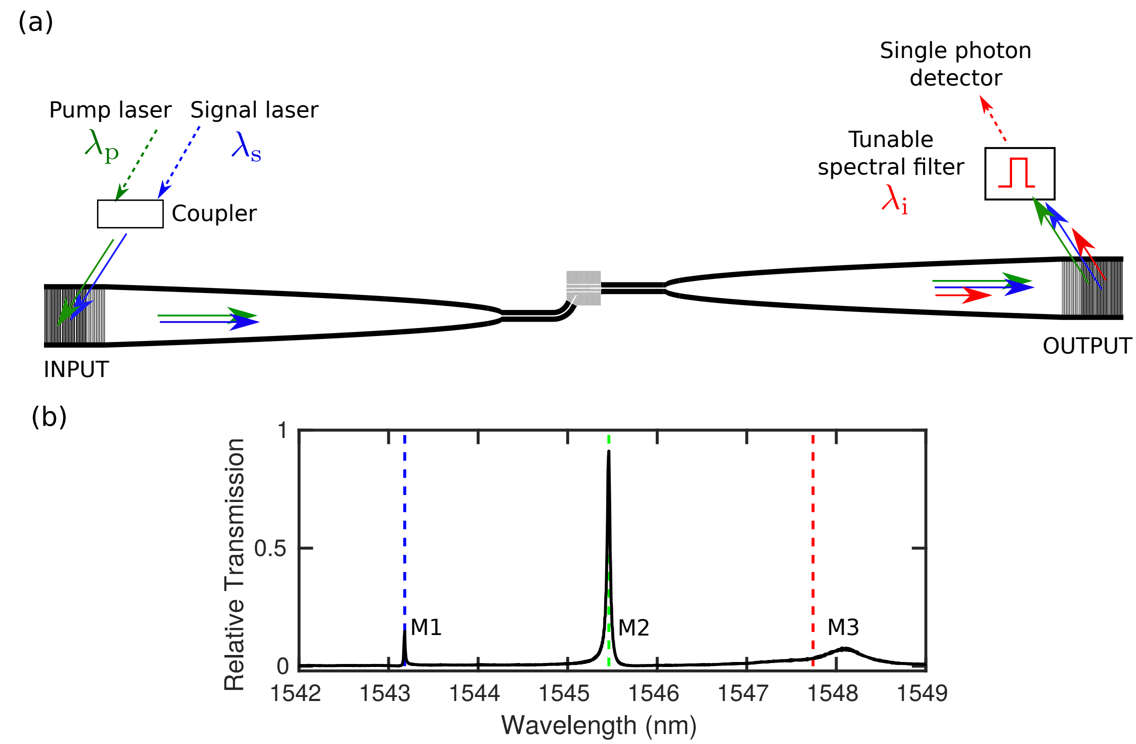

Figure 2.9: (a) Simplified schematic of the stimulated four-wave mixing (FWM) set-up. Pump and signal lasers tuned to wavelengths λ_{p} and λ_{s} are coupled into the input waveguide of the multimode microcavity and the light collected is sent through a spectral filter, to extract the idler photons at wavelength λ_{i}, before measurement by a single photon detector. The green and blue arrows represent path the pump and signal continuous wave excitations, respectively, and the red arrows represent the path of the idler photons generated through FWM. (b) Transmission spectrum for a triple photonic crystal microcavity. The three frequencies involved in FWM are indicated with dashed lines, and the three microcavity modes are labelled M1, M2 and M3.

the idler power depends quadratically on the pump power, and linearly on the signal power, as is illustrated in Fig. 2.10(a). These dependencies are somewhat intuitive, as the FWM process involves two pump photons and one signal photon that get converted to one idler photon.

When the pump and/or signal powers are sufficiently high, nonlinear absorption losses affect all three modes, and cause reductions in the idler power. Free-carrier effects reduce the total microcavity cavity lifetimes of all three modes, resulting in a reduction in the amount of energy that can be optimally loaded into the pump and signal modes, and absorption of the generated photons. The nonlinear absorption effects also cause the resonant wavelengths to shift due to changes in the real part of the refractive index. It is common practice to adjust the pump, signal and idler wavelengths as a function of pump/signal power to *track* the mode peaks and maintain

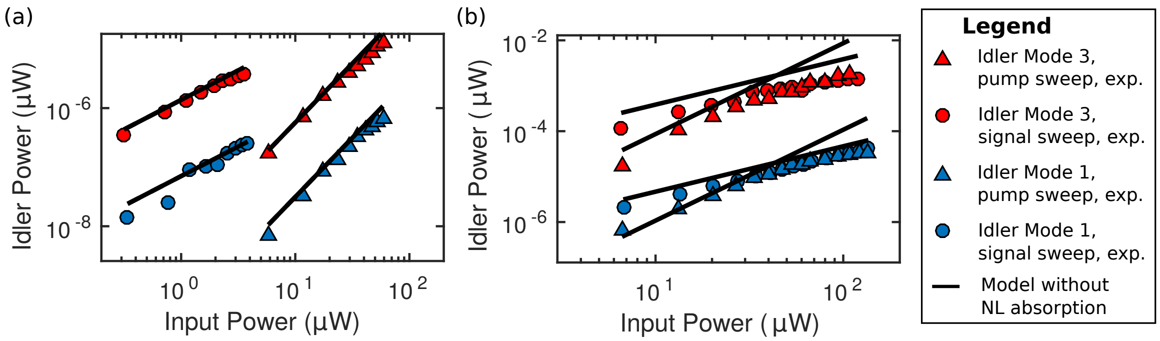

Figure 2.10: Examples of stimulated four-wave mixing (FWM) idler powers experimentally measured for triple photonic crystal microcavity devices. The red and blue markers indicate that the FWM configuration implemented resulted in idler photons generated near Mode 3 and Mode 1, respectively. Circles and triangles indicate that the power measured as a function of signal and pump power, respectively. The solid lines are estimates of what the idler powers are predicted to be in the absence of nonlinear losses (linear/quadratic for signal/pump power dependencies). (a) Stimulated FWM results for a triple cavity probed largely in the low power limit. The signal power sweep has a fixed pump power of 29 μW , and the pump power sweep has a fixed signal power = 3.6 μW. Nonlinear loss effects result in sub-linear and sub-quadratic power dependencies near the ends of the sweeps. (b) A different triple cavity device probed largely in the high power limit. The signal power sweep has a fixed pump power of 44 μW , and the pump power sweep has a fixed signal power = 44 μW.

equal spacing. The modes typically shift very close to the same amount as they have similar mode field distributions relative to silicon and the surrounding materials (air, oxide).

Nonlinear losses cause the FWM idler power pump dependence to become sub-quadratic and the signal dependence to become sub-linear, as shown in Fig. 2.10(b). A subtle but important consequence is that at low pump *or* signal sweep powers, the generation rate does not necessarily return to the nonlinear loss-free quadratic or linear trend, respectively, as the trends may be shifted to overall lower powers due to nonlinear losses induced by the other (fixed) input excitation.

The least-squares analysis for each device involves four FWM data sets: the idler powers measured separately as a function of pump and signal powers, for both excitation configurations (signal/pump/idler modes as M1/M2/M3 and M3/M2/M1). In the presence of nonlinear losses, the model function used to predict the idler powers depends on 14 microcavity parameters, as indicated in Table 2.1. There are only two fit parameters for this analysis, $\eta_2^{\rm wg} = \tau_2^{\rm out}/\tau_2^{\rm in}$ and $\eta_3^{\rm wg} = \tau_3^{\rm out}/\tau_3^{\rm in}$, and the rest of the model parameters are informed from the linear and nonlinear transmission measurements.

2.3.1 Technical consideration: four-wave mixing set-up

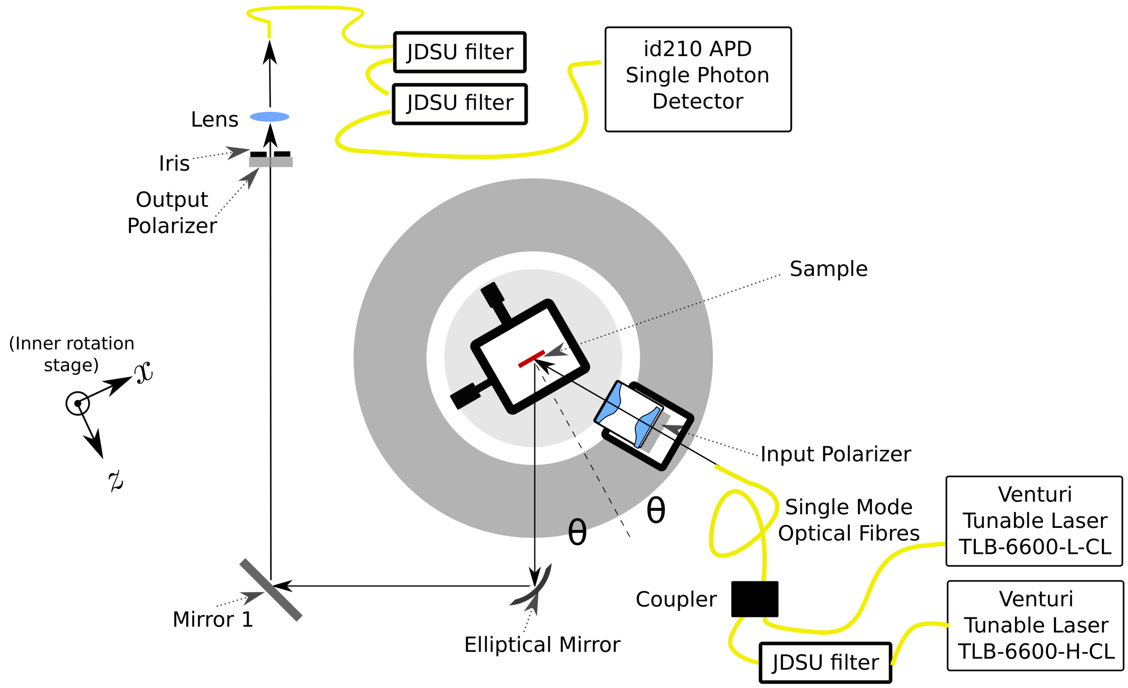

Figure 2.11: Optical set-up used to measure four-wave mixing. Light from the pump and signal lasers are coupled into a single mode fibre and focused on the input grating coupler of a triple microcavity device. Light that leaves the sample surface is collected and focused by an elliptical mirror, and an iris in the image plane is used to transmit only the light leaving the output grating. A lens is then used to focus the light into an optical fibre, that is connected to two JDSU TB9 Tunable Grating Filter, tuned to the idler wavelength, such that idler photons are detected by the id210 avalanche photodetector. See Fig. 2.3 for more details on unlabelled components.

The transmission set-up for four-wave mixing measurements is shown in Fig. 2.11. The base components in this set-up are the same as the ones in the transmission set-up, shown in Fig. 2.5, however there are modifications to the excitation and detection schemes. Two lasers, a Venturi TLB 6600-H-CL and a Venturi TLB 6600-L-CL are included in this set-up to provide the pump and signal excitations. The Venturi TLB 6600-H-CL is a higher power laser with a noise level of -43 dB below the continuous-wave power, due to spontaneously emitted photons. A JDSU TB9 Tunable Grating Filter is placed along the optical path of this laser to reduce the noise level to ~ -90 dB. This noise reduction is necessary to maximize the signal to noise ratio obtained when measuring the photon power generated by FWM. The noise level of the Venturi TLB 6600-L-CL lower power laser is ~ -80 dB, so no filtering is required. A 50/50 coupler is used to couple the light from both lasers into a single optical fibre.

The detection scheme is modified such that in lieu of putting a photodetector or CCD camera in the image plane, the output light propagates to a lens where it is focused into a single mode fibre. The fibre is connected to two tunable JDSU filters that are used to filter out the pump and signal photons, and transmit the idler photons, by providing a total of ~ 100 dB rejection at ~ 2.5 nm away from the center wavelength, as reported in Appendix D. The idler photons are then sent to a ID Quantique id210 single photon detector, which is an avalanche photodetector (APD).

Stimulated four-wave mixing measurements are critically dependent on the pump and signal wavelengths, as well as the idler filter wavelength. Special care is taken to choose the wavelengths that optimize the generated photon rate. This presents an added challenge when pump and/or signal excitations introduce nonlinear absorption effects. In this regime, resonant wavelengths shift as a function of *both* the pump and signal powers. This is exemplified in Figs. 2.7(c) and (d) where the nonlinear resonant wavelength shifts of modes M1 and M2, respectively, are plotted as a function of the energies simultaneously loaded into these modes. In Appendix A, the procedures used to align the pump, signal and idler wavelengths are discussed for the triple cavity, where the modes are unequally spaced and have different Q's. Different strategies are used for optimal alignment, depending on whether the signal is exciting the high Q outer mode, or the low Q mode.

Chapter 3

Design and fabrication

In this chapter, the triple microcavity structure central to this thesis is described in detail. The original design goal was to engineer a resonator structure suitable for spontaneous FWM in silicon-on-insulator, that supports three high Q modes that are spatially overlapping, and equally spaced in frequency. Ideally, the center mode couples preferentially to the input waveguide and the outer modes preferentially couple to the output waveguide, to enable efficient loading of the pump photons and efficient unloading of the signal and idler photons spontaneously generated.

The full microcavity structure for spontaneous FWM, that includes three side-coupled heterostructure cavities, and input and output waveguides, is plotted in Fig. 3.1(a) and a scanning electron microscope (SEM) image of a fabricated structure is shown in Fig. 3.1(b). The microcavity structure is defined in an SOI wafer with a silicon device layer thickness of $t_{\mathrm{Si}} = 220$ nm and a buried oxide thickness of $t_{\mathrm{SiO_2}} = 3$ μm, however after fabrication the oxide beneath the microcavity is removed, to leave the silicon device layer suspended (also called "undercut"). The optimized structure is defined by 19 design parameters, listed in Table 3.1.

The quality factors numerically simulated for the optimized design structure are reported in Table 3.2, for each of the three resonant modes of interest. Also reported here are the probabilities that a photon generated in a microcavity mode couples to the output waveguide, and the peak relative transmission values.

3.1 Numerical simulations

Numerical simulations play a very important role in both the design and analysis procedures. Due to the complexity of the dielectric structures considered, it is not practically possible to study the electromagnetic responses analytically, and numerical approaches are required. The numerical

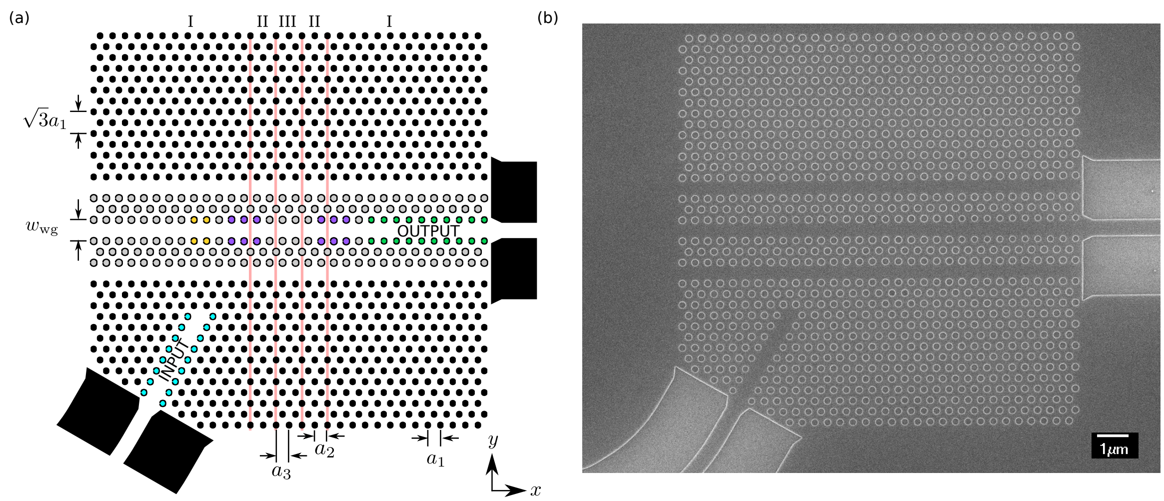

Figure 3.1: Triple photonic crystal (PC) microcavity with input and output waveguides. (a) Schematic of the microcavity with design parameters highlighted. The heterostructure is composed of photonic crystal regions labelled I, II, and III, and separated by red lines, where the lattice spacings in the x direction are a_1, a_2 and a_3, respectively, while the row spacing of the bulk PCs is $\sqrt{3}a_1/2$ throughout. The widths of the three line defects are $w_{\rm wg}$. The solid black circles represent holes with radius r, while the circles coloured in gray have radius $r_{\rm mid}$. The input and output waveguides are labelled, and the holes lining the waveguides are coloured cyan and green, and have radii $r_{\rm wg}^{\rm in}$ and $r_{\rm wg}^{\rm out}$, respectively. The 12 holes that finely control the mode spacing are coloured purple, and have radius $r_{\rm mid,ms}$ and are shifted outward from the line defect by a distance $h_{\rm ms}$. The four yellow holes have radius $r_{\rm wg,sym}$. (b) Scanning electron microscope image of a fabricated triple microcavity device.

approach that is primarily used in this thesis is the finite-difference time-domain (FDTD) method, which effectively evaluates Maxwell's equations on a spatial discretized grid, at discrete time steps. The method is described in greater detail in Appendix B. All FDTD simulations are done using Lumerical FDTD Solutions software [79].

3.1.1 Microcavity simulations

Simulation set-up considerations

A typical microcavity simulation studied in this thesis shown in Fig. 3.2(a). This simulation is used to extract the mode frequencies, Q's and mode profiles of the triple cavity shown in Fig. 3.1. The approach taken here is generally applicable to 2D planar PC microcavities. The silicon device layer is shown in red and the etched holes defining the PC microcavity are gray. The orange box shows the boundaries of the simulations volume. The blue double arrow shows a dipole source, polarized in the $\hat{\mathbf{y}}$ direction. This is a passive "soft" source that introduces a polarization

Table 3.1: Design parameters for the triple photonic crystal microcavity device coupled to input and output waveguides.

	Parameters	Value	Description
PC microcavity	a_1	410 nm	Lattice spacing for Region I
	a_2	418 nm	Region II lateral lattice spacing for
	a_3	425 nm	Region III lateral lattice spacing for
	w_{wg}	693 nm	Waveguide width
	$N_{y,cav}$	3	Inter-cavity separation (# of rows)
	r	124 nm	Radius of holes in top and bottom PCs
	r_{mid}	126 nm	Radius of holes in middle two PCs
	$r_{\text{mid,ms}}$	variable	Radius of holes that finely tune mode spacing
	h_{ms}	variable	Shift of holes that finely tune mode spacing
PC waveguide	$r_{\text{wg,sym}}$	115 nm	Hole radius
	$r_{\text{wg}}^{\text{in}}$	111 nm	Radius of holes lining input PC waveguide
	$r_{\text{wg}}^{\text{out}}$	108 nm	Radius of holes lining output PC waveguide
	$X_{\text{wg}}^{\text{in}}$	7	Starting X position of input waveguide
	$Y_{\text{wg}}^{\text{in}}$	4	Starting Y position of input waveguide
	$X_{\text{wg}}^{\text{out}}$	7	Starting X position of input waveguide
	v_{in}	14 nm	Input PC to channel waveguide impedance matching parameter
	v_{out}	14 nm	Output PC to channel waveguide impedance matching parameter
	t_{in}	341 nm	Input PC to channel waveguide impedance matching parameter
	t_{out}	346 nm	Output PC to channel waveguide impedance matching parameter
	h_{in}	146 nm	Input PC to channel waveguide impedance matching parameter
	h_{out}	166 nm	Output PC to channel waveguide impedance matching parameter

density pulse to one rectangle of the spatial grid, and allows scattered fields to pass through the source unperturbed. The source pulse length is typically ~ 9 fs, resulting in a spectral bandwidth $\delta f = 50$ THz that is centered near the cavity resonant mode frequencies, such that these modes

Table 3.2: Summary of the quality factors simulated for triple photonic crystal microcavity devices with input and output waveguides. The quality factors Q_m^{in}, Q_m^{out}, Q_m^{other} correspond to coupling to the input waveguide, the output waveguide, and other loss channels including scattering absorption, respectively, while Q_m is the total quality factor, for modes $m = 1, 2, 3$. The probability that photons generated in the cavity will couple to the output waveguide is given by $p_m^{\mathrm{out}} = Q_m/Q_m^{\mathrm{out}}$. The relative transmission from the input to the output waveguide is given by $\overline{T} = 4Q_m^2/(Q_m^{\mathrm{in}}Q_m^{\mathrm{out}})$. The total quality factors for the microcavity structure *without* input and output waveguides, Q_m^{nowg}, are also included.

		Mode, m		
Parameter	Description	1	2	3
Q_m	Total quality factor	2.8×10^4	1.3×10^5	3.7×10^3
Q_m^{in}	Input coupling quality factor	1.5×10^6	1.5×10^5	1.4×10^5
Q_m^{out}	Output coupling quality factor	3.2×10^4	2.6×10^6	4.1×10^3
Q_m^{other}	Scattering/other losses quality factor	3.2×10^5	9.7×10^5	4.5×10^4
Q_m^{nowg}	Total quality factor in absence of waveguides	2.2×10^6	1.4×10^6	8.1×10^5
p_m^{out}	Probability of output waveguide coupling	0.89		0.89
$\overline{T}_m$	Relative transmission	0.065	0.16	0.096

are transiently excited, and then gradually leak out of the cavity region after the excitation pulse has completely disappeared from the simulation volume. The yellow cross is a time monitor that records the fields at the nearest mesh cell as a function of time. A number of planar 2D frequency monitors are also included (outlined in yellow). Two of these monitors lie at the ends of the PC waveguides, and six form a box around the simulation volume. These record the fields at each of the mesh points within the monitor, in the frequency domain, by implementing a numerical Fourier transform. The power transmission through the monitors is calculated based on the fields. It is also possible to include a 3D frequency monitor that records the fields over a volume (not shown).

There are a number of considerations that are involved in setting up the simulation. The simulation boundaries are chosen to be "perfectly matched layers" (PML), which absorb all outgoing radiation. In the $\hat{\mathbf{z}}$ direction, a symmetric boundary condition is applied to the "undercut" suspended microcavity (indicated by the blue shading in the $x - z$ view), that effectively reduces the simulation volume and run-time by half. The symmetry is known a priori to be consistent with the symmetry of the modes of interest (here the base silicon layer of the SOI is ignored). It is important that the hole pitch is an integer multiple of the mesh size to maintain the periodicity

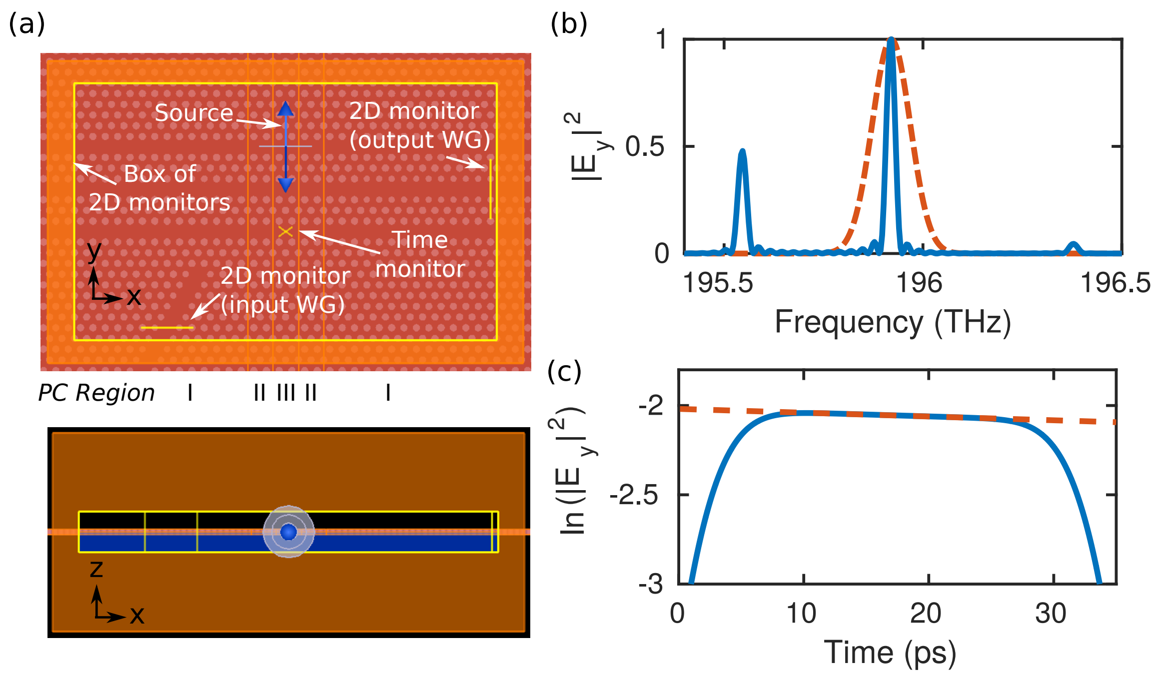

Figure 3.2: Finite-difference time-domain (FDTD) microcavity simulations using Lumerical FDTD [79]. (a) The simulation layout of the triple microcavity device is shown in the $x-y$ (top) and $x-z$ (bottom) planes. The thick orange regions outline the simulation volume and the perfectly matched layers (PML). The blue region in the bottom plots show the symmetric boundary condition applied in $\hat{\mathbf{z}}$. The thin orange lines in the top image show the boundaries of the heterostructure mesh override regions. A source polarized in $\hat{\mathbf{y}}$ is placed at an antinode in the top defect region to excite the modes. A time monitor (yellow cross) is placed at the location of an antinode in the bottom defect. Two-dimensional planar frequency monitors are placed at the outputs of the two waveguides (WGs) to measure waveguide transmission (yellow lines in the top image) and a box of 2D monitors encloses the full simulation power to measure all power leaving the volume. (b) Fourier transform of the E_y field measured by the time monitor (blue), apodized to remove the source excitation. A Gaussian spectral filter around the center mode is shown as a dashed red line. (c) Natural logarithm of E_y decay envelope for center mode, found from the inverse Fourier transmission of the filter spectrum. The dashed red lines is the line of best fit.

of the PC. For the “heterostructure” cavity studied here, which has five regions with different PC lattice spacings (labelled with I,II, and III in Fig. 3.1(a), and discussed in greater detail in Section 3.2), five mesh override regions are appropriately defined. The mesh override regions are outlined in orange in Fig. 3.2(a), and have $\Delta x = a_x/15$, $\Delta y = a_1\sqrt{3}/30$ and $\Delta z = t_{\mathrm{Si}}/20 = 110$ nm, where a_x is the horizontal lattice spacing of the heterostructure region, and a_1 is the lattice spacing in Region I PC. The dipole source and time monitor are also deliberately located at two antinodes of all three cavity modes of interest and the dipole polarization direction ($\hat{\mathbf{y}}$) is consistent with the field direction at the source antinode. These decisions are informed by knowledge from previous simulations involving randomly placed monitors and dipoles, the latter with randomized polarization directions. The simulation time is 35 ps, which is not long enough to fully resolve modal spectral properties, due to the high Q's of the modes, but it is sufficiently long to accurately capture the information of interest.

Analysis of simulation results

Modal frequencies and lifetimes The mode frequencies appear as peaks in the spectrum found by taking the Fast Fourier Transform (FFT) of the E_y field recorded by the time monitor. The linewidths of the peaks in the FFT spectrum are not resolved due to the short simulation time, resulting in the sinc functions plotted in Fig. 3.2(b). The quality factors (and actual linewidths) are extracted from the decay characteristics of the time monitor signal. After the excitation has passed, the cavity has the following time dependence,

$$E(t) = A \sin(-i2\pi f_m t) \exp(-t/\tau_m) \tag{3.1}$$

where f_m is the mode frequency and τ_m is the total lifetime of the mode. The total quality factor, $Q_m = \pi f_m \tau_m$, is extracted using a multi-step process: i) a Gaussian filter is applied around the "positive frequency peak" of the mode of interest in the FFT data, as illustrated in Fig. 3.2(b), ii) the inverse FFT of the filtered signal is computed, iii) the absolute value is taken to remove the $e^{-i2\pi f_m t}$ carrier signal time dependence, leaving the envelope of the mode time decay, clear of the fast carrier oscillations and the responses of other modes, iv) the natural logarithm is taken and is fit with a line, as shown in Fig. 3.2(c), where the slope is $-1/\tau_m$, and the Q is computed. This process is repeated for each of the three modes of interest.

The two-dimensional planar frequency monitors at the ends of the input and output PC waveguides measure the power transmitted through the monitor, $P_{\text{in}}(\lambda)$ and $P_{\text{out}}(\lambda)$, respectively, and the box of monitors around the whole simulation volume monitor the total power leaving the volume, $P_{\text{box}}(\lambda)$. The individual quality factors for the PC waveguides are found by studying the relative power transmitted on resonance through these monitors, where $Q_m^{\text{i}} = Q_m P_m^{\text{box}}/P_m^i$, with $i =$ "in", "out" and "other", and $P_m^{\text{other}} = P_m^{\text{box}} - P_m^{\text{in}} - P_m^{\text{out}}$. This relationship between the transmitted power and the quality factors is found by considering that the energy in the cavity mode m decays as $U_m \sim \exp(-2t/\tau_m)$, such that the power lost to each channel is $P_m^i \sim (-2/\tau_m^i)\exp(-2t/\tau_m^i)$, resulting in $P_m^i(f_m) \propto 1/\tau_m^i \propto 1/Q_m^i$.

Modal field distributions To find the mode field distributions in the centre of the silicon slab, $\mathbf{E}_m(x, y, z = 0; f_m)$, a 2D planar frequency monitor is placed in the $x-y$ plane at $z = 0$ (not shown in Fig. 3.2(a)), and the recorded fields are evaluated at the mode frequencies, f_m. The time signal that enters the FFT begins after the source excitation has passed, such that only the resonant field is involved in the calculation.

For some calculations, it is necessary to extract the mode field distributions over the microcavity volume, $\mathbf{E}_m(\mathbf{r}; f_m)$, in which case a 3D frequency monitor is implemented. For example, 3D frequency monitors are used to find the four-wave mixing coefficient β_{FWM}, introduced in Chapter 2, based on volume overlap integrals involving the three mode field distributions and the silicon.

The 3D modal field distributions are also used in a perturbative approach to study changes in the mode frequencies due to small perturbations in the dielectric environment, by calculating [39],

$$\frac{\delta f_m}{f_m} = -\frac{1}{2}\frac{\int d\mathbf{r}\delta\epsilon(\mathbf{r})|\mathbf{E}_m(\mathbf{r})|^2}{\int d\mathbf{r}\epsilon(\mathbf{r})|\mathbf{E}_m(\mathbf{r})|^2}, \tag{3.2}$$

where $\epsilon(\mathbf{r})$ is the original permittivity, $\mathbf{E}_m(\mathbf{r})$ is the original mode profile for mode m, and $\delta\epsilon(\mathbf{r}) = \epsilon_{\mathrm{new}}(\mathbf{r}) - \epsilon(\mathbf{r})$, with $\epsilon_{\mathrm{new}}(\mathbf{r})$ as the new permittivity. While there are some known issues with this approach [39], it appears to give sufficiently accurate results for the cases tested here, and is used to quickly test microcavity geometries.

3.1.2 Bandstructure simulations

Numerical FDTD simulations are also used to extract the mode bandstructures for periodic dielectric structures, which is useful for identifying the photonic band gap of the host 2D PCs and the waveguide modes supported by PC waveguides. A typical simulation for a PC waveguide is shown as an example in Fig. 3.3(a). The simulation span in x is equal to the lateral pitch a_x, while the span in y encompasses 7 rows on both sides of the waveguide. “Bloch” boundary conditions are applied for the x boundaries, while PML is applied for the y and z boundaries, in addition to a

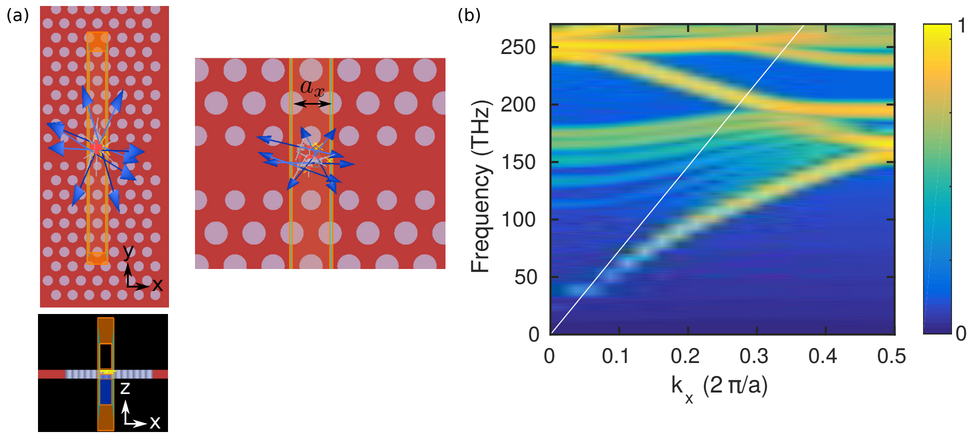

Figure 3.3: Bandstructure simulations using Lumerical FDTD Solutions [79]. (a) The simulation layout for photonic crystal line defect is shown in the $x-y$ (top) and $x-z$ (bottom) planes. The $x-y$ plane near the center axis is expanded in the image to the right. The simulation volume spans one lattice spacing in $\hat{\mathbf{x}}$, a_x and is outlined in orange. Symmetric boundary conditions are applied in $\hat{\mathbf{z}}$, as indicated by the coloured blue region in the bottom image, and Bloch boundary conditions are applied in $\hat{\mathbf{x}}$. Dipole sources (blue double arrows) are randomly placed to excite the Bloch mode. Time monitors (yellow crosses) are also randomly placed to measure the field excited in the silicon. (b) Example of the bandstructure measured for a line defect. The base 10 logarithm of the intensity spectrum extracted from simulations with fixed k_x are plotted. The light line is shown with the white line.

symmetric boundary condition applied in z to study the transverse electric modes of interest only. The Bloch boundaries apply the following condition:

$$\mathbf{F}_{k_x}(x+a_x, y, z) = \exp(ik_x a_x)\mathbf{F}_{k_x}(x, y, z), \tag{3.3}$$

where $\mathbf{F}_{k_x}(x+a_x, y, z)$ is the electric or magnetic field for a mode labelled by k_x, where k_x is the wavevector in the $\hat{\mathbf{x}}$ direction set for the simulation. A cluster of broadband dipole sources oriented in the plane are used to excite the modes and time monitors record the fields at various locations. The Fourier transforms of the time signals are computed after apodizing the signal to remove the source pulse, and their squared magnitudes are summed together. The spectra are plotted in Fig.3.3(b), on a logarithmic (base 10) color scale, as a function of k_x, from 0 to π/a_x. The air light line, $\omega = ck_x$, where c is the speed of light in vacuum, is also included as the white line. The mode frequencies correspond to the peaks in the spectra, and these shift as a function of k_x, revealing the mode dispersion. The mode shapes associated with different bands can be extracted by including a 2D planar frequency monitor.

3.2 Device design

3.2.1 Microcavity design

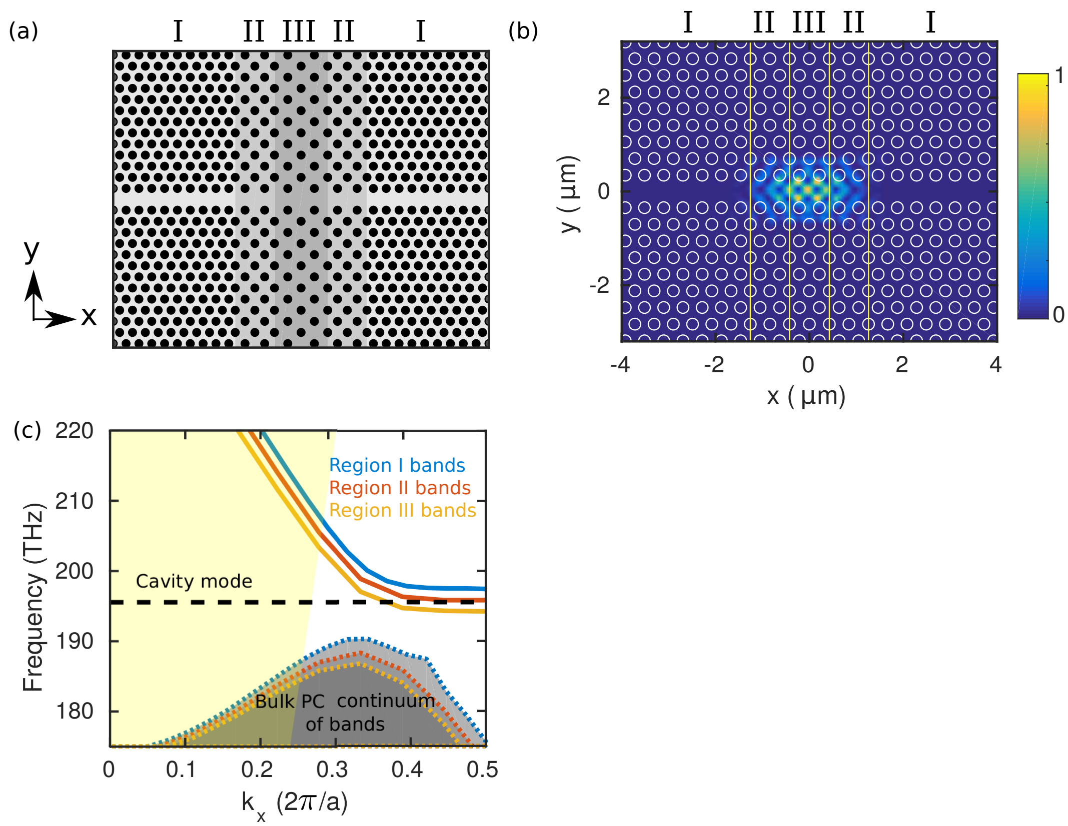

Figure 3.4: Single photonic crystal (PC) heterostructure microcavity. (a) Schematic of the structure, where the different PC regions are highlighted in different shades of gray and labelled I, II and III. The horizontal lattice spacings are exaggerated for clarity. (b) Electric field intensity of the mode profile. The PC heterostructure boundaries are highlighted with yellow lines and the PC holes are outlined in white. The horizontal lattice spacings are $a_1 = 410$ nm, $a_2 = 418$ nm and $a_3 = 425$ nm, respectively. (c) Bandstructure calculation for the PC line defects (missing row of holes) in Regions I, II and III. The wavevector on the x axis is given in terms of the horizontal lattice spacing a for each region considered (i.e. $a = a_1, a_2, a_3$). The solid lines indicate the PC waveguide bands. The continuum of bulk PC bands are colored in gray, and are outlined for each region with dotted lines. The black dashed line shows the resonant cavity mode frequency, and the light cone is shaded in yellow.

The microcavity structure in Fig. 3.1(a) is composed of three nearly identical PC heterostructure cavities located in close proximity (along the y direction), allowing them to couple, lifting the degeneracy of the three modes' frequencies. An example of a single heterostructure cavity, known to support high Q, small volume modes [81], is illustrated in Fig. 3.4(a). The regions highlighted I,II and III are derived from three different hexagonal photonic crystals, with lattice constants $a_1 = 410$

nm, $a_2 = 418$ nm and $a_3 = 425$ nm, respectively, and hole radius $r = 124$ nm. The modification to the lattice is that the row separation in $\hat{\mathbf{y}}$ is held constant at $a_y = \sqrt{3}a_1/2$ throughout all PC regions. In Fig. 3.4(a), the spacings a_2 and a_3 are exaggerated for clarity. There is a line defect of omitted holes along the center of the microcavity, with width $w_{\mathrm{wg}} = \sqrt{3} \times 400$ nm $= 693$ nm. The intensity profile of the fundamental mode of this cavity is plotted in Fig. 3.4(b).

The mechanism by which this structure localizes light in region III can be understood by considering how the dispersion of the 1D waveguide modes supported in the line defect (missing row of holes), at frequencies within the band gap of the bulk PC, varies between Regions I, II, and III. As shown in Fig. 3.4(c), there is a range of frequencies where waveguide modes can propagate in Regions II and III, but not in Regions I. The Regions I therefore act as "potential barriers", or more specifically as mirrors that define a Fabry-Perot like cavity between them. Regions II are introduced, instead of directly interfacing Regions I and III, in order to make the transition more gentle, such that scattering is minimized and high Q's are achieved. The separation of the "mirrors" (the effective width of Regions II and III) affects the cavity mode frequency. It is important that all of the relevant 1D bands involved in all regions exist below the light line, to avoid intrinsic out-of-plane scattering losses.

In order to achieve three equally spaced modes, three heterostructure cavities are side-coupled, as shown in Fig. 3.5, where the mode intensity profiles are plotted for the triple cavity version of the structure presented in Fig. 3.4. Three rows of holes are chosen to separate the cavities, $N_{\mathrm{y,cav}} = 3$, resulting in mode spacings of $\Delta f_{\mathrm{ms}} \simeq (f_3 - f_1)/2 \simeq 0.4$ THz [$\Delta\lambda_{\mathrm{ms}} \simeq (\lambda_3 - \lambda_1)/2 \simeq 3$ nm]. In contrast, when the cavities are spaced by a single row (i.e. $N_{\mathrm{y,cav}} = 1$), the modes are very strongly coupled and the spacing is $\Delta f_{\mathrm{ms}} \simeq 8$ THz ($\Delta\lambda_{\mathrm{ms}} \simeq 65$ nm). With such high frequency shifts, the high energy mode is no longer reflected by Regions I, and the low energy mode gets pushed below the bulk PC band-edge of Region III: the Q values then degrade and the mode separation becomes asymmetric. For an intercavity spacing $N_{\mathrm{y,cav}} = 2$, the x positions of omitted the holes are different in the outer cavity line defects as compared to the center line defect, and only two distinct cavity modes appear in the spectra.

The design process to determine the microcavity parameters in Table 3.1, is outlined in Fig. 3.6. The waveguide width $w_{\mathrm{wg}} = 693$ nm is chosen to appropriately shift the waveguide band away

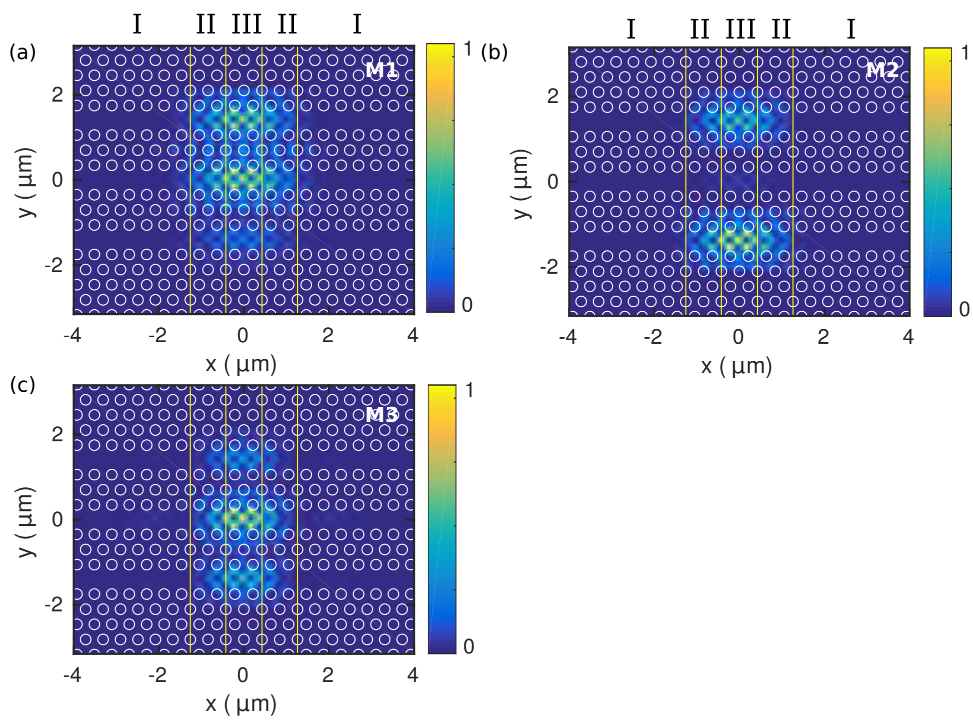

Figure 3.5: Simulation results for a triple heterostructure photonic crystal (PC) microcavity with hole sizes r = 124 nm throughout and waveguide width w_{wg} = 693 nm. Electric field intensity mode profiles are plotted for modes (a) M1, (b) M2 and (c) M3. The heterostructure boundaries are shown with yellow lines and the PC holes are outlined in white.

from the lower band edge of the host PC while maintaining resonant frequencies within the laser tuning range ($\lambda_{\text{laser}} = 1520$ to 1610 nm). Figure 3.7(a) shows the waveguide dispersion curves as a function of the waveguide width, where dashed-dotted, solid and dashed blue lines correspond to waveguide modes supported when $w_{\text{wg}} = 675, 693$ and 710 nm, respectively. The resonant mode frequencies f_1 (blue), f_2 (green) and f_3 (red) are also plotted for each of the three triple microcavity structures. As expected, the waveguide and resonant cavity modes shift to lower energies as the width is increased, due to an increase in the amount of the mode energy concentrated in the high index silicon, as opposed to the low index air [3]. The Q's for modes 1,2 and 3 are plotted in Fig. 3.7(b), as circles, triangles and squares as a function of w_{wg}. The Q's decrease when w_{wg} is increased from 693 nm to 710 nm because the waveguide band become closer to the bulk PC band-edge resulting in greater leakage into the bulk PC. For $w_{\text{wg}} = 675$ nm, the cavity modes f_1

[3]This is effectively due to the variational principle for electromagnetic modes. The energy functional, $U_f = (\int d^3\mathbf{r}|\nabla \times E(\mathbf{r}, f_m)|^2)/(\int d^3\mathbf{r}\epsilon(\mathbf{r})E(\mathbf{r}, f_m)|^2)$, is minimized for each mode [38]. Modes concentrated in high dielectric constant regions have relatively low mode frequencies (energies).

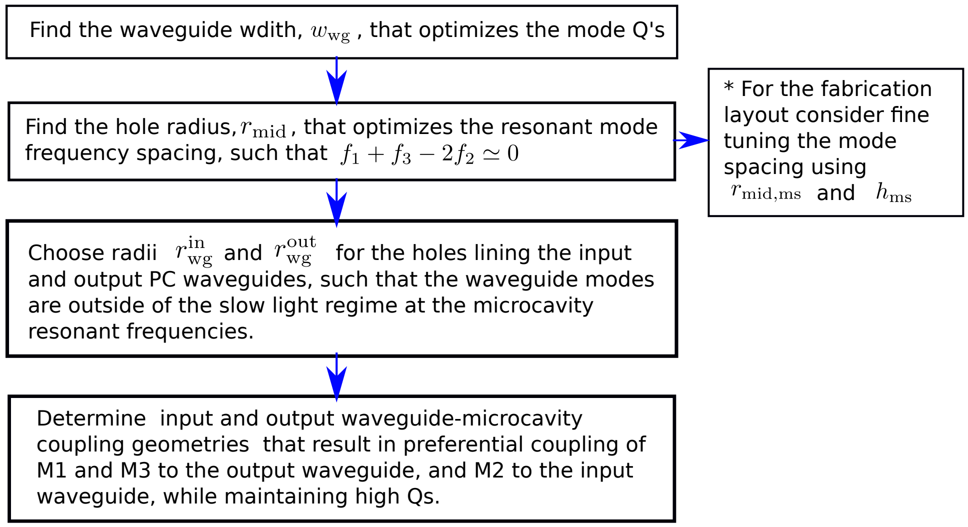

Figure 3.6: Process followed to design the triple photonic crystal (PC) microcavity for spontaneous four-wave mixing applications. The microcavity parameters are defined in Table 3.1 and highlighted in Fig. 3.1.

and f_2 are closer to the waveguide band, leading to a reduction in Q_1 and Q_2. The $w_{\mathrm{wg}} = 693$ nm is chosen to achieve modes with relatively high Q's ($Q_1 = 2.3 \times 10^5, Q_2 = 1.4 \times 10^5, Q_3 = 7.2 \times 10^4$), and frequencies within the laser tuning range. At this point, the mode frequencies are $f_1 = 195.72$, $f_2 = 195.46$ and $f_3 = 194.94$ THz ($\lambda_1 = 1531.77$, $\lambda_3 = 1533.75$ and $\lambda_2 = 1537.83$ nm), which is within ~ 1.5 THz (~ 10 nm) of the laser tuning range edge.

The resonant frequencies presented above for this structure are not equally spaced: there is a frequency offset of $\Delta f_{\mathrm{off}} = f_3 - f_3^{\mathrm{FWM}} = f_1 + f_3 - 2f_2 = -0.26$ THz, where $f_3^{\mathrm{FWM}} = 2f_2 - f_1$ is the four-wave mixing frequency. The mode profiles in Fig. 3.5(b) show that the center mode has relatively little of its field in the center cavity region, thus if the structure is perturbed in this region, one would expect it to affect this mode less than the others, thus making it possible to tune the outer mode frequencies relative to the center mode frequency. The hole radii for the center two blocks of the structure (with three rows each), gray holes in Fig. 3.1, are tuned from $r_{\mathrm{mid}} = 124$ to 128 nm, and the resulting resonant frequencies are plotted in Fig. 3.8(a). The Δf_{off} is plotted in Fig. 3.8(b) as yellow diamonds. This tuning method is effective and $r_{\mathrm{mid}} = 126$ nm is chosen, to reduce the offset to $\Delta f_{\mathrm{off}} = 0.085$ THz ($\Delta\lambda_{\mathrm{off}} = \lambda_1 + \lambda_3 - 2\lambda_2 = -0.65$ nm).

Fine tuning of the mode spacing is incorporated across the fabrication layout, to ensure that a subset of devices are near equally spaced. In the tuning method present above, Δf_{off} changes

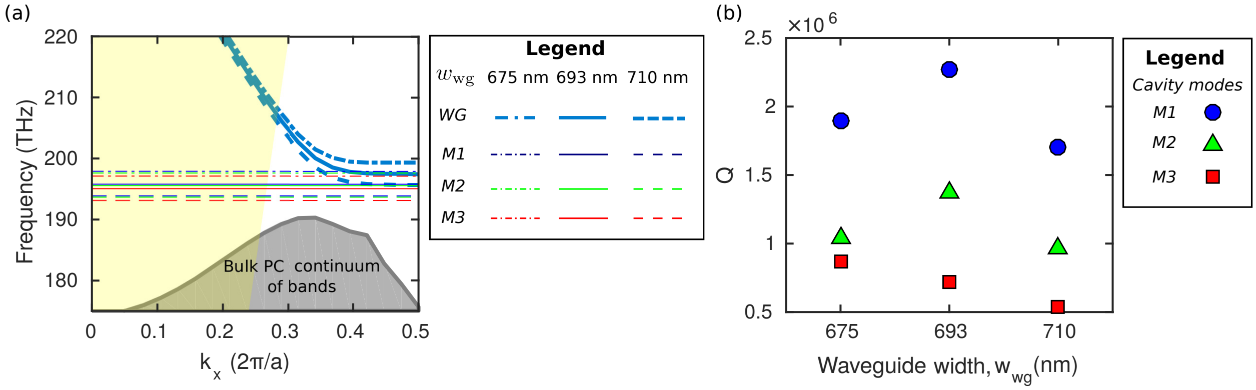

Figure 3.7: Triple photonic crystal (PC) microcavity designs as a function of waveguide width w_{wg}. (a) Bandstructure calculation for the line defect of Region I (outermost PC) of the heterostructure. The bulk PC mode continuum is shown in gray, and the PC waveguide (WG) modes are shown as thick dash-dotted, solid, and dashed blue lines for structures with $w_{\mathrm{wg}} = 675, 693$ and 710 nm, respectively. The resonant frequencies for each of these structures are shown as thin lines blue, green and red lines for modes M1, M2 and M3 respectively. The highlighted yellow shows the region above the air light-line. (b) Total quality factors for M1, M2 and M3.

by $\sim$ 0.17 THz per nanometer increase in the hole radius ($\Delta\lambda_{\mathrm{off}}$ changes by ~ -1.3 nm per nanometer), which is large relative to the typical linewidth of the lowest Q mode of the fabricated devices, $\delta f_3 \simeq 0.065$ THz ($\delta\lambda_3 \simeq 0.5$ nm). To achieve finer tuning of the mode spacing, the hole radius is tuned for only 12 holes in the middle two PC blocks, highlighted in purple in Fig. 3.1, as opposed to all of them. When $r_{\mathrm{mid}} = 126$ nm and the 12 hole radii are tuned from $r_{\mathrm{mid,ms}} = 122$ to 128 nm, the resulting Δf_{off} change by $\sim$ 0.056 THz per nanometer increase in radius, as shown by the empty diamonds in Fig. 3.8(b), simulated using perturbation theory. Alternatively, the mode spacing is tuned by *shifting* these 12 holes. Figures 3.8(c) and (d) show the mode frequencies and Δf_{off} calculated both full FDTD simulations (filled markers) and using perturbation theory (empty markers), for $r_{\mathrm{mid}} = 126$ nm and hole shifts $h_{\mathrm{ms}} = -4$ to 8 nm (outward from the waveguide is a "positive" shift), in respectively. Both simulation approaches yields similar results, with Δf_{off} changing by $\sim$ 0.028 THz per nanometer shift. The fine tuning methods, using $r_{\mathrm{mid,ms}}$ and h_{ms}, are both applied in the fabrication layout to bracket the mode spacing.

At this stage, the microcavity structure with $N_{y,cav} = 3$, $w_{\mathrm{wg}} = 693$ nm, $r = 124$ nm and $r_{\mathrm{mid}} = 126$ nm, supports three nearly equally spaced modes with high Qs. The input and output waveguides are now introduced.

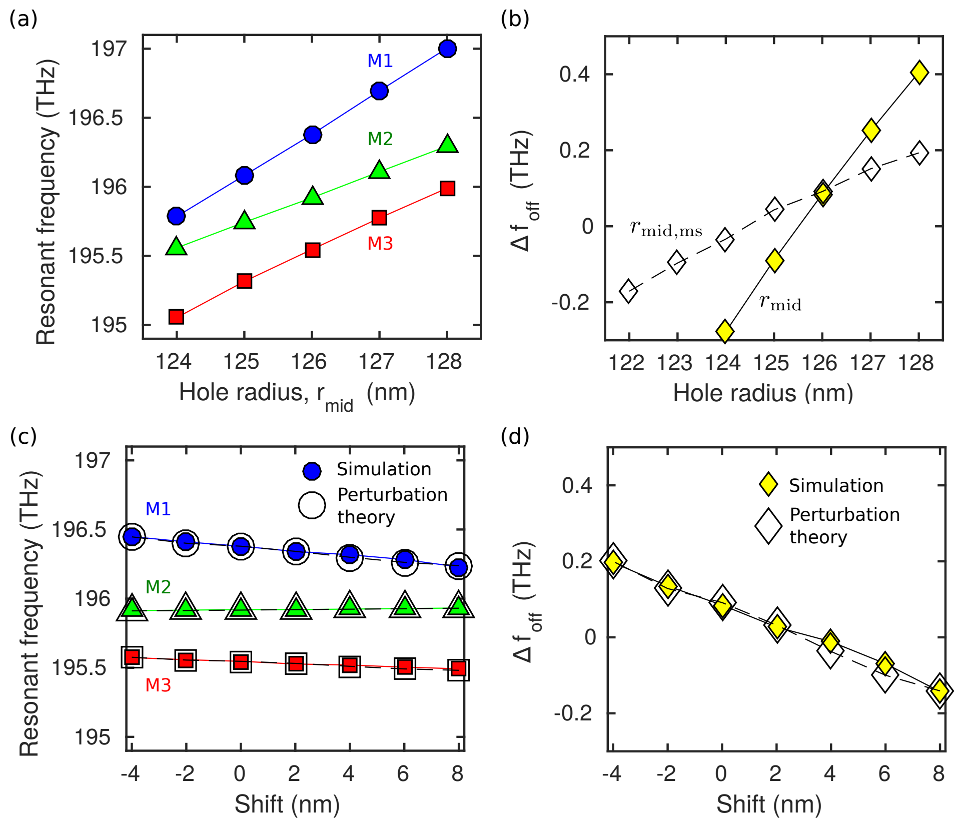

Figure 3.8: Resonant frequencies of the triple microcavity structures as a function of mode spacing tuning parameters described in Fig. 3.1. (a) The resonant frequencies found from FDTD simulations for M1 (blue circles), M2 (green triangles) and M3 (red squares) are plotted as a function of $r_{\rm mid}$. (b) Frequency offset, $\Delta f_{\rm off} = f_1 + f_2 - 2f_2$, as a function of $r_{\rm mid}$ (yellow diamonds) calculated with FDTD simulations, and $r_{\rm mid,ms}$ (empty diamonds) with fixed $r_{\rm mid} = 126$ nm calculated with perturbation theory, where f_m are the mode resonant frequencies. (c) Mode frequencies found from FDTD simulations plotted as a function of the shift $h_{\rm ms}$ [markers same as in (a)]. The large open markers show the mode frequencies calculated using perturbation theory. (d) Frequency offsets plotted for the resonant frequencies presented in (c), found from FDTD simulations (filled yellow diamonds) and perturbation theory (empty diamonds).

Input and output photonic crystal waveguides

The input and output photonic crystal waveguides defined in the microcavity structure are labelled in Fig. 3.1. The output waveguide is introduced by reducing the radii of holes lining the center line defect (highlighted in green), and the input waveguide is defined by introducing a line defect on the diagonal and reducing the radii of holes lining it (highlighted in cyan).

Photonic crystal waveguide structure The first step in designing the input and output waveguides is to ensure that the waveguides support modes at the cavity resonant frequencies. The

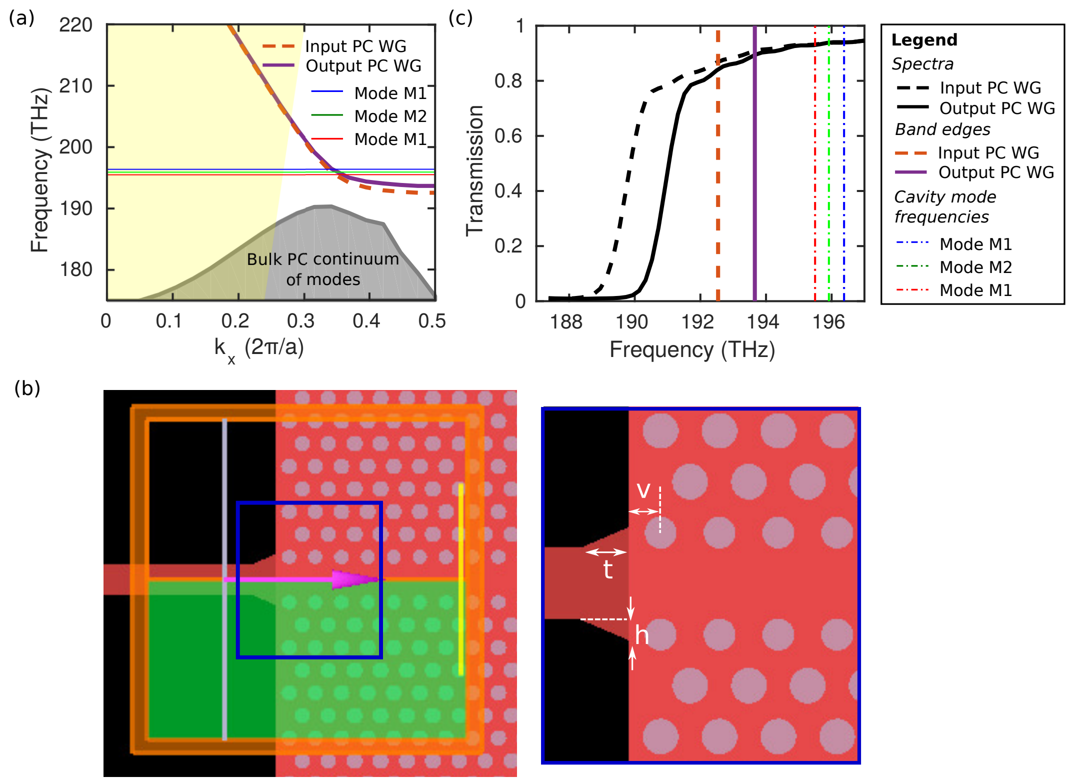

Figure 3.9: Input and output photonic crystal waveguides (PC WG) and the coupling to single-mode channel waveguides. (a) Bandstructure plots for the input and output PC WG modes. The bulk PC mode continuum is shown in gray for the Region I PC with $r = 124nm$. The mode frequencies are plotted for modes M1, M2 and M3 respectively. The region above the air light-line is shaded in pale yellow. (b) Finite-difference time-domain (FDTD) simulation layout [79] of the impedance matching region between the PC and single-mode waveguides. The simulation volume is outlined in orange. A mode source is used to launch the TE channel waveguide mode , and a planar two-dimensional monitor is used to measure the transmission into the PC WG. The region contained in the blue box is expanded to the right, where the design parameters of the impedance matching region are labelled. (c) Transmission spectra measured by the simulation layout in (b), for the input and output waveguides. The dashed and solid vertical lines show the bottom of the input and output waveguide bands, respectively. The dashed-dotted lines show the resonant frequencies of the triple microcavity.

waveguide band energies are lowered, to intersect with the resonant mode frequencies, by reducing the hole radii lining the input and output waveguides to $r_{\rm wg}^{\rm in} = 108$ nm and $r_{\rm wg}^{\rm out} = 111$ nm, as is plotted in Fig. 3.9(a) with dashed and solid thick lines, respectively. These radii are chosen so that the bands intersect the resonant frequencies *above* the “slow light” region where the bands are flat and propagation losses are high due to enhanced interaction with the photonic crystal waveguide structure scattering off non-uniformities. The hole radii are different because the waveguides have different widths and the bulk PC holes have different radii as the input waveguide is defined in the bulk PC in Region I, while the output waveguide is defined in the line defect (input $w_{\text{wg}} = 710$ nm, $r = 124$ nm; output $w_{\text{wg}} = 693$ nm, $r_{\text{mid}} = 126$ nm).

Impedance matching region between photonic crystal and channel waveguides The coupling efficiencies between the PC waveguide modes and the single mode waveguides is briefly visited before taking a closer look at the resonant cavity mode coupling lifetimes. Figure 3.9(b) shows the simulation set-up employed to study the impedance matching region between the two types of waveguides, which is parameterized by three labelled properties, h, t and v [59]. A mode source is used to excite the fundamental mode of the channel waveguide at $f = 196$ THz and the power transmitted into the PC waveguide is monitored 7 lattice spacings away from the edge. Lumerical FDTD Solutions's optimization algorithm is used to find the set of properties that optimizes the transmission. The optimal transmission efficiency at $f = 196$ THz is 0.93 for both waveguides, achieved with $h_{\text{in}} = 146$ nm, $t_{\text{in}} = 341$ nm, $v_{\text{in}} = 9$ nm and $h_{\text{out}} = 166$ nm, $t_{\text{out}} = 346$ nm, $v_{\text{out}} = 14$ nm for the input and output PC waveguides respectively. The transmission spectra found for the input and output waveguides using the optimal impedance matching regions are plotted as dashed and solid black lines in Fig. 3.9(c), respectively. Also plotted are the waveguide band-edge frequencies as dashed and solid thick lines, and the mode resonant frequencies (blue, green and red thin lines). The coupling efficiencies increase from near zero to > 0.75 quickly for resonant frequencies approaching the waveguide band-edges, and then they level out at ~ 0.93.

Input and output waveguide coupling geometries Input and output waveguides are first independently introduced to the microcavity structure, and two different geometries for each are investigated, as is illustrated in Fig. 3.10. The coupling strengths are studied using the procedure outlined in Section 3.1. The best combination of four possibilities is identified, and then the full microcavity structure, with both input and output coupling is simulated.

Figures 3.10(a) and (b) show the two input waveguide geometries, where the diagonal waveguide begins on the third and fourth rows, respectively. In both cases the waveguide begins seven holes away from the center such that the geometries are defined as $(X_{\text{in}}^{\text{wg}}, Y_{\text{wg}}^{\text{out}}) = (7, 3)$ and $(7, 4)$. The input coupling quality factors, Q_m^{in}, are summarized in Fig. 3.11(a) for all three modes. The Q_m^{in} is

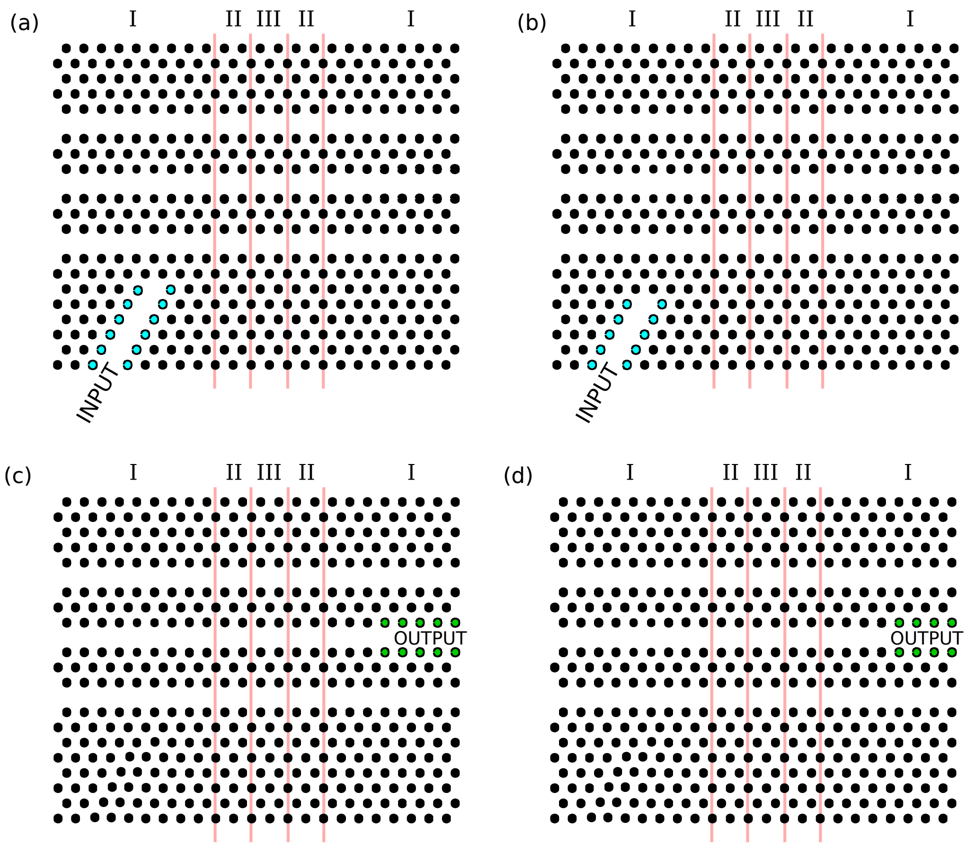

Figure 3.10: Triple photonic crystal (PC) microcavity waveguide coupling geometries. The heterostructure PC region boundaries are shown with red lines and are labelled I, II and III. Input waveguides are introduced in (a) and (b), and the holes lining the waveguide are highlighed in cyan. The coupling geometries are (a) $(X_{\rm in}^{\rm wg}, Y_{\rm in}^{\rm wg}) = (3, 7)$ and (b) $(X_{\rm in}^{\rm wg}, Y_{\rm in}^{\rm wg}) = (4, 7)$. Output waveguide are introduced in (c) and (d), and the holes lining the waveguide are highlighed in green. The coupling geometries are (c) $X_{\rm out}^{\rm wg} = 7$ and (d) $X_{\rm out}^{\rm wg} = 8$.

approximately an order of magnitude larger for the second configuration.

Figures 3.10(c) and (d) show the two output waveguide geometries, where the in-line waveguide begins seven and eight holes from the center, such that $X_{\rm wg}^{\rm out} = 7$ and 8, respectively. The output coupling quality factors, $Q_m^{\rm out}$, are summarized in Fig. 3.11(b) for all three modes. For M1, $Q_m^{\rm out}$ is approximately the same for both geometeries, while for M2 and M3, $Q_m^{\rm out}$ increases by over one, and three order(s) of magnitude when $X_{\rm wg}^{\rm out}$ goes from 7 to 8, respectively. The $X_{\rm wg}^{\rm out} = 8$ coupling scheme is clearly not an option, as $Q_3^{\rm out}$ is so high that M3 cannot preferentially coupling to the output waveguide, for either of the input waveguides chosen.

The design waveguide is chosen to have $(X_{\rm in}^{\rm wg}, Y_{\rm wg}^{\rm out}) = (7, 4)$ and $X_{\rm wg}^{\rm out} = 7$. The former is chosen in order to promote preferential coupling of M1 to the output waveguide, as $Q_1^{\rm in}$ is over an of magnitude larger than Q_1^{out} for $(X_{\text{in}}^{\text{wg}}, Y_{\text{wg}}^{\text{out}}) = (7,4)$, while for the other input coupling scheme, they are much closer. The quality factors for the microcavity with both input and output waveguides are summarized in Table 3.2. The probability that a photon couples to the output channel is calculated as $p_m^{\text{out}} = Q_m/Q_m^{\text{out}}$, and is included in the table for the signal/idler modes M1 and M3. Both p_1^{out} and p_3^{out} are equal to 0.89, and thus meet the qualitative design requirement for preferential coupling to the output waveguide. The predicted transmission from the input to the output waveguide, $\overline{T} = 4Q_m^2/(Q_m^{\text{in}} Q_m^{\text{out}})$, is also included in the table. The pump mode transmission is 0.16, which is fairly low due to the weak coupling to the output channel, and also qualitatively meets the design requirement.

It is also interesting to compare Q_m^{other} to the total quality factors of the microcavity structure *without* input and output waveguides, Q_m^{nowg}, which are also included in Table 3.2. The Q_m^{nowg} are found to be higher than Q_m^{other}, which suggests that the waveguides introduce additional scattering losses (i.e. light scattered off the waveguides radiates out of the microcavity, instead of coupling to a waveguide mode).

At this stage, the main design for the microcavity has been described. Preferential waveguide coupling of the signal and idler modes to the output waveguide is achieved, and the center mode transmission is low. Overall, the Q's are high, relative to the previously reported nanobeam design, where Q_2 is 7 times larger than that of the nanobeam, Q_1 is 4.6 times larger, and Q_3 is on par.

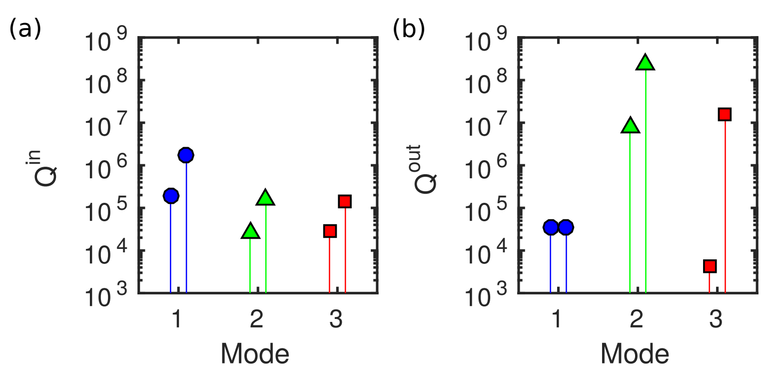

Figure 3.11: Input and output quality factors for waveguide coupling. (a) Input waveguide quality factors, Q_m^{in} are shown for modes M1 (blue circles), M2 (green triangles) and M3 (red squares) simulated for coupling geometries $(X_{\text{in}}^{\text{wg}}, Y_{\text{in}}^{\text{wg}}) = (3,7)$ (left) and $(4,7)$ (right). (b) Output waveguide quality factors, Q_m^{out} are shown simulated for coupling geometries $X_{\text{out}}^{\text{wg}} = 7$ (left) and $X_{\text{out}}^{\text{wg}} = 8$ (right).

Symmetrizing holes One final microcavity design parameter is introduced, $s_{\mathrm{wg,sym}}$, in an effort to lower Q_1^{out}, so that it's closer to Q_3^{out}, for better symmetry. To achieve this, the four holes along the center axis, opposite the output waveguide, are perturbed to have radii $r_{\mathrm{wg,sym}} = s_{\mathrm{wg,sym}} \times r$, where $s_{\mathrm{wg,sym}}$ is a scaling factor. These holes are labelled in yellow in Fig. 3.1, and the new quality factors are included in Table 3.3. The output waveguide coupling is strengthened (Q_1^{out} is reduced), however the scattering is also increased (Q_1^{other} is reduced). The increased scattering is somewhat surprising as Q_1^{nowg} is roughly the same for the waveguide-less microcavities with $s_{\mathrm{wg,sym}} = 0.912$ and $s_{\mathrm{wg,sym}} = 1$ (unperturbed). Both types of microcavities ($s_{\mathrm{wg,sym}} = 1, \neq 1$) are ultimately included in the fabrication layout, as is described below in Section 3.3.1.

Table 3.3: Summary of the quality factors simulated for triple photonic crystal microcavity devices with input and output waveguides, and hole radii $r_{\mathrm{wg,sym}} = 0.912r$ for the holes are labelled in yellow in Fig. 3.1 (i.e. $s_{\mathrm{wg,sym}} = 0.912$). The quality factors Q_m^{in}, Q_m^{out}, Q_m^{other} correspond to coupling to the input waveguide, the output waveguide, and other loss channels including scattering absorption, respectively, while Q_m is the total quality factor, for modes $m = 1, 2, 3$. The probability that photons generated in the cavity will couple to the output waveguide is given by $p_m^{\mathrm{out}} = Q_m/Q_m^{\mathrm{out}}$. The relative transmission from the input to the output waveguide is given by $\overline{T} = 4Q_m^2/(Q_m^{\mathrm{in}}Q_m^{\mathrm{out}})$. The total quality factors for the microcavity structure *without* input and output waveguides, Q_m^{nowg}, are also included.

		Mode, m		
Parameter	Description	1	2	3
Q_m	Total quality factor	5.4×10^3	1.3×10^5	4.1×10^3
Q_m^{in}	Input coupling quality factor	1.6×10^6	1.5×10^5	1.6×10^5
Q_m^{out}	Output coupling quality factor	5.9×10^3	2.9×10^6	4.6×10^3
Q_m^{other}	Scattering/other losses quality factor	6.7×10^4	9.9×10^5	4.8×10^4
Q_m^{nowg}	Total quality factor in absence of waveguides	2.0×10^6	1.4×10^6	6.2×10^5
p_m^{out}	Probability of output waveguide coupling	0.91		0.89
$\overline{T}_m$	Relative transmission	0.013	0.14	0.091

3.2.2 Input and output ports

The input and output ports of the microcavity devices consist of 20 μm wide grating couplers that terminate 150 μm long parabolic waveguides that narrow to 500 nm wide single mode channel waveguides, as is shown in Fig. 3.12. The relatively large grating width is designed to accommodate the free-space coupling scheme used in this thesis, shown in Fig. 2.3, where light from a single mode

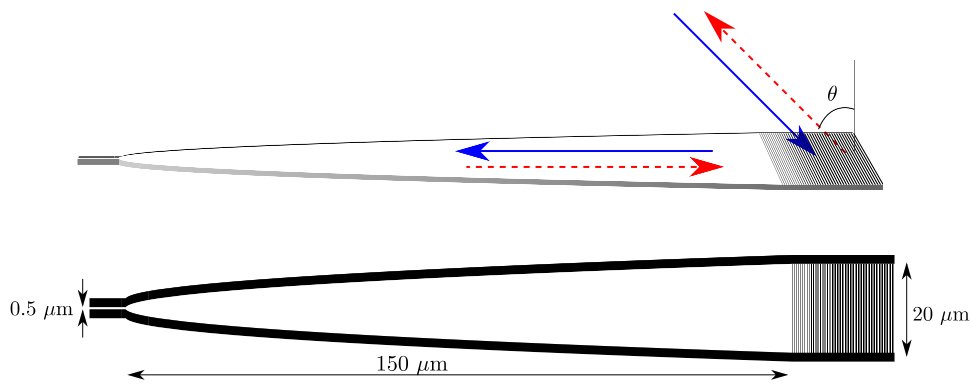

Figure 3.12: Input/output port for the microcavity device. The single-mode channel waveguide is expanded from 0.5 μm to 20 μm by a parabolic waveguide, which is terminated by a grating coupler. The black regions show where silicon is removed to define the structure. The grating coupler is defined by an array of slots with apodized widths, designed for coupling light between the waveguide and light propagating backwards in free-space at an angle $\theta = 45°$. Input and output coupling are shown in the top diagram with pairs of solid blue and dashed red the arrows, respectively.

optical fibre is focused on the input grating coupler with a $1/e^2$ intensity Gaussian beam diameter of ~ 10 μm, and light from the output grating coupler is collected by an elliptical mirror with a numerical aperture, NA$= 0.06$.

The grating couplers are designed to efficiently couple light near the microcavity resonant frequencies into and out of device at a $-45°$ angle, as is illustrated in Fig. 3.12. The negative angle is chosen so that uncoupled incident light is scattered away from the rest of the device, such that background noise is reduced. The 45° angle is chosen to be compatible with another optical-setup (ultimately not used in this thesis) where the sample is placed within a cryostat with windows at $-45°$ and 45°.

The grating coupler is composed of a series of slots, with widths and spacings that are carefully engineered so that the spatial profile and direction of light coupled out of the grating roughly matches the spatial profile and direction of the excitation beam. The better the overlap between these two profiles, the higher the coupling efficiency. Another aim of the design is to keep reflections between the parabolic section and the grating coupler at a minimum. The design of the grating coupler is outlined in Appendix C. A schematic of the apodized grating design is shown in Fig. 3.13(a), along with an SEM image of a fabricated grating, in 3.13(b).

The parabolic waveguide has a full width that is given by,

$$w(x) = \sqrt{w_{\mathrm{i}}^2 - \left[w_{\mathrm{i}}^2 - w_{\mathrm{f}}^2\right] \frac{x}{L}}, \tag{3.4}$$

where $w_f = 20$ μm is the final width, $w_i = 500$ nm is the initial width, $L = 150$ μm is the length, and x goes from 0 to L. The length of the parabolic waveguide is chosen to be long enough to reduce propagation losses, and short enough to be convenient for the fabrication and measurement processes. The final width, w_f, is chosen to be small enough to minimize propagation losses, and also large enough that its wider than the input excitation beam diameter, and also sufficiently large that out-coupled light diffracts over a small enough angle for efficient collection by the elliptical mirror.

The transmission efficiency of light from free-space into the single-mode channel waveguide is estimated using a combination of FDTD simulations and simulations with Lumerical's MODE solver [80]. A similar approach is taken to estimate the transmission efficiency of light from the single-mode waveguide, to beyond the elliptical collection mirror. These are described in Appendix C.

The in-coupling and out-coupling transmission efficiencies between the single-mode waveguide and free-space directly above the grating-coupler (elliptical mirror collection not included here) are plotted in Fig. 3.13(c). These are plotted as a function of wavelength to be consistent with measurement results presented later in this thesis. The in-coupling spectrum peaks around $\lambda = 1535$ nm ($f = 195.4$ THz), while the out-coupling exhibits modulations due to multiple reflections occuring in the 3 μm thick buried oxide. The lack of a peak is because the transmission is taken to be the integral over all outgoing radiation, such that all diffraction angles are accepted.

Figures 3.13(d) and (e) shows a plot of the far field distribution at $\lambda = 1530$ and 1565 nm over the surface of a half sphere of radius $R = 15$ cm, along with a contour of the mirror collection area on this surface. Here it is shown that light at $\lambda = 1530$ nm diffracts at an angle close to $-45°$ and is collected by the mirror, while that at $\lambda = 1565$ nm diffracts away from the mirror. The collection efficiency of the elliptical mirror is estimated by considering the fraction of light intensity that falls within the elliptical mirror, and is explained in further detail in Appendix C. The total output

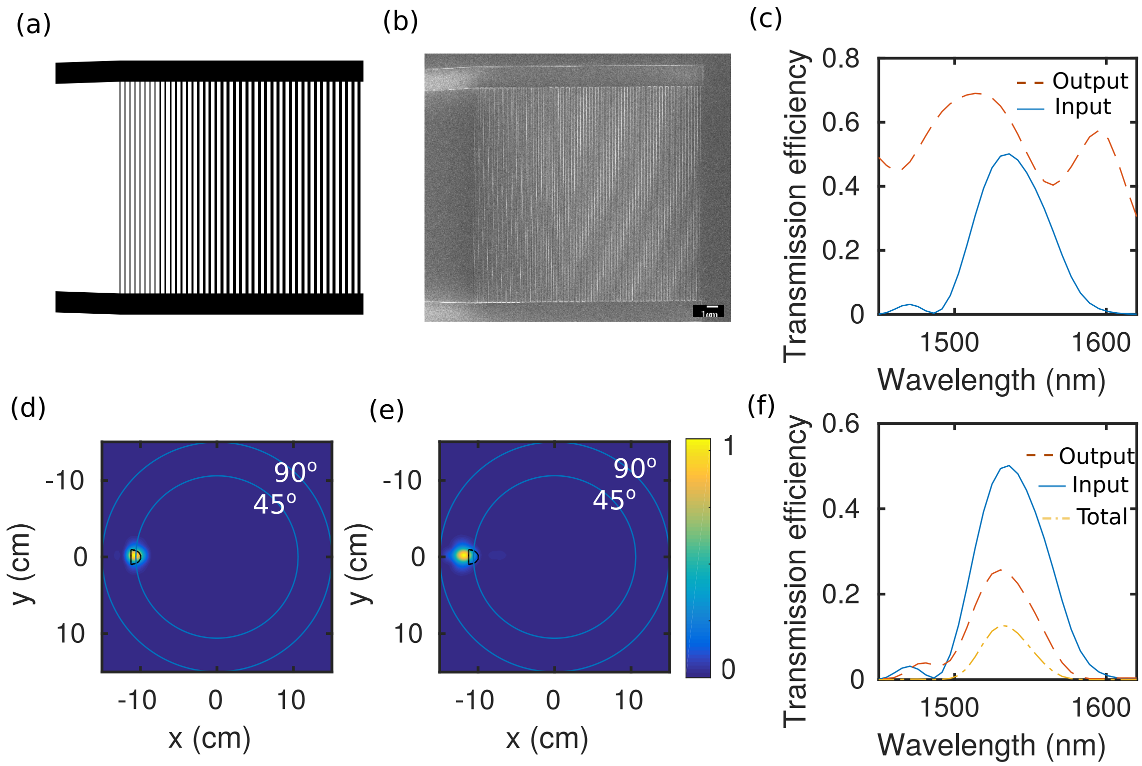

Figure 3.13: Apodized grating coupler design and simulation results. (a) Schematic of the apodized grating coupler, where black regions show where the silicon is removed. (b) Scanning electron microscope image of an apodized grating coupler. (c) Simulated input and output transmission efficiencies between free-space and the single mode waveguide (via the grating coupler and parabolic waveguide). (d) Far field electrical field intensity projection on a 15 cm hemisphere of the field monitored 1 μm off the grating surface when the single-mode waveguide is excited at $\lambda = 1530$ nm. The collection area of the elliptical mirror, that is situated on the hemisphere at an angle of $-45°$ from the vertical, is outlined in black. (e) Same as in (d) but for light launched in the single mode waveguide at $\lambda = 1565$ nm. (f) Simulated input and output, and total transmission efficiencies. The output transmission efficiency shown in this plot accounts for the collection efficiency of the elliptical mirror [unlike the plot in (c)].

efficiency is plotted in Fig. 3.13(f), along with the input efficiency and the product of in-coupling and out-coupling spectra. The bandwidth of the full transmission spectrum is 35 nm.

The ratio between the in-coupling and out-coupling efficiencies, which is not possible to experimentally measure, is required for the nonlinear analysis. For the grating coupler described above, the peak input efficiency is 1.96 times larger than the peak output efficiency. The calculation presented here is repeated for each of the four grating coupler structures used in the nonlinear characterization analysis.

3.3 Fabrication

The devices are fabricated by electron beam lithography (EBL) with a 100 keV JEOL JBX-6300FS writing system at the University of Washington Microfabrication/Nanotechnology User Facility. In this EBL process, the "5th lens" writing mode is employed, with a low beam current of 500pA, and a shot pitch of 2 nm (minimum beam translation step distance). The electon beam writes the pattern by selectively exposing the ZEP-520 A positive resist (Nippon-Zeon Co. Ltd.) that covers the SOI. The exposed resist is chemically removed, then the exposed silicon is etched using an Oxford PlasmaLab System 100 with chlorine gas. The layout pattern submitted for fabrication is composed of the geometric shapes that define the etched silicon areas.

Two fabrication iterations were done as part of this project, where the second iteration produced the Chips A and B studied in this thesis. The first iteration is not discussed in detail here, however the results from this iteration were used to guide the design second iteration, and is acknowledged in this context.

3.3.1 Fabrication layout

The fabrication layout for each chip is shown schematically in Fig. 3.14. It contains 168 microcavity devices, and 48 reference devices, with different device parameters systematically varied over a range that includes the nominal design value.

Reference devices

The four different types of reference devices included in the layout are illustrated in Fig. 3.15. The reference devices are designed to mimic either the input or output components of the triple microcavity (TMC) devices. The reference device in Fig. 3.15(a), contains PC waveguide properties identical to the input waveguide of the TMC, and is referred to here as $\mathrm{PCWG_{in}}$. The PC waveguide length is twice as long as that in the TMC device such that the full $\mathrm{PCWG_{in}}$ device, including input and ouput parabolic waveguides and grating couplers, is effectively a mirrored version of the TMC input components. Similarly, the reference device in Fig. 3.15(b), $\mathrm{PCWG_{out}}$, contains a mirrored version of the TMC output components, including the appropriate output PC

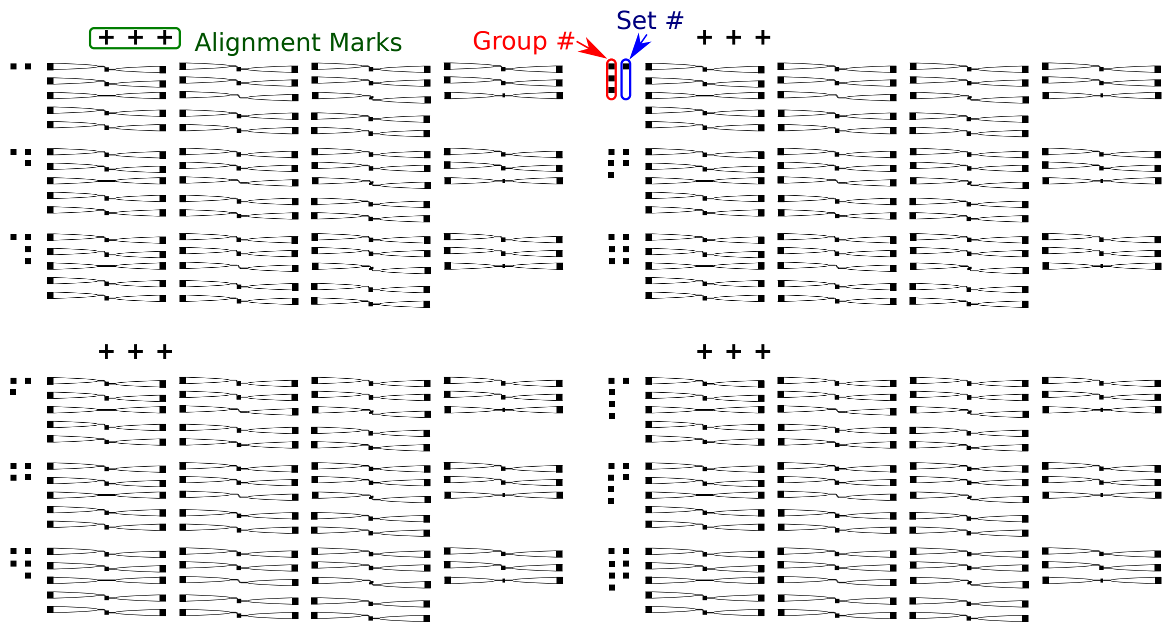

Figure 3.14: Fabrication layout of the devices studied in this thesis. There are 168 microcavity devices, and 48 reference devices. Markings on the chip are used to identify the Group number and Set number of the devices adjacent. Devices in the same group have identical grating couplers, while devices in the same set have identical hole size scale factors. Alignment marks are also included for the post-fabrication photolithography process.

waveguide. The devices in Fig. 3.15(c) and (d) are grating-to-grating devices $G2G_{in}$ and $G2G_{out}$, respectively, that are the same as $PCWG_{in}$ and $PCWG_{out}$, however without the PC waveguides. The total length of each device is made the same by choosing appropriate lengths of the single mode channel waveguides. This makes it possible to layout devices in columns with their input and ouput grating couplers aligned, which makes measurements within a column convenient. Transmission measurements of the reference devices are used to determine the efficiencies of input and output grating couplers, parabolic waveguides and the PC waveguides, that affect the TMC device response.

Bracketing

In anticipation of deviations between the design and the *actual* devices, a number of device parameters are varied across the layout. This increases the probability that there is a subset of devices on the chip that have similar properties as the target. The device parameters that are varied across the chip are summarized in Table 3.4 and are discussed below. The ranges over which each parameter

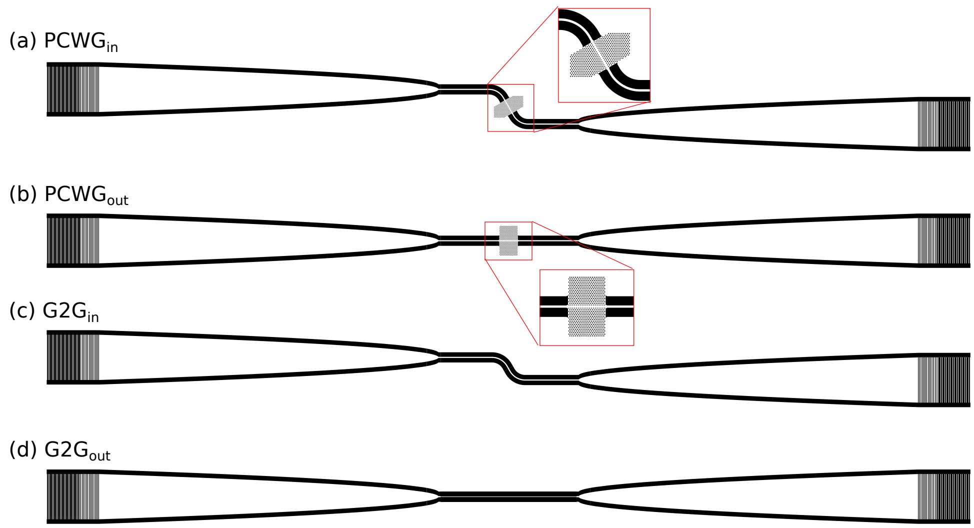

Figure 3.15: Reference devices included in the fabrication layout that contain input and output grating couplers and parabolic waveguides. In (a) and (b) PCWG$_{\mathrm{in}}$ and PCWG$_{\mathrm{out}}$ devices are shown that contain photonic crystal (PC) waveguides with structural parameters identical to those of the input and output PC waveguides of the triple microcavity device, respectively. In (c) and (d), the PC waveguides are omitted and the channel waveguides are directly connected to form G2G$_{\mathrm{out}}$ and G2G$_{\mathrm{out}}$ references devices.

is varied are chosen based on the results from the first iteration of fabrication.

The grating coupler groove widths are bracketed over the layout to ensure that light can be coupled into and out of at least a subset of microcavity devices. Each quadrant of the layout in Fig. 3.14 contains groups of gratings, where Groups 1 to 4 are indicated by the number of squares in the first column of markers to the left of each set of devices. For Groups 1, 2 and 3, the grating slot widths are scaled by factors $s_{\mathrm{gc}} = 0.91, 0.94$ and 0.97, respectively. The devices within each of these groups are otherwise identical. Group 4 contains gratings with $s_{\mathrm{gc}} = 0.94$, and modified microcavity devices, addressed shortly. These s_{gc} are chosen because, in the previous iteration, the transmission of the $s_{\mathrm{gc}} = 1$ grating peaked at $f \simeq 197.4$ THz ($f \simeq 1520$ nm), which is in good agreement with the simulated result and at higher energy than the target resonant mode center wavelength $f_2 \simeq 196$ THz ($\lambda_2 \simeq 1530$ nm). The scaling factors of $s_{\mathrm{gc}} = 0.91, 0.94$ and 0.97 are simulated to give a peaks near $\lambda \simeq 193.5, 194.8$ and 196 THz, respectively. The choice is made to err on the side of small hole sizes, because the grating coupling peaks can be shifted to higher frequencies by decreasing the magnitude of the coupling angle from $45°$ down to $10°$ (shift is ~ 0.5 THz per degree), while the angle can only be increased to $\sim 50°$, limiting the lowest achievable peak frequencies.

Table 3.4: Summary of device parameters bracketed across the layout. The set of values is given for each bracket parameter. The "Bracket name" describes how each bracket is referred to in the text, usually followed by a number (e.g. Group 1 corresponds to devices with $s_{\mathrm{gc}} = 0.91$), with the exception of "Type" where they are labelled as Type I ($s_{\mathrm{wg,sym}} = 1$) and II ($s_{\mathrm{wg,sym}} = 0.912$). The "Affected" column describes which of the microcavity and reference devices are affected by this parameter.

Parameters	Bracket name	Affected	Description
$s_{\mathrm{gc}} = 0.91, 0.94, 0.97, 0.94$	Group	All	Grating groove width scaling factor
$s_{\mathrm{h}} = 0.91, 0.94, 0.97, 0.94$	Set	TMC, $\mathrm{PCWG_{in}}$, $\mathrm{PCWG_{out}}$	PC hole radius scaling factor
$h_{\mathrm{ms}} = -4, -2, 0, 2, 4, 6, 8$ nm	Number	TMC†	Mode spacing tuning hole shift
$s_{\mathrm{ms}} = 0.97$ to 1.02^{*}	Number	TMC‡	Mode spacing tuning hole radius scaling factor
$s_{\mathrm{wg,sym}} = 1, 0.912$	Type	TMC	Symmetrizing hole radius scaling factor

† Only affects TMC devices in Groups 1 to 3
* Linearly spaced over 7 devices
‡ Only affects TMC devices in Group 4

Within each group, the overall hole sizes are scaled by three different factors, $s_{\mathrm{h}} = 0.91, 0.94$ and 0.97, for Sets 1, 2 and 3, indicated by the number of squares in the second column of markers to the left of each set. The scaling factors are applied to all hole radii, including $r, r_{\mathrm{mid}}, r_{\mathrm{wg,sym}}, r_{\mathrm{wg}}^{\mathrm{in}}$ and $r_{\mathrm{wg}}^{\mathrm{out}}$. These scaling factors are chosen because, in the first iteration, the microcavity mode energies for $s_{\mathrm{gc}} = 1$ were $\sim$ 197.3 THz, which is 1.4 THz higher than the simulated result, such that many of the mode frequencies coincided with the high energy end of the laser tuning range (197.3 THz). Simulations show that decreasing the hole radii by a 3% shifts the modes by ~ -1.4 THz, so the bracket used incrementally shifts the modes away from the laser tuning limit.

For Groups 1 to 3, the mode spacing of the microcavities is fine-tuned by shifting the targeted holes near the center of the microcavity. The shifts are $h_{\mathrm{ms}} = -4, -2, 0, 2, 4, 6$ and 8 nm, for device Numbers 1 to 7. The two nanometer increment is the minimum shift possible given that the shot pitch is 2 nm for this EBL process. In Group 4, instead of shifting holes, the mode spacing is tuned by scaling the radii by $s_{\mathrm{ms}} = 0.97$ to 1.02 nm over 7 devices ($r_{\mathrm{mid,ms}} = 122$ to 128 nm, when

$s_{\rm h} = 1$). The mode spacing parameters are chosen because, the "identical" TMC target devices on the first iteration chip have $\Delta f_{\rm off}$ between -0.10 to 0.18 THz, and the chosen $h_{\rm ms}$ and $s_{\rm ms}$ result in mode spacing tuning roughly over this range, as shown in Fig. 3.8(d) and (c), respectively. The shift is chosen as the primary tuning method (Groups 1 to 3) because it was anticipated to be more reliably reproduced than the hole size tunings of $\Delta r \sim 1$ nm.

Finally, for each of the brackets described above, two types of microcavity devices are included in the layout. Type I devices are defined by setting $r_{\rm wg,sym} = r_{\rm mid}$ for the holes that aim to provide symmetry around the output waveguide, such that the scaling factor applied to these holes is $s_{\rm wg,sym} = 1$. In Type II devices, symmetrization is applied and $s_{\rm wg,sym} = 0.912$. Within each set of the layout, the seven Type I and II devices are laid out, paired as the top two devices in each column, and the bottom two. The center device of each column is a reference device (G2G$_{\rm out}$,G2G$_{\rm in}$, PCWG$_{\rm in}$,PCWG$_{\rm out}$, from left to right).

Alignment marks are included in the fabrication layout (crosses in Fig. 3.14) to aid the photolithography process described in the next section.

3.3.2 Post-fabrication processing

Once the silicon-on-insulator chips are fabricated, the buried oxide layer (silicon dioxide, SiO_2) is removed from underneath the microcavity regions defined in the silicon device layer in order to achieve high Q modes. This processing involves photolithography and a hydrofluoric acid (HF) etch.

The full undercutting procedure is outlined in Table 3.5. First, photoresist is spin-coated on the fabricated microchip. The photoresist is selectively exposed with ultra-violet radiation by using a mask that covers all but the regions around the microcavities and a mask aligner. The exposed resist is removed using a developer and the microchip is submerged in HF to etch the silicon dioxide. Finally, remaining photoresist is removed from the sample.

An optical microscope images of Chip B, after the photoresist is developed is shown in Figs. 3.16(a) and (b). The light pink strips show where the photoresist has been removed. Figure 3.16(c) shows TMC device after the undercutting process is complete. The darker pink hallow roughly outlines where the silicon dioxide is removed beneath the silicon device layer.

Table 3.5: Recipe for post-fabrication undercutting.

	Step	Procedure	Time Duration
Process	1	Cover with HMDS Primer	
	2	Ramp up to 500 rpm/s	
	3	Spin at 1700 rpm	40s
	4	Spin down at 500 rpm	
	5	Let HMDS dry	1 min
	6	Cover with AZ P4110 photoresist	
	7	Repeat steps 2 to 4	
	8	Soft bake at 90°C	10 min
Exposure	9	Align mask	
	10	Expose with 320 nm light at 22 W/cm^2	45 s
Development	11	Emerse in AZ P4110 developer solution (4:1, developer: DI water)	90 s
	12	Rinse with DI water and dry with N_2 gas	
	13	Hard bake at 120°C	10 min
Etch	14	Emerse in HF solution (10 parts 40% NH4F to 1 part 49% HF)	15-20 min
	15	Rinse with DI water and dry with N_2 gas	

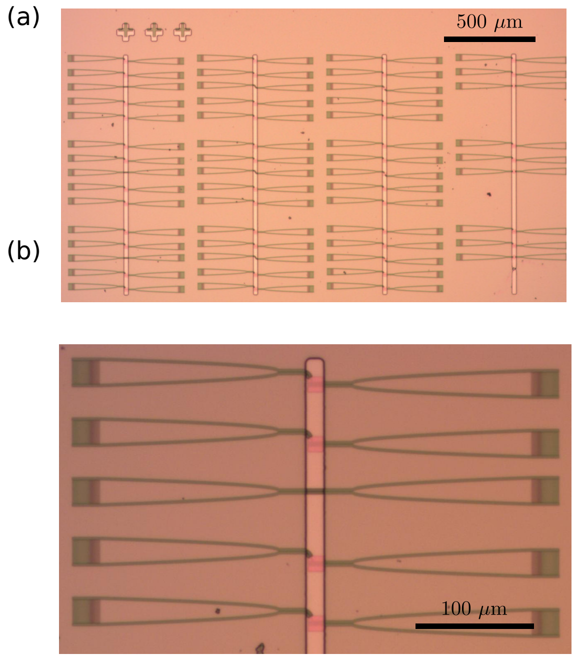

Figure 3.16: Optical microscope images of the silicon microchip at various stages in undercutting process. (a) Image taken post-photolithography, such that the developed photoresist is intact. Light pink lines where the bare silicon is exposed. (b) Same as in (a), but with higher magnification. (c) Image taken after the hydrofluoric acid etch and the photoresist removal. The pink hallow around the photonic crystal region outlines where the oxide is removed beneath the silicon.

Chapter 4

Survey results to identify the best devices for full FWM analysis

In this chapter, a survey of the linear transmission spectra for devices across the microchip is described that was used to identify the specific structures used for the nonlinear characterization reported in the following chapter.

4.1 Survey of devices across microchips

The transmission spectra of the grating couplers are first studied, in order to ensure that light is appropriately coupled into and out of the devices. As discussed in Section 3.3.1, the grating coupler groove widths are bracketed with three different scaling factors, where $s_{\mathrm{gc}} = 0.91, 0.94, 0.97$ and 0.94, for Groups 1,2,3 and 4, respectively. Figure 4.1 plots the raw transmission spectra measured for grating-to-grating $\mathrm{G2G_{in}}$ devices in each of the four groups on Chip A, that directly link input and output gratings with parabolic and channel waveguides. In Fig. 4.1(a), the angle of incidence is $\theta = -41°$ for all devices measured, and in (b) the angles of incidence, $-37°$, $-39°$, $-42°$ and $-39°$, are chosen for Groups 1 to 4, to achieve peak coupling at ~ 1545 nm, which is near the target microcavity resonant wavelengths. The peaks shift by ~ 4 nm/degree, and by adjusting the grating coupling angle (adjustable between $\sim 10° - 50°$), it is possible to shift the grating coupling peaks over the full tuning range of both lasers ($\lambda = 1520$ nm to 1610 nm). This means that any microcavity devices with resonant wavelengths within the tuning range of the lasers are accessible with these gratings. Similar results are found for the grating couplers on Chip B.

There is good agreement between the transmission spectra measured for "identical" (same layout) grating-to-grating reference devices within the same group: the transmission efficiencies vary within ±3 %, while the peak wavelengths vary within ±1 nm. This indicates that the reference devices can be used to reliably estimate the input and output coupling efficiencies of the microcavity devices. However, the fast sinusoidal modulations in the spectra (see Fig. 4.1), caused by multiple reflections off the grating and parabolic waveguide components, have phase-shifts that vary significantly from device to device. The approach to dealing with this issue is discussed in greater detail in Appendix D.

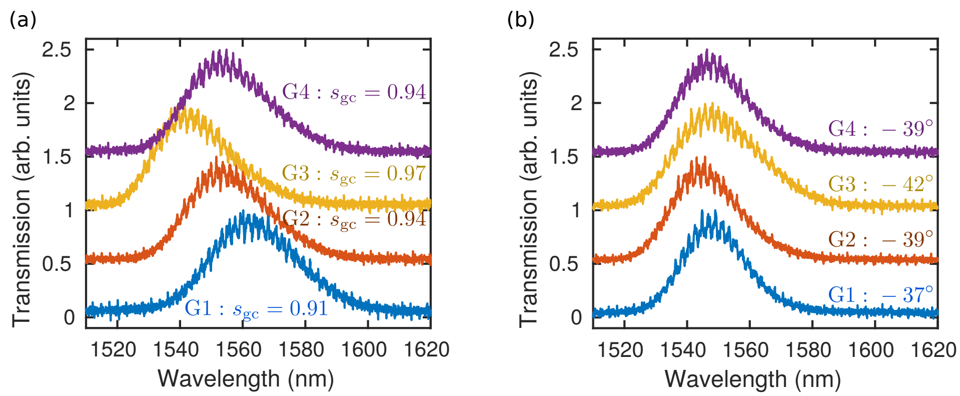

Figure 4.1: Transmission measurements for $G2G_{in}$ devices in Groups 1 to 4 of Chip A (bottom to top), (a) taken with a $-41°$ coupling angle, (b) taken with coupling angles between $-42°$ and $-37°$ (labelled on plot) to achieve peaks near $\lambda = 1545$ nm.

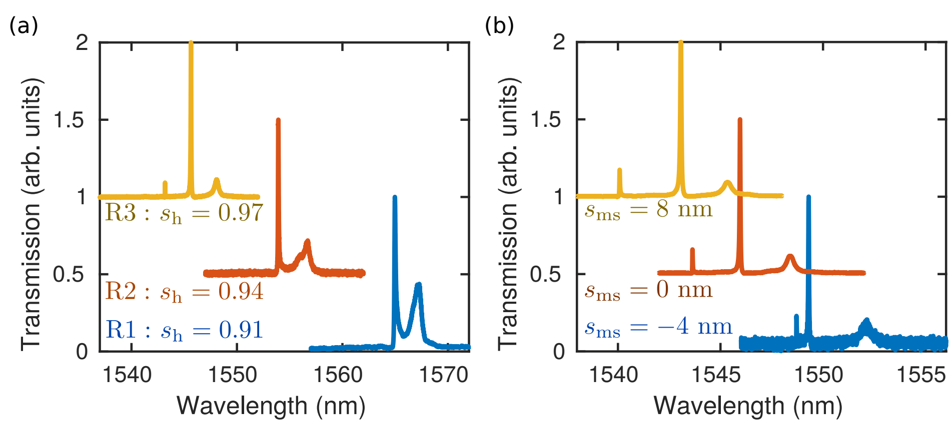

Figure 4.2: (a) Transmission measurements of Type I microcavity devices on Chip A, with mode spacing parameter $s_{ms} = 0$ nm, for the three hole size brackets labelled on the plot. (b) Transmission measurements of Type II microcavity devices on Chip A, with $s_h = 0.97$ and mode spacing parameters labelled on the plot.

The microcavity transmission is studied by adjusting the grating coupler angle appropriately such that the coupling peak is near the resonant mode wavelengths. Only a subset of all fabri-

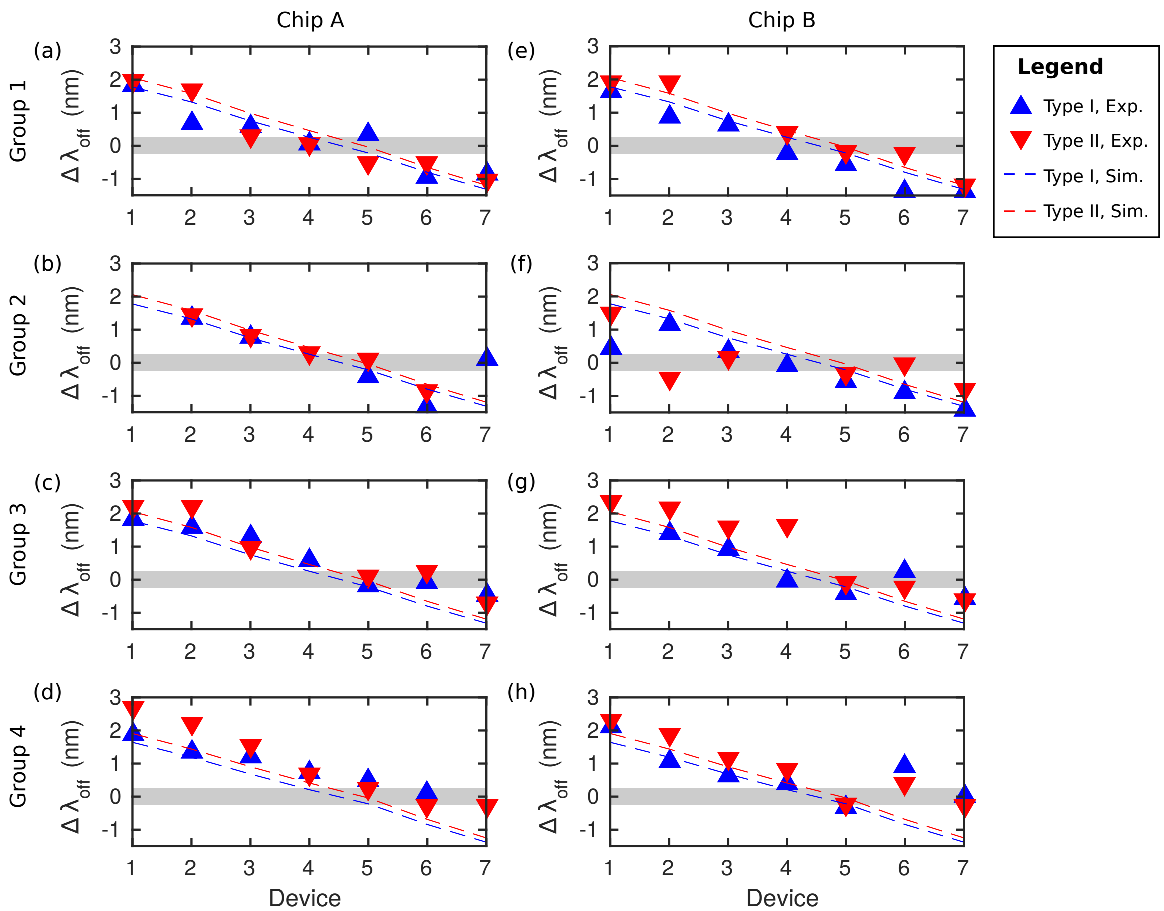

Figure 4.3: Microcavity mode spacing offsets, $\Delta\lambda_{\text{off}} = \lambda_1 + \lambda_3 - 2\lambda_2$ found from transmission measurements, plotted as a function of device number in the $s_{\text{h}} = 0.97$ set, where λ_m are the resonant wavelength, for Type I and Type II microcavities. (a)-(d) Results for Groups 1 to 4 (top to bottom) devices on Chip A. (e)-(h) Results for Groups 1 to 4 (top to bottom) devices on Chip B. In Groups 1 to 3, each device has a different mode spacing parameter, with $s_{\text{ms}} = 8, 4, 2, 0, -2, -4$ nm for Devices 1 to 7, where s_{ms} is the position shift of a select group of holes. In Group 4, the mode spacing is modified by scaling a select group of holes by $s_{\text{ms}} = 0.968$ to 1.02, linearly over the seven devices. Data is omitted in cases where three modes are not observed in the transmission spectrum. The dashed lines show the simulated results (from perturbation theory) for Type I and II microcavities. The gray region has a width of 0.5 nm, which is a typical linewidth for the M3 mode (the lowest Q mode).

cated microcavity devices are expected to have resonant mode wavelengths near the target, due to bracketing of the PC hole sizes across the microchip. The overall hole size is bracketed with scaling factors, $s_{\text{h}} = 0.91, 0.94$ and 0.97, for Sets 1 to 3, and the resonant wavelengths are red-shifted by 10 nm per 3% decrease in hole size, as shown in the transmission spectra in Fig. 4.2(a). Transmission spectra for the last set, with the largest holes ($s_{\text{h}} = 0.97$), have resonant wavelengths near ~ 1545 nm, and there are three well defined resonant peaks for most devices in Set 3. Devices from this set are best suited for FWM measurements and are the ones used for the studies reported in Chapter 5.

Within each set with $s_{\rm h} = 0.97$, the mode spacing tuning parameter, $h_{\rm ms}$, is bracketed over seven different values, for the two types of microcavity devices, resulting in a total of 14 devices per set. The raw transmission spectra for the third, fifth (target), and seventh Type II devices of a $s_{\rm ms} = 0.97$ bracket on Chip A are plotted in Fig. 4.2(b). The mode spacing offsets, ($\Delta\lambda_{\rm off} = \lambda_1 + \lambda_3 - 2\lambda_2$), extracted from the transmission spectra of all devices in the four sets of each chip are summarized in Figs. 4.3(a)-(d) and 4.3(e)-(h) for Chips A and B respectively. The mode spacings roughly follow the simulated results (using perturbation theory), which are shown as dashed lines[4]. There are 10 and 12 devices on Chips A and B, respectively, that have mode spacing offsets within roughly a linewidth of the third mode (typical linewidth is ~ 0.5 nm), and are "good" candidates for four-wave mixing.

In Table 4.1, the average experimental results for "good" candidate devices are compared to simulation results for the designed Type I and II microcavity structures (with the layout hole scaling, $s_{\rm h} = 0.97$). The center mode (M2) resonant wavelengths are fairly close to those simulated, however the simulated mode spacings are larger. The quality factors of the lowest Q mode (Q_3) agrees well with those simulated, while the higher Q's don't agree as well.

Table 4.1: Comparison of experimental results averaged over "good" candidate devices, and simulation results for the designed structures. λ_2 is the resonant wavelength of the center mode, $\Delta\lambda_{\rm ms}$ is the mode separation, and Q_m are the total quality factors for modes $m = 1, 2, 3$. Type II microcavities have four holes that are scaled by $s_{\rm wg,sym} = 0.912$. These holes are not scaled in Type I microcavities ($s_{\rm wg,sym} = 1$).

	Experiment		Simulation	
Parameter	Type I	Type II	Type I	Type II
λ_2 (nm)	1546	1547	1541	1541
$\Delta\lambda_{\rm ms}$ (nm)	2.4	2.4	3.1	3.1
Q_1	73,000	74,000	59,000	16,000
Q_2	30,000	37,000	102,000	102,000
Q_3	3,200	3,100	3,800	3,300

[4]The simulated results are evaluated for discrete $h_{\rm ms}$ and $s_{\rm ms}$, and the dashed lines in Fig. 4.3 are actually the connections between the discrete results.

4.2 Stimulated four-wave mixing spectrum

Stimulated four-wave mixing measurement results for a typical "good" candidate device, are presented in Fig. 4.4. The linear transmission spectrum is shown in Fig. 4.4(a), where the dashed blue and green lines coincide with the resonant wavelengths of M1 and M2, while the dashed red line coincides with $\lambda_3^{\rm FWM} = 2\lambda_2 - \lambda_1$. Figures 4.4(b) and (c) show the stimulated FWM idler power (circles) as a function of the output filter center wavelengths when signal wavelength is set to λ_1 and $\lambda_3^{\rm FWM}$, respectively, and the pump wavelength is tuned to λ_2. The pump and signal powers are 38.5 μW and 22.4 μW, respectively. The idler power spectra are essentially a convolution between the filter transmission spectrum, $\eta_{\rm filter}(\lambda)$, and the *actual* spectrum of idler power in the output PC waveguide. The filter transmission spectrum lineshape is plotted as the gray shaded regions in these figures. The idler power closely follows the filter lineshape near the peak, which means that the linewidth over which the idler photons are actually generated is much much smaller than the linewidth of the filter (0.17 nm). Also included in Fig. 4.4(b) and (c) is the background power measured (triangles) when the signal laser is turned off, but the pump power remains active. While in Chapter 1, this excitation configuration was suggested for measuring spontaneous FWM, it is not currently clear if the background signal here is due to spontaneous nonlinear FWM, or perhaps some other processes. This is discussed further in Chapter 7.

4.3 Analysis of survey results

After surveying the linear transmission data from a large number of devices, examples of which were provided above, it was clear that the fabricated structures behaved only qualitatively as the simulations done during their design. While the absolute resonant wavelengths were within ~ 10 nm of those expected, and their dependences on systematic, bracketed parameter sweeps agreed well, many other properties did not. In particular, the absolute Q values of M1 and M2 were off (some higher, some lower) by as much as a factor of 5, and the absolute on-resonant transmission values were often off by factors of 3. The wavelength separation of the modes was also off by as much as 1 nm. Clearly the original simulations of various device parameters can not be used to accurately predict or explain the nonlinear behaviour of the actual samples.

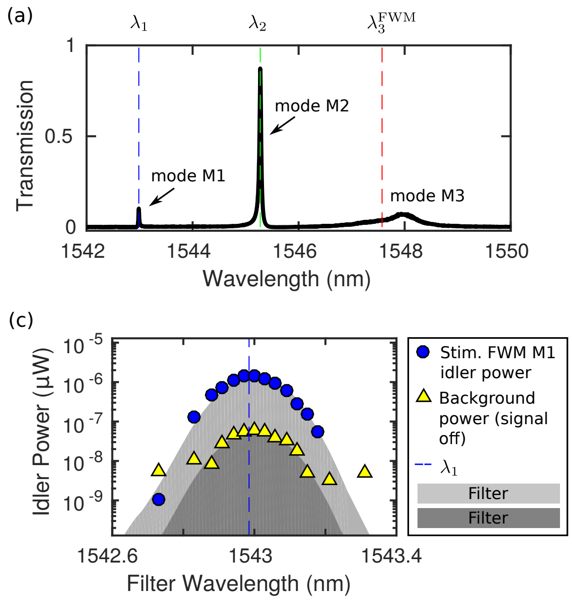

Figure 4.4: (a) Linear transmission for a microcavity structure studied with four-wave mixing (FWM). Resonant wavelengths λ_1, λ_2, and equally spaced $\lambda_3^{\mathrm{FWM}} = 2\lambda_2 - \lambda_1$, are plotted as the dashed blue, green and red lines, respectively. (b)-(d), Four-wave mixing results, measured using pump and signal powers 38.5 μW and 22.4 μW respectively. The idler power is reported relative to the output PC waveguide (without accounting for the output spectral filtering). (b) Stimulated FWM idler power as a function of the filter center wavelength for $\lambda_{\mathrm{signal}} = 1543.01$ nm (circles). The dashed line shows the wavelength λ_3^{FWM}. (c) Same as (b) but with $\lambda_{\mathrm{signal}} = 1547.58$ nm. The shaded regions in (b)-(c) are the scaled filter transmission spectra, and the triangles show the background power when the signal laser is turned off and the pump laser remains on.

The bulk of this thesis work addressed a solution to this problem. By quantitatively and thoroughly measuring and modelling the nonlinear transmission of modes M1 and M2, *and* the power dependence of the stimulated FWM response measured using both M1 and M3 as separate signal channels, a least-squares minimization of the modelled and actual data yields well-defined values for all relevant linear and nonlinear device parameters of the actual devices. This overall characterization protocol for a triple-microcavity nonlinear structure therefore represents a novel means of extracting detailed *linear* and nonlinear device parameters that cannot be obtained using linear transmission spectroscopy alone.

Chapter 5

Nonlinear characterization

Three types of optical measurements are used to characterize the triple microcavity performance and develop a model to predict its nonlinear response: linear transmission, nonlinear transmission and stimulated four-wave mixing measurements. Least-squares analyses of the nonlinear experimental results are used to determine the 15 unknown microcavity parameters, and two Fabry-Perot parameters, described in Chapter 2, that enter the nonlinear response models.

5.1 Measurement and modelling results

Four devices with nearly identical designs are measured and modelled. The microcavity structures are differentiated by only small perturbations. The design parameters for these four devices are summarized in Table 5.1. Three are from Chip A and one is from Chip B.

Table 5.1: Design parameters for the triple microcavity devices studied in this thesis. The factor s_{h} scales the holes radii r, r_{mid}, $r_{\mathrm{mid,ms}}$, $r_{\mathrm{wg}}^{\mathrm{in}}$, $r_{\mathrm{wg}}^{\mathrm{out}}$, and $r_{\mathrm{wg,sym}}$ described in Table 3.1 and illustrated in Fig. 3.1. The hole shift h_{ms} is also presented therein. The factor $s_{\mathrm{wg,sym}}$ applies an additional scaling factor to $r_{\mathrm{wg,sym}}$.

Device	Chip	s_{h}	h_{ms}	$s_{\mathrm{wg,sym}}$
1	A	0.97	0 nm	1
2	A	0.97	-2 nm	0.912
3	A	0.97	0 nm	0.912
4	B	0.97	0 nm	0.912

The linear transmission spectra are plotted in Fig. 5.1. All peaks are resolved in these plots. The resonant wavelengths λ_m, total quality factors Q_m^{lin} and maximum transmissions $\overline{T}_m^{\mathrm{lin}}$ extracted from these results are summarized in Figs. 5.2(a), (b) and (c), respectively. The quality factor is estimated as $Q = \delta\lambda_m/\lambda_m$, where $\delta\lambda_m$ is the full-width at half maximum. It is unknown why the low Q mode, M3, is not Lorentzian for Devices 2 to 4, as FDTD simulations predict a Lorentzian lineshape.

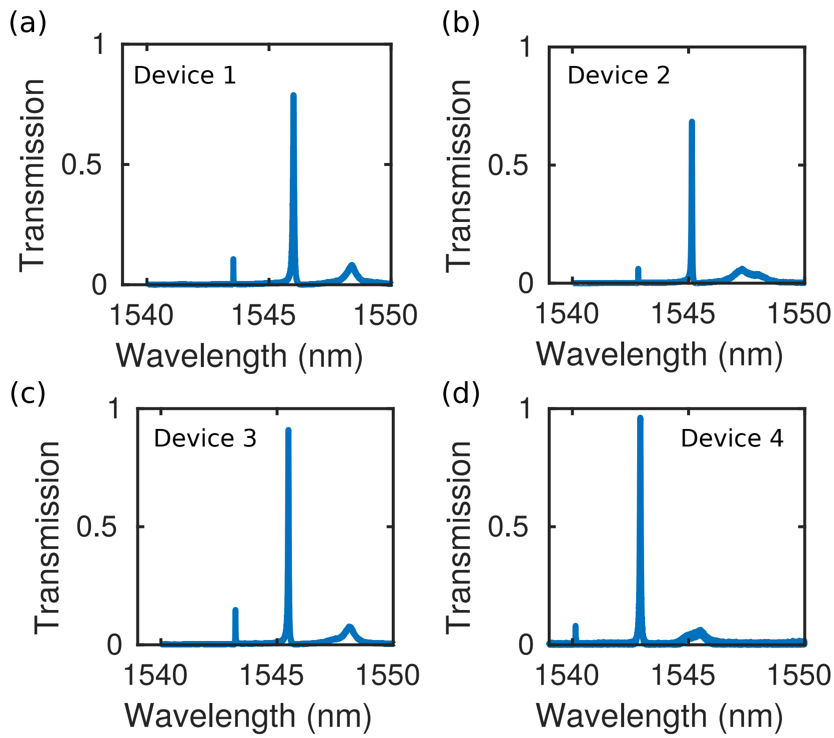

Figure 5.1: Linear transmission spectra for (a) Device 1, (b) Device 2, (c) Device 3 and (d) Device 4. The transmission is calculated using the best fit Fabry-Perot parameters, ϕ_{in} and ϕ_{out}.

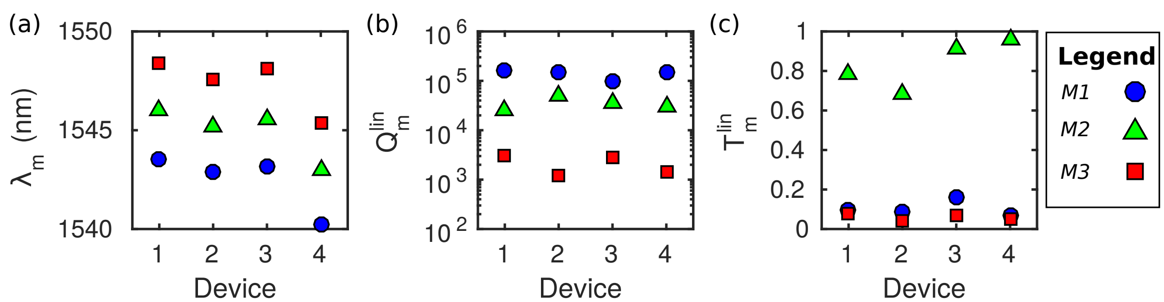

Figure 5.2: Linear transmission results for the four devices characterized: (a) resonant wavelengths, λ_m, (b) total quality factors, Q_m^{lin}, and (c) peak transmission, T_m^{lin}. The results are plotted for modes M1, M2 and M3. The T_m^{lin} are calculated using the best fit Fabry-Perot parameters, ϕ_{in} and ϕ_{out}.

Figure 5.3 shows the experimental results for nonlinear transmission and stimulated four-wave mixing measurements for the four devices (results for Devices 1 to 4 are shown in Rows 1 to 4 (top

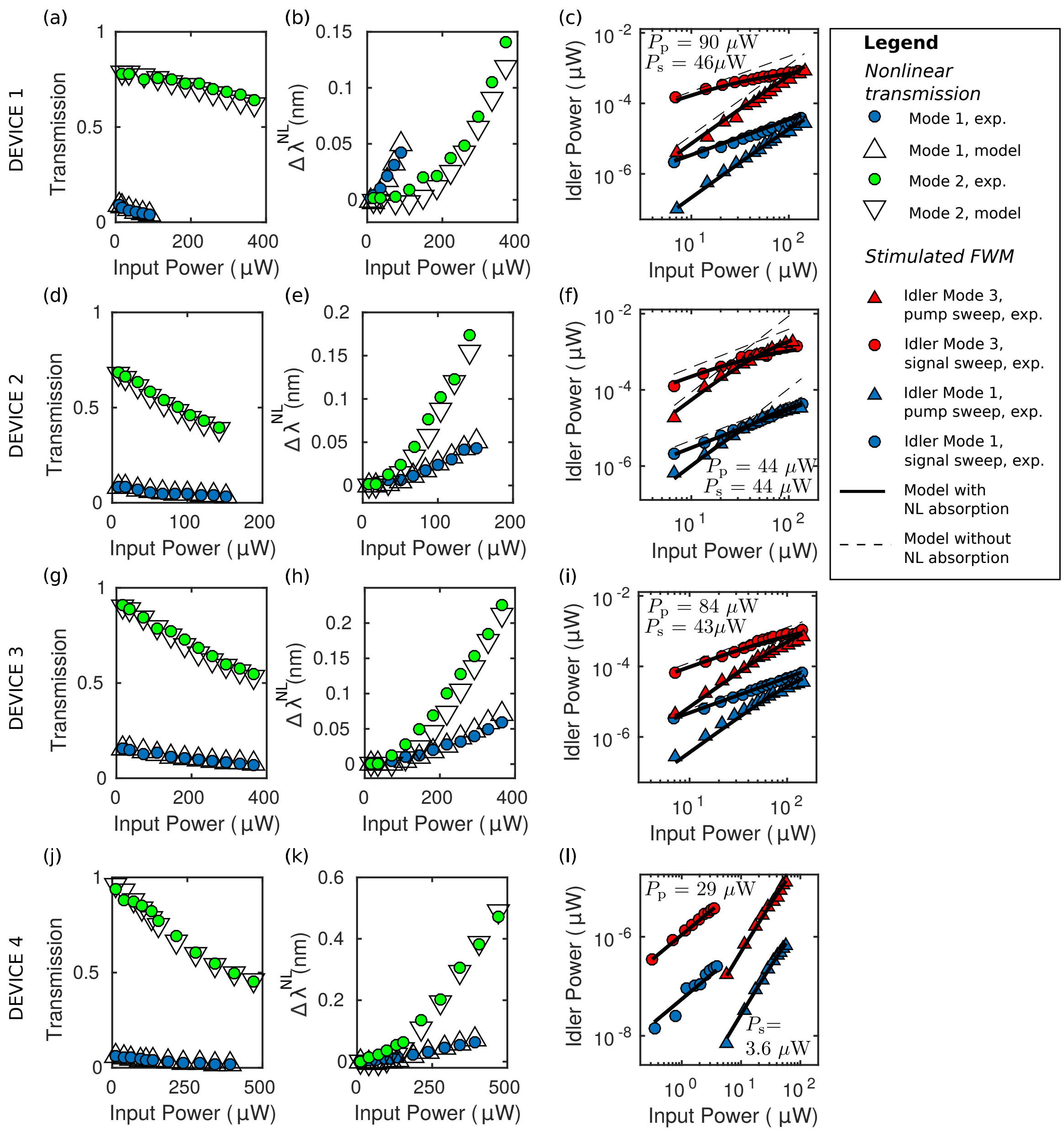

Figure 5.3: Nonlinear transmission and four-wave mixing analysis results for Devices 1 to 4 (top to bottom rows). Columns 1 and 2 contain the peak transmission and resonant wavelength shifts, respectively, for Mode 1 (blue) and Mode 2 (green), found experimentally (filled circles), and using the model with best fit parameters (open markers). Column 3 shows the experimental FWM idler power in Mode 1 (blue) and Mode 3 (red), as a function of pump power (triangles) for fixed signal power at P_s (labelled on the plots) and as a function signal power (circles) for fixed pump power at P_p (also labelled). The fixed pump power The predicted idler powers are shown with thick black lines. The dashed lines show the predicted power when nonlinear absorption is ignored.

to bottom), respectively). The data sets presented here are used in the least-squares analyses for each device, where the experimental data is compared against model functions. The model function predictions, that apply the extracted best fit values, are also plotted in Fig. 5.3. The first two columns show nonlinear transmission results, where the experimental results for Modes 1 and 2 are blue and green filled circles, respectively, while the model predictions are upward and downward open triangles. The last column shows four-wave mixing results, where circles and triangles show experimental idler powers measured as a function of the signal and pump power, respectively, while the other input power is fixed. The red filled markers are for idler photons generated in M3, and the blue markers are for idler photons generated in M1. The black lines show the predicted idler powers.

Figure 5.4 shows the experimental nonlinear transmission spectra, from which the peak transmission and wavelength shifts in Fig. 5.3 are extracted. The spectra predicted based on the model functions are also plotted, where results for Devices 1 to 4 are shown in Rows 1 to 4 (top to bottom), respectively. The left and right columns show the transmission spectra for M1 and M2, respectively.

The results presented in Fig. 5.3 are replotted in Fig. 5.5, where new model functions apply microcavity parameters extracted from a modified analysis procedure. In the modified procedure, a subset of the parameters (R_{th}, τ_{carrier}, and τ_{abs}) are held fixed at the average best fit values found across Devices 2 to 4, instead of entering the analyses as fit parameters. These parameters are expected to be roughly the same for all devices as they are relatively insensitive to small perturbations in the photonic structures (introduced by design or due to fabrication imperfections). The Device 1 best fit parameters are excluded from the average because they couldn't be reliably extracted, as the sum of the least-squares wasn't minimized across all parameters.

5.2 Derivation of model functions

The models used in the microcavity least-squares analyses are derived using temporal coupled mode theory (TCMT). In this theory, localized microcavity modes and propagating waveguide modes are weakly coupled through a small perturbation. Conservation of energy is used to calculate the steady-state energy in the microcavity modes for a given continuous-wave waveguide excitation scheme. This method is appropriate for studying resonant modes with $Q \gtrsim 30$ [38], as is the case here. The triple microcavity is modelled as a single resonator that supports multiple modes. The

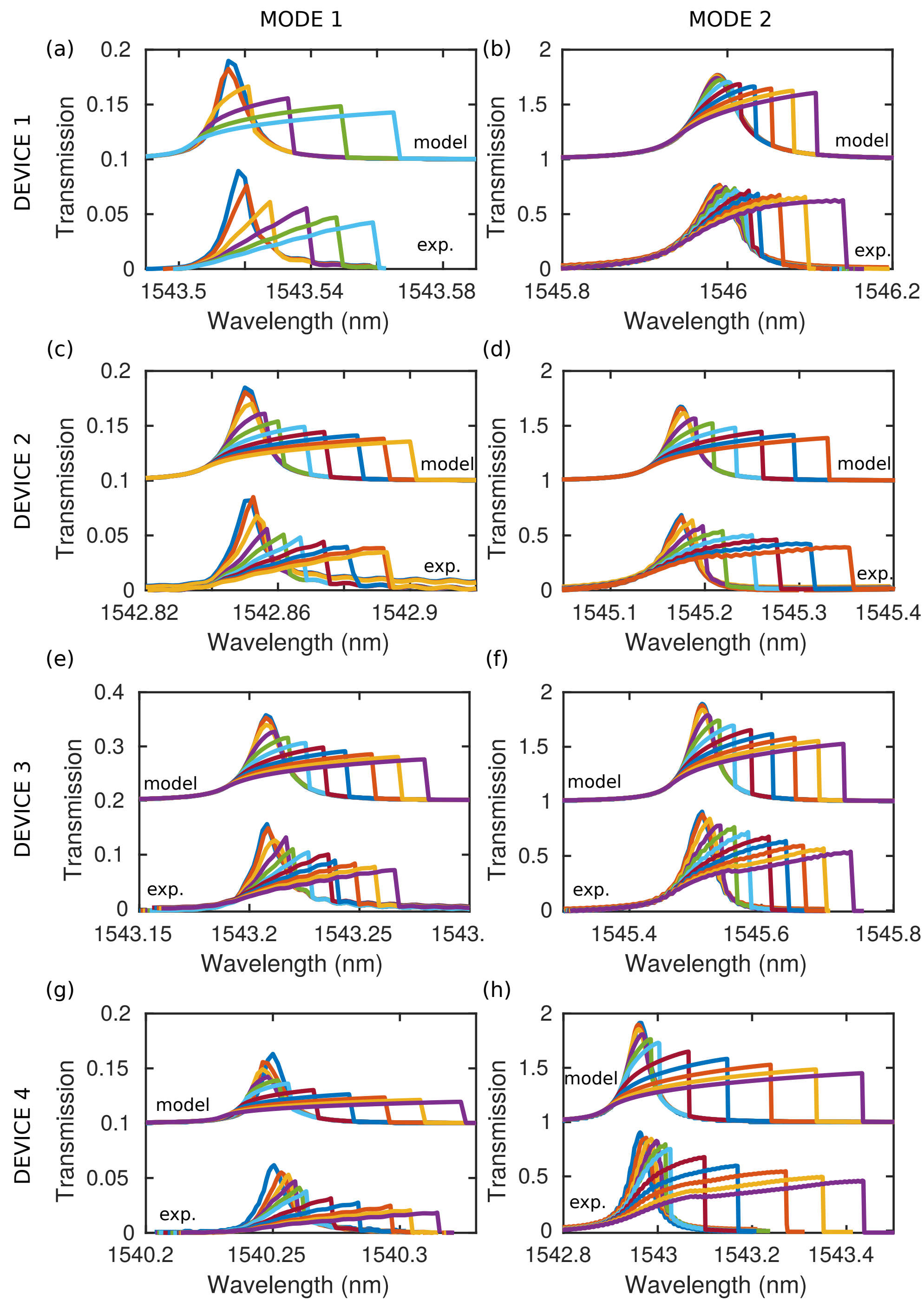

Figure 5.4: Nonlinear transmission results for Devices 1 to 4 (top to bottom rows), for Modes 1 and 2 (left and right columns). Bottom plots show the experimental data and top plots show the spectra predicted using the model with best fit parameters, where both are plotted on absolute transmission scales, shifted relative to each other. The input powers for each spectrum corresponds power for each marker in the nonlinear transmission data plots of Fig. 5.3 (first two columns).

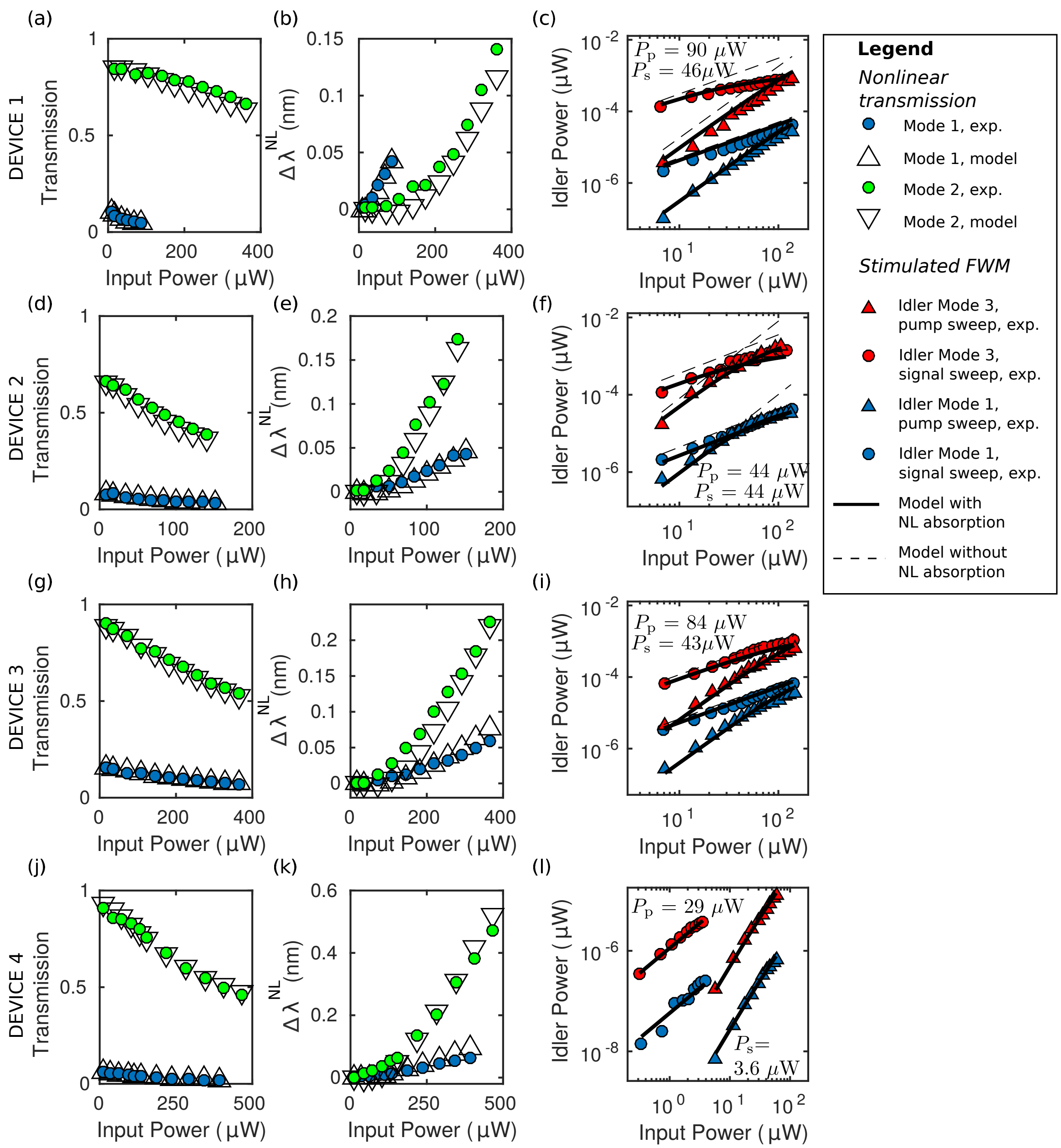

Figure 5.5: Nonlinear transmission and four-wave mixing analysis results for Devices 1 to 4 (top to bottom rows) when $R_\mathrm{th}, Q_\mathrm{abs}$ and τ_carrier are held fixed at their average values. Columns 1 and 2 contain the peak transmission and resonant wavelength shifts, respectively, for Mode 1 (blue) and Mode 2 (green), found experimentally (filled circles), and using the model with best fit parameters (open markers). Column 3 shows the experimental FWM idler power in Mode 1 (blue) and Mode 3 (red), as a function of pump power (triangles) when the signal power is fixed at P_s (labelled) and signal power (circles) when the pump power is fixed at P_p (labelled). The predicted idler power are shown with thick black lines. The dashed lines show the predicted power when nonlinear absorption is ignored.

equations of motion are decoupled in the linear regime and become coupled in the nonlinear regime, where the refractive index of the silicon can, in general, be dependent on the electromagnetic energy stored in any of the three modes.

The TCMT is first considered in the case where nonlinear effects are negligible. Next, nonlinear frequency conversion and absorption effects are introduced and included in the TCMT model, and the nonlinear transmission and FWM formulations are reported.

5.2.1 Linear model

The cavity modes considered here are coupled to one input and output waveguide, as well as loss channels, including radiation and material absorption, as illustrated in Fig. 5.6. The electric field of light in the cavity mode is $\mathbf{E}_m(\mathbf{r},t) = \mathrm{Re}\left[a_m(t)\breve{\mathbf{E}}_m(\mathbf{r})/\sqrt{\int d^3\mathbf{x}\frac{1}{2}\varepsilon(\mathbf{r})|\breve{\mathbf{E}}_m(\mathbf{r})|^2}\right]$, where $\breve{\mathbf{E}}_m(\mathbf{r})$ is the unnormalized electric field mode profile and $|a_m(t)|^2$ is the energy stored in the cavity. Here, $a_m(t)$ is a classical amplitude, not a quantum operator. In the linear regime, the equation of motion of the amplitude, $a_m(t)$, for cavity mode m is [38],

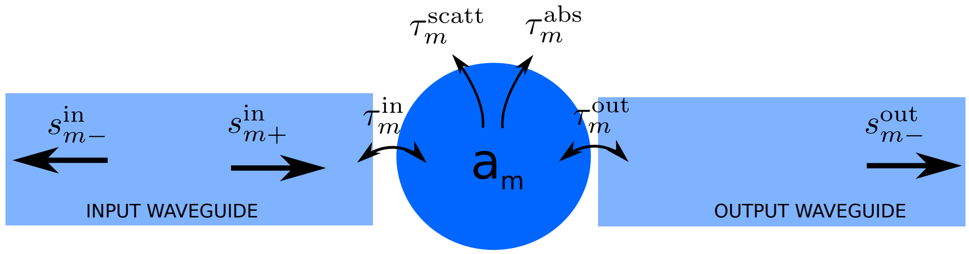

Figure 5.6: Schematic of coupled-mode theory for cavity supporting three modes. Cavity mode m has field amplitude a_m and energy $|a_m|^2$. The mode is coupled with lifetime τ_m^i to channel i. The optical power of light propagating toward the microcavity is $|s_{m+}^{\mathrm{in}}|^2$, and the optical powers exiting through the input and output waveguides are $|s_{m-}^{\mathrm{in}}|^2$ and $|s_{m-}^{\mathrm{out}}|^2$, respectively.

$$\dot{a}_m(t) = -(i\omega_m + \tau_m^{-1})a_m(t) + \sqrt{\frac{2}{\tau_m^{\mathrm{i}}}}s_{m+}^{\mathrm{in}}(t) \tag{5.1}$$

where ω_m is the mode resonance frequency, ${\tau_m}^{-1} = \sum_i (\tau_m^i)^{-1}$ where τ_m^i are the coupling lifetimes for channel $i = \{\mathrm{in}, \mathrm{out}, \mathrm{scatt}, \mathrm{abs}\}$, and $|s_{m+}^{\mathrm{in}}(t)|^2$ is the power that is launched into the input waveguide from an external source (here the output waveguide is not excited). The total quality factor of the mode is $Q_m = \omega_m\tau_m/2$. The power leaving via channel i, $|s_{m-}^i|^2$, is described by,

$$s_{m-}^i(t) = \zeta s_{m+}^i(t) + \sqrt{\frac{2}{\tau_m^{\mathrm{i}}}}a_m(t). \tag{5.2}$$

where $s^{\mathrm{in}}_{m+}(t) \neq 0$ and $s^{\mathrm{out}}_{m+}(t) = s^{\mathrm{scatt}}_{m+}(t) = s^{\mathrm{abs}}_{m+}(t) = 0$. The first term on the right hand side is a contribution from input light that is directly (non-resonantly) reflected from the microcavity, while the second term is a contribution from light that leaks into the i^{th} channel from energy stored in the m^{th} mode of the microcavity. Time reversal symmetry requires that $\zeta = -1$ [38].

In the linear transmission measurements studied in this thesis, continuous-wave excitation is launched into the input waveguide, and the power transmitted to the output waveguide is measured in steady-state. The drive amplitude of the input excitation is $s^{\mathrm{in}}_{m+}(t) = s^{\mathrm{in}}_{m+}e^{-i\omega_d t}$, and in steady-state, the electric field in the cavity oscillates at the drive frequency, such that $a_m(t) = a_m e^{-i\omega_d t}$, where the steady-state amplitude a_m is described by,

$$0 = i\omega^d_m a_m - i\omega_m a_m - \tau_m^{-1} a_m + \sqrt{\frac{2}{\tau^{\mathrm{in}}_m}} s^{\mathrm{in}}_{m,+}, \tag{5.3}$$

and

$$s^{\mathrm{i}}_{m-} = -s^{\mathrm{i}}_{m+} + \sqrt{\frac{2}{\tau^{\mathrm{i}}_m}} a_m, \tag{5.4}$$

where $s^{\mathrm{out}}_{m+} = s^{\mathrm{scatt}}_{m+} = s^{\mathrm{abs}}_{m+} = 0$. The steady-state energy stored in the cavity is,

$$U_m = |a_m|^2 = \frac{2{\tau^{\mathrm{in}}_m}^{-1} P^{\mathrm{in}}_m}{(\omega^d_m - \omega_m)^2 + \tau_m^{-2}}, \tag{5.5}$$

where $P^{\mathrm{in}}_m = |s^{\mathrm{in}}_{m+}|^2$, which has a Lorentzian lineshape. The transmission spectrum of power in the output channel is, directly proportional to U_m,

$$T_m(\omega_d) = \frac{2}{\tau^{\mathrm{out}}_m} U_m = \frac{4{\tau^{\mathrm{in}}_m}^{-1} {\tau^{\mathrm{out}}_m}^{-1} P^{\mathrm{in}}_m}{(\omega^d_m - \omega_m)^2 + \tau_m^{-2}}, \tag{5.6}$$

thus it also has a Lorentzian lineshape.

5.2.2 Nonlinear model

In this section, nonlinear absorption effects are included in the model, along with nonlinear frequency conversion through the third order nonlinearity, $\boldsymbol{\chi}^{(3)}$. These effects are discussed here and derived in Appendix E.

The equations of motion that include nonlinear absorption and frequency conversion are given by [52, 71, 110],

$$\begin{aligned}\dot{a}_1(t) = &-i[\omega_1 + \Delta\omega_1^{\mathrm{NL}}(|a_1|^2, |a_2|^2, |a_3|^2)]a_1(t) - \tau_1(|a_1|^2, |a_2|^2, |a_3|^2)^{-1}a_1(t) \\ &+ i\omega_1\beta_1[a_2(t)]^2 a_3^*(t) + \sqrt{\frac{2}{\tau_1^{\mathrm{in}}}} s_{1+}^{\mathrm{in}}(t), \end{aligned} \tag{5.7}$$

$$\begin{aligned}\dot{a}_2(t) = &-i[\omega_2 + \Delta\omega_2^{\mathrm{NL}}(|a_1|^2, |a_2|^2, |a_3|^2)]a_2(t) - \tau_2(|a_1|^2, |a_2|^2, |a_3|^2)^{-1}a_2(t) \\ &+ i\omega_2\beta_2 a_1(t)a_3(t)a_2^*(t) + \sqrt{\frac{2}{\tau_2^{\mathrm{in}}}} s_{2+}^{\mathrm{in}}(t), \end{aligned} \tag{5.8}$$

$$\begin{aligned}\dot{a}_3(t) = &-i[\omega_3 + \Delta\omega_3^{\mathrm{NL}}(|a_1|^2, |a_2|^2, |a_3|^2)]a_3(t) - \tau_3|a_1|^2, |a_2|^2, |a_3|^2)^{-1}a_3(t) \\ &+ i\omega_3\beta_3[a_2(t)]^2 a_1^*(t) + \sqrt{\frac{2}{\tau_3^{\mathrm{in}}}} s_{3+}^{\mathrm{in}}(t). \end{aligned} \tag{5.9}$$

and

$$s_{m-}^{\mathrm{out}}(t) = \sqrt{\frac{2}{\tau_m^{\mathrm{out}}}} a_m(t). \tag{5.10}$$

Three main modifications are made to the linear equation of motion in Eqn. (5.1) to arrive at Eqns. (5.7) to (5.9). Nonlinear frequency shifts, $\Delta\omega^{\mathrm{NL}}(|a_1|^2, |a_2|^2, |a_3|^2)$, are introduced, which depend on the energies $|a_m|^2$ loaded in each of the modes. These shifts arise to due nonlinear effects that perturb the real part of the refractive index of the silicon. The total mode lifetimes $\tau_m(|a_1|^2, |a_2|^2, |a_3|^2)$ are also modified to include the mode energy dependent perturbations to the imaginary part of the refractive index of the silicon. In steady-state, the frequency shifts and lifetimes depend on the steady-state mode energies, U_1, U_2 and U_3. Finally frequency conversion/mixing terms involving the conversion coefficient β_m are included. Each of these nonlinear effects is now briefly described in more detail.

The steady-state nonlinear total cavity lifetime, $\tau_m(U_1, U_2, U_3)$ is given by,

$$\tau_m(U_1, U_2, U_3)^{-1} = \tau_m^{\mathrm{in}^{-1}} + \tau_m^{\mathrm{out}^{-1}} + \tau_m^{\mathrm{scatt}^{-1}} + \tau_m^{\mathrm{abs}^{-1}} + \tau_m^{\mathrm{TPA}}(U_1, U_2, U_3)^{-1} + \tau_m^{\mathrm{FCA}}(U_1, U_2, U_3)^{-1}, \tag{5.11}$$

where the first four terms are linear contributions discussed above, $\tau_m^{\mathrm{TPA}}(U_1, U_2, U_3)$ is the two-photon absorption lifetime, and $\tau_m^{\mathrm{FCA}}(U_1, U_2, U_3)$ is the free-carrier absorption lifetime. As discussed

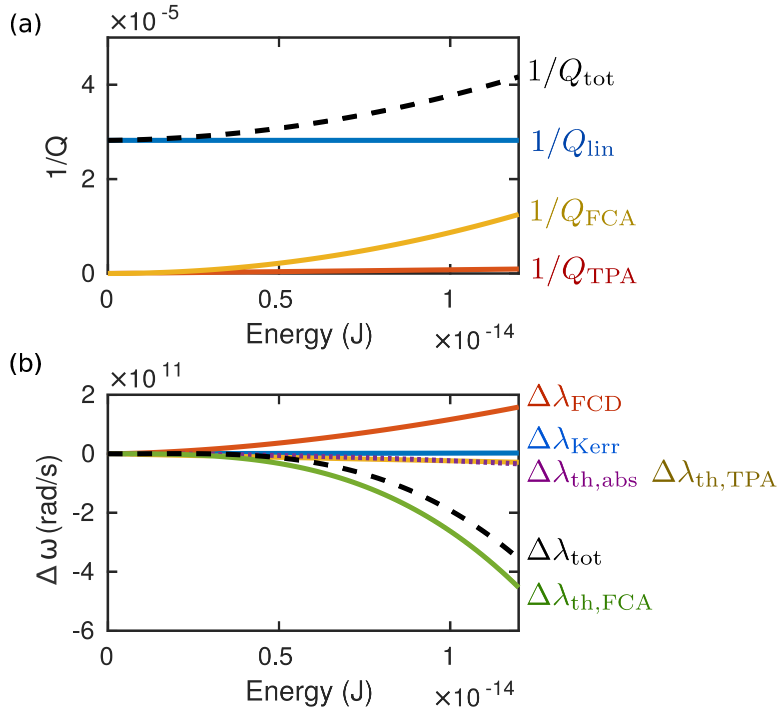

Figure 5.7: Nonlinear effects in a typical triple microcavity, as a function of energy loaded in the microcavity mode M2, under single frequency excitation. (a) The inverse of the nonlinear quality factors due to two-photon absorption (TPA), Q_{TPA}, and free-carrier absorption (FCA), Q_{FCA}, along with the linear and total quality factors, Q_{lin} and Q_{tot} (dashed), respectively. The quality factors are related to the lifetimes through $Q = \omega\tau/2$. (b) Nonlinear wavelength shifts are plotted for contributions including the Kerr effect, $\Delta\lambda_{\mathrm{Kerr}}$, free-carrier dispersion (FCD), $\Delta\lambda_{\mathrm{FCD}}$, and thermal effects due to power absorption through the linear material absorption $\Delta\lambda_{\mathrm{th,abs}}$, TPA, $\Delta\lambda_{\mathrm{th,TPA}}$, and FCA, $\Delta\lambda_{\mathrm{th,FCA}}$. The total shift is also plotted $\Delta\lambda_{\mathrm{th,tot}}$. The shifts $\Delta\lambda_{\mathrm{th,abs}}$ and $\Delta\lambda_{\mathrm{th,abs}}$ have similar values for the range of energies studied, and $\Delta\lambda_{\mathrm{th,abs}}$ is dotted for clarity.

in Chapter 2, two photon absorption occurs when two photons are absorbed in the silicon to excite an electron above the electronic bandgap of silicon. This process is associated with the imaginary part of the third order susceptibility, $\boldsymbol{\chi}^{(3)}(\mathbf{r})$ of silicon. In addition, the free-carriers excited through TPA absorb photons. Both absorption processes depend on the energy loaded in the cavity, and reduce the total mode lifetimes. Figure 5.7(a) shows an example of the energy dependent quality factors (proportional to lifetimes) when mode M2 of a triple microcavity is excited by a single excitation frequency.

The steady-state nonlinear frequency shift, $\Delta\omega^{\mathrm{NL}}(U_1, U_2, U_3)$, is given by,

$$\begin{aligned}\Delta\omega_m^{\mathrm{NL}}(U_1, U_2, U_3) =& \Delta\omega_m^{\mathrm{Kerr}}(U_1, U_2, U_3) \\ &+ \Delta\omega_m^{\mathrm{FCD,e}}(U_1, U_2, U_3) + \Delta\omega_m^{\mathrm{FCD,h}}(U_1, U_2, U_3) \\ &+ \Delta\omega_m^{\mathrm{thermal}}(U_1, U_2, U_3)\end{aligned} \tag{5.12}$$

where $\Delta\omega_m^{\mathrm{Kerr}}(U_1, U_2, U_3)$ is the Kerr nonlinearity shift, $\Delta\omega_m^{\mathrm{FCD,e}}(U_1, U_2, U_3)$ and $\Delta\omega_m^{\mathrm{FCD,h}}(U_1, U_2, U_3)$ are free-carrier dispersion shifts for electrons and holes, respectively, and $\Delta\omega_m^{\mathrm{thermal}}(U_1, U_2, U_3)$ is the thermal shift due to heating of the silicon. The Kerr shift is associated with the real part of the $\boldsymbol{\chi}^{(3)}$ susceptibility of silicon. Free-carrier dispersion is caused by the free-carriers excited through TPA. The thermal shift depends on the total power absorbed through linear material absorption (τ_m^{abs}), TPA [$\tau_m^{\mathrm{TPA}}(U_1, U_2, U_3)$] and FCA [$\tau_m^{\mathrm{FCA}}(U_1, U_2, U_3)$]. Figure 5.7(b) shows the energy dependent frequency shifts for the example introduced above.

It is important to note that both free-carrier absorption and dispersion depend on the density of free-carriers present, which in turn depends on the lifetime of the free-carriers in the vicinity of the cavity. The lifetime is sensitive to the carrier density, proximity of carriers to surfaces and the nature of the surfaces. An effective free-carrier lifetime, τ_{carrier}, is often considered that captures the net lifetime across the microcavity, and has been found to saturate at effective free-carrier densities $\gtrsim 10^{16}$ cm^{-3} [11, 50]. The saturated τ_{carrier} is one of the key parameters sought after in the characterization scheme.

The frequency conversion terms in Eqns. (5.7) to (5.9) arise due to the presence of light in the three microcavity modes (and only these three modes), which undergo mixing through the third order nonlinear $\boldsymbol{\chi}^{(3)}$ of silicon. The factors involving the β_m introduce nonlinear driving terms to each equation of motion. The conversion coefficient β_m is based on an overlap integral between the mode profiles of the three modes and the silicon.

Model functions that describe the nonlinear effects are summarized in Tables 5.2 and 5.3. In Table 5.2, expressions are given for the various contributions to $\Delta\omega_m^{\mathrm{NL}}(U_1, U_2, U_3)$ and $\tau_m(U_1, U_2, U_3)$. These include coefficients that depend on material parameters and overlap integrals between the silicon and the mode fields, which are given in Tables 5.3 and 5.4. The frequency conversion coefficients β_m are also given in Table 5.3. The model functions are derived using perturbation theory.

In the perturbation theory, weak changes to the real and imaginary parts of dielectric constant of silicon, $\delta\varepsilon_m^{\mathrm{NL}}(\mathbf{r})$, at mode frequency ω_m, result in a complex valued change $\delta\omega_m^{\mathrm{NL}}$ to the resonant frequencies ω_m, where [39, 71],

$$\frac{\delta\omega_m^{\mathrm{NL}}}{\omega_m} = -\frac{1}{2}\frac{\int d^3\mathbf{x}\delta\varepsilon_m^{\mathrm{NL}}(\mathbf{r})|\mathbf{E}_m(\mathbf{r})|^2}{\int d^3\mathbf{x}\varepsilon(\mathbf{r})|\mathbf{E}_m(\mathbf{r})|^2}. \tag{5.13}$$

The linear equation of motion [Eqn. (5.1)], is modified such that $\omega_m \rightarrow \omega_m + \delta\omega_m^{\mathrm{NL}}$, and the nonlinear equations of motion [Eqns . (5.8) to (5.9)] result. The perturbed resonant frequencies are,

$$\delta\omega_m^{\mathrm{NL}} = \delta\omega_m^{\mathrm{Kerr}} + \delta\omega_m^{\mathrm{thermal}} + \delta\omega_m^{\mathrm{FCD}} + \delta\omega_m^{\mathrm{TPA}} + \delta\omega_m^{\mathrm{FCA}} + \delta\omega_m^{\mathrm{FWM}}, \tag{5.14}$$

and are alternatively expressed as,

$$\delta\omega_1^{\mathrm{NL}} = \Delta\omega_1^{\mathrm{NL}} - i\left(\tau_1^{\mathrm{TPA}}(U_1,U_2,U_3)^{-1} + \tau_1^{\mathrm{FCA}}(U_1,U_2,U_3)^{-1}\right) - \omega_1\beta_1(a_2)^2(a_3)^*/a_1, \tag{5.15}$$

$$\delta\omega_2^{\mathrm{NL}} = \Delta\omega_2^{\mathrm{NL}} - i\left(\tau_2^{\mathrm{TPA}}(U_1,U_2,U_3)^{-1} + \tau_2^{\mathrm{FCA}}(U_1,U_2,U_3)^{-1}\right) - \omega_2\beta_2 a_1 a_3(a_2)^*/a_2, \tag{5.16}$$

$$\delta\omega_3^{\mathrm{NL}} = \Delta\omega_3^{\mathrm{NL}} - i\left(\tau_3^{\mathrm{TPA}}(U_1,U_2,U_3)^{-1} + \tau_3^{\mathrm{FCA}}(U_1,U_2,U_3)^{-1}\right) - \omega_3\beta_3(a_2)^2(a_1)^*/a_3. \tag{5.17}$$

The derivations for the nonlinear contributions are in Appendix E. In this appendix, the subset of perturbations that arise directly due to the third order polarization, $\mathbf{P}_m^{(3)}(\mathbf{r})$, through the susceptibility $\boldsymbol{\chi}^{(3)}$, are found by re-expressing the perturbation equation above as,

$$\frac{\delta\omega_m^{(3)}}{\omega_m} = -\frac{1}{2}\frac{\int d^3\mathbf{x}\mathbf{P}_m^{(3)}(\mathbf{r})\cdot\mathbf{E}_m^*(\mathbf{r})}{\int d^3\mathbf{x}\varepsilon(\mathbf{r})|\mathbf{E}_m(\mathbf{r})|^2}. \tag{5.18}$$

where $\mathbf{P}_m^{(3)}(\mathbf{r}) = \delta\varepsilon_m^{(3)}(\mathbf{r})\mathbf{E}_m(\mathbf{r})$, and $\delta\omega_m^{(3)} = \delta\omega_m^{\mathrm{Kerr}} + \delta\omega_m^{\mathrm{FWM}} + \delta\omega_m^{\mathrm{TPA}}$.

Nonlinear transmission

In nonlinear transmission measurements, light from a CW laser excites the microcavity through the input waveguide, and the steady-state transmission for each fixed wavelength is recorded. A

Table 5.2: Summary of the cavity lifetimes and nonlinear frequency shifts. The summation indices m', l, l' are over $\{1, 2, 3\}$.

Cavity lifetime	
Linear	τ_m^{in}
	τ_m^{out}
	τ_m^{scatt}
	τ_{abs}
Two-photon absorption	$\tau_m^{\mathrm{TPA}^{-1}} = \rho_0 \sum_{m'} \alpha_{m,m'} U_{m'}$
Free-carrier absorption	$\tau_m^{\mathrm{FCA}^{-1}} = \kappa_0 \sum_{l,l'} \kappa_{m,l,l'}^{\mathrm{FCA}} U_l U_{l'}$
Resonant frequency shift	
Kerr effect	$\Delta\omega_m^{\mathrm{Kerr}} = -\alpha_0 \sum_{m'} \alpha_{m,m'} U_{m'}$
Free-carrier dispersion	$\Delta\omega_m^{\mathrm{FCD,e}} = \nu_0^{\mathrm{FCD,e}} \sum_{l,l'} \kappa_{m,l,l'}^{\mathrm{FCA}} U_l U_{l'}$
	$\Delta\omega_m^{\mathrm{FCD,h}} = \nu_0^{\mathrm{FCD,h}} \sum_{l,l'} \kappa_{m,l,l'}^{\mathrm{FCD,h}} \left(U_l U_{l'}\right)^{0.8}$
Thermal effects	$\Delta\omega_m^{\mathrm{thermal}} = -2 \frac{\Gamma_m^{\mathrm{th}}}{n_{\mathrm{Si}}} \frac{dn}{dT} R_{\mathrm{th}} \omega_m \sum_{m'} \left(\tau_{m'}^{\mathrm{abs}^{-1}} + \tau_{m'}^{\mathrm{TPA}^{-1}} + \tau_{m'}^{\mathrm{FCA}^{-1}}\right) U_{m'}$

model for the nonlinear transmission is found by considering the equation of motion for a single cavity mode in the presence of excitation $s_{m+}^{\mathrm{in}}(t)$,

$$\dot{a}_m(t) = -i[\omega_m + \Delta\omega_m^{\mathrm{NL}}(|a_m|^2)]a_m(t) - \tau_m(|a_m|^2)^{-1} a_m(t) + \sqrt{\frac{2}{\tau_m^{\mathrm{in}}}} s_{m+}^{\mathrm{in}}(t). \tag{5.19}$$

This is obtained from the general equations of motion [Eqns. (5.7) to (5.9)] by assuming there is excitation at a single frequency, such that no frequency mixing occurs, and the terms with β_m are set to 0. The steady-state equations for CW excitation $s_{m+}^{\mathrm{in}}(t) = s_{m+}^{\mathrm{in}} e^{-i\omega_m^d t}$ are,

$$0 = i\omega_m^d a_m - i[\omega_m + \Delta\omega_m^{\mathrm{NL}}(U_m)]a_m - \tau_m(U_m)^{-1} a_{\mathrm{m}} + \sqrt{\frac{2}{\tau_{\mathrm{m}}^{\mathrm{in}}}} s_{\mathrm{m}+}^{\mathrm{in}}, \tag{5.20}$$

and

$$s_{m-}^{\mathrm{out}} = \sqrt{\frac{2}{\tau_m^{\mathrm{out}}}} a_m. \tag{5.21}$$

Table 5.3: Summary of nonlinear coefficients derived from perturbation theory. $\chi^{(3)}_{\mathrm{Si}}$ is the diagonal element of the $\boldsymbol{\chi}^{(3)}$ tensor for silicon.

α_0	$= \frac{\omega_m}{4}\varepsilon_0 \,\mathrm{Re}(\chi^{(3)}_{\mathrm{Si}})$
ρ_0	$= \frac{\varepsilon_0 \,\mathrm{Im}(\chi^{(3)}_{\mathrm{Si}})\omega_m}{4}$
κ_0	$= \frac{\sigma^{\mathrm{FCA}}\tau_{\mathrm{carrier}}\,\mathrm{Im}(\chi^{(3)}_{\mathrm{Si}})\varepsilon_0 c}{8\hbar n_{\mathrm{Si}}}$
$\nu_0^{\mathrm{FCD,e}}$	$= \frac{\omega_m \zeta^{\mathrm{e}}_{\mathrm{Si}}\tau_{\mathrm{carrier}}\varepsilon_0\,\mathrm{Im}(\chi^{(3)}_{\mathrm{Si}})}{4\hbar n_{\mathrm{Si}}}$
$\nu_0^{\mathrm{FCD,h}}$	$= \frac{\omega_m}{n_{\mathrm{Si}}}\left(\frac{\zeta^{\mathrm{h}}_{\mathrm{Si}}\tau_{\mathrm{carrier}}\varepsilon_0\,\mathrm{Im}(\chi^{(3)}_{\mathrm{Si}})}{4\hbar}\right)^{0.8}$
$\alpha_{m,m}$	$= \frac{\int_{\mathrm{Si}} d^3\mathbf{x}\big[(\breve{\mathbf{E}}^*_m\cdot\breve{\mathbf{E}}^*_m)(\breve{\mathbf{E}}_m\cdot\breve{\mathbf{E}}_m)+2\lvert\breve{\mathbf{E}}_m\rvert^4\big]}{(\int d^3\mathbf{x}\varepsilon(\mathbf{r})\lvert\breve{\mathbf{E}}_m\rvert^2)^2}$
$\alpha_{m,m'}$	$= 2\frac{\int_{\mathrm{Si}} d^3\mathbf{x}\big[(\breve{\mathbf{E}}_m\cdot\breve{\mathbf{E}}_{m'})(\breve{\mathbf{E}}^*_m\cdot\breve{\mathbf{E}}^*_{m'})+(\breve{\mathbf{E}}_m\cdot\breve{\mathbf{E}}^*_{m'})(\breve{\mathbf{E}}^*_m\cdot\breve{\mathbf{E}}_{m'})+\lvert\breve{\mathbf{E}}_m\rvert^2\lvert\breve{\mathbf{E}}_{m'}\rvert^2\big]}{(\int d^3\mathbf{x}\varepsilon(\mathbf{r})\lvert\breve{\mathbf{E}}_m\rvert^2)(\int d^3\mathbf{x}\varepsilon(\mathbf{r})\lvert\breve{\mathbf{E}}_{m'}\rvert^2)}$
$\kappa^{\mathrm{FCA}}_{m,l,l}$	$= \frac{\int_{\mathrm{Si}} d^3\mathbf{x}\big[(\breve{\mathbf{E}}^*_l\cdot\breve{\mathbf{E}}^*_l)(\breve{\mathbf{E}}_l\cdot\breve{\mathbf{E}}_l)+2\lvert\breve{\mathbf{E}}_l\rvert^4\big]\varepsilon\lvert\breve{\mathbf{E}}_m\rvert^2}{(\int d^3\mathbf{x}\varepsilon\lvert\breve{\mathbf{E}}_m\rvert^2)(\int d^3\mathbf{x}\varepsilon\lvert\breve{\mathbf{E}}_l\rvert^2)^2}$
$\kappa^{\mathrm{FCA}}_{m,l,l'}$	$= 2\frac{\int_{\mathrm{Si}} d^3\mathbf{x}\big[(\breve{\mathbf{E}}_l\cdot\breve{\mathbf{E}}_{l'})(\breve{\mathbf{E}}^*_l\cdot\breve{\mathbf{E}}^*_{l'})+(\breve{\mathbf{E}}_l\cdot\breve{\mathbf{E}}^*_{l'})(\breve{\mathbf{E}}^*_l\cdot\breve{\mathbf{E}}_{l'})+\lvert\breve{\mathbf{E}}_l\rvert^2\lvert\breve{\mathbf{E}}_{l'}\rvert^2\big]\varepsilon\lvert\breve{\mathbf{E}}_m\rvert^2}{(\int d^3\mathbf{x}\varepsilon\lvert\breve{\mathbf{E}}_m\rvert^2)(\int d^3\mathbf{x}\varepsilon\lvert\breve{\mathbf{E}}_l\rvert^2)(\int d^3\mathbf{x}\varepsilon\lvert\breve{\mathbf{E}}_{l'}\rvert^2)}$
$\kappa^{\mathrm{FCD,h}}_{m,l,l}$	$= \frac{\int_{\mathrm{Si}} d^3\mathbf{x}\big[(\breve{\mathbf{E}}^*_l\cdot\breve{\mathbf{E}}^*_l)(\breve{\mathbf{E}}_l\cdot\breve{\mathbf{E}}_l)+2\lvert\breve{\mathbf{E}}_l\rvert^4\big]^{0.8}\varepsilon\lvert\breve{\mathbf{E}}_m\rvert^2}{(\int d^3\mathbf{x}\varepsilon\lvert\breve{\mathbf{E}}_m\rvert^2)(\int d^3\mathbf{x}\varepsilon\lvert\breve{\mathbf{E}}_l\rvert^2)^{1.6}}$
$\kappa^{\mathrm{FCD,h}}_{m,l,l'}$	$= 2^{0.8}\frac{\int_{\mathrm{Si}} d^3\mathbf{x}\big[(\breve{\mathbf{E}}_l\cdot\breve{\mathbf{E}}_{l'})(\breve{\mathbf{E}}^*_l\cdot\breve{\mathbf{E}}^*_{l'})+(\breve{\mathbf{E}}_l\cdot\breve{\mathbf{E}}^*_{l'})(\breve{\mathbf{E}}^*_l\cdot\breve{\mathbf{E}}_{l'})+\lvert\breve{\mathbf{E}}_l\rvert^2\lvert\breve{\mathbf{E}}_{l'}\rvert^2\big]^{0.8}\varepsilon\lvert\breve{\mathbf{E}}_m\rvert^2}{(\int d^3\mathbf{x}\varepsilon\lvert\breve{\mathbf{E}}_m\rvert^2)(\int d^3\mathbf{x}\varepsilon\lvert\breve{\mathbf{E}}_l\rvert^2)^{0.8}(\int d^3\mathbf{x}\varepsilon\lvert\breve{\mathbf{E}}_{l'}\rvert^2)^{0.8}}$
Γ^{th}_m	$= \frac{\int_{\mathrm{Si}} d^3\mathbf{x}\varepsilon(\mathbf{r})\lvert\mathbf{E}_m(\mathbf{r})\rvert^2}{\int d^3\mathbf{x}\varepsilon(\mathbf{r})\lvert\mathbf{E}_m(\mathbf{r})\rvert^2}$
β_2	$= \frac{1}{2}\frac{\int_{\mathrm{Si}} d^3\mathbf{x}\varepsilon_0\,\mathrm{Re}(\chi^{(3)}_{\mathrm{Si}})\big[(\breve{\mathbf{E}}^*_2\cdot\breve{\mathbf{E}}^*_2)(\breve{\mathbf{E}}_1\cdot\breve{\mathbf{E}}_3)+2(\breve{\mathbf{E}}^*_2\cdot\breve{\mathbf{E}}_1)(\breve{\mathbf{E}}^*_2\cdot\breve{\mathbf{E}}_3)\big]}{(\int d^3\mathbf{x}\varepsilon(\mathbf{r})\lvert\breve{\mathbf{E}}_2\rvert^2)(\int d^3\mathbf{x}\varepsilon(\mathbf{r})\lvert\breve{\mathbf{E}}_1\rvert^2)^{1/2}(\int d^3\mathbf{x}\varepsilon(\mathbf{r})\lvert\breve{\mathbf{E}}_3\rvert^2)^{1/2}} = 2\beta_1^* = 2\beta_3^*$

The steady-state energy stored in the cavity is,

$$U_m = \frac{2{\tau_m^{\mathrm{in}}}^{-1} P_m^{\mathrm{in}}}{(\omega_m^d - [\omega_m + \Delta\omega_m^{\mathrm{NL}}(U_m)])^2 + \tau_m(U_m)^{-2}}, \tag{5.22}$$

and the absolute cavity transmission spectrum is,

$$T_m(\omega_m^d) = \frac{2}{\tau_m^{\mathrm{out}}} U_m = \frac{4{\tau_m^{\mathrm{in}}}^{-1}{\tau_m^{\mathrm{out}}}^{-1} P_m^{\mathrm{in}}}{(\omega_m^d - [\omega_m + \Delta\omega_m^{\mathrm{NL}}(U_m)])^2 + \tau_m(U_m)^{-2}}. \tag{5.23}$$

Table 5.4: Summary of linear and nonlinear silicon material constants. Dispersive constant are given near $\lambda = 1540$ nm.

Parameter	Value	Units	Source
n_{Si}	3.478		[67]
$n_{2,\mathrm{Si}}$	4.4×10^{-18}	$\mathrm{m^2W^{-1}}$	[11, 23]
$\beta_{\mathrm{Si}}^{\mathrm{TPA}}$	8.4×10^{-12}	$\mathrm{mW^{-1}}$	[11, 23]
$\mathrm{Re}(\chi_{\mathrm{Si}}^{(3)})$	1.88×10^{-19}	$\mathrm{m^2V^{-2}}$	Calculated†
$\mathrm{Im}(\chi_{\mathrm{Si}}^{(3)})$	4.4×10^{-20}	$\mathrm{m^2V^{-2}}$	Calculated†
$\sigma_{\mathrm{Si}}^{\mathrm{FCA}}$	14.5×10^{-22}	$\mathrm{m^2}$	[21, 82]
ζ_{Si}^{e}	8.8×10^{-28}	$\mathrm{m^3}$	[21, 82]
ζ_{Si}^{h}	4.6×10^{-28}	$\mathrm{m^3}$	[21, 82]
dn_{Si}/dT	1.86×10^{-4}	$\mathrm{K^{-1}}$	[18]

† $\chi_{\mathrm{Si}}^{(3)} = \frac{4\varepsilon_0 c^2 n_{\mathrm{Si}}(\omega)^2}{3\omega}\left(\frac{\omega}{c} n_{2,\mathrm{Si}}(\omega) + \frac{i\beta_{\mathrm{Si}}^{\mathrm{TPA}}(\omega)}{2}\right)$ [51]

The nonlinear transmission in Eqn. (5.23) depends on the cavity energy U_m, which is found by numerically solving Eqn. (5.22). For a certain range of driving frequencies and input powers, there are three solutions to U_m, and the cavity exhibits bistable behaviour, otherwise there is a single solution.

The nonlinear transmission solutions for the microcavity studied in Section 2.2 are plotted as a function of wavelength, for two different input powers in Fig. 5.8(a). For the higher input power, the spectrum has a range of wavelengths where three solutions exist, marked by $+$, $\square$ and $\times$. While the top ($+$) and bottom ($\times$) branches are stable, the middle branch is not ($\square$) [20]. The transmission spectrum depend on the sweep direction, as shown in Fig. 5.8(b). In this example, the forward sweep transmission follows the top stable branch and then drops down to the stable single solutions ($\circ$) at higher wavelengths. The backward sweep transmission follows the bottom stable branch until it jumps up the to the stable single solutions at lower wavelengths.

Stimulated four-wave mixing

In stimulated four-wave mixing measurements, the pump and signal CW lasers excite two of the microcavity modes, and idler photons are generated in the third mode. Here, temporal coupled-

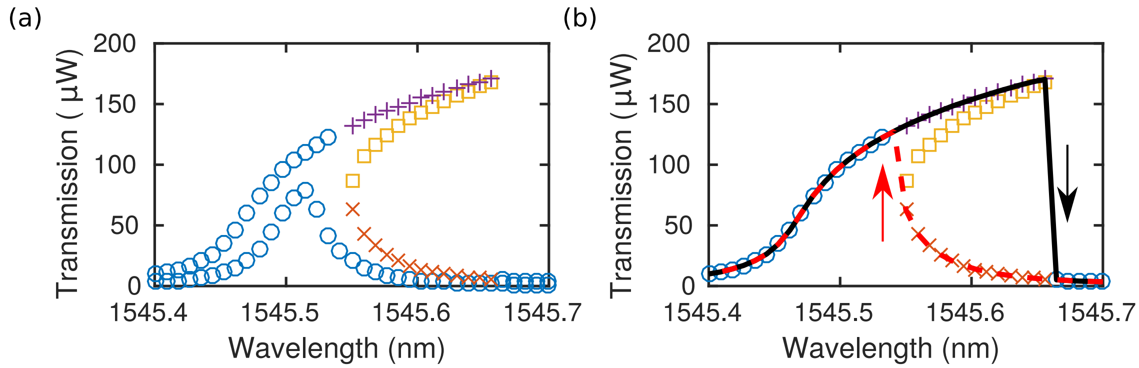

Figure 5.8: Numerical solutions for the nonlinear transmission predicted for triple microcavity Device 3, Mode 2. (a) Solutions for input powers $P_2^{\text{in}} = 100$ and 300 μW. Circles show where a single solution is found, while the top, middle and bottom branches in the bistable regime are marked by $+$, $\square$ and $\times$, respectively. (b) Solutions for $P_2^{\text{in}} = 300$ μW are shown as in (a), and the transmission spectra predicted for forward (solid black) and backward (dashed red) wavelength sweeps are also shown.

mode theory is used to predict the idler generation rate in mode M3 in steady-state when a cavity is excited by continuous-wave pump tuned near M2 and a signal tuned near M1. The other signal/idler configuration (M3/M1) is described by the same theory, but with $1 \to 3$ and $3 \to 1$. The equations of motion that describe this excitation scheme in the nonlinear regime are given by,

$$\begin{aligned}\dot{a}_1(t) =& -i[\omega_1 + \Delta\omega_1^{\text{NL}}(|a_1|^2, |a_2|^2, |a_3|^2)]a_1(t) - \tau_1(|a_1|^2, |a_2|^2, |a_3|^2)^{-1}a_1(t) \\ &+ i\omega_1\beta_1[a_2(t)]^2 a_3^*(t) + \sqrt{\frac{2}{\tau_1^{\text{in}}}}s_{1+}^{\text{in}}(t),\end{aligned} \tag{5.24}$$

$$\begin{aligned}\dot{a}_2(t) =& -i[\omega_2 + \Delta\omega_2^{\text{NL}}(|a_1|^2, |a_2|^2, |a_3|^2)]a_2(t) - \tau_2(|a_1|^2, |a_2|^2, |a_3|^2)^{-1}a_2(t) \\ &+ i\omega_2\beta_2 a_1(t)a_3(t)a_2^*(t) + \sqrt{\frac{2}{\tau_2^{\text{in}}}}s_{2+}^{\text{in}}(t),\end{aligned} \tag{5.25}$$

$$\begin{aligned}\dot{a}_3(t) =& -i[\omega_3 + \Delta\omega_3^{\text{NL}}(|a_1|^2, |a_2|^2, |a_3|^2)]a_3(t) - \tau_3(|a_1|^2, |a_2|^2, |a_3|^2)^{-1}a_3(t) \\ &+ i\omega_3\beta_3[a_2(t)]^2 a_1^*(t).\end{aligned} \tag{5.26}$$

For CW signal and pump driving amplitudes $s_{1+}^{\text{in}}e^{-i\omega_1^d t}$ and $s_{2+}^{\text{in}}e^{-i\omega_2^d t}$, respectively, the steady-state cavity M1 and M2 amplitudes oscillate at their respective drive frequencies such that $a_1(t) = a_1 e^{-i\omega_1^d t}$ and $a_2(t) = a_2 e^{-i\omega_2^d t}$. This results in idler amplitude $a_3(t) = a_3 e^{-i\omega_3^d t}$, where $\omega_3^d = 2\omega_2^d - \omega_1^d$, which comes from the photon generation term ($\sim (a_2)^2 a_1^*$). The steady-state field amplitudes are described by,

$$0 = i\omega_1^d a_1 - i[\omega_1 + \Delta\omega_1^{\mathrm{NL}}(U_1, U_2, U_3)]a_1 - \tau_1(U_1, U_2, U_3)^{-1}a_1 + \sqrt{\frac{2}{\tau_1^{\mathrm{in}}}}s_{1+}^{\mathrm{in}} \tag{5.27}$$

$$0 = i\omega_2^d a_2 - i[\omega_2 + \Delta\omega_2^{\mathrm{NL}}(U_1, U_2, U_3)]a_2 - \tau_2(U_1, U_2, U_3)^{-1}a_2 + \sqrt{\frac{2}{\tau_2^{\mathrm{in}}}}s_{2+}^{\mathrm{in}} \tag{5.28}$$

$$0 = i\omega_3^d a_3 - i[\omega_3 + \Delta\omega_3^{\mathrm{NL}}(U_1, U_2, U_3)]a_3 - \tau_3(U_1, U_2, U_3)^{-1}a_3 + i\omega_3\beta_3(a_2)^2(a_1)^*. \tag{5.29}$$

and Eqn. (5.21). It is important to note that here the undepleted pump approximation has been applied to remove the frequency conversion terms from the M1 and M2 equations of motion. This assumes that the number of photons generated or lost in the four-wave mixing process is only very small compared to the total number of photons in the cavity, which is a good assumption for the measurements studied here. This assumption is crucial to being able to find a solution for the steady-state idler mode amplitude a_3.

The steady-state idler output power, $P_3^{\mathrm{out}} = |s_{m-}^{\mathrm{out}}|^2$, is given by,

$$P_3^{\mathrm{out}} = \frac{2}{\tau_3^{\mathrm{out}}} \frac{\omega_3^2|\beta_3|^2(U_2)^2U_1}{(\omega_3^d - [\omega_3 + \Delta\omega_3^{\mathrm{NL}}(U_1, U_2, U_3)])^2 + \tau_3(U_1, U_2, U_3)^{-2}}, \tag{5.30}$$

where U_1 and U_2 are the cavity mode energies given by,

$$U_{m'} = \frac{2{\tau_{m'}^{\mathrm{in}}}^{-1}P_{m'}^{\mathrm{in}}}{(\omega_{m'}^d - [\omega_{m'} + \Delta\omega_{m'}^{\mathrm{NL}}(U_1, U_2, U_3)])^2 + \tau_{m'}(U_1, U_2, U_3)^{-2}}, \tag{5.31}$$

for $m' = \{1, 2\}$. The M1 and M2 cavity mode energies are essentially the same as those found for the nonlinear transmission in Eqn. (5.22), except here $\Delta\omega_{m'}^{\mathrm{NL}}$ and $\tau_{m'}$ depend on all mode energies, although here the dependence on U_3 is ignored as the idler cavity energy is much smaller than the signal and pump cavity energies. It is possible to calculate the idler power P_3^{out} once U_1 and U_2 are found. While there is no analytical solution for these, they are found numerically using an iterative method, that achieves consistency between $U_1, U_2, \Delta\omega_{m'}^{\mathrm{NL}}(U_1, U_2)$ and $\tau_{m'}(U_1, U_2)$.

In the simplified case where the microcavity modes have equally spaced resonant frequencies, and the signal and pump powers are low enough that nonlinear absorption is negligible, such that

$\omega_1^{\mathrm{d}} = \omega_1$, $\omega_2^{\mathrm{d}} = \omega_2$ and $\omega_3^{\mathrm{d}} = \omega_3 = 2\omega_2 - \omega_1$, the idler power is,

$$P_3^{\mathrm{out}} = 256|\beta_3|^2 \frac{\omega_3}{\omega_2^2 \omega_1} \frac{(Q_2)^4 (Q_1)^2 (Q_3)^2 (P_2^{\mathrm{in}})^2 P_1^{\mathrm{in}}}{(Q_2^{\mathrm{in}})^2 Q_1^{\mathrm{in}} Q_3^{\mathrm{out}}}, \tag{5.32}$$

The output power of generated photons is optimized for high Q cavities with efficient loading into the pump and signal modes, as well as efficient unloading from the idler (generated photon) mode.

5.3 Impact of microcavity parameters

The least-squares fitting procedure used to extract the best fit microcavity parameters involves model functions of the experimentally measured quantities that are based on the theory presented in Section 5.2. The sensitivities of the measured quantities on key microcavity parameters are explored here, to help develop intuition for the competing effects at play, before presenting the model functions, analysis procedure and results in Section 5.4. Figures 5.9 and 5.10 include plots of the nonlinear transmission spectral features and the FWM idler power, respectively, as a function of one parameter, while the rest of the microcavity parameters in the calculation are held fixed at the best fit values for Device 3. The best fit parameters values extracted for Device 3 are reported in Table 5.7 and Fig. 5.17. The parameters are also described in Table 2.1 and discussed in Chapter 2. The competing parameter dependencies shown in this section illustrate why it is difficult to untangle the various contributions to extract parameter values from experimental data.

In Figs. 5.9(a) and (b), the peak relative transmission is plotted for excitation of M2, with an input power of 300 μW. The transmission decreases with increasing waveguide coupling ratio $\eta_2^{\mathrm{wg}} = \tau_2^{\mathrm{out}}/\tau_2^{\mathrm{in}}$ because light is more efficiently loaded in the microcavity when η_2^{wg} is large, leading to greater nonlinear absorption. The transmission also decreases with increasing effective free-carrier lifetime, τ_{carrier}, because the steady-state carrier density is higher, leading to greater free-carrier absorption. The peak wavelength shift is plotted in Figs. 5.9(c)-(f). The shift increases a function of both η_2^{wg} and R_{th}, due to increased heating of the silicon. The shift is fairly insensitive to the quality factor associated with linear material absorption, $Q_{\mathrm{abs}} = \omega\tau_{\mathrm{abs}}/2$, because this absorption mechanism is weak relative to the others at play. The shift is also fairly insensitive to τ_{carrier} because the blue-shift of free-carrier dispersion competes against the red-shift of thermal

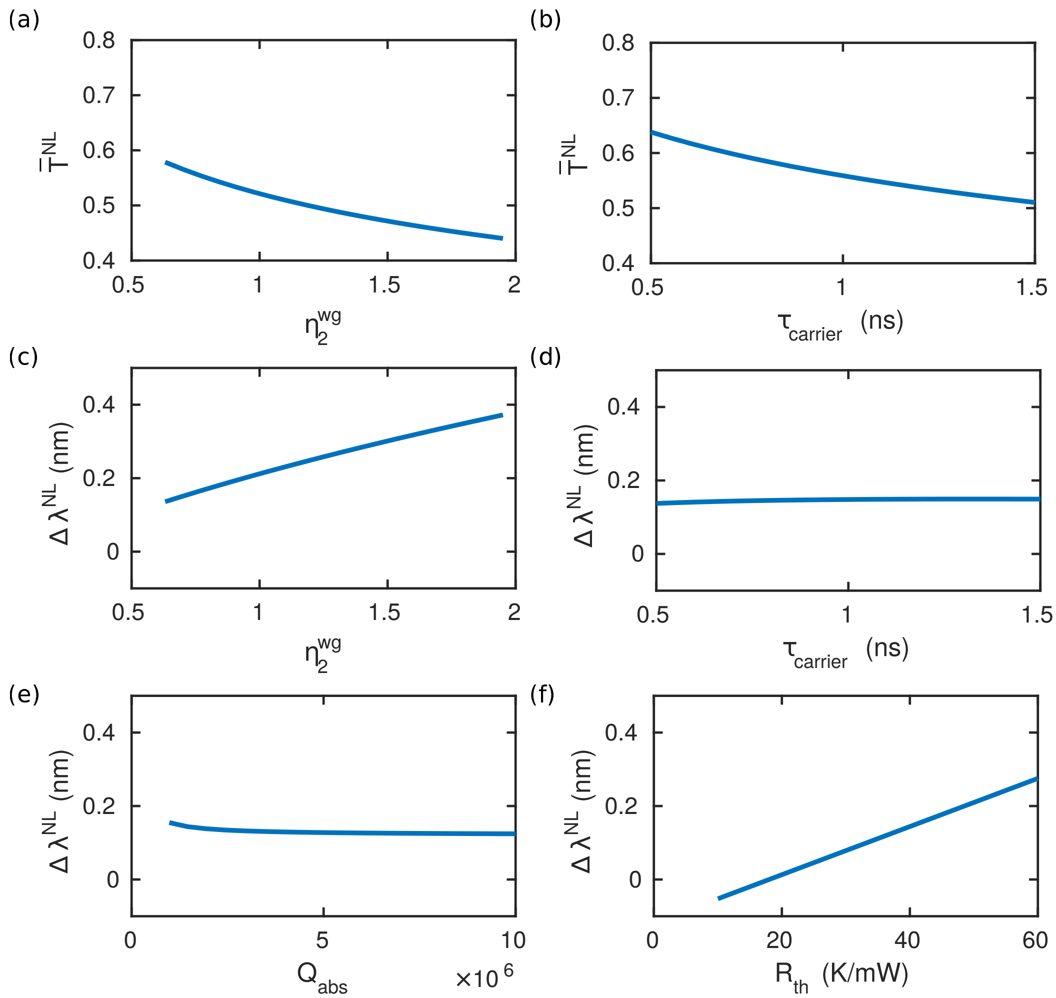

Figure 5.9: Nonlinear transmission spectral features calculated for an excitation power of 300 μW, using best fit parameter values for M2 of Device 3 (given in Table 5.7 and Fig. 5.17), while one parameter is free to vary on the x-axis. (a)-(b) Peak relative transmission, $\overline{T}^{\mathrm{NL}}$. (c)-(f) Peak wavelength shift, $\Delta\lambda^{\mathrm{NL}}$. $\eta_2^{\mathrm{wg}} = \tau_2^{\mathrm{out}}/\tau_2^{\mathrm{in}}$ and $Q_{\mathrm{abs}} = \omega\tau_{\mathrm{abs}}/2$.

dispersion from free-carrier absorption (see Fig. 5.7).

In Fig. 5.10, the FWM idler powers are calculated as a function of key parameters, with pump and signal powers of 84 μW and 43 μW, respectively, for two configurations, one where M1/M3 correspond to signal/idler modes, and the other where M3/M1 correspond. In Fig. 5.10(a), the idler power generated in idler mode M3 increases with η_1^{wg}, while that in M1 decreases. This is because a large η_1^{wg} loads energy efficiently *into* signal mode M1, and unloads energy inefficiently *out of* idler mode M1. An equivalent argument can be made for η_3^{wg}, where M1 and M3 are swapped. Meanwhile, a large η_2^{wg} loads the pump energy efficiently, thus increases the idler power

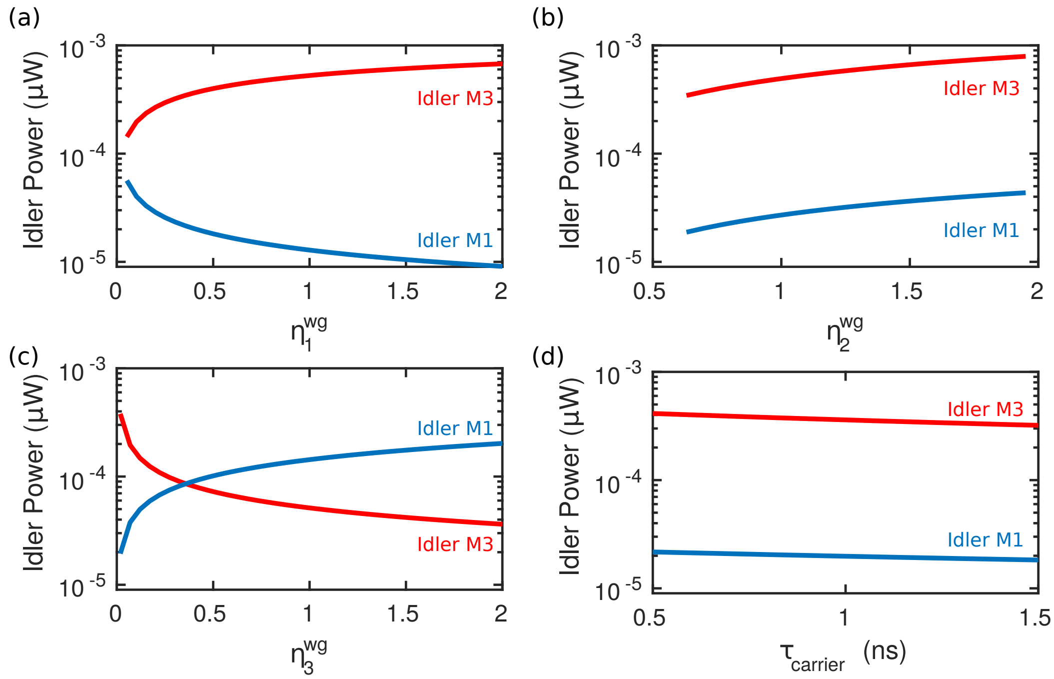

Figure 5.10: Four-wave mixing idler power calculated for pump and signal excitations of 84 μW and 43 μW, respectively, using best fit parameter values for Device 3 (given in Table 5.7 and Fig. 5.17), while one parameter is free to vary on the x-axis. Two excitation configurations are included: M1/M3 are the signal/idler modes (red), and M3/M1 are the signal/idler modes (blue). $\eta_m^{\rm wg} = \tau_m^{\rm out}/\tau_m^{\rm in}$.

for both FWM configurations. The idler power is relatively insensitive to $\tau_{\rm carrier}$ because free-carrier absorption is weak at these excitation powers.

5.4 Analysis procedure

As discussed in Chapter 2, the model functions that describe linear transmission, nonlinear transmission and stimulated four-wave mixing involve 15 unknown microcavity parameters (see Table 2.1) that are found using least-squares calculations. The model functions are based on the temporal coupled-mode theory Eqns. [(5.7)-(5.9)].

This analysis process requires that the nonlinear coefficients in Table 5.3 ($\alpha, \kappa^{\rm FCA}, \kappa^{\rm FCD,h}, \Gamma_m^{\rm th}$ and β) are first calculated using finite-difference time domain simulations. The simulated coefficients used for Devices 1 to 4 are summarized in Appendix F.

5.4.1 Calculations of the sum of the squared differences, X^2

Nonlinear transmission X_{T}^2

In the nonlinear transmission analysis, the experimental wavelength shifts, $\Delta\lambda_m^{\mathrm{NL}}$, and peak transmission values, $\overline{T}_m^{\mathrm{NL}}$, measured as a function of input power for Modes 1 and 2, with forward wavelength sweeps, are involved in the least-squares fitting scheme. The model function that simultaneously predicts $\Delta\lambda_1^{\mathrm{NL}}$, $\Delta\lambda_2^{\mathrm{NL}}$, $\overline{T}_1^{\mathrm{NL}}$ and $\overline{T}_2^{\mathrm{NL}}$ depends on 13 parameters: $\lambda_1, \lambda_2, \tau_1^{\mathrm{in}}, \tau_2^{\mathrm{in}}, \tau_1^{\mathrm{out}}, \tau_2^{\mathrm{out}}$, $\tau_1^{\mathrm{scatt}}, \tau_2^{\mathrm{scatt}}, \tau_{\mathrm{abs}}, \tau_{\mathrm{carrier}}, R_{\mathrm{th}}, \phi_{\mathrm{in}}$ and ϕ_{out}. However, given the information gained from the linear transmission measurements, these are reduced to seven unknown parameters: $\eta_1^{\mathrm{wg}}, \eta_2^{\mathrm{wg}}, Q_{\mathrm{abs}}, R_{\mathrm{th}}$, $\tau_{\mathrm{carrier}}, \phi_{\mathrm{in}}$, and ϕ_{out}, where $\eta_m^{\mathrm{wg}} = \tau_m^{\mathrm{out}}/\tau_m^{\mathrm{in}}$ and $Q_{\mathrm{abs}} = \omega\tau_{\mathrm{abs}}/2$ ($\omega = \omega_2 \simeq \omega_1 \simeq \omega_3$).

The sum of the square differences, X_{T}^2, is calculated as,

$$X_{\mathrm{T}}^2 = \sum_m \sum_i \left[\left(\frac{\Delta\lambda_{m,i}^{\mathrm{NL}} - \Delta\lambda_{m,i}^{\mathrm{NL,model}}}{\delta\Delta\lambda_{m,i}^{\mathrm{NL}}} \right)^2 + \left(\frac{\overline{T}_{m,i}^{\mathrm{NL}} - \overline{T}_{m,i}^{\mathrm{NL,model}}}{\delta\overline{T}_{m,i}^{\mathrm{NL}}} \right)^2 \right] \tag{5.33}$$

where the first sum is over both modes $m = \{1, 2\}$, and the second sum is over the number of input powers considered in each data set. Only input powers that are sufficiently high, such that the free-carrier lifetime is saturated, are considered. The uncertainties $\delta\overline{T}_m^{\mathrm{NL}}/\overline{T}_{m,i}^{\mathrm{NL}} = 0.04$, and $\delta\Delta\lambda_m(P_{m,i}^{\mathrm{in}}) = 0.002$ for $m = 1$, and $\delta\Delta\lambda_{m,i}^{\mathrm{NL}} = 0.005$ for $m = 2$. The relative uncertainty in $\overline{T}_{m,i}^{\mathrm{NL}}$ is discussed in Appendix D, and the uncertainty in the wavelength shift is the sweep step size.

For each set of these seven parameters, the following procedure is followed to calculate X_{T}^2:

1. The experimental linear transmission data $\left[\overline{T}_1^{\mathrm{lin}}(\phi_{\mathrm{in}}, \phi_{\mathrm{out}}), \overline{T}_2^{\mathrm{lin}}(\phi_{\mathrm{in}}, \phi_{\mathrm{out}})\right]$ and nonlinear transmission data $\left[\overline{T}_1^{\mathrm{NL}}(\phi_{\mathrm{in}}, \phi_{\mathrm{out}}), \overline{T}_2^{\mathrm{NL}}(\phi_{\mathrm{in}}, \phi_{\mathrm{out}})\right]$ are calculated (see Appendix D).

2. The following lifetimes are calculated as,

$$\tau_m^{\mathrm{in}} = \sqrt{\frac{4(\tau_m^{\mathrm{lin}})^2}{\overline{T}_m^{\mathrm{lin}}(\phi_{\mathrm{in}}, \phi_{\mathrm{out}})\eta_m^{\mathrm{wg}}}}, \tag{5.34}$$

$$\tau_m^{\mathrm{out}} = \sqrt{\frac{4(\tau_m^{\mathrm{lin}})^2\eta_m^{\mathrm{wg}}}{\overline{T}_m^{\mathrm{lin}}(\phi_{\mathrm{in}}, \phi_{\mathrm{out}})}}, \tag{5.35}$$

and

$$\tau_m^{\text{scatt}} = \left(\tau_m^{\text{lin}^{-1}} - \tau_{\text{abs}}{}^{-1} - \sqrt{\frac{\overline{T}_m^{\text{lin}}(\phi_{\text{in}}, \phi_{\text{out}})}{4(\tau_m^{\text{lin}})^2 \eta_m^{\text{wg}}}} (\eta_m^{\text{wg}} + 1) \right)^{-1}. \tag{5.36}$$

3. The following model functions for peak transmission and the wavelength shift are calculated for both modes ($m = 1, 2$), at each input power "i", as,

$$\overline{T}_{m,i}^{\text{NL,model}} = \frac{4\tau_m^{\text{in}^{-1}} \tau_m^{\text{out}^{-1}}}{\left(\tau_m^{\text{lin}^{-1}} + \rho_0 \alpha_{m,m} U_{m,i} + \tau_{\text{carrier}} \frac{\sigma^{\text{FCA}} \operatorname{Im}(\chi_{\text{TPA}}^{(3)}) \varepsilon_0 c}{8\hbar n_{\text{Si}}} \kappa_{m,m,m}^{\text{FCA}} (U_{m,i})^2 \right)^2}, \tag{5.37}$$

and $\Delta\lambda_{m,i}^{\text{NL,model}} = \lambda_m \Delta\omega_{m,i}^{\text{NL,model}} / \omega_m$, where

$$\begin{aligned}
\Delta\omega_{m,i}^{\text{NL,model}} = & -\alpha_0 \alpha_{m,m} U_{m,i} \qquad (5.38) \\
& + \tau_{\text{carrier}} \frac{\omega_m \zeta_{\text{Si}}^{\text{e}} \varepsilon_0 \operatorname{Im}(\chi_{\text{TPA}}^{(3)})}{4\hbar n_{\text{Si}}} \kappa_{m,m,m}^{\text{FCA}} (U_{m,i})^2 \\
& + (\tau_{\text{carrier}})^{0.8} \frac{\omega_m}{n_{\text{Si}}} \left(\frac{\zeta_{\text{Si}}^{\text{h}} \varepsilon_0 \operatorname{Im}(\chi_{\text{TPA}}^{(3)})}{4\hbar} \right)^{0.8} \kappa_{m,m,m}^{\text{FCD,h}} (U_{m,i})^{1.6} \\
& - 2 \frac{\Gamma_m^{\text{th}}}{n_{\text{Si}}} \frac{dn}{dT} R_{\text{th}} \Big(\tau_{\text{abs}}{}^{-1} + \rho_0 \alpha_{m,m} U_{m,i} \qquad (5.39) \\
& \qquad + \tau_{\text{carrier}} \frac{\sigma^{\text{FCA}} \operatorname{Im}(\chi_{\text{TPA}}^{(3)}) \varepsilon_0 c}{8\hbar n_{\text{Si}}} \kappa_{m,m,m}^{\text{FCA}} (U_{m,i})^2 \Big) U_{m,i},
\end{aligned}$$

and

$$U_{m,i} = \frac{\tau_m^{\text{out}}}{2} \overline{T}_{m,i}^{\text{NL}}. \tag{5.40}$$

Equations (5.37) and (5.38) are based the nonlinear shifts and lifetimes summarized in Table 5.2, and the nonlinear transmission in Eqn. (5.23) taken on resonance. Here the experimental transmission is used to calculate the microcavity energy that enters the model calculation.

Four-wave mixing X_{FWM}^2

There are four sets of experimental four-wave mixing data measured for each device that are involved in the least-squares analysis, as shown in the final column of Fig. 5.3. Here the idler power is measured separately as a function of pump power and signal power, for both of the two signal/idler excitation configurations. The model function that describes the idler powers depends on 16 parameters: $\lambda_m, \tau_m^{\text{in}}, \tau_m^{\text{out}}, \tau_m^{\text{scatt}}, \tau_{\text{abs}}, \tau_{\text{carrier}}, \phi_{\text{in}}$ and ϕ_{out}, where $m = 1, 2$ and 3. However, with information gained from linear transmission measurements, this set is reduced to seven parameters: $\eta_1^{\text{wg}}, \eta_2^{\text{wg}}, \eta_3^{\text{wg}}, Q_{\text{abs}}, \tau_{\text{carrier}}, \phi_{\text{in}}$, and ϕ_{out}.

The sum of the square differences is calculated as,

$$X_{\text{FWM}}^2 = \sum_q \sum_i \left(\frac{P_{q,i}^{\text{exp,idler}} - P_{q,i}^{\text{model,idler}}}{\delta P_{q,i}^{\text{exp,idler}}} \right)^2 \tag{5.41}$$

where q is the data set number ($q = \{1, 2, 3, 4\}$ here), i is i^{th} data point in set q, and $P_{q,i}^{\text{exp,idler}}$ and $P_{q,i}^{\text{model,idler}}$ are the i^{th} experimental and calculated idler powers in data set q, respectively. The calculation of the relative uncertainty in the idler power, $\delta P_{q,i}^{\text{exp,idler}}/P_{q,i}^{\text{exp,idler}}$ is described in Appendix D. The following procedure is followed to calculate X_{FWM}^2 for a given set of seven parameters:

1. The experimental input pump and signal powers are appropriately calculated given the ϕ_{in}, and the idler power is appropriately calculated using both ϕ_{in} and ϕ_{out} (see Appendix D).

2. The $\tau_m^{\text{in}}, \tau_m^{\text{out}}$ and τ_m^{scatt} lifetimes are calculated using Eqns. (5.34), (5.35) and (5.36).

3. The idler power model function is calculated is based on Eqn. (5.30), which is rewritten as,

$$P^{\text{model,idler}} = \frac{2}{\tau_{\text{idler}}^{\text{out}}} \frac{(\omega_{\text{idler}})^2 |\beta_{\text{idler}}|^2 (U_{\text{pump}})^2 U_{\text{signal}}}{(\delta\omega_{\text{idler}})^2 + \tau_{\text{idler}}(U_{\text{signal}}, U_{\text{pump}})^{-2}}, \tag{5.42}$$

   where "pump", "signal", and "idler" label the modes excited by pump, signal and idler photons, and $\delta\omega_{\text{idler}}$ is the detuning between the idler frequency and the idler resonant mode frequency. For each excitation scheme, the idler power is calculated by first determining the pump and signal energies, U_{pump} and U_{signal}, which are then used to calculate the energy dependent idler mode lifetime, $\tau_{\text{idler}}(U_{\text{signal}}, U_{\text{pump}})$. The U_{signal} and U_{pump} energies are calculated with an iterative process, for each input power pair of a data set, in order to account for the interplay between the nonlinear effects of the two modes. This process is described below and is summarized in the flowchart in Fig. 5.11:

   (a) The pump and signal cavity peak energies, $U_{\text{signal}}^{\text{tmp,1}}$ and $U_{\text{pump}}^{\text{tmp,1}}$ are first estimated as the

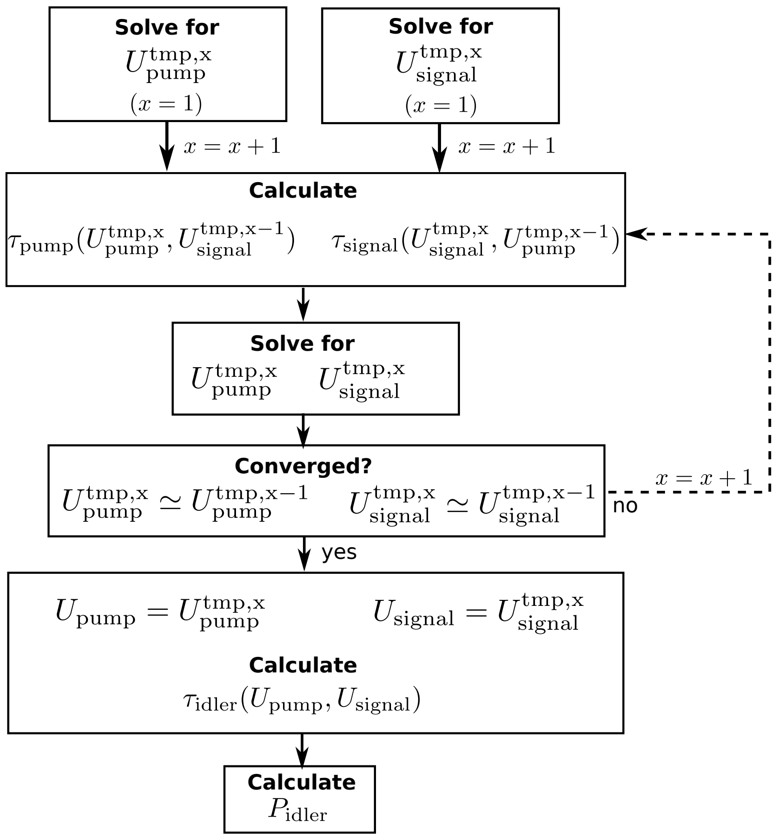

Figure 5.11: Four-wave mixing idler power calculation flowchart. The solid arrows indicate the step sequence and the dashed arrow indicates an iterative loop that continues until convergence is met.

energies that would be loaded by independent probing of the pump and signal, and are found by numerically solving Eqn. (5.22),

$$U_m^{\text{tmp},1} = \frac{2{\tau_m^{\text{in}}}^{-1} P_m^{\text{in}}}{(\delta\omega_m)^2 + \tau_m(U_m^{\text{tmp},1})^{-2}}, \tag{5.43}$$

where $\delta\omega_{\text{pump}} = 0$, and $\delta\omega_{\text{signal}} = 0$ when the signal mode is the high Q M1 mode, and $\delta\omega_{\text{signal}} = 2\omega_2 - \omega_1 - \omega_3$ when it is the low Q M3 mode. This is consistent with the experimental wavelength tuning scheme described in Section 2.3.

(b) Using the $U_{\text{pump}}^{\text{tmp},1}$ and $U_{\text{signal}}^{\text{tmp},1}$ found in the previous step, the energies are recalculated by numerically solving for $U_{\text{pump}}^{\text{tmp},2}$ and $U_{\text{signal}}^{\text{tmp},2}$ below:

$$U_{\text{pump}}^{\text{tmp},2} = \frac{2{\tau_{\text{pump}}^{\text{in}}}^{-1} P_{\text{pump}}^{\text{in}}}{(\delta\omega_{\text{pump}})^2 + \tau_{\text{pump}}(U_{\text{pump}}^{\text{tmp},2}, U_{\text{signal}}^{\text{tmp},1}, U_{\text{idler}} = 0)^{-2}}, \tag{5.44}$$

and

$$U_{\text{signal}}^{\text{tmp},2} = \frac{2\tau_{\text{signal}}^{\text{in}}{}^{-1} P_{\text{signal}}^{\text{in}}}{(\delta\omega_{\text{signal}})^2 + \tau_{\text{signal}}(U_{\text{signal}}^{\text{tmp},2}, U_{\text{pump}}^{\text{tmp},1}, U_{\text{idler}} = 0)^{-2}}, \tag{5.45}$$

with

$$\tau_m(U_{\text{pump}}^{\text{tmp},x}, U_{\text{signal}}^{\text{tmp},x}, U_{\text{idler}} = 0)^{-1} = \tau_m^{\text{lin}}{}^{-1} + \rho_0 \sum_{m'} \alpha_{m,m'} U_{m'} + \kappa_0 \sum_{l,l'} \kappa_{m,l,l'}^{\text{FCA}} U_l U_{l'},$$

where $m', l, l' = \{1, 2, 3\}$, and the superscripts "x" in $U_{\text{pump}}^{\text{tmp},x}$ and $U_{\text{signal}}^{\text{tmp},x}$ in Eqn. (5.46) are substituted with the appropriate numbers that appear in Eqns. (5.44) and (5.45).

(c) Step 2 is iterated until U_{pump} and U_{signal} have converged. Typically only one or two iterations are necessary.

(d) The total lifetime of the idler mode is calculated, given the presence of nonlinear losses induced by the energy in the pump and signal modes. It is given by,

$$\begin{aligned} \tau_{\text{idler}}{}^{-1} &= \tau_{\text{idler}}^{\text{lin}}{}^{-1} + \tau_{\text{idler}}^{\text{TPA}}{}^{-1} + \tau_{\text{idler}}^{\text{FCA}}{}^{-1} \\ &= \tau_{\text{idler}}^{\text{lin}}{}^{-1} + \rho_0 \sum_{m'} \alpha_{\text{idler},m'} U_{m'} + \kappa_0 \sum_{l,l'} \kappa_{\text{idler},l,l'}^{\text{FCA}} U_l U_{l'}, \end{aligned} \tag{5.46}$$

where the sums of m', l and l' are done over only the pump and signal modes. This assumes that the idler mode contributions to τ_m^{TPA} and τ_m^{FCA} are negligible.

(e) The idler power is calculated using Eqn. (5.42), with $\delta\omega_{\text{idler}} = 2\omega_2 - \omega_1 - \omega_3$ when the idler corresponds to the low Q mode, and $\delta\omega_{\text{idler}} = 0$ when it corresponds to the high Q mode. The use of $\delta\omega_3 = 2\omega_2 - \omega_1 - \omega_3$ here and in Step 1 assumes that the detuning does not change, even in the presence of nonlinear absorption at excitation high powers. This assumption is valid if all three modes shift by the same amount, and provided laser and filter wavelengths appropriately track the high Q mode (and idler) resonant wavelengths, as is done experimentally (see Appendix A). The assumption of equally shifting modes appears to be valid to first order, as a uniform change in the refractive index is predicted to shift all modes, to within 0.3 % of each other. This was verified by examining Γ_m^{th} given in Appendix F.

5.4.2 Least-squares analysis

One approach to extracting the 15 unknown microcavity parameters and the 2 unknown Fabry-Perot parameters from the nonlinear experimental data would be to find the parameter set $\{\eta_1^{\mathrm{wg}}$, $\eta_2^{\mathrm{wg}}, \eta_3^{\mathrm{wg}}, Q_{\mathrm{abs}}, \tau_{\mathrm{carrier}}, R_{\mathrm{th}}, \phi_{\mathrm{in}}, \phi_{\mathrm{out}}\}$ that minimizes the total squared difference $X^2_{\mathrm{tot}} = X^2_{\mathrm{T}} + X^2_{\mathrm{FWM}}$. These 8 fit parameters, along with nine pieces of information extracted from the linear transmission measurements complete the characterization. Unfortunately, this approach is not practical because each computation of X^2_{FWM} takes a relatively large amount of time as the model idler powers are not calculated directly, instead they require that multiple equations are solved numerically.

Alternatively, to reduce the computation time, a more practical approach is taken where X^2_{FWM} is evaluated over only $\eta_1^{\mathrm{wg}}, \eta_2^{\mathrm{wg}}$ and η_3^{wg}, which have the greatest impact on the idler power model. In this approach, for each set of $\{\eta_1^{\mathrm{wg}}, \eta_2^{\mathrm{wg}}, \eta_3^{\mathrm{wg}}\}$, the remaining parameters that enter the model (Q_{abs}, $\tau_{\mathrm{carrier}}, \phi_{\mathrm{in}}, \phi_{\mathrm{out}}$), are evaluated at the parameter values that minimize X^2_{T} for this $\{\eta_1^{\mathrm{wg}}, \eta_2^{\mathrm{wg}}\}$ pair. The total $X^2_{\mathrm{tot}} = X^2_{\mathrm{T}} + X^2_{\mathrm{FWM}}$ is then minimized to extract the set of best fit parameters.

In the main approach taken in this work, the computation time is reduced further by separately minimizing X^2_{T} and X^2_{FWM}, in an iterative process that achieves consistency between the two calculations. This iterative process was conceived after careful consideration of the X^2_{T} and X^2_{FWM} topographies across the relevant parameter spaces.

Figure 5.12 plots the base 10 logarithm of the X^2_T for Device 2 as a function of fit parameters from the set $\{\eta_1^{\mathrm{wg}}, \eta_2^{\mathrm{wg}}, Q_{\mathrm{abs}}, R_{\mathrm{th}}, \tau_{\mathrm{carrier}}, \phi_{\mathrm{in}}, \phi_{\mathrm{out}}\}$. These results are generally representative of the results for all devices. For each plot, the parameters on the x and y axis are held fixed, and the minimum X^2_{T} is found across all other fit parameters for each (x, y) pair. The same color scale is used for each plot (shown to the right of each row), and the color is left blank (white) when there are no viable parameter sets (energy conservation limits the ranges of the cavity lifetimes). Figures 5.12(a) and (b) show that R_{th} decreases with increasing η_1^{wg} and η_2^{wg}, respectively. These correlations arise due to the dependence of the nonlinear wavelength shifts and peak transmissions on the energy loaded in the cavity. The microcavity energy increases with η_m^{wg}, and R_{th} must be reduced to maintain the same nonlinear wavelength shifts. Similarly, τ_{carrier} is also reduced for increasing η_m^{wg}, in order to maintain both the same shifts and peak transmissions, as shown in Figs.

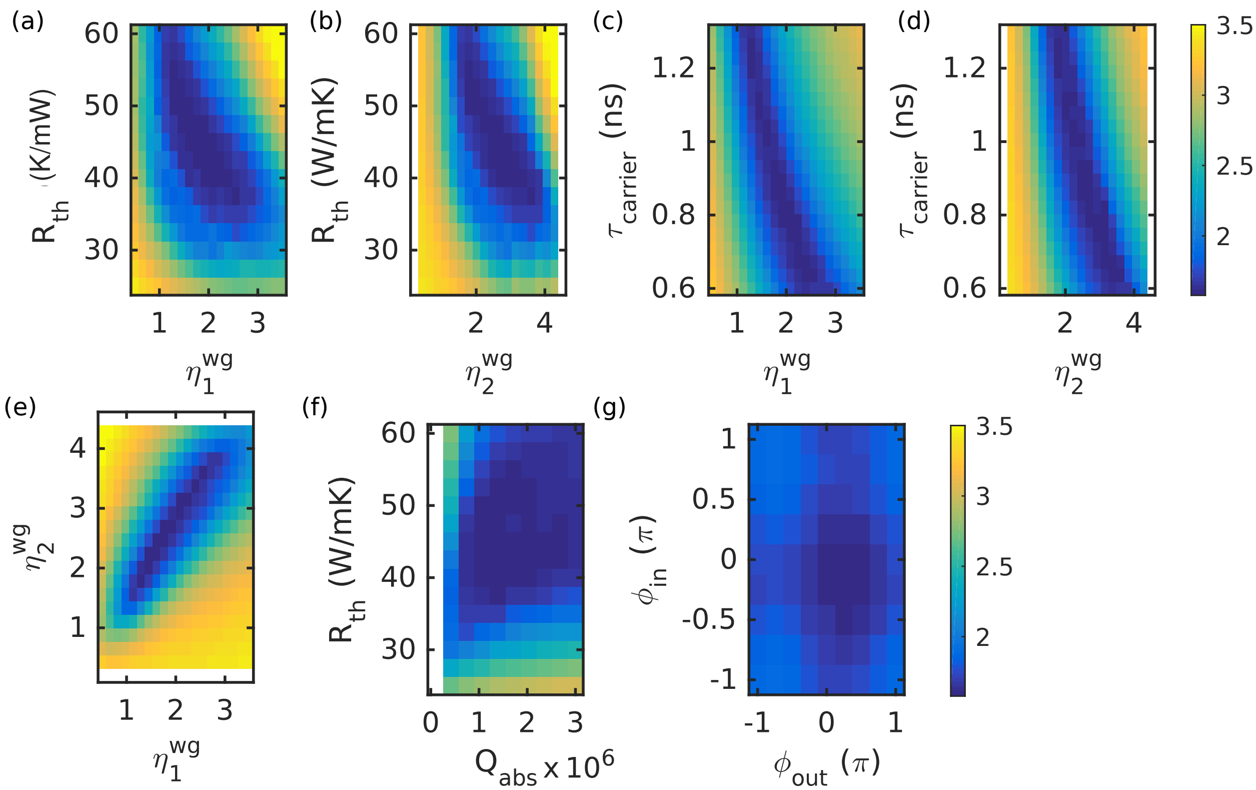

Figure 5.12: Nonlinear transmission analysis example results for Device 2. The base 10 logarithm X_{T}^2 is plotted across the parameter set $\{\eta_1^{\mathrm{wg}}, \eta_2^{\mathrm{wg}}, Q_{\mathrm{abs}}, R_{\mathrm{th}}, \tau_{\mathrm{carrier}}, \phi_{\mathrm{in}}, \phi_{\mathrm{out}}\}$. For each parameter pair on the x and y axes, the minimum $\log 10(X_{\mathrm{T}}^2)$ across all other parameters is plotted. Blank results show where no viable parameter sets exist due to a lack of energy conservation. Each plot has the same color scale (shown to the right of each row). There is a total of 13 degrees of freedom in the X_{T}^2 calculation.

5.12(c) and (d). As a result of these correlations, η_2^{wg} and η_1^{wg} are also correlated, as shown in Fig. 5.12(e). The minimization of X_{T}^2 as a function of $Q_{\mathrm{abs}}, \phi_{\mathrm{in}}$ and ϕ_{out} is relatively weak compared to the other parameters, as is shown in Figs. 5.12(f) and (g), where the minimum X_{T}^2 vary by less than an order of magnitude over the majority of the parameters spaces, in contrast to Figs. 5.12(a) and (e), where the minimum X_{T}^2 vary by ~ 2 orders of magnitude over the parameter spaces.

Figures 5.13 shows the X_{FWM}^2 as a function of parameters $\eta_1^{\mathrm{wg}}, \eta_2^{\mathrm{wg}}$ and η_3^{wg}. For each $(\eta_x^{\mathrm{wg}}, \eta_y^{\mathrm{wg}})$ pair in the plots, the minimum X_{FWM}^2 across the third parameter is shown. The values for $\tau_{\mathrm{carrier}}, Q_{\mathrm{abs}}, \phi_{\mathrm{in}}$ and ϕ_{out} are held fixed at the values that minimize X_{T}^2 in Fig. 5.12. Figure 5.13(a) shows a strong correlation between η_3^{wg} and η_1^{wg}. The physics of this correlation is explained by first considering the data sets where M1 is the signal mode and M3 is the idler mode. When η_1^{wg} is increased, the signal energy in the microcavity is increased, and in order to compensate, η_3^{wg} is

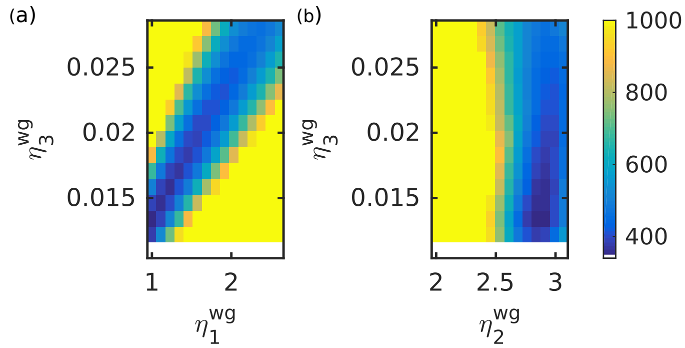

Figure 5.13: Four-wave mixing example results for Device 2. The $X^2_{\rm FWM}$ is plotted across the parameter set $\{\eta_1^{\rm wg}, \eta_2^{\rm wg}, \eta_3^{\rm wg}\}$, while $Q_{\rm abs}, \tau_{\rm carrier}, \phi_{\rm in}$ and $\phi_{\rm out}$ are held fixed at the values that minimize $X^2_{\rm T}$. For each parameter pair on the x and y axes, the minimum $X^2_{\rm FWM}$ across the other parameter is plotted. Blank results show where no viable parameter sets exist due to a lack of energy conservation. Each plot has the same color scale (shown to the right). There are 55 degrees of freedom in the $X^2_{\rm FWM}$ calculation.

also increased such that coupling of the generated idler photons to the output channel is weakened. The same arguments apply when the signal and idler modes are exchanged. Figure 5.13(b) shows that $X^2_{\rm FWM}$ is minimized as a function of $\eta_2^{\rm wg}$. Only a very weak correlation exists between $\eta_2^{\rm wg}$ and $\eta_3^{\rm wg}$, which is unsurprising as both idler powers scale with $\eta_2^{\rm wg}$ in the linear regime and there is no symmetry between the pump and the signal/idler.

It is important to note that there is no clear minimum for $X^2_{\rm T}$, nor $X^2_{\rm FWM}$, when they are considered separately. However, their sum, $X^2_{\rm tot}$, does have a clear minimum, which is why it is crucial that both nonlinear transmission and four-wave mixing data are included in this analysis. The $X^2_{\rm tot}$ is plotted as a function of $\eta_1^{\rm wg}, \eta_2^{\rm wg}$, and $\eta_3^{\rm wg}$ in Figure 5.14, along with $X^2_{\rm T}$ and $X^2_{\rm FWM}$. The minimization of $X^2_{\rm tot}$ can be understood by first noting that $X^2_{\rm FWM}$ in Fig. 5.13(b) is minimized as a function of $\eta_2^{\rm wg}$. Given the correlations in $X^2_{\rm T}$ shown in Figs. 5.12(a)-(e), the minimization as a function of $\eta_2^{\rm wg}$ is sufficient to minimize $X^2_{\rm T}$ over the rest of the parameters involved in this analysis. In turn, given the correlations in $X^2_{\rm FWM}$ shown in Fig. 5.13(a), the minimization of $X^2_{\rm T}$ as a function of $\eta_1^{\rm wg}$ results in a minimization of $X^2_{\rm FWM}$ over $\eta_3^{\rm wg}$.

The iterative method employed in this thesis that accounts for these correlations and involves independent minimizations of $X^2_{\rm T}$ and $X^2_{\rm FWM}$, yields essentially identical results as the $X^2_{\rm tot}$ minimization (calculated with the reduced $\chi^2_{\rm FWM}$ parameter space). It is outlined here:

1. The set of seven parameters $\{\eta_1^{\rm wg}, \eta_2^{\rm wg}, R_{\rm th}, \tau_{\rm carrier}, Q_{\rm abs}, \phi_{\rm in}, \phi_{\rm out}\}$ that minimize $X^2_{\rm T}$ are found

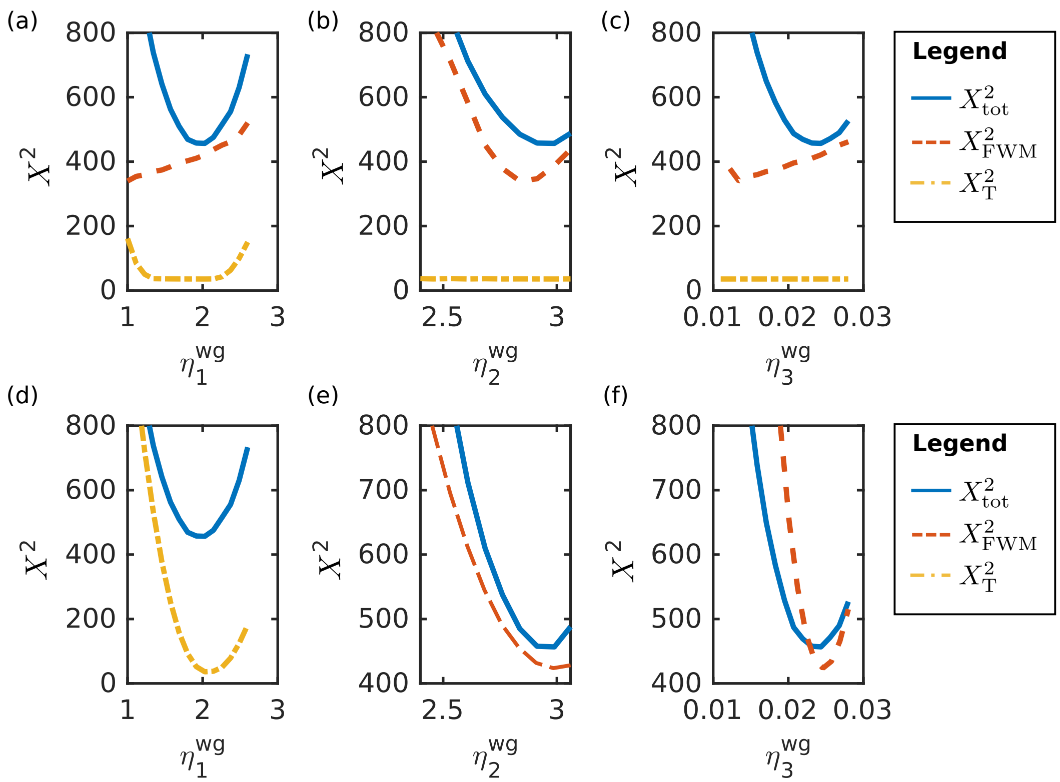

Figure 5.14: Nonlinear transmission results for Device 2. Plots (a)-(c) show X^2_{tot}, X^2_{FWM} , and X^2_{T}. The parameter on each x axis is fixed and the minimum X^2 over all other fit parameters involved in the respective analysis is shown. X^2_{T} is calculated as a function of $\eta_1^{\mathrm{wg}}, \eta_2^{\mathrm{wg}}, R_{\mathrm{th}}, \tau_{\mathrm{carrier}}, Q_{\mathrm{abs}}, \phi_{\mathrm{in}}$ and ϕ_{out}. X^2_{FWM} is calculated as a function of $\eta_1^{\mathrm{wg}}, \eta_2^{\mathrm{wg}}, \eta_3^{\mathrm{wg}}$, while $\tau_{\mathrm{carrier}}, Q_{\mathrm{abs}}, \phi_{\mathrm{in}}$ and ϕ_{out} are held fixed at the values that minimize X^2_{T}. X^2_{tot} is the sum over X^2_{T} and X^2_{FWM}. Plots (d)-(e) show X^2_{tot} and the X^2 minimization that is used to determine the fit parameter on the x axis using the iterative fitting process, where X^2_{T} in (d) is calculated for fixed η_2^{wg} and X^2_{FWM} in (e) and (f) is calculated with fixed η_1^{wg}.

from the nonlinear transmission least-squares analysis. There is an element of randomness to this, as X^2_{T} is not well minimized (η_2^{wg} is not yet constrained).

2. The best fit parameters found in Step 1 are applied to the FWM analysis as fixed values, excluding η_2^{wg}, which is introduced as a free fit parameter, along with η_3^{wg}. The (η_2^{wg}, η_3^{wg}) pair that minimize X^2_{FWM} is found.

3. The nonlinear transmission analysis is repeated with η_2^{wg} held fixed at the FWM best fit value, and the set of six parameters $\{\eta_1^{\mathrm{wg}}, R_{\mathrm{th}}, \tau_{\mathrm{carrier}}, Q_{\mathrm{abs}}, \phi_{\mathrm{in}}, \phi_{\mathrm{out}}\}$ that minimize X^2_{T} are found.

4. Steps 2 and 3 are repeated until the best fit η_2^{wg} from the FWM least-squares converges. This

typically only requires one or two iterations.

Figure 5.15 illustrates how fixing the value of η_2^{wg} in the X_{T}^2 analysis of Device 2 results in a minimization across the remaining fit parameters. In this example, $\eta_2^{\text{wg}} = 3$, which is the best fit value extracted from the FWM analysis. The white contour lines show where $X_{\text{T}}^2 = \min(X_{\text{T}}^2) + 1$. The extremes of the contours in the x and y directions show the limits of the $\pm 1\sigma$ uncertainty range for the parameters on the respective axes.

A correlation between R_{th} and Q_{abs} is also revealed in Fig. 5.15(c), where an increase in R_{th} results in an increase in Q_{abs}, in order to maintain the same thermal shift (larger Q_{abs} results in less linear material absorption). Beyond a certain point, the R_{th} essentially becomes independent of Q_{abs} (where the X_{T}^2 trough flattens towards horizontal), because at some point Q_{abs} is so high that linear material absorption is insignificant compared to nonlinear absorption through the TPA and FCA processes.

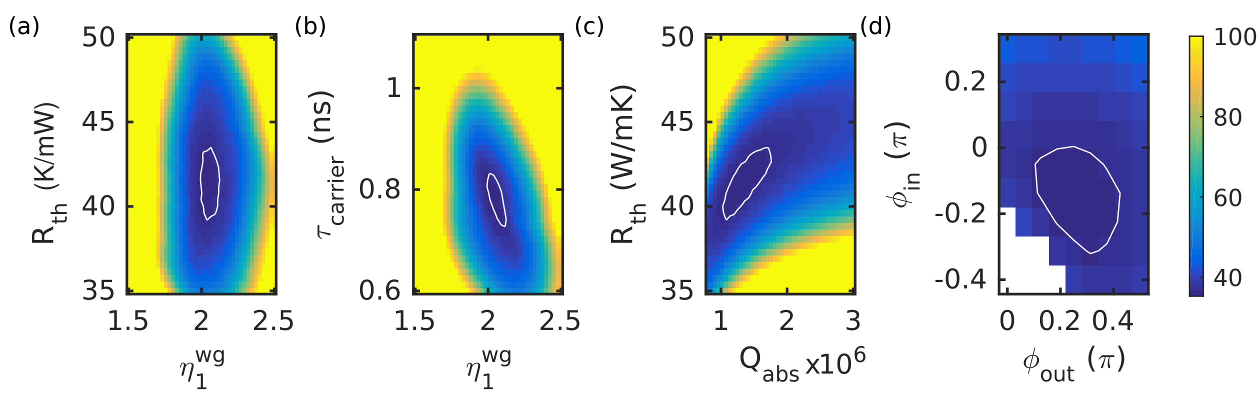

Figure 5.15: Nonlinear transmission analysis example results for Device 2. The X_{T}^2 is plotted across the parameter set $\{\eta_1^{\text{wg}}, Q_{\text{abs}}, R_{\text{th}}, \tau_{\text{carrier}}, \phi_{\text{in}}, \phi_{\text{out}}\}$, when $\eta_2^{\text{wg}} = 3$ is held fixed at the best fit values from the four-wave mixing analysis. For each parameter pair on the x and y axes, the minimum X_{T}^2 across all other parameters is plotted. Each plot has the same color scale (shown to the right), where $X_{\text{T}}^2 > 100$ at set the maximum of the color scale range. White lines contour $X_{\text{T}}^2 = \min(X_{\text{T}}^2) + 1$. There is a total of 12 degrees of freedom in the X_{T}^2 calculation.

The X_{tot} minimization curves for Device 2 are compared to those found using this iterative method in Fig. 5.14(d)-(f). In Fig. 5.14(d), the minimization of X_{T}^2 with respect to η_1^{wg} is shown, while in Figs. 5.14(d) the minimization of X_{FWM}^2 with respect to η_2^{wg} and η_3^{wg} is shown. There is close agreement between the values of $\eta_1^{\text{wg}}, \eta_2^{\text{wg}}$ and η_3^{wg} that minimize X_{tot}^2 and the X^2's from the iterative process (X_{T}^2 or X_{FWM}^2).

The resulting Device 2 best fit values for $R_{\rm th}, Q_{\rm abs}$ and $\tau_{\rm carrier}$, given in Table 5.5 are consequently very close as well. In the iterative method, the $\pm 1\sigma$ uncertainties in $\eta_1^{\rm wg}, R_{\rm th}, Q_{\rm abs}, \tau_{\rm carrier}, \phi_{\rm in}$ and $\phi_{\rm out}$ are all estimated by finding the parameter ranges where $X_{\rm T}^2 < \min(X_{\rm T}^2) + 1$, while the uncertainties in $\eta_2^{\rm wg}$ and $\eta_2^{\rm wg}$ are estimated from $\min(X_{\rm FWM}^2) + 1$. For the $X_{\rm tot}^2$ method example given above, the uncertainties in $\eta_1^{\rm wg}, \eta_2^{\rm wg}$ and $\eta_3^{\rm wg}$ are estimated from $\min(X_{\rm tot}^2) + 1$, while those for $R_{\rm th}, Q_{\rm abs}, \tau_{\rm carrier}, \phi_{\rm in}$ are estimated from looking at $\min(X_{\rm T}^2) + 1$ when $\eta_1^{\rm wg}, \eta_2^{\rm wg}$ are limited to be within the 1σ uncertainty.

Table 5.5: Best fit parameters found from an analysis involving the minimization of $X_{\rm tot}^2$, and from a separate analysis where an iterative approach is taken to find $X_{\rm T}^2$ and $X_{\rm FWM}^2$. $R_{\rm th}$ is the thermal resistance, $\tau_{\rm carrier}$ is the effective saturated free-carrier lifetime and $Q_{\rm abs}$ is the quality factor associated with linear material absorption.

	$X_{\rm tot}^2$ method			Iterative method		
	Best fit	-1σ	$+1\sigma$	Best fit	-1σ	$+1\sigma$
$R_{\rm th}$ (K/mW)	40.7	39.3	42.0	40.7	39.8	43.0
$\tau_{\rm carrier}$ (ns)	0.79	0.783	0.828	0.78	0.754	0.804
$Q_{\rm abs}(\times 10^6)$	1.16	1.0	1.34	1.22	1.1	1.77

For the analyses of the four devices, the typical parameter space used for the iterative least-squares minimization approach is shown in Table 5.6. In order to satisfy energy conservation, given the linear transmission $\tau_m^{\rm lin}$ and $\overline{T}_m^{\rm lin}$, $\eta_m^{\rm wg}$ is constrained to be between,

$$\min \eta_m^{\rm wg} = \left(\frac{1}{\sqrt{\overline{T}_m^{\rm lin}}} - \sqrt{\frac{1}{\overline{T}_m^{\rm lin}} - 1} \right)^2 \tag{5.47}$$

and

$$\max \eta_m^{\rm wg} = \left(\frac{1}{\sqrt{\overline{T}_m^{\rm lin}}} + \sqrt{\frac{1}{\overline{T}_m^{\rm lin}} - 1} \right)^2 . \tag{5.48}$$

Parameter sets that result in a negative $\tau_m^{\rm scatt}$ calculated by Eqn. (5.36) are discarded. Once the minimum $\chi_{\rm T}^2$ and $\chi_{\rm FWM}^2$ have been identified, the parameter space is typically narrowed and refined to achieve better resolution.

Table 5.6: Typical parameter space initially tested for nonlinear transmission analysis. $Q_{\text{abs}} = \omega_m \tau_{\text{abs}}/2$.

Parameter	Min	Max	# of points
η_1^{wg}	$\min \eta_1^{\text{wg}}$	5	20
η_2^{wg}	$\min \eta_2^{\text{wg}}$	$\max \eta_2^{\text{wg}}$	20
ϕ_{in}	$-\pi$	π	7
ϕ_{out}	$-\pi$	π	7
R_{th}	5 K/mW	100 K/mW	20
Q_{abs}	1×10^5	4×10^6	20
τ_{carrier}	0.3 ns	1.5 ns	20

5.4.3 Best fit parameters

The best fit parameters and the $\pm 1\sigma$ uncertainties are plotted in Fig. 5.16, where the gray rectangles show the $\pm 1\sigma$ uncertainties (see Appendix G for X^2 minimization plots for all devices). Red markers indicate the parameters for which the relevant X^2 (X_{T}^2 or X_{FWM}^2) is not minimized. The minimum $\overline{X}_{\text{T}}^2 = X_{\text{T}}^2/(N_{\text{T}} - k_{\text{T}})$ and $\overline{X}_{\text{FWM}}^2 = X_{\text{FWM}}^2/(N_{\text{FWM}} - k_{\text{FWM}})$ are also plotted for the four devices in Fig. 5.16, where N_{T} and N_{FWM} are the total number of data points in the fits, and $k_{\text{T}} = 6$ and $k_{\text{FWM}} = 2$ are total number of fit parameters.

These characterization results show that the parameters $R_{\text{th}}, Q_{\text{abs}}$ and τ_{carrier} are generally consistent for Devices 2 to 4, while for Device 1, R_{th} and Q_{abs} are significantly higher than the others. Given that each device is processed the same way and nominally support similar modes (mode wavelengths and quality factors), these three parameters are expected to be close for each device. In contrast, the waveguide coupling ratios differ more from device to device, as they are more sensitive to structural non-uniformities. The inconsistency in the R_{th} and Q_{abs} parameters of Device 1 is likely related to the fact that X_{FWM}^2 does not reach a minimum as a function of η_2^{wg}, which is a key parameter in this iterative approach.

Table 5.7 reports the weighted means of $R_{\text{th}}, Q_{\text{abs}}$ and τ_{carrier}, across Devices 2 to 4, where the weights are taken to be $1/[(\delta X_{\text{upper}} - \delta X_{\text{lower}})/2]^2$. This ignores asymmetries in the parameter uncertainties, which is not expected to have a large impact, given that the unweighted mean values are close to the weighted values ($R_{\text{th}} = 41.4$ K/mW, $Q_{\text{abs}} = 1.5 \times 10^6$ and $\tau_{\text{carrier}} = 0.97$ ns).

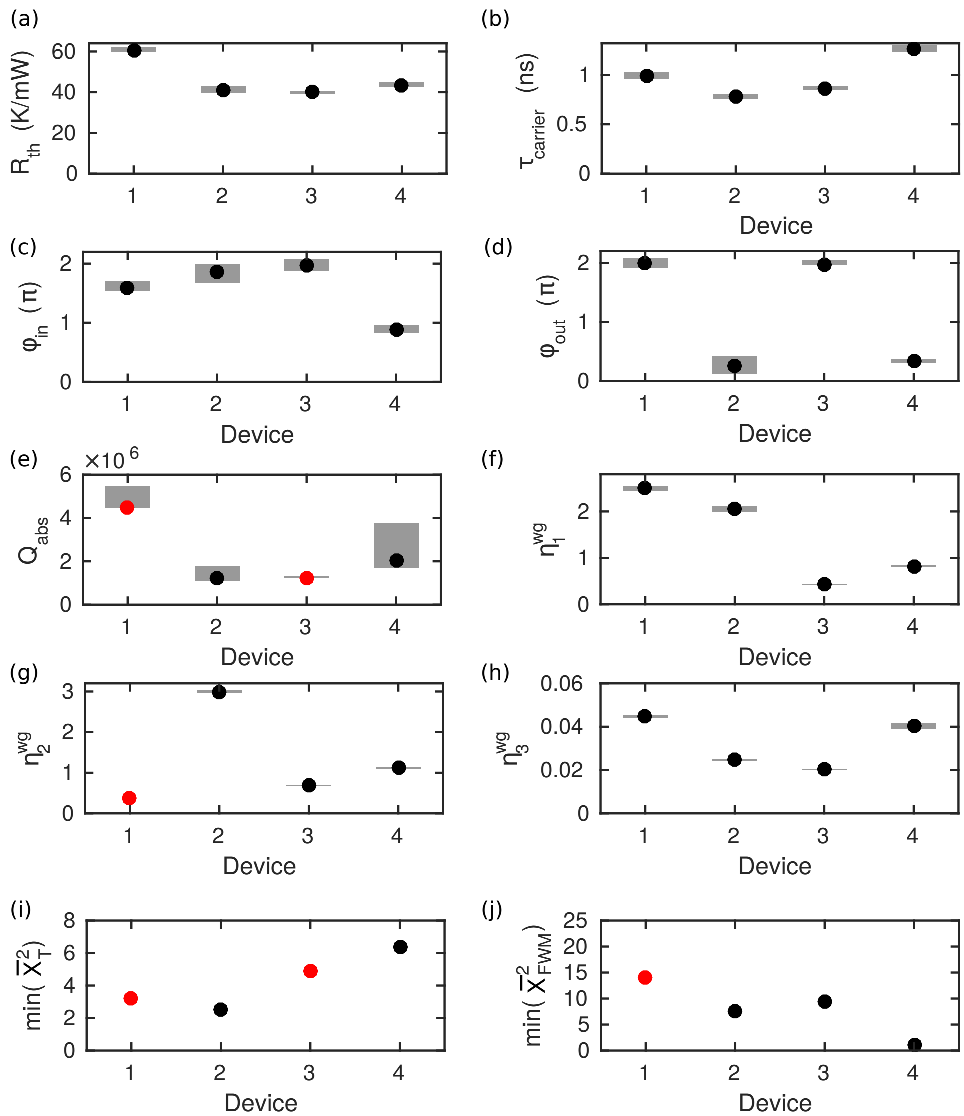

Figure 5.16: Nonlinear characterization results. (a)-(h) Best fit parameters (markers), with $\pm 1\sigma$ uncertainties (rectangles). Parameters that minimize the X^2 are shown with black markers, and those that do not are red. (i)-(j) The minimum $\overline{X}^2 = X^2/(N-k)$ from the nonlinear transmission and the four-wave mixing analyses are shown, where N is the number of data points in the fit and k is the number of fit parameters. Fits where X^2 does not reach a minimum with respect to all parameters are marked as red.

To check for consistency between the devices, the least-squares analyses are repeated with $R_{\text{th}}, Q_{\text{abs}}$ and τ_{carrier} held fixed at the average values. The fit results from these analyses are compared to the original results in Fig. 5.17, and the agreement for Devices 2 to 4 is generally very good, while that for Device 1 is poor. For this analysis, best fit values for $\eta_1^{\text{wg}}, \eta_2^{\text{wg}}$ and η_3^{wg} are extracted by minimizing the total X^2_{tot} instead of using the iterative method, and ϕ_{in} and ϕ_{out}

Table 5.7: Summary of mean best fit values found from analyses of linear transmission, nonlinear transmission and four-wave mixing measurements for Devices 2 to 4.

Parameter	Weighted Mean
R_{th}	40.5 ± 0.4 K/mW
Q_{abs}	$1.26 \pm 0.04 \times 10^6$
τ_{carrier}	0.92 ± 0.02 ns

are held fixed at the original best fit values. The reduced parameter space makes it possible to run this calculation over a practical time scale. Figure 5.18 shows plots of the X^2_{tot} (solid), X^2_{T} (dash-dotted) and X^2_{FWM} (dashed) as a function of the fit parameters for Device 2.

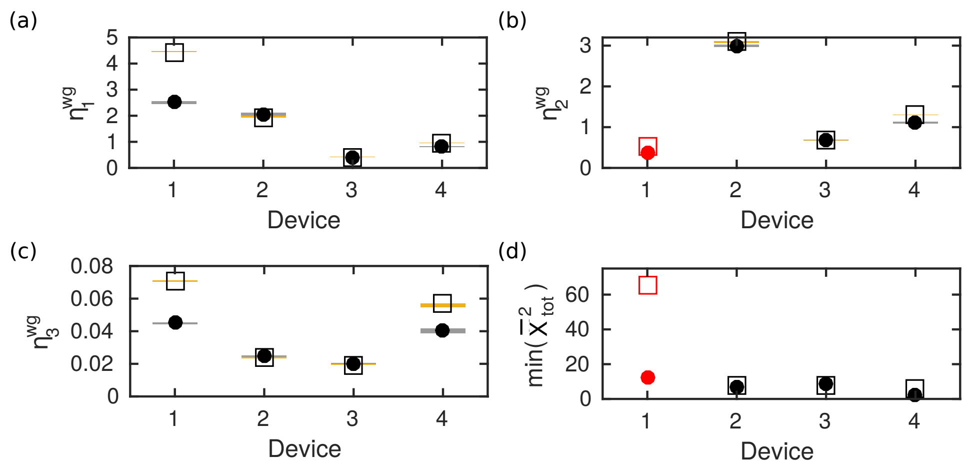

Figure 5.17: Nonlinear characterization results, for both the original individual devices analyses (circles), for when $R_{\mathrm{th}}, Q_{\mathrm{abs}}$ and τ_{carrier} are fixed to the average values in the model functions (squares). (a)-(c) Best fit parameters (markers), with $\pm 1\sigma$ uncertainties (gray rectangles for original fit parameters, and yellow rectangles for the new fit parameters). Parameters that minimize the X^2_{tot} are shown with black markers, and those that do not are red. (d) The minimum $\overline{X}^2_{\mathrm{tot}} = X^2_{\mathrm{tot}}/(N_{\mathrm{tot}} - k_{\mathrm{tot}})$ is shown, where N_{tot} is the number of data points in the fit and k_{tot} is the number of fit parameters. Fits where X^2_{tot} is not fully minimized are marked as red.

5.4.4 Consistency checks

Energy $U_{m,i}$ calculation

The nonlinear transmission $\Delta\lambda_m^{\mathrm{NL,model}}$ and $\overline{T}_m^{\mathrm{NL,model}}$ data plotted in the first two columns of Fig. 5.15 are calculated using the model functions in Eqns. (5.38) and (5.37), and by calculating the

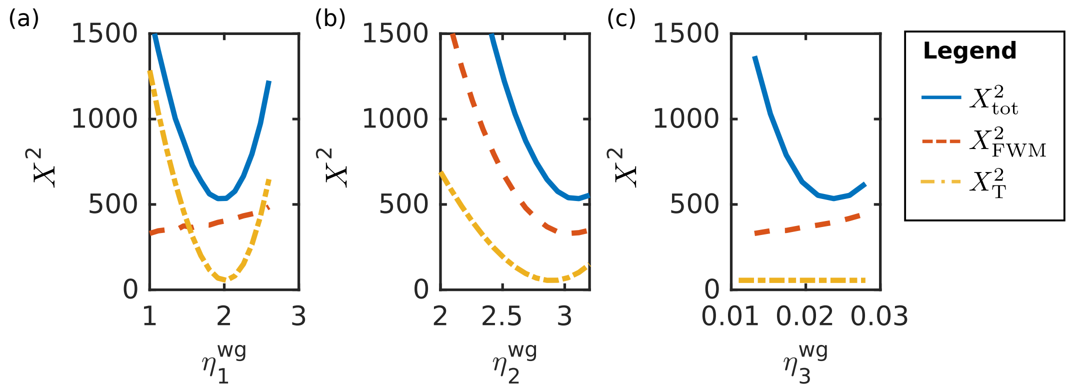

Figure 5.18: Nonlinear transmission results for Device 2 when $R_{\text{th}}, Q_{\text{abs}}$ and τ_{carrier} are held fixed at the mean values. The parameter on each x axis is fixed and the minimum X^2_{tot}, X^2_{T}, and X^2_{FWM}, over all other fit parameters involved in the respective analysis is shown. X^2_{T} is calculated as a function of $\eta_1^{\text{wg}}, \eta_2^{\text{wg}}$. X^2_{FWM} is calculated as a function of $\eta_1^{\text{wg}}, \eta_2^{\text{wg}}, \eta_3^{\text{wg}}$, while ϕ_{in} and ϕ_{out} are held fixed at the best fit values from the X^2_{T} minimization. X^2_{tot} is the sum over X^2_{T} and X^2_{FWM}.

resonant microcavity energy $U_{m,i}$ by numerically solving,

$$U_{m,i} = 2{\tau_m^{\text{in}}}^{-1} P_{m,i}^{\text{in}} \tau_m (U_{m,i})^2. \tag{5.49}$$

In the X^2_{T} calculation, the microcavity energy $U_{m,i}$ is directly calculated based on the experimental nonlinear transmission using Eqn. (5.40), instead of calculating it based on the input power. This method is computationally much faster, and is more practical for the large parameters spaces tested. A consistency test is done by repeating the X^2_{T} minimization using the $\overline{T}_{m,i}^{\text{NL,model}}$ values in the $U_{m,i}$ calculation in Eqn. (5.40). This is iterated until convergence is met in the best fit parameters (typically between 2 to 4 iterations). Figure 5.19 shows that the resulting minimum X^2_{T} and best fit parameters are not significantly different from those found using the original fitting scheme, for the four devices studied here.

Saturated free-carrier lifetime

A consistency test is also done to ensure that the effective free-carrier lifetime does indeed appear to be saturated for the data used in the nonlinear transmission fitting analysis (which is a subset of the full data set). The effective free-carrier lifetime is estimated by solving Eqn. (5.37) for τ_{carrier}, where all other best fit parameters are applied, $\overline{T}_{m,i}^{\text{NL,model}}$ is replaced by $\overline{T}_{m,i}^{\text{NL}}$, and $U_{m,i}$ is

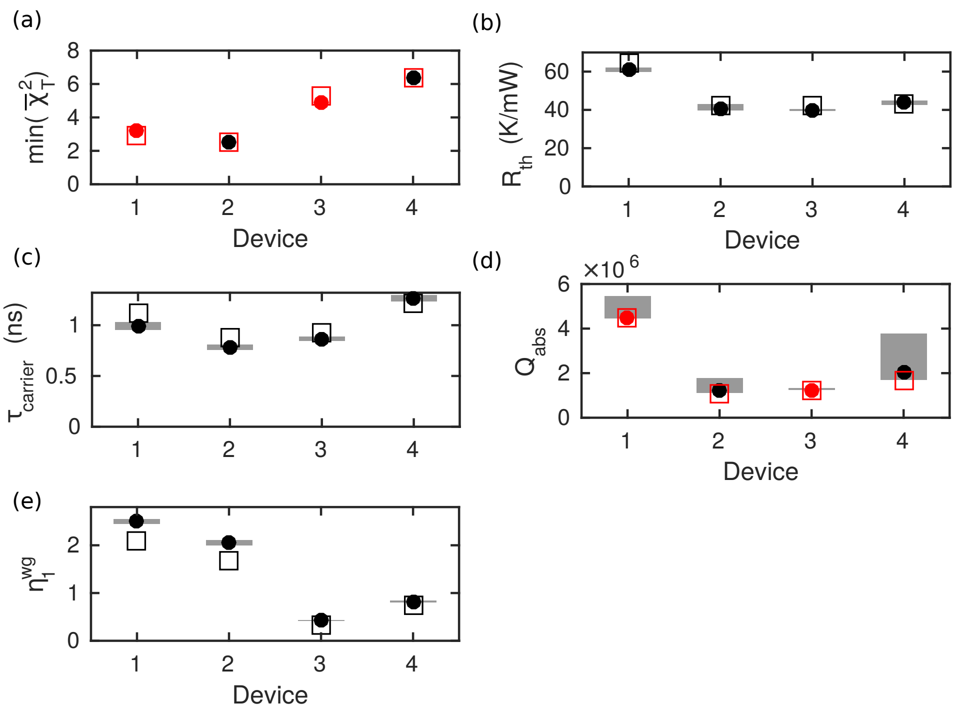

Figure 5.19: Nonlinear characterization results for the best fit analysis (filled circles) and for the converged results (empty squares) when $\overline{T}^{\mathrm{NL,model}}_{m,i}$ is used to calculate the $U_{m,i}$ in the model functions [Eqns. (5.37),(5.38) and (5.40)]. The minimum $\overline{X}^2_{\mathrm{T}} = X^2_{\mathrm{T}}/(N_{\mathrm{T}} - k_{\mathrm{T}})$ from the nonlinear transmission is shown in (a), where N_{T} is the number of data points in the fit and k_{T} is the number of fit parameters. Fits where X^2_{T} does not reach a minimum with respect to all parameters are marked as red. (b)-(e) Best fit values with $\pm 1\sigma$ uncertainties (gray rectangles) are shown, along with the converged parameter values. Parameters that minimize the X^2_{T} are shown with black markers, and those that do not are red.

calculating by Eqn. (5.40). The effective free-carrier density, N, is estimated using Eqns. (E.33) and (E.40) as,

$$N = \frac{2}{\tau_m^{\mathrm{FCA}} \sigma^{\mathrm{FCA}} v_{\mathrm{g}}} = \frac{2\kappa_0 \kappa_{m,m,m} U^2_{m,i}}{\sigma^{\mathrm{FCA}} v_{\mathrm{g}}} \tag{5.50}$$

Figure 5.20 shows a plot of the resulting $\tau_{\mathrm{carrier}}(N)$ for the M1 data (circles) and M2 data (triangles) of Devices 1 to 4. The best fit τ_{carrier}'s are drawn as dashed lines. The effective free-carrier lifetime appears to be relatively constant over almost all carrier densities. Deviations of the calculated carrier lifetimes from the best fit carrier lifetimes increase for densities $N \lesssim 2.0 \times 10^{16}$ cm^{-3}, and τ_{carrier} for $N \gtrsim 2.0 \times 10^{16}$ cm^{-3} appear to be saturated. In the analysis for Device 2, the fitting data included the right-most (highest power) four data points for M1 and the right-most six data points for M2, which appear to be consistent with a saturated τ_{carrier}.

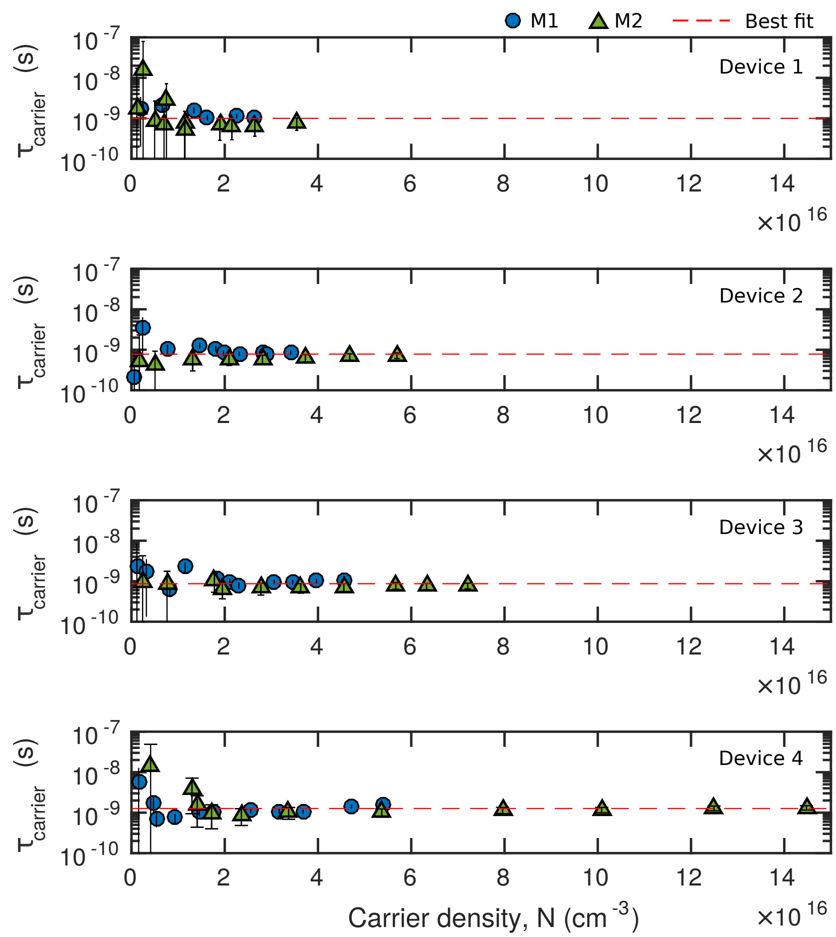

Figure 5.20: Effective free-carrier lifetime calculated for both M1 (circles) and M2 (triangles) of Devices 1 to 4 (top to bottom). The best fit τ_{carrier} are drawn as dashed lines.

Roles of $\phi_{\text{in}}, \phi_{\text{out}}, Q_{\text{abs}}$ and τ_{carrier} in the FWM analysis

As described above ϕ_{in} and ϕ_{out} are not included as free parameters in the FWM analysis, despite the dependence of the experimental idler powers on these parameters. Much like the nonlinear transmission analysis, these two parameters do not play a crucial role in determining the topography of X^2_{FWM}, thus these parameters are held fixed to limit the computational time required to complete the analysis. For example, the best fit parameters were found to vary insignificantly when the ϕ_{in} value for Device 2 was shifted by π, and the analysis was repeated. The Q_{abs} parameter is also held fixed in the FWM least-squares analysis. This is appropriate as this idler powers do not directly depend on this parameter, given that thermal shifts are ignored. The only impact that it has is on limiting the range of possible η_m^{wg} that give positive (physical) τ_{scatt} by Eqn. (5.36).

The free-carrier lifetime τ_{carrier} is also held fixed in this analysis. This parameter is not generally expected to play a significant role in determining the true X^2_{FWM} topography (when included as a free parameter) because the majority of FWM measurements are taken in the low power regime (due to technical challenges of performing FWM measurements in the bistable limit), where nonlinear absorption plays only a small role in determining the idler power, as compared to the waveguide coupling ratios η_m^{wg}. In addition, for the low power measurements, the effective free-carrier lifetime is not in the saturated limit, and is power-dependent, thus τ_{carrier} is not a reliable fit parameter for this analysis. The current analysis scheme is a compromise, where τ_{carrier} is held fixed at the saturated value found from the nonlinear transmission analysis. This results in an underestimate of τ_{carrier} at low powers, which has the potential to push the best fit η_2^{wg} to slightly lower values, however the minimization of X^2_{tot} with respect to τ_{carrier} is expected to be dominated by X^2_{T}, thus this effect is expected to be very small.

Chapter 6

Discussion

In this chapter, the nonlinear performance and nonlinear characterization results for the triple microcavity devices are discussed.

6.1 Triple microcavity performance

6.1.1 Four-wave mixing efficiency

The four-wave mixing results presented in Chapter 5 demonstrate that the triple microcavity structure has potential to be considered for frequency conversion applications. A common metric used to quantify the frequency conversion performance is the FWM idler power efficiency, $\eta^{\mathrm{P}}_{\mathrm{FWM}} = P_{\mathrm{i}}/(P_{\mathrm{p}}^2 P_{\mathrm{s}})$, where P_{i}, P_{p} and P_{s} are the idler, pump and signal powers in the input waveguide. Here $\eta^{\mathrm{P}}_{\mathrm{FWM}}$ is reported in units of $\mu\mathrm{W}^{-2}$. When evaluated in the linear regime, the efficiency predicts the idler power for a given pump and signal power. Devices with higher $\eta^{\mathrm{P}}_{\mathrm{FWM}}$ are favorable for most applications, as lower input powers are required to achieve the same idler power. An alternative definition for four-wave mixing efficiency is sometimes given as $\eta^{\mathrm{sig}}_{\mathrm{FWM}} = P_{\mathrm{i}}/P_{\mathrm{s}}$, which is a unitless parameter that describes the conversion of signal photons to idler photons. This metric requires knowledge of the pump power to put it in context. Due to this lack of generality, the choice is made to report $\eta^{\mathrm{P}}_{\mathrm{FWM}}$ instead of $\eta^{\mathrm{sig}}_{\mathrm{FWM}}$ in the following.

The experimental four-wave mixing idler power efficiencies are plotted in Fig. 6.1 for Devices 1 to 4. Data is shown for idler photon generation in M1 (blue) and M3 (red), measured as a function of the pump power (triangles) for fixed signal power at P_{s} (labelled on the plots), and as a function of signal power (circles) for fixed pump power at P_{p} (also labelled). The efficiencies predicted based on the model function, with the best fit parameters from the least-squares analysis with fixed average value $R_{\mathrm{th}}, \tau_{\mathrm{carrier}}$ and Q_{abs}, are also plotted as thick solid and dash-dotted black lines

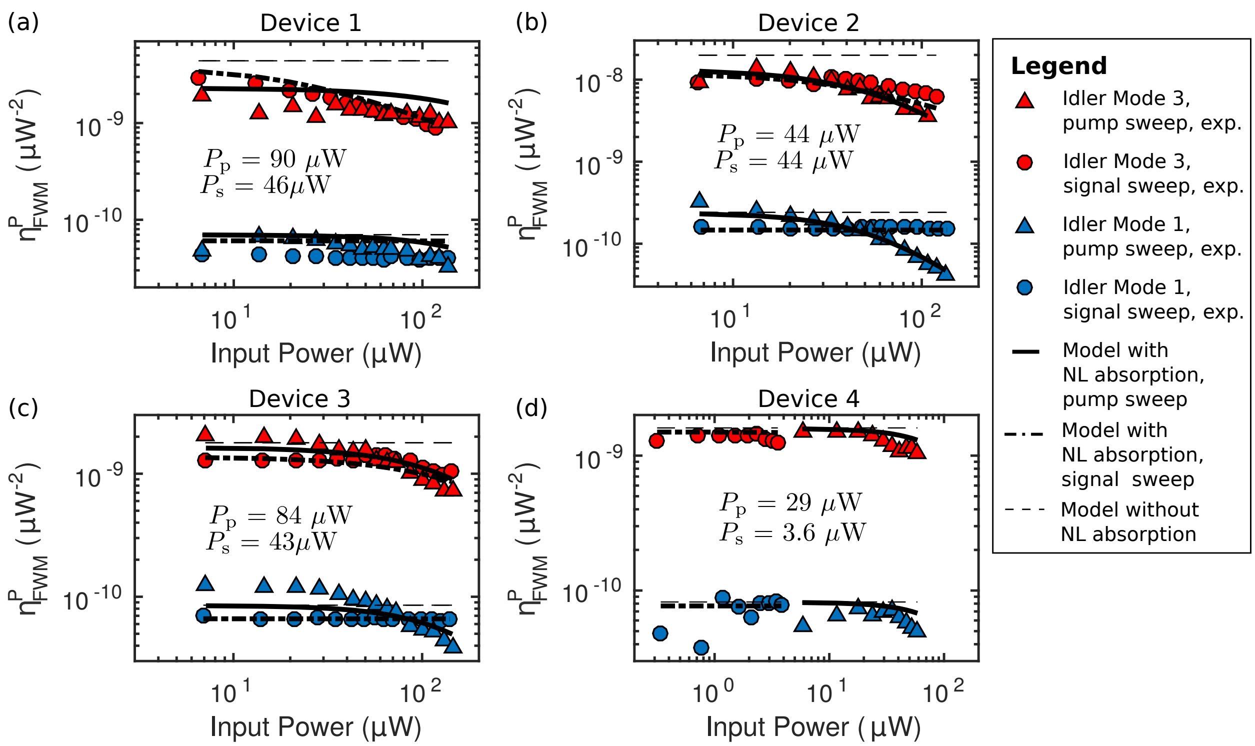

Figure 6.1: Four-wave mixing efficiency $\eta^{\mathrm{P}}_{\mathrm{FWM}} = P_{\mathrm{i}}/(P_{\mathrm{p}}^2 P_{\mathrm{s}})$ for (a) Device 1, (b) Device 2, (c) Device 3 and (d) Device 4. The experimental FWM idler powers for idler photons in Mode 1 and Mode 3 are plotted as a function of pump power (triangles) when the signal power is fixed at P_{s} (labelled) and signal power (circles) when the pump power is fixed at P_{p} (labelled). The idler powers predicted using the model function with best fit parameters found from the least-squares analysis when $R_{\mathrm{th}}, Q_{\mathrm{abs}}$ and τ_{carrier} are held fixed at their average values are shown with thick solid and dashed-dotted black lines for the pump and signal sweeps. The dashed lines show the predicted power when nonlinear absorption is ignored.

for the pump and signal dependences, respectively. Also shown is the model function prediction for the efficiency when nonlinear absorption is disabled (thin dashed line). For the majority of data sets, the efficiency decreases as a function of power, due to nonlinear absorption effects. For a given idler mode, the efficiencies of the two data sets (pump and signal power sweeps) do not necessarily return to the same value at low powers. This is because the fixed power for these sweeps is in some cases large enough to induce nonlinear absorption, and as a result, the data set is entirely taken in a nonlinear absorption regime.

The highest experimental four-wave mixing efficiencies for the data sets shown in Fig. 6.1 are summarized and compared to those in the literature in Table 6.1. The $\eta^{\mathrm{P}}_{\mathrm{FWM}}$ efficiencies for the M3 idler mode data are $1.4 - 14 \times 10^{-9}\ \mu\mathrm{W}^{-2}$, while those for the M1 idler mode data are substantially lower, $6.8 \times 10^{-11} - 3.2 \times 10^{-10}\ \mu\mathrm{W}^{-2}$. This large difference is qualitatively explained by considering, that in the linear regime, $\eta_{\mathrm{FWM}}^{\mathrm{P}} \propto (Q_{\mathrm{p}}^{\mathrm{tot}})^4 (Q_{\mathrm{s}}^{\mathrm{tot}})^2 (Q_{\mathrm{i}}^{\mathrm{tot}})^2 / [(Q_{\mathrm{p}}^{\mathrm{in}})^2 Q_{\mathrm{s}}^{\mathrm{in}} Q_{\mathrm{i}}^{\mathrm{out}}]$ for equally spaced modes, as is found from Eqn. (5.42), where "p", "s" and "i" subscripts are for the pump, signal and idler modes. While the total quality factors and $Q_{\mathrm{p}}^{\mathrm{in}}$ are the same for both of the pumping configurations, $Q_{\mathrm{s}}^{\mathrm{in}}$ and $Q_{\mathrm{i}}^{\mathrm{out}}$ are different. The efficiency is much higher when M3 is the idler mode because Q_3^{out} is over two orders of magnitudes smaller than Q_1^{out}, while Q_3^{in} is approximately an order magnitude smaller than Q_1^{in}.

As shown in Table 6.1, the highest measured FWM efficiency, 1.4×10^{-8} μW^{-2} (Device 2 with M3 as the idler mode) is an order of magnitude higher, or more, than the efficiencies found for a triple nanobeam cavity [8], a triple microring resonator [109], a coupled travelling wave resonator [5] and microrings with radii $R = 5$ μm [7] and $R = 10$ μm [92]. The triple nanobeam structure's efficiency is likely lower as it supports modes with lower total Q's than the 2D PC triple cavity presented in this work. While the triple microring resonator, the coupled travelling wave resonator and the $R = 10$ μm microring resonator support three high Q modes, the mode volumes are relatively large, which results in weaker nonlinear interactions. The microring with radius $R = 5$ μm has an even smaller conversion efficiency, despite the smaller mode volume, due to its relatively low Q caused by the TIR condition on the tight waveguide bend. An additional PC structure, with 10 coupled microcavities, is also included in Table 6.1 [55], which is made in Gallium Indium Phosphide (GaInP), and has a very high $\eta_{\mathrm{FWM}}^{\mathrm{P}} = 3 \times 10^{-6}$ μW^{-2}, owing to the small mode volume, high Q's and the Kerr coefficient, n_2, that is nearly twice as large as that for silicon.

6.1.2 Kerr effect input power threshold

The nonlinear transmission spectra presented in Chapter 5 for modes M1 and M2 of the triple microcavity demonstrate that the Kerr effect is significant when probed at sufficiently high power. The minimum power at which the Kerr effect is strong enough for a structure to be considered for all-optical processing applications, like all-optical switching, is called the power threshold, P_{th} [63]. This figure-of-merit coincides with the minimum power where bistable behaviour is observed. Microcavities with lower P_{th}, can operate more efficiently, and are better candidates for scalable integration. In general, a low P_{th} is achieved by microcavities with high Q, low mode volumes [46], V_{eff}, and high efficiency loading of light into the microcavity. High thermal resistances and effective

Table 6.1: Four-wave mixing idler power efficiency, $\eta^{\mathrm{P}}_{\mathrm{FWM}} = P_{\mathrm{i}}/(P_{\mathrm{p}}^2 P_{\mathrm{s}})$. For the devices in this work, the η^{P}_{FWM} listed are reported for the maximum experimental FWM with M3 as the signal mode (first), then M1 as the signal mode (second). The mode quality factors for each structure is also given. When the Q's of the three modes are approximately equal, a single Q is reported. For the first and third structures reported, the Q's are listed in order of signal, pump then idler. For the devices in this thesis, the Q's are listed in the order of M1, M2 and M3. Estimates of the device areas are also provided. The structures are made in silicon, unless noted by ‡.

Structure	$\eta^{\mathrm{P}}_{\mathrm{FWM}}$ (μW^{-2})	Q	Device area (μm^2)	Source
Triple nanobeam cavity	1.2×10^{-9}	3×10^3 4×10^3 6×10^3	10	[8]
Triple microring resonator	8×10^{-10}	$\sim 5 \times 10^4$	200	[109]
Coupled travelling wave resonator	2.2×10^{-11}	$\sim 1 \times 10^{4\dagger}$	130	[5]
Microring resonator ($R = 10\mu$m)	7.8×10^{-10}	2.3×10^4	310	[92]
Microring resonator ($R = 5\mu$m)	1.2×10^{-10}	7.9×10^3	80	[7]
Coupled PC microcavities‡	3×10^{-6}	2.4×10^4 8.3×10^4 1.4×10^5	150	[55]
Triple microcavity, Device 1	$2.9 \times 10^{-9}, 6.8 \times 10^{-11}$	1.6×10^5 2.6×10^4 3.0×10^3	50	This work
Triple microcavity, Device 2	$1.4 \times 10^{-8}, 3.2 \times 10^{-10}$	1.5×10^5 4.8×10^4 1.2×10^3	50	This work
Triple microcavity, Device 3	$2 \times 10^{-9}, 1.2 \times 10^{-10}$	9.7×10^4 3.5×10^4 2.8×10^3	50	This work
Triple microcavity, Device 4	$1.4 \times 10^{-9}, 8 \times 10^{-11}$	1.5×10^5 2.9×10^4 1.4×10^3	50	This work

† Estimated from spectrum.

‡ Made in a suspended Gallium Indium Phosphide membrane.

free-carrier lifetimes also lead to low P_{th}, but typically result in a trade-off with the switching speed. The resonant wavelength shifts observed for the triple microcavities studied in this thesis are dominated by thermal effects, where the primary source of power absorption comes from free-carrier absorption, as is illustrated in Fig. 5.7. The P_{th} for these devices are compared to those in the literature in Table 6.2.

The P_{th} for the triple microcavities entries in Table 6.2 are estimated by looking for the sharp drop in the nonlinear transmission spectra, which is a signature of the bistable regime. Here P_{th} is taken to be the input power for the first (lowest power) spectrum where bistable features appear, and is found separately for M1 and M2. The triple microcavity P_{th} ranges from $17-172$ μW, which is in range of the P_{th} reported for other suspended silicon 2D PC microcavities in the literature. The total quality factors and effective mode volumes (estimated from simulations) are also given, as these both play important roles in the nonlinear interactions that give rise to the bistable state. For the 2D PC microcavities, differences in P_{th} for modes with similar Q's and mode volumes are likely attributed to differences in the coupling efficiencies of light into the cavities, as the thermal resistance and effective free-carrier lifetimes are likely to be similar. In the case of the 1D PC nanocavity, the P_{th} is significantly lower, due to its higher thermal resistance.

6.2 Best fit parameters

The model functions resulting from the analysis procedure generally do a good job of simultaneously describing the linear and nonlinear functionalities measured in this thesis. One way to assess whether the parameters extracted from the analysis procedure are reasonable (physically sensible), is to compare them to those reported in the literature, for comparable photonic structures in silicon. These comparisons can be made for R_{th}, τ_{carrier} and Q_{abs}, as they are generally consistent for structures with similar geometries and mode profiles (surface to volume ratios).

6.2.1 Thermal resistance R_{th}

The average best fit thermal resistance found in this work is $R_{\mathrm{th}} = 40 \pm 0.4$ K/mW. This compares well with other R_{th} reported in the literature for similar suspended 2D planar photonic crystal

Table 6.2: Estimates of threshold input power, P_{th}, required to excite a bistable response of the microcavity. The threshold power is measured relative to the input 2D photonic crystal waveguide, unless noted by ‡. The quality factor, Q, effective mode volume, V_{eff}, and thermal resistance, R_{th}, of the bistable mode are also given. The P_{th} and Q's reported for the devices in this work are listed for M1, then M2.

Structure	P_{th} (μW)	Q	V_{eff} $(\lambda/n)^3$	R_{th} (K/mW)	Source
2D PC microcavity	200	3.8×10^4	0.9	$15 - 35$	[11, 84]
2D PC microcavity	40	3.3×10^5	1.1		[63]
2D PC microcavity	$10 - 28^{\dagger}$	2.3×10^5	1.2	50	[94]
1D PC nanocavity	$1.6^{\ddagger}$	2.5×10^5	1.4	550	[31]
Triple microcavity Device 1	17, 172	$1.6 \times 10^5, 2.6 \times 10^4$	1.7, 2.1	40.5	This work
Triple microcavity Device 2	34, 33	$1.5 \times 10^5, 4.8 \times 10^4$	1.6, 2.1	40.5	This work
Triple microcavity Device 3	105, 102	$9.7 \times 10^4, 3.5 \times 10^4$	1.7, 2.1	40.5	This work
Triple microcavity Device 4	93, 150	$1.5 \times 10^5, 2.9 \times 10^4$	1.7, 2.1	40.5	This work

† Estimated from spectra.

‡ P_{th} is relative to the channel waveguide.

structures in silicon, where $R_{\text{th}} \simeq 16 - 50$ K/mW [4, 11, 30, 31, 75], as is summarized in Table 6.3. The thermal resistance describes how easily heat is transfered from the microcavity to the surrounding environment, and is found to be reduced when the buried oxide layer beneath the silicon is left intact, due to the difference in the relative thermal conductivities of air and SiO_2 (SiO_2: 1.05 K/mW, air: 0.026 W/mK, silicon: 149 K/mW) [65]. The suspended 2D PC thermal resistances are lower than those estimated for 1D PC stack and ladder microcavities, 250 K/mW and 550 K/mW respectively [31]. The 1D PC stack microcavity consists of isolated boxes of silicon (1.45 μm $\times$0.18 μm $\times$200 nm) that sit on SiO_2, such that a significant amount of heat diffuses through the oxide. In contrast, the ladder microcavity is a 1D nanobeam microcavity that is bridged in air, such that heat primarily diffuses through the silicon contact points at the ends of the nanobeam. In both of these examples, the thermal resistance is high because heat diffuses primarily in one direction, unlike the 2D PC microcavity, where it diffuses over the planar slab. For similar reasons, a microdisk resonator ($R = 1.16$ μm) supported by an oxide pedestal, surrounded by a sunflower-type circular PC, is found to have a high thermal resistance, $R_{\mathrm{th}} = 530$ K/mW, due to the limited directionality of diffusion [88]. Devices with large thermal resistances have low thermo-optic bistable switching powers, however, this comes at the cost of lower switching speeds (which are typically limited by thermal effects), as it takes longer for heat to diffuse.

Table 6.3: Thermal resistance, R_{th} reported for suspended photonic crystal (PC) structures. It is noted whether the value was found experimentally or from modelling.

Structure	R_{th} (K/mW)	Method	Source
PC microcavity	15-35	Exp.	[11]
PC microcavity with metallic pads	16.8	Modelling	[30]
PC microcavity	20	Modelling	[31]
PC microcavity	$50^{\dagger}$	Exp.	[4]
PC waveguide	18.5	Exp.	[75]
Triple PC microcavity	40.5	Exp.	This work

†Used as a model parameter in Refs. [94, 111], and good agreement is found with the respective experimental data presented.

6.2.2 Saturated free-carrier lifetime τ_{carrier}

The average best fit saturated effective free-carrier lifetime is 0.92±0.02 ns. This compares well with other reports in the literature for suspended PC photonic crystal cavities, where $\tau_{\mathrm{carrier}} \simeq 0.5 - 1.8$ ns [11, 95, 105], as is summarized in Table 6.4. The effective free-carrier lifetime is expected to be dominated by recombination at surfaces, and is sensitive to the surface conditions [89, 95]. The free-carrier lifetime for an unsuspended 2D PC microcavity, lying on the burried oxide is found to be 0.12 ns [65]. These lifetimes can be compared to the lifetimes for bulk silicon ($\sim 1 - 10$ μs [66]), submicron waveguides (1 ns [66]), and a microring resonator (~ 0.5 ns [2]).

The saturation characteristics of the effective free-carrier lifetime are plotted in Fig. 5.20. The lifetime appears to be relatively constant for carrier densities $N > 2{\times}10^{16}$ cm^{-3}. Below $N \simeq 2{\times}10^{16}$ cm^{-3}, the scatter of the calculated lifetimes from the best fit values increases. The uncertainties also increase, as the free-carrier lifetime plays a relatively small role at low carrier densities, thus it is more difficult to extract from fits accurately. There appears to be a general trend of τ_{carrier} increasing for low densities, where the highest τ_{carrier} are roughly an order of magnitude larger than the saturated value (with the exception of Device 2, where the scatter is fairly evenly distributed). This is in comparison to other studies of the free-carrier lifetime that show an increase of 1-2 orders of magnitude, for densities $N < 1 \times 10^{16}$ cm^{-3}, such that the lifetime is saturated for $N \gtrsim 1 \times 10^{16}$ cm^{-3} [11, 50].

Table 6.4: Effective free-carrier lifetimes, τ_{carrier} reported based on experimental findings for suspended photonic crystal (PC) structures.

Structure	τ_{carrier} (ns)	Source
PC microcavity	$0.5^{\dagger}$	[11]
PC microcavity	0.5	[105]
PC microcavity	1.4-1.8	[95]
Triple PC microcavity	0.92	This work

†Used as a model parameter in Refs. [94, 111], and good agreement is found with the respective experimental data presented.

6.2.3 Linear absorption quality factor Q_{abs}

The average best fit linear material absorption quality factor was found to be $Q_{\mathrm{abs}} = 1.26 \pm 0.04 \times 10^6$, however the X_{T}^2 doesn't generally change significantly when it is increased, which implies that the linear material absorption plays a relatively small role compared to the TPA and FCA absorption in the measurements reported here. In the literature, the absorption quality factor has been estimated to be $Q_{\mathrm{abs}} \sim 4 \times 10^4 - 2.7 \times 10^5$ [11, 13] and $Q_{\mathrm{abs}} \simeq 1.4 \times 10^6$ [40, 106, 111]. In a number of different studies Q_{abs} is not included in optical bistability analyses likely due to its small role relative to other effects [88, 94, 105].

6.2.4 Waveguide coupling efficiencies

The waveguide coupling quality factors extracted from the least-squares analysis, performed with the fixed averaged $R_{\mathrm{th}}, \tau_{\mathrm{carrier}}$ and Q_{abs} values, are compared to those found from FDTD simulations of the microcavity structures. The waveguide quality factors Q_{in} and Q_{out} are calculated using the best fit waveguide coupling efficiencies, η_m^{wg}, and Eqns. (5.34) and (5.35). These are plotted, along with the total Q's (labelled Q_{tot}), in Figs. 6.2(a), (b) and (c) for modes M1, M2, and M3, respectively. Closed and open markers are used for the nonlinear characterization (NLC) and simulated results, respectively. Similar trends are found from device to device. Generally, there is reasonably good agreement between the NLC and simulated input coupling Q_{in} values. However, there is very poor agreement in the output coupling Q_{out} values for M1 and M2, while the M3 values agree reasonably well.

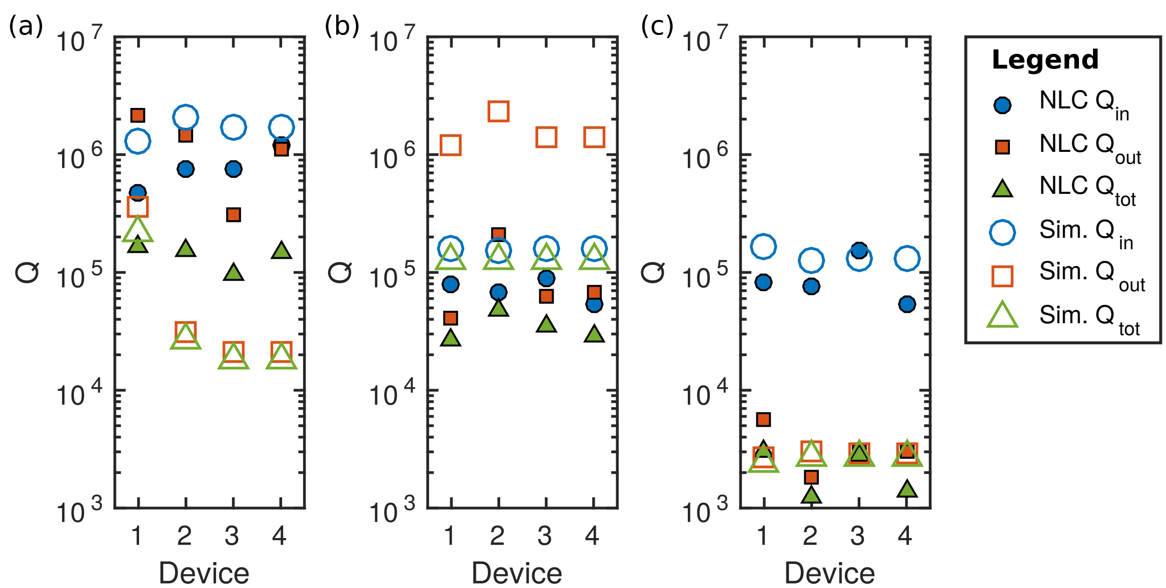

Figure 6.2: Quality factors for Devices 1 to 4, found by the nonlinear characterization (NLC) performed with the average values for $R_{\mathrm{th}}, \tau_{\mathrm{carrier}}$ and Q_{abs}, and by simulations, are plotted for modes (a) M1, (b) M2, and (c) M3. The total quality factor Q_{tot}, the input waveguide quality factor, Q_{in} and the output waveguide quality factor Q_{out} are all plotted, as is summarized in the legend.

To gain insight on the variable agreement in the NLC and simulated Q_{in} and Q_{out}, the $Re(E_y)$ field profiles for modes M1, M2 and M3 of the triple microcavity in the absence of waveguides are plotted in Figs. 6.3(a),(b) and (c), respectively. The waveguide coupling strengths depend on the field overlaps between the cavity modes and the waveguide mode. For M2, there is essentially no field in the center defect, and the uppermost and lowermost defects localize fields with opposite parity, such that the mode is anti-symmetric, and coupling to the output waveguide mode (symmetric about $y = 0$) is suppressed. The simulated coupling strength isn't perfectly zero because the

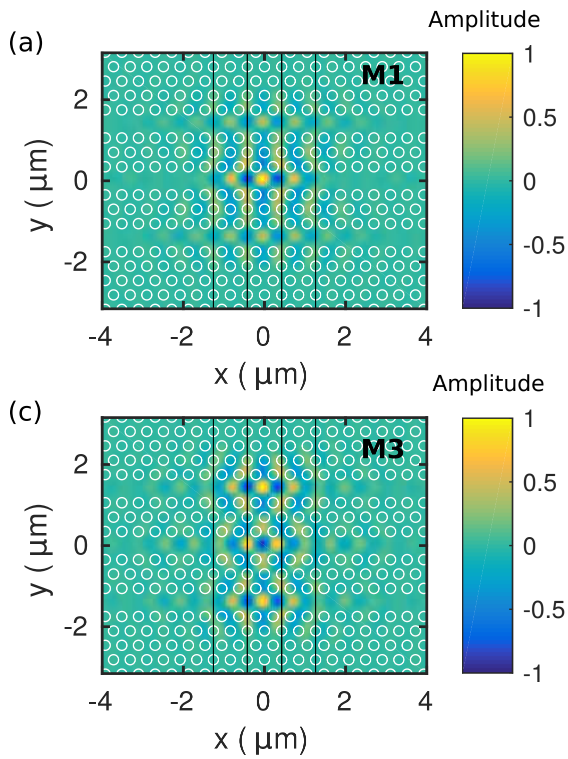

Figure 6.3: Mode field profiles for heterostructure photonic crystal (PC) microcavities. Electric field $\mathrm{Re}(E_y)$ mode profiles in the center plane of the silicon are plotted for modes (a) M1, (b) M2 and (c) M3 of a triple microcavity, in the absence of input and output waveguides. The heterostructure boundaries are shown with black lines and the PC holes are outlined in white.

diagonal input waveguide weakly breaks the symmetry of the mode. This suggests that Q_{out} for M2 is likely sensitive to fabrication imperfections that further break the mode symmetry, and might explain why the experimental Q_{out} are significantly lower than the simulated values.

The coupling of M1 to the output waveguide is likely also sensitive to fabrication imperfections, as the field localized to the outer defects destructively interferes with the field localized to the center defect, where the fields extend into the output waveguide region. The experimental Q_{out} are higher than those simulated, which suggests that the fabricated devices support greater destructive interference. It is interesting to note that the simulated Q_{out} for M1 of Device 1, is an order of magnitude higher than those for Devices 2 to 4. For these three devices, the radius of four holes along the center line defect, opposite the waveguide, are shrunk by scaling factor $s_{\mathrm{wg,sym}} = 0.912$ (see Fig. 3.1), while for Device 1 they are not shrunk ($s_{\mathrm{wg,sym}} = 1$). It is unclear why there is a significant difference in the Q_{out}, as inspection of the simulated mode profiles does not reveal significantly different relative weightings of the field concentrations in the outer and inner defects. However, this further supports the hypothesis that Q_{out} for M1 is very sensitive to perturbations in the structure.

In contrast, for M3, the field parity in the outer defects is opposite to the center defect such that constructive interference happens in the output waveguide, rendering this mode less sensitive to fabrication imperfections. This is consistent with the good agreement found between experimental and simulated Q_{out} for M3.

The input waveguide mode primarily overlaps with the fields localized to the lowermost defect. This coupling scheme is not particularly sensitive to the mode symmetries, and thus is consistent with relatively good agreement between experiment and simulation for Q_{in}.

6.3 Novelty of the nonlinear characterization procedure

In the nonlinear characterization method presented here, the 15 unknown microcavity parameters, and the two Fabry-Perot parameters, are extracted for each of the four devices by analyzing a combination of results from linear transmission, nonlinear transmission and four-wave mixing measurements. This characterization procedure was generally successful, despite the relative complexity of the analysis, and technical challenges associated with the nonlinear measurements of the triple microcavity devices. For three of the four devices studied here (Device 2 to 4), the X^2 was well minimized across the parameters of interest, with the minimum X^2_{tot} per degree of freedom $\lesssim 10$, and the best fit results agreed well with those in the literature. The analysis of Device 1 was less successful, where X^2 was not minimized as a function of the key microcavity parameter η_2^{wg}, within the range of possible values. While the source of this issue is unclear, the nonlinear transmission and four-wave mixing physics is still reasonably well captured using the average parameter results. As discussed above, the $R_{\text{th}}, \tau_{\text{carrier}}$ and Q_{abs} parameters extracted agree well with those in the literature.

The method used here to extract the parameters is unique from those presented in the literature for a number of reasons. To the best of our knowledge, this is the first characterization presented for the linear and nonlinear parameters of a coupled-cavity device with distinct, independent input *and* output waveguides. The closest microcavity characterization reported is for one mode of a 2D PC microcavity coupled to just one PC waveguide [11], which was completed using only linear and nonlinear reflection data. The use of only reflection data in Ref. [11] was possible because when a microcavity is coupled to a single waveguide, there is one less unknown parameter and the waveguide coupling efficiency is extracted directly from the linear reflection data (or transmission data for side-coupled geometries). With the waveguide coupling lifetime as a known parameter, the nonlinear transmission X^2_{T} analysis for a single mode is much better minimized as a function of the rest of the microcavity parameters, and supplementary data and analysis is not required to extract the best fit values.

In other reports in the literature, experiments are designed to characterize a single nonlinear parameter, for example either R_{th} [4, 30, 88] or τ_{carrier} [2, 65, 95, 105], but not all parameters simultaneously. In some studies, previously published nonlinear parameters are used to populate model functions that are compared to experimental data, in efforts to qualitatively seek consistencies in the nonlinear behaviour [94, 111].

As described above, four-wave mixing measurements are not typically used to directly characterize the linear and nonlinear parameters, because when the waveguide coupling efficiencies are known for linear measurements, the four-wave mixing analysis is not required to complete the analysis. However, stimulated and spontaneous four-wave mixing measurements commonly observe nonlinear absorption effects, where the results are often studied in the context of how these effects degrade the device performance [34, 35], as opposed to as a characterization tool.

Chapter 7

Conclusion

A triple photonic crystal microcavity device with independent input and output waveguides was designed, externally fabricated, and its linear and nonlinear responses were thoroughly characterized and modelled. The experimental results demonstrate that this structure offers nonlinear functionality at least on par with, and in some cases better than, other integrated nonlinear optical devices structures. The four-wave mixing is potentially relevant in all-optical processing, including wavelength conversion [25] and signal generation [92]. The bistable behaviour has potential relevance to all-optical switching [63] and all-optical memories [62]. More generally, the triple microcavity device may be considered for other applications that require strong light-matter interactions, like cavity quantum-electrodynamics (cQED), owing to the high Q modes and small mode volumes [96].

The best device studied in this work exhibits a four-wave mixing conversion efficiency that is over an order of magnitude higher than microring based structures [6, 7, 92, 109], owing to the smaller mode volumes. The top efficiency measured here is also 10 times higher than that of the triple nanobeam cavity in Ref. [8]. The 2D PC triple microcavity from this work has greater potential for reaching high Q's than the nanobeam (and consequently high conversion efficiencies) in future iterations, as this structure can be suspended, while the nanobeam structure requires an oxide layer below the silicon. There is also greater flexibility in terms of waveguide coupling thanks to the 2D PC structure. One benefit of the current design is that it provides a good compromise between achieving high Q's for high efficiency conversion, while maintaining one lower Q mode with a large enough linewidth that the requirement for equally spaced modes is relaxed. As a result, the fabrication yield for "good" FWM candidates (FWM frequency within a linewidth of the low Q mode resonance frequency) is fairly high, as most groups of 7 devices over which the mode spacing is bracketed have at least one good FWM candidate, as shown in Fig. 4.3. Given that the good candidates fairly consistently fall close to the center of the bracket, the bracket range could arguably be reduced, therefore increasing the yield. In contrast, for the triple microring structure supporting only high Q modes, microheaters are required to tune resonant frequencies [109].

The inclusion of both input and output waveguides makes it possible to use relatively straightforward measurement techniques, as compared to many related devices reported in the literature. In some cases, the dual-waveguide coupling also makes the device more eligible for scalable integration. For example, the FWM coupled PC cavity structure in Ref. [55] has a single end-coupled waveguide, such that a free-space circulator is required to deal with the input and output light exchanged with the waveguide. For the bistability measurements presented in [11], a technically challenging fibre taper coupling scheme is used to manage excitation of, and collection from, a single PC waveguide end-coupled to the microcavity. Other microcavity structures implement a single side-coupled waveguide, such that non-resonant light is transmitted and resonant light is reflected [111], however this coupling scheme has limited design flexibility as the input and output coupling rates are the same.

For applications where two modes of a microcavity are used for bistable switching, the triple microcavity with independent input and output coupling has some potential advantages over single 2D PC cavity devices [63]. In this application, a strongly modulated pump excitation is tuned to the control mode resonant wavelength, and a weak unmodulated probe excitation is tuned near the probe mode. Excitation of the control mode induces nonlinear effects in the microcavity, that in turn shift the resonant wavelength of the probe mode, and cause modulations in the transmission of probe light. Ideally, the pump mode is efficiently loaded with energy, while the probe mode is efficiently transmitted. Not only does the triple microcavity support two high Q modes with low mode volumes, the mode profiles are spatially distinct across the three defects, which makes it possible to engineer unique waveguide coupling for the two modes. This is in contrast to the single 2D PC microcavity geometry, where the modes are roughly localized to the same defect region, making it more difficult to customize coupling. Devices 1 and 2 are potentially good candidates for this application as M1 has a high Q ($> 1 \times 10^4$) low bistability power threshold, which is good for the control mode, while M2 has a relatively high "cold" transmission, > 0.6 (in the absence of nonlinear loss), as well as a high Q ($> 1 \times 10^4$), which is good for the probe mode.

There are however some disadvantages of working with this triple microcavity structure. The primary disadvantage is that the waveguide coupling strengths to the output waveguide for M1 and M2 are critically dependent on symmetries in the mode profiles, and as a result are sensitive to fabrication imperfections. This means that reproducibility is poor, as two devices with the same layout (like Devices 3 and 4 in this study), can have significantly different *actual* coupling strengths to the output waveguide (for example M1 in Fig. 6.2). It also means that there are large deviations from the simulation results, which make it difficult to engineer the waveguide coupling. In recent work, where 2D PC triple microcavities are proposed for frequency conversion applications, using structures that involve nontrivial coupling geometries, Monte Carlo simulations are used to model fabrication imperfections [58]. While this may make it possible to plan for the worst, there are likely to be unavoidable trade-offs between device performance and fabrication yield.

With respect to four-wave mixing applications, the other main disadvantage of this structure is that it promotes strong nonlinear absorption effects. While these effects make the triple microcavity a good candidate for bistable switching, the same effects put an upper limit on the conversion efficiency, as shown in Fig. 6.1. Given that the free-carrier lifetime is approximately the same for 2D PC structures and microring resonators, the structure itself is not the fundamental issue. The main issue is the large TPA coefficient for silicon, at wavelengths near 1550 nm. A common solution proposed to help resolve this problem is to install p-i-n junctions across the structure and apply a bias to sweep out the carriers [70, 73, 93]. The p-i-n junction is compatible with CMOS fabrication methods such that the proposed devices are still leveraged by the benefits of working with silicon. Alternatively, amorphous hydrogenated silicon, a-Si:H, is also being explored as it exhibits a lower TPA coefficient and a higher Kerr nonlinearity, which both improve the nonlinear behaviour, however these devices are plagued by linear losses that limit their performance [34].

The input and output ports of the microcavity devices also proved to be problematic due to the relatively high reflections between components, that caused sinusoidal modulations in the transmitted intensity, which in turn complicated the analysis process. These effects can be avoided using alternative coupling schemes, for example, low reflection parabolic grating couplers [1] that focus light into the 500 nm wide channel waveguide over a relatively short distance of ~ 20 μm, instead of 150 μm (parabolic waveguide length used in this work), such that the Fabry-Perot modulation is minimized, free-spectral range is longer, and the structure response is less sensitive to fabrication imperfections.

Beyond the study of these specific triple microcavity devices, the nonlinear characterization results presented in this thesis are also of potential interest to the nonlinear photonics community in general, as there are currently limited publications citing measurements of R_{th} and τ_{carrier} for microcavity structures. The values reported here are in agreement with those previously reported, further supporting this literature. Additionally, as increasingly complex microcavity structures, variously and non-trivially coupled to waveguides, are designed for applications in classical and quantum photonics [58], sophisticated characterization methods will be required to understand the microcavity physics, increasing the demand for robust characterization methods like that presented here.

7.1 Suggestions for future work

As alluded to above, the basic concept of a triple coupled PC microcavity coupled to independent input and output waveguides does have a number of potential nonlinear optical applications. The work in this thesis suggests the need to explore different types of microcavities and coupling geometries that would retain the good qualities identified in the current design, namely the three spatially overlapping high Q modes with nearly equally spaced resonant frequencies and small mode volumes, but be less sensitive to the fabrication imperfections. As a guide, it would be ideal to avoid using coupled microcavity modes with waveguide coupling strengths that critically depend on mode symmetries with respect to the waveguide axis. The problematic output waveguide coupling geometry presented here was a consequence of the attempt to suppress the pump mode transmission down to $\sim$0.1 in the original design. In hindsight, since approximately 10 orders of magnitude pump suppression is ultimately required for the pump mode transmission, it will have to be accomplished external to the cavity, so this design constraint on the microcavity can easily be lifted going forward. Pump suppression of over 95 dB has been achieved on-chip using Bragg reflectors and ring resonators [32].

was originally designed to suppress the pump mode transmission down to $\sim$0.1, in an effort to reduce the need for external spectral filters around the idler frequencies. However given that approximately 10 orders of magnitude pump suppression is ultimately required for four-wave mixing measurements, even the best-case scenario suppression was hardly worth the fabrication imperfection sensitivity introduced.

From a scientific point of view, further studies of *spontaneous* four-wave mixing in this device would be of great interest to the quantum photonics community. This device was originally designed for applications as a photon pair source, however, this was not ultimately pursued due to unexplained nonlinear behaviour observed, that rendered the device ineligible as a photon pair source. When the microcavity is excited with a single pump laser tuned to M2, one would expect photon pairs to be generated over the same bandwidths (near M1 and M3), where the bandwidth of the joint density of states for this nonlinear interaction is expected to be limited by the narrow M1 bandwidth. Here, photon generation is observed over the entire bandwidths of both the high Q M1 mode and the low Q M3 mode, as can be seen by observing the background spectra (triangles) in Fig. 4.4. Correlation measurements between the photons generated at the signal and idler frequencies were attempted, to study the photon pair statistics (not reported in this thesis), however they failed, possibly due to the large spectral mismatch between the photons generated in the high Q M1 (~ 0.01 nm bandwidth), and the photons generated in M3 (~ 0.5 nm bandwidth), which could only be resolved with a large bandwidth filter (~ 0.17 nm). Even if a narrow (~ 0.01 nm) filter were available to better match the spectral bandwidths of the signal and idler photons in the correlation measurement, the signals would be very weak and it would be unlikely that a correlation signal could be detected above the avalanche single photon detector noise. However, the use of superconducting single photon detectors, which are known to have much lower dark count rates, may make it possible to study these correlations.

It is possible that other types of nonlinear processes contribute to, and even dominate, the background spectrum. For example, silicon photonic crystal microcavity structures have been found to exhibit broadband photoluminescence, covering the wavelength range of interest ($\lambda \sim$ 1500 to 1600 nm), when excited with light above the silicon electronic bandgap (e.g. $\lambda = 532$ nm) [76]. This photoluminescence occurs due to optically active defects that are introduced when the silicon-on-insulator wafer is manufactured. If this is the case, the above-bandgap excitation may arise here due to two-photon absorption, or second and third harmonic generation. These harmonic generation processes have been observed, where the third-order process is found to be a $\chi^{(3)}$ bulk silicon effect, while the second-order process is a $\chi^{(2)}$ surface-related effect occurring at the hole sidewall boundaries [27]. Measurements of the photoluminescence and harmonic generation are required to better understand the background spectrum, and help elucidate the contribution of spontaneous four-wave mixing.

Bibliography

[1] Mohsen K. Akhlaghi, Ellen Schelew, and Jeff F. Young. Waveguide integrated superconducting single-photon detectors implemented as near-perfect absorbers of coherent radiation. *Nature Communications*, 6:8233, September 2015.

[2] Vilson R. Almeida, Carlos A. Barrios, Roberto R. Panepucci, and Michal Lipson. All-optical control of light on a silicon chip. *Nature*, 431(7012):1081–1084, October 2004.

[3] Vilson R. Almeida and Michal Lipson. Optical bistability on a silicon chip. *Opt. Lett.*, 29(20):2387–2389, Oct 2004.

[4] T. Asano, W. Kunishi, M. Nakamura, B. S. Song, and S. Noda. Dynamic wavelength tuning of channel-drop device in two-dimensional photonic crystal slab. *Electronics Letters*, 41(1):37–38, Jan 2005.

[5] A. H. Atabaki and A. Adibi. Demonstration of wavelength conversion in a reconfigurable coupled resonator in silicon. In *IEEE Photonic Society 24th Annual Meeting*, pages 399–400, Oct 2011.

[6] A. H. Atabaki, E. Shah Hosseini, A. A. Eftekhar, S. Yegnanarayanan, and A. Adibi. Optimization of metallic microheaters for high-speed reconfigurable silicon photonics. *Opt. Express*, 18(17):18312–18323, Aug 2010.

[7] Stefano Azzini, Davide Grassani, Matteo Galli, Lucio Claudio Andreani, Marc Sorel, Michael J. Strain, L. G. Helt, J. E. Sipe, Marco Liscidini, and Daniele Bajoni. From classical four-wave mixing to parametric fluorescence in silicon microring resonators. *Opt. Lett.*, 37(18):3807–3809, Sep 2012.

[8] Stefano Azzini, Davide Grassani, Matteo Galli, Dario Gerace, Maddalena Patrini, Marco Liscidini, Philippe Velha, and Daniele Bajoni. Stimulated and spontaneous four-wave mixing in silicon-on-insulator coupled photonic wire nano-cavities. *Appl. Phys. Lett.*, 103(3):031117–, July 2013.

[9] Toshihiko Baba. Slow light in photonic crystals. *Nat Photon*, 2(8):465–473, August 2008.

[10] Luciano Bachmann, Denise Maria Zezell, and Edison Puig Maldonado. Determination of beam width and quality for pulsed lasers using the knife-edge method. *Instrumentation Science & Technology*, 31(1):47–52, 2003.

[11] Paul E. Barclay, Kartik Srinivasan, and Oskar Painter. Nonlinear response of silicon photonic crystal microresonators excited via an integrated waveguide and fiber taper. *Opt. Express*, 13(3):801–820, Feb 2005.

[12] W. Bogaerts, P. Dumon, D. V. Thourhout, D. Taillaert, P. Jaenen, J. Wouters, S. Beckx, V. Wiaux, and R. G. Baets. Compact wavelength-selective functions in silicon-on-insulator photonic wires. *IEEE Journal of Selected Topics in Quantum Electronics*, 12(6):1394–1401, Nov 2006.

[13] Matthew Borselli, Kartik Srinivasan, Paul E. Barclay, and Oskar Painter. Rayleigh scattering, mode coupling, and optical loss in silicon microdisks. *Applied Physics Letters*, 85(17):3693–3695, 2004.

[14] Robert W. Boyd. *Nonlinear Optics, Third Edition*. Academic Press, 3rd edition, 2008.

[15] Sonia Buckley, Kelley Rivoire, and Jelena Vuckovic. Engineered quantum dot single-photon sources. *Reports on Progress in Physics*, 75(12):126503, 2012.

[16] P. N. Butcher and D. Cotter. *The Elements of Nonlinear Optics*. Cambridge University Press, October 1991.

[17] Xiong Chunle, Bell Bryn, and Eggleton Benjamin J. *CMOS-compatible photonic devices for single-photon generation*, volume 5. De Gruyter Open, 2016.

[18] G. Cocorullo and I. Rendina. Thermo-optical modulation at 1.5 mu m in silicon etalon. *Electronics Letters*, 28(1):83–85, Jan 1992.

[19] M.J. Collins, C. Xiong, I.H. Rey, T.D. Vo, J. He, S. Shahnia, C. Reardon, T.F. Krauss, M.J. Steel, A.S. Clark, and B.J. Eggleton. Integrated spatial multiplexing of heralded single-photon sources. *Nat Commun*, 4:–, 2013.

[20] A. R. Cowan and Jeff F. Young. Optical bistability involving photonic crystal microcavities and fano line shapes. *Phys. Rev. E*, 68:046606, Oct 2003.

[21] A. Cutolo, M. Iodice, P. Spirito, and L. Zeni. Silicon electro-optic modulator based on a three terminal device integrated in a low-loss single-mode soi waveguide. *Journal of Lightwave Technology*, 15(3):505–518, Mar 1997.

[22] Christof P. Dietrich, Andrea Fiore, Mark G. Thompson, Martin Kamp, and Sven Hofling. Gaas integrated quantum photonics: Towards compact and multi-functional quantum photonic integrated circuits. *Laser & Photonics Reviews*, 10(6):870–894, 2016.

[23] M. Dinu, F. Quochi, and H. Garcia. Third-order nonlinearities in silicon at telecom wavelengths. *Applied Physics Letters*, 82(18):2954–2956, 2003.

[24] Charles Alden Foell III. *Luminescent properties of Pb-based (PbX) colloidal quantum dots (CQDs) in vacuum, on silicon and integrated with a silicon-on-insulator (SOI) photonic integrated circuit (PIC)*. PhD thesis, University of British Columbia, 2016.

[25] Mark A. Foster, Amy C. Turner, Jay E. Sharping, Bradley S. Schmidt, Michal Lipson, and Alexander L. Gaeta. Broad-band optical parametric gain on a silicon photonic chip. *Nature*, 441(7096):960–963, June 2006.

[26] Hiroshi Fukuda, Koji Yamada, Tetsufumi Shoji, Mitsutoshi Takahashi, Tai Tsuchizawa, Toshifumi Watanabe, Jun ichi Takahashi, and Sei ichi Itabashi. Four-wave mixing in silicon wire waveguides. *Opt. Express*, 13(12):4629–4637, Jun 2005.

[27] Matteo Galli, Dario Gerace, Karl Welna, Thomas F. Krauss, Liam O'Faolain, Giorgio Guizzetti, and Lucio Claudio Andreani. Low-power continuous-wave generation of visible

harmonics in silicon photonic crystal nanocavities. *Opt. Express*, 18(25):26613–26624, Dec 2010.

[28] Nicolas Gisin and Rob Thew. Quantum communication. *Nat Photon*, 1(3):165–171, 2007.

[29] Davide Grassani, Stefano Azzini, Marco Liscidini, Matteo Galli, Michael J. Strain, Marc Sorel, J. E. Sipe, and Daniele Bajoni. Micrometer-scale integrated silicon source of time-energy entangled photons. *Optica*, 2(2):88–94, Feb 2015.

[30] L.-D. Haret, A. Ghrib, X. Checoury, N. Cazier, Z. Han, M. El Kurdi, S. Sauvage, and P. Boucaud. Effective thermal resistance of a photonic crystal microcavity. *Opt. Lett.*, 39(3):458–461, Feb 2014.

[31] Laurent-Daniel Haret, Takasumi Tanabe, Eiichi Kuramochi, and Masaya Notomi. Extremely low power optical bistability in silicon demonstrated using 1d photonic crystal nanocavity. *Opt. Express*, 17(23):21108–21117, Nov 2009.

[32] Nicholas C. Harris, Davide Grassani, Angelica Simbula, Mihir Pant, Matteo Galli, Tom Baehr-Jones, Michael Hochberg, Dirk Englund, Daniele Bajoni, and Christophe Galland. Integrated source of spectrally filtered correlated photons for large-scale quantum photonic systems. *Phys. Rev. X*, 4:041047, Dec 2014.

[33] T. Hashimoto, Y. Nakasuga, Y. Yamada, H. Terui, M. Yanagisawa, Y. Akahori, Y. Tohmori, K. Kato, and Y. Suzuki. Multichip optical hybrid integration technique with planar lightwave circuit platform. *Journal of Lightwave Technology*, 16(7):1249–1258, Jul 1998.

[34] Elizabeth Hemsley, Damien Bonneau, Jason Pelc, Ray Beausoleil, Jeremy L. O'Brien, and Mark G. Thompson. Photon pair generation in hydrogenated amorphous silicon microring resonators. *Scientific Reports*, 6:38908–, December 2016.

[35] Chad A. Husko, Alex S. Clark, Matthew J. Collins, Alfredo De Rossi, Sylvain Combrie, Gaelle Lehoucq, Isabella H. Rey, Thomas F. Krauss, Chunle Xiong, and Benjamin J. Eggleton. Multi-photon absorption limits to heralded single photon sources. *Sci. Rep.*, 3:3087, November 2013.

[36] Shadbolt P. J., Verde M. R., Peruzzo A., Politi A., Laing A., Lobino M., Matthews J. C. F., Thompson M. G., and O'Brien J. L. Generating, manipulating and measuring entanglement and mixture with a reconfigurable photonic circuit. *Nat Photon*, 6(1):45–49, January 2012.

[37] B. Jalali and S. Fathpour. Silicon photonics. *Journal of Lightwave Technology*, 24(12):4600–4615, Dec 2006.

[38] John D. Joannopoulos, Steven G. Johnson, Joshua N. Winn, and Robert D. Meade. *Photonic Crystals: Molding the Flow of Light*. Princeton University Press, 2nd edition, 2008.

[39] Steven G. Johnson, M. Ibanescu, M. A. Skorobogatiy, O. Weisberg, J. D. Joannopoulos, and Y. Fink. Perturbation theory for maxwell's equations with shifting material boundaries. *Phys. Rev. E*, 65:066611, Jun 2002.

[40] Thomas J. Johnson, Matthew Borselli, and Oskar Painter. Self-induced optical modulation of the transmission through a high-q silicon microdisk resonator. *Opt. Express*, 14(2):817–831, Jan 2006.

[41] F Kaiser, A Issautier, L A Ngah, O Danila, H Herrmann, W Sohler, A Martin, and S Tanzilli. High-quality polarization entanglement state preparation and manipulation in standard telecommunication channels. *New Journal of Physics*, 14(8):085015, 2012.

[42] Sokratis Kalliakos, Yarden Brody, Andre Schwagmann, Anthony J. Bennett, Martin B. Ward, David J. P. Ellis, Joanna Skiba-Szymanska, Ian Farrer, Jonathan P. Griffiths, Geb A. C. Jones, David A. Ritchie, and Andrew J. Shields. In-plane emission of indistinguishable photons generated by an integrated quantum emitter. *Applied Physics Letters*, 104(22):221109, 2014.

[43] M. Kawachi. Recent progress in silica-based planar lightwave circuits on silicon. *IEE Proceedings - Optoelectronics*, 143(5):257–262, Oct 1996.

[44] T. J. Kippenberg, R. Holzwarth, and S. A. Diddams. Microresonator-based optical frequency combs. *Science*, 332(6029):555–559, 2011.

[45] E. Knill, R. Laflamme, and G. J. Milburn. A scheme for efficient quantum computation with linear optics. *Nature*, 409(6816):46–52, 2001.

[46] P. T. Kristensen, C. Van Vlack, and S. Hughes. Generalized effective mode volume for leaky optical cavities. *Opt. Lett.*, 37(10):1649–1651, May 2012.

[47] J. Leuthold, C. Koos, and W. Freude. Nonlinear silicon photonics. *Nat Photon*, 4(8):535–544, August 2010.

[48] Zhaohui Li, Ivan Shubin, and Xiang Zhou. Optical interconnects: recent advances and future challenges. *Opt. Express*, 23(3):3717–3720, Feb 2015.

[49] D. Liang and J. E. Bowers. Photonic integration: Si or inp substrates? *Electronics Letters*, 45(12):578–581, June 2009.

[50] T. K. Liang and H. K. Tsang. Role of free carriers from two-photon absorption in raman amplification in silicon-on-insulator waveguides. *Applied Physics Letters*, 84(15):2745–2747, 2004.

[51] Q. Lin, Oskar J. Painter, and Govind P. Agrawal. Nonlinear optical phenomena in silicon waveguides: Modeling and applications. *Opt. Express*, 15(25):16604–16644, Dec 2007.

[52] Zin Lin, Thomas Alcorn, Marko Loncar, Steven G. Johnson, and Alejandro W. Rodriguez. High-efficiency degenerate four-wave mixing in triply resonant nanobeam cavities. *Phys. Rev. A*, 89:053839, May 2014.

[53] M. Loncar, T. Doll, J. Vuckovic, and A. Scherer. Design and fabrication of silicon photonic crystal optical waveguides. *Journal of Lightwave Technology*, 18(10):1402–1411, Oct 2000.

[54] Zeqin Lu, Han Yun, Yun Wang, Zhitian Chen, Fan Zhang, Nicolas A. F. Jaeger, and Lukas Chrostowski. Broadband silicon photonic directional coupler using asymmetric-waveguide based phase control. *Opt. Express*, 23(3):3795–3808, Feb 2015.

[55] Aude Martin, Grégory Moille, Sylvan Combrie, Gaëlle Lehoucq, Thierry Debuisschert, Jin Lian, Sergei Sokolov, Allard Mosk, and Alfredo De Rossi. Triply-resonant continuous wave parametric source with a microwatt pump. In *Conference on Lasers and Electro-Optics*, page FM1A.1. Optical Society of America, 2016.

[56] Nobuyuki Matsuda, Hiroki Takesue, Kaoru Shimizu, Yasuhiro Tokura, Eiichi Kuramochi, and Masaya Notomi. Slow light enhanced correlated photon pair generation in photonic-crystal coupled-resonator optical waveguides. *Opt. Express*, 21(7):8596–8604, Apr 2013.

[57] Jonathan C. F. Matthews, Alberto Politi, StefanovAndre, and Jeremy L. O'Brien. Manipulation of multiphoton entanglement in waveguide quantum circuits. *Nat Photon*, 3(6):346–350, 2009.

[58] Momchil Minkov and Vincenzo Savona. A compact, integrated silicon device for the generation of spectrally filtered, pair-correlated photons. *Journal of Optics*, 18(5):054012, 2016.

[59] Eiji Miyai and Susumu Noda. Structural dependence of coupling between a two-dimensional photonic crystal waveguide and a wire waveguide. *J. Opt. Soc. Am. B*, 21(1):67–72, Jan 2004.

[60] M. Notomi, A. Shinya, K. Nozaki, T. Tanabe, S. Matsuo, E. Kuramochi, T. Sato, H. Taniyama, and H. Sumikura. Low-power nanophotonic devices based on photonic crystals towards dense photonic network on chip. *IET Circuits, Devices Systems*, 5(2):84–93, March 2011.

[61] Masaya Notomi. Manipulating light with strongly modulated photonic crystals. *Reports on Progress in Physics*, 73(9):096501, 2010.

[62] Masaya Notomi, Kengo Nozaki, Akihiko Shinya, Shinji Matsuo, and Eiichi Kuramochi. Toward fj/bit optical communication in a chip. *Optics Communications*, 314:3 – 17, 2014. Energy efficient nanophotonics: Engineered light-matter interaction in sub-wavelength structures.

[63] Masaya Notomi, Akihiko Shinya, Satoshi Mitsugi, Goh Kira, Eiichi Kuramochi, and Takasumi Tanabe. Optical bistable switching action of si high-q photonic-crystal nanocavities. *Opt. Express*, 13(7):2678–2687, Apr 2005.

[64] Jeremy O'Brien, Brian Patton, Masahide Sasaki, and Jelena Vuckovic. Focus on integrated quantum optics. *New Journal of Physics*, 15(3):035016, 2013.

[65] Yuta Ooka, Tomohiro Tetsumoto, Akihiro Fushimi, Wataru Yoshiki, and Takasumi Tanabe.

Cmos compatible high-q photonic crystal nanocavity fabricated with photolithography on silicon photonic platform. *Scientific Reports*, 5:11312–, June 2015.

[66] Özdal Boyraz, Prakash Koonath, Varun Raghunathan, and Bahram Jalali. All optical switching and continuum generation in silicon waveguides. *Opt. Express*, 12(17):4094–4102, Aug 2004.

[67] Edward D. Palik, editor. *Handbook of Optical Constants of Solids*, volume I-III. Academic Press, 1997.

[68] W.H.P Pernice, C. Schuck, O. Minaeva, M. Li, G.N. Goltsman, and H.X. Tang. High-speed and high-efficiency travelling wave single-photon detectors embedded in nanophotonic circuits. *Nat. Commun.*, 3:1325, 2012.

[69] Alberto Politi, Martin J. Cryan, John G. Rarity, Siyuan Yu, and Jeremy L. O'Brien. Silica-on-silicon waveguide quantum circuits. *Science*, 320(5876):646–649, 2008.

[70] Stefan F. Preble, Qianfan Xu, Bradley S. Schmidt, and Michal Lipson. Ultrafast all-optical modulation on a silicon chip. *Opt. Lett.*, 30(21):2891–2893, Nov 2005.

[71] Alejandro Rodriguez, Marin Soljačić, J. D. Joannopoulos, and Steven G. Johnson. $\chi(2)$ and $\chi(3)$ harmonic generation at a critical power in inhomogeneous doubly resonant cavities. *Opt. Express*, 15(12):7303–7318, Jun 2007.

[72] Steven Rogers, Xiyuan Lu, Wei C. Jiang, and Qiang Lin. Twin photon pairs in a high-q silicon microresonator. *Applied Physics Letters*, 107(4):041102, 2015.

[73] Haisheng Rong, Ying-Hao Kuo, Ansheng Liu, Mario Paniccia, and Oded Cohen. High efficiency wavelength conversion of 10 gb/s data in silicon waveguides. *Opt. Express*, 14(3):1182–1188, Feb 2006.

[74] Reza Salem, Mark A. Foster, Amy C. Turner, David F. Geraghty, Michal Lipson, and Alexander L. Gaeta. Signal regeneration using low-power four-wave mixing on silicon chip. *Nat Photon*, 2(1):35–38, January 2008.

[75] Raymond Sarkissian and John O'Brien. Cross two photon absorption in a silicon photonic crystal waveguide fiber taper coupler with a physical junction. *Journal of Applied Physics*, 117(3):033101, 2015.

[76] R. Lo Savio, S. L. Portalupi, D. Gerace, A. Shakoor, T. F. Krauss, L. O'Faolain, L. C. Andreani, and M. Galli. Room-temperature emission at telecom wavelengths from silicon photonic crystal nanocavities. *Applied Physics Letters*, 98(20):201106, 2011.

[77] P. Shadbolt, J. C. F. Mathews, A. Laing, and J. L. O'Brien. Testing foundations of quantum mechanics with photons. *Nat. Phys.*, 10(4):278–286, 2014.

[78] J. W. Silverstone, R. Santagati, D. Bonneau, M. J. Strain, M. Sorel, J. L. O'Brien, and M. G. Thompson. Qubit entanglement between ring-resonator photon-pair sources on a silicon chip. *Nature Communications*, 6:7948–, August 2015.

[79] Lumerical Solutions. Accessed online June 2017, at http://www.lumerical.com/tcad-products/fdtd/.

[80] Lumerical Solutions. Accessed online June 2017, at http://www.lumerical.com/tcad-products/mode/.

[81] Bong-Shik Song, Susumu Noda, Takashi Asano, and Yoshihiro Akahane. Ultra-high-q photonic double-heterostructure nanocavity. *Nat Mater*, 4(3):207–210, March 2005.

[82] R. Soref and B. Bennett. Electrooptical effects in silicon. *IEEE Journal of Quantum Electronics*, 23(1):123–129, January 1987.

[83] R. Soref and J. Larenzo. All-silicon active and passive guided-wave components for λ; = 1.3 and 1.6 μm. *IEEE Journal of Quantum Electronics*, 22(6):873–879, Jun 1986.

[84] Kartik Srinivasan, Paul E. Barclay, Matthew Borselli, and Oskar Painter. Optical-fiber-based measurement of an ultrasmall volume high-q photonic crystal microcavity. *Phys. Rev. B*, 70:081306, Aug 2004.

[85] Daniel A. Steck. Classical and modern optics. Accessed online June 2017, at http://steck.us/teaching, 2006.

[86] M. Streshinsky, R. Ding, Y. Liu, A. Novack, C. Galland, A. E.-J. Lim, P. Guo-Qiang Lo, T. Baehr-Jones, and M. Hochberg. The road to affordable, large-scale silicon photonics. *Opt. Photon. News*, 24(9):32–39, Sep 2013.

[87] Harish Subbaraman, Xiaochuan Xu, Amir Hosseini, Xingyu Zhang, Yang Zhang, David Kwong, and Ray T. Chen. Recent advances in silicon-based passive and active optical interconnects. *Opt. Express*, 23(3):2487–2511, Feb 2015.

[88] Xiankai Sun, Xufeng Zhang, Carsten Schuck, and Hong X. Tang. Nonlinear optical effects of ultrahigh-q silicon photonic nanocavities immersed in superfluid helium. *Scientific Reports*, 3:1436–, March 2013.

[89] Takasumi Tanabe, Hideaki Taniyama, and Masaya Notomi. Carrier diffusion and recombination in photonic crystal nanocavity optical switches. *J. Lightwave Technol.*, 26(11):1396–1403, Jun 2008.

[90] S. Tanzilli, A. Martin, F. Kaiser, M.P. De Micheli, O. Alibart, and D.B. Ostrowsky. On the genesis and evolution of integrated quantum optics. *Laser & Photonics Reviews*, 6(1):115–143, 2012.

[91] David Thomson, Aaron Zilkie, John E Bowers, Tin Komljenovic, Graham T Reed, Laurent Vivien, Delphine Marris-Morini, Eric Cassan, Leopold Virot, Jean-Marc Fedeli, Jean-Michel Hartmann, Jens H Schmid, Dan-Xia Xu, Frederic Boeuf, Peter O'Brien, Goran Z Mashanovich, and M Nedeljkovic. Roadmap on silicon photonics. *Journal of Optics*, 18(7):073003, 2016.

[92] Amy C. Turner, Mark A. Foster, Alexander L. Gaeta, and Michal Lipson. Ultra-low power parametric frequency conversion in a silicon microring resonator. *Opt. Express*, 16(7):4881–4887, Mar 2008.

[93] Amy C. Turner-Foster, Mark A. Foster, Jacob S. Levy, Carl B. Poitras, Reza Salem, Alexander L. Gaeta, and Michal Lipson. Ultrashort free-carrier lifetime in low-loss silicon nanowaveguides. *Opt. Express*, 18(4):3582–3591, Feb 2010.

[94] Toshitsugu Uesugi, Bong-Shik Song, Takashi Asano, and Susumu Noda. Investigation of optical nonlinearities in an ultra-high-q si nanocavity in a two-dimensional photonic crystal slab. *Opt. Express*, 14(1):377–386, Jan 2006.

[95] Jeremy Upham, Yuu Fujita, Yousuke Kawamoto, Yoshinori Tanaka, Bong Shik Song, Takashi Asano, and Susumu Noda. The capture, hold and forward release of an optical pulse from a dynamic photonic crystal nanocavity. *Opt. Express*, 21(3):3809–3817, Feb 2013.

[96] Kerry J. Vahala. Optical microcavities. *Nature*, 424(6950):839–846, August 2003.

[97] Silverstone J. W., Bonneau D., Ohira K., Suzuki N., Yoshida H., Iizuka N., Ezaki M., Natarajan C. M., Tanner M. G., Hadfield R. H., Zwiller V., Marshall G. D., Rarity J. G., O'Brien J. L., and Thompson M. G. On-chip quantum interference between silicon photon-pair sources. *Nat Photon*, 8(2):104–108, February 2014.

[98] Silverstone J.J. W., Bonneau D., OhiraK., Suzuki N., Yoshida H., Iizuka N., Ezaki M., Natarajan C. M., Tanner M. G., Hadfield R. H., Zwiller V., Marshall G. D., Rarity J. G., O'Brien J. L., and Thompson M. G. On-chip quantum interference between silicon photon-pair sources. *Nat Photon*, 8(2):104–108, February 2014.

[99] Nicholas A. Wasley. *Nano-photonics in III Semiconductors for Integrated Quantum Optical Circuits*. Springer International Publishing, 2014.

[100] Fengnian Xia, Mike Rooks, Lidija Sekaric, and Yurii Vlasov. Ultra-compact high order ring resonator filters using submicron silicon photonic wires for on-chip optical interconnects. *Opt. Express*, 15(19):11934–11941, Sep 2007.

[101] C. Xiong, T. D. Vo, M. J. Collins, J. Li, T. F. Krauss, M. J. Steel, A. S. Clark, and B. J. Eggleton. Bidirectional multiplexing of heralded single photons from a silicon chip. *Opt. Lett.*, 38(23):5176–5179, Dec 2013.

[102] C. Xiong, X. Zhang, Z. Liu, M. J. Collins, A. Mahendra, L. G. Helt, M. J. Steel, D. Y. Choi, C. J. Chae, P. H. W. Leong, and B. J. Eggleton. Active temporal multiplexing of indistinguishable heralded single photons. *Nature Communications*, 7:10853–, March 2016.

[103] Chunle Xiong, C. Monat, M.J. Collins, L. Tranchant, D. Petiteau, AS. Clark, C. Grillet, G.D. Marshall, M.J. Steel, Juntao Li, L. O'Faolain, T.F. Krauss, and B.J. Eggleton. Characteristics of correlated photon pairs generated in ultracompact silicon slow-light photonic crystal waveguides. *Selected Topics in Quantum Electronics, IEEE Journal of*, 18(6):1676–1683, 2012.

[104] Qianfan Xu, Bradley Schmidt, Sameer Pradhan, and Michal Lipson. Micrometre-scale silicon electro-optic modulator. *Nature*, 435(7040):325–327, May 2005.

[105] Jinghui Yang, Tingyi Gu, Jiangjun Zheng, Mingbin Yu, Guo-Qiang Lo, Dim-Lee Kwong, and Chee Wei Wong. Radio frequency regenerative oscillations in monolithic high-q/v heterostructured photonic crystal cavities. *Applied Physics Letters*, 104(6):061104, 2014.

[106] Xiaodong Yang and Chee Wei Wong. Coupled-mode theory for stimulated raman scattering in high-q/vm silicon photonic band gap defect cavity lasers. *Opt. Express*, 15(8):4763–4780, Apr 2007.

[107] Kane Yee. Numerical solution of initial boundary value problems involving maxwell's equations in isotropic media. *IEEE Transactions on Antennas and Propagation*, 14(3):302–307, May 1966.

[108] Juan Yin, Ji-Gang Ren, He Lu, Yuan Cao, Hai-Lin Yong, Yu-Ping Wu, Chang Liu, Sheng-Kai Liao, Fei Zhou, Yan Jiang, Xin-Dong Cai, Ping Xu, Ge-Sheng Pan, Jian-Jun Jia, Yong-Mei Huang, Hao Yin, Jian-Yu Wang, Yu-Ao Chen, Cheng-Zhi Peng, and Jian-Wei Pan. Quantum teleportation and entanglement distribution over 100-kilometre free-space channels. *Nature*, 488(7410):185–188, 2012.

[109] Xiaoge Zeng, Cale M. Gentry, and Miloš A. Popović. Four-wave mixing in silicon coupled-cavity resonators with port-selective, orthogonal supermode excitation. *Opt. Lett.*, 40(9):2120–2123, May 2015.

[110] Xiaoge Zeng and Miloš A. Popović. Design of triply-resonant microphotonic parametric oscillators based on kerr nonlinearity. *Opt. Express*, 22(13):15837–15867, Jun 2014.

[111] Y. Zhang, D. Li, C. Zeng, X. Qiu, G. Gao, Y. Wang, Q. Huang, J. Yu, and J. Xia. Low power and large modulation depth optical bistability in an si photonic crystal l3 cavity. *IEEE Photonics Technology Letters*, 26(23):2399–2402, Dec 2014.

Appendix A

Nonlinear measurement considerations

A.1 Instability

In nonlinear transmission measurements, the system is least stable during forward sweeps through the high transmission bistable section. There are a number of things that can potentially cause a premature drop in the transmission (unloading of the cavity energy), down to the low transmission value.

It is critical that the wavelength step between individual transmission measurements is sufficiently small. When the forward step is too large in the bistable regime, the laser wavelength surpasses the transient resonant wavelength causing a detuning that leads to energy unloading from the microcavity. When smaller steps are taken, the nonlinear effects incrementally strengthen to the steady-state values, and the laser wavelength continues to chase the ever red-shifting resonant wavelength. In this thesis, typical wavelength steps are between $\Delta\lambda = 0.002$ nm and 0.005 nm. The small wavelength step also provides good resolution for the transmission spectra. Given that the time step is ~ 50 ms, and measurements are typically taken over ~ 0.5 nm, the time to run each spectrum is less than 15 s.

Instabilities in the measurement environment also cause the transmission to drop in the bistable regime. For example, a drop may be caused by a fluctuation of the power launched in the input waveguide. While the lasers employed in this experimental work are stable enough to avoid problems like this, displacement of the excitation beam on the input grating coupler can lead to a reduction in power. This displacement can be caused by a disturbance in the optical set-up, like an accidental nudge of the optical table, or even natural vibrations (in more extreme cases). Changes in the temperature of the room can also cause a drop due to the change it induces in the index of refraction, which causes the mode to shift off resonance. Alignment and temperature fluctuations do not typically cause premature drops in the transmission during nonlinear transmission measurements. They are more likely to be problematic when the aim is to maintain a microcavity in a bistable state over some period of time. This is the case for stimulated four-wave mixing measurements. The likelihood that these fluctuations cause an unwanted drop partly depends on how close the laser wavelength is tuned to the edge of the bistability. The closer to the edge, the system is less stable, it takes less of a disturbance to cause a drop.

A.2 Four-wave mixing excitation

There are two excitation configurations for four-wave mixing that are employed in this thesis. In both configurations, the center M2 mode is pumped on-resonance. In one configuration, the high Q M1 mode is excited on-resonance by the signal laser, and the output filter is centred to the idler wavelength near the low Q M3. In the other configuration, signal wavelength is tuned near M3, but not necessarily on-resonance, so that idler photons are generated on-resonance with M1. The different procedures are followed to optimally tune the pump, signal excitation wavelengths, and the spectral filter idler wavelength.

A.2.1 Signal: high Q mode

In this excitation configuration, the goal is to optimally load pump and signal light into the two high Q microcavity modes, by tuning the wavelengths to the resonant wavelengths. The idler filter wavelength is then set so that the signal and idler wavelengths are equally spaced from the pump wavelength. The idler wavelength is easily estimated with a quick calculation, and then refined by sweeping the filter center wavelength until there is a peak in the idler photon generation rate. The idler wavelength does not necessarily coincide with the resonant frequency of the low Q mode, as the microcavity modes are generally not perfectly spaced.

When both the pump and signal powers are sufficiently low that nonlinear absorption effects are negligible (as in the linear limit), the laser wavelengths are simply tuned to the cold cavity resonant wavelengths λ_m of the two respective modes. The resonant wavelengths are found by sequential wavelength sweeps of the two excitation lasers to find the appropriate resonant peak wavelengths in the transmission spectra. With the optical set-up implemented in this experimental work, it is easy to go between doing the transmission measurements required wavelength alignment, and the four-wave mixing measurements, as the transmission set-up is simply a subset of the four-wave mixing measurement set-up.

In the nonlinear regime, when one or both of the pump and signal excitations induce nonlinear absorption effects, the aim remains to tune to the pump and signal lasers to the resonants wavelengths of the high Q modes, however this becomes significantly more technically difficult than in the linear limit due to the changes refractive index of the silicon that simultaneously affect both modes as energy is loaded in the microcavity. As an example, Fig. 2.7(c) shows the nonlinear resonant wavelength shift of mode M1 as a function of the energies loaded in both this mode, and M2. Meanwhile, Fig. 2.7(d) shows the resonant wavelength shift of M2, as a function of the energies in M1 and M2.

When only the pump laser is sufficiently strong to induce nonlinear effects, the following strategy is used for optimal loading. The pump excitation is first turned on, while the signal laser remains off. The optimal wavelength of the pump is that which maximizes the nonlinear transmission at the given pump power. A full forward sweep is run to identify the optimal wavelength (assuming red-shift dominates, otherwise backward sweep would be used), then the sweep is redone but stopped just short of the large drop in transmission, so that the high transmission is achieved. The pump is fixed at this wavelength. The signal laser is then turned on and swept to its peak transmission wavelength, and fixed at this wavelength. At this point, both microcavities are optimally loaded. It's important to note that the peak resonant wavelength for the signal mode is shifted from its cold cavity λ_m, and the maximum transmission is lower than the cold cavity peak, due to the energy loaded in the pump mode that is causing changes to the real and imaginary parts of the refractive index, respectively. This makes the order of the sweeps important, because if the signal mode were to be sought and fixed first, then the signal laser wavelength would be off resonance (suboptimal) after the pump energy is subsequently loaded.

When both of the mode excitations are in bistable limits, it becomes even more challenging to optimally load both cavity modes, and an iterative process is required. One laser is turned is on and a forward sweep is used to identify the peak wavelength (again, assuming red-shift dominates). The laser wavelength is fixed near this wavelength (just before the large drop in transmission) and then the second laser is turned on, swept to find its peak wavelength, and swept once more to reach the peak, without going too far. At this stage, the modes are likely not optimally loaded, as the nonlinear effects introduced by the second mode have likely caused the peak wavelength of the first mode to red-shift, leaving the laser for the first mode detuned. To reach simultaneous optimal loading for both cavities, the wavelength for each laser is iteratively increased in very small steps (~ 0.002 nm), taking turns between the two lasers, to account for the red-shifting of both modes. This iterative process is terminated when the transmission ceases to increase (or the increase is very small compared to the increases observed in previous iterations). The modes are then very close to optimally loaded. This is a very unstable excitation, and is prone to sudden drops in the power loaded in both cavities.

A.2.2 Signal: low Q mode

In the second excitation configuration, the signal wavelength excites the low Q mode, and the idler wavelength coincides with the outer high Q mode resonant wavelength. The most important difference between this configuration and the previous one is that, in this case, the goal is not to tune the signal wavelength such that it optimizes the signal light loaded in the low Q mode, the goal is actually to optimize the wavelength so that the *idler* photons generated are on resonance with the high Q *idler* mode. The pump wavelength tuning process does remain similar however, it is tuned to optimally load energy in the center mode.

The signal wavelength optimization is challenging because it cannot be guided by transmission measurements. Instead, the signal wavelength is tuned by directly optimizing the idler generation rate, with the idler filter wavelength set to the idler mode resonant wavelength. For each signal wavelength tested in the optimization process, the single photon detector is observed after waiting sufficient time for the average count rate to settle. Sometimes it requires many of these wavelength steps to complete the optimization, because a small wavelength step is used due to the small linewidth of the high Q mode. The count rate only surpasses the noise once the idler wavelength is within a couple linewidths of the high Q mode resonant wavelength (typical linewidth < 0.05 nm).

Appendix B

Finite-difference time-domain analysis

B.1 The finite-difference time-domain method

The finite-difference time-domain method is an exact numerical approach to solving the macroscopic Maxwell's equations, which in differential form are,

$$\nabla \times \mathbf{E}(\mathbf{r}, t) = -\frac{\partial \mathbf{B}(\mathbf{r}, t)}{\partial t} \tag{B.1}$$

$$\nabla \times \mathbf{H}(\mathbf{r}, t) = \mathbf{J}(\mathbf{r}, t) + \frac{\partial \mathbf{D}(\mathbf{r}, t)}{\partial t} \tag{B.2}$$

$$\nabla \cdot \mathbf{D}(\mathbf{r}, t) = \rho(\mathbf{r}, t) \tag{B.3}$$

$$\nabla \cdot \mathbf{B}(\mathbf{r}, t) = 0 \tag{B.4}$$

where $\mathbf{E}(\mathbf{r}, t)$ is the electric field, $\mathbf{H}(\mathbf{r}, t)$ is the magnetic field, $\mathbf{D}(\mathbf{r}, t)$ is the displacement field, $\mathbf{B}(\mathbf{r}, t)$ is the magnetic flux, ρ is the free electric charge density (not including bound charges) and $\mathbf{J}(\mathbf{r}, t)$ is the free current density (not including bound polarization and magnetization currents). In this thesis, all FDTD simulations are done in the linear regime where $\mathbf{D}(\mathbf{r}, t) = \epsilon(\mathbf{r})\mathbf{E}(\mathbf{r}, t)$ and $\mathbf{H}(\mathbf{r}, t) = \mu(\mathbf{r})\mathbf{B}(\mathbf{r}, t)$, where $\epsilon(\mathbf{r})$ and $\mu(\mathbf{r})$ are material electric permittivity and magnetic permeability, respectively. For the materials considered here $\mu(\mathbf{r}) = \mu_0$, where μ_0 is the permeability of free space.

Lumerical FDTD Solutions software implements the Yee Algorithm approach [79, 107], such that the simulation volume is discretized into Yee cells, illustrated in Fig. B.1. The $\hat{\mathbf{x}}$, $\hat{\mathbf{y}}$ and $\hat{\mathbf{z}}$ electric and magnetic field components are evaluated at different positions, staggered over the grid. The time step between when the fields are evaluated is Δt. In this approach, the electric field calculations occur at times offset by $\Delta t/2$ from the magnetic field calculations. For example, the

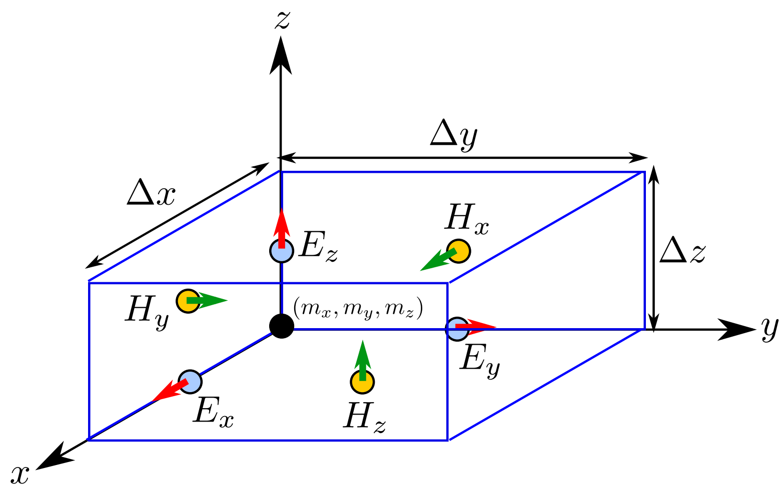

Figure B.1: Schematic of a Yee cell [107].

$E_x(\mathbf{r}, t)$ fields are evaluated at,

$$t \to n\Delta t \tag{B.5}$$

$$x \to (m_x + \frac{1}{2})\Delta x \tag{B.6}$$

$$y \to m_y \Delta y \tag{B.7}$$

$$z \to m_z \Delta z \tag{B.8}$$

where n is the integer time index, $\Delta x, \Delta y$ and Δz are the mesh step sizes in the $\hat{\mathbf{x}}$, $\hat{\mathbf{y}}$, and $\hat{\mathbf{z}}$ directions, and m_x, m_y and m_z are the x, y and z coordinates of the Yee cell in terms of the integer step number, respectively. The basic update equations, in the absence of free currents and charges, are,

$$\mathbf{E}^{n+1} = \mathbf{E}^n + \frac{\Delta t}{\epsilon} \nabla \times \mathbf{H}^{n+\frac{1}{2}} \tag{B.9}$$

$$\mathbf{H}^{n+3/2} = \mathbf{H}^{n+\frac{1}{2}} - \frac{\Delta t}{\mu_0} \nabla \times \mathbf{E}^{n+1} \tag{B.10}$$

(B.11)

where the spatial curls are evaluated at each of the field component positions. For example, the

E_x update is,

$$E_x{}^{n+1}_{m_x+\frac{1}{2},m_y,m_z} = E_x{}^{n}_{m_x+\frac{1}{2},m_y,m_z} \tag{B.12}$$

$$+ \frac{\Delta t}{\epsilon}\left(\frac{H_z{}^{n+\frac{1}{2}}_{m_x+\frac{1}{2},m_y+\frac{1}{2},m_z} - H_z{}^{n+\frac{1}{2}}_{m_x+\frac{1}{2},m_y-\frac{1}{2},m_z}}{\Delta y} \right. \tag{B.13}$$

$$\left. - \frac{H_y{}^{n+\frac{1}{2}}_{m_x+\frac{1}{2},m_y,m_z+\frac{1}{2}} - H_z{}^{n+\frac{1}{2}}_{m_x+\frac{1}{2},m_y,m_z-\frac{1}{2}}}{\Delta z} \right) \tag{B.14}$$

Appendix C

Grating coupler design

The first step of the design procedure considers gratings with uniform slot widths, w_{s}, and spacings, a_{s}. In 2D FDTD simulations, a Gaussian beam with $1/e^2$ diameter $d_0 = 10$ μm is incident on the uniform grating at $-45°$ with $f = 196$ THz (near the simulated resonant mode frequencies) and the light coupled into the fundamental mode of the 20 μm wide waveguide is monitored, as shown in Fig. C.1(a). The simulation spans the entire depth of the SOI, including the buried oxide and the top of the base silicon layer. The slot spacing that optimizes the transmission for each grating width tested is determined, and is plotted in Fig. C.1(b). It approximately follows: $a_{\mathrm{s}} = 0.58w_{\mathrm{s}} + 415$ nm.

In the next step, light with $f = 196$ THz is launched into the fundamental mode of the waveguide, and the spatial profile of out-coupled light 1 μm above the uniform grating coupler is studied using the 2D simulations shown in Fig. C.1(c). The spatial profile for the uniform grating with w_{s} = 100 nm and a_{s} = 474 nm (optimized pair) is shown in Fig. C.1(d), where the trend shows that the intensity exponentially decays following $\sim \exp(-\alpha x)$. The decay rates, $\alpha(w_{\mathrm{s}})$, are plotted in Fig. C.1(e), where for each w_{s}, $a_{\mathrm{s}} = 0.58w_{\mathrm{s}} + 415$ nm is applied. The exponential decay does not mimic that profile of the Gaussian beam (incident at 45°), also plotted in Fig. C.1(d), thus the uniform grating is not optimal.

An apodization scheme is then determined that helps match the profiles of the out-coupled light and the excitation beam. The slot widths are chosen so that the decay rate starts small, to minimize radiation immediately at the beginning of the grating, then increases quickly to match the drop of Gaussian excitation. At this stage, the design chosen has the following composition: 7 slots with $w_{\mathrm{s}} = 100$ nm, 15 slots over which the width is linearly varied between $w_{\mathrm{s}} = 100$ nm and 300 nm, followed by 300 nm slots out to the simulation boundary, all separated by the appropriate

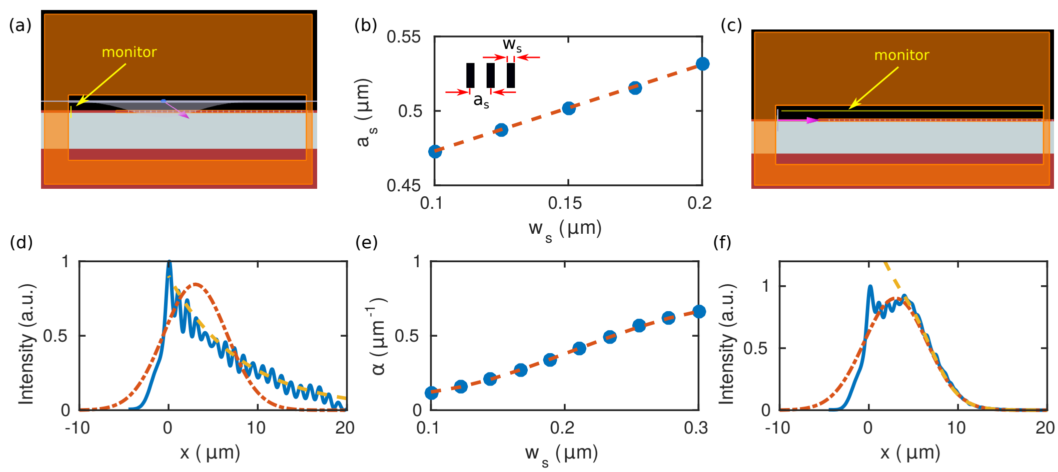

Figure C.1: Apodized grating coupler design. (a) FDTD simulation layout for in-coupling of light from a Gaussian beam with a $1/e^2$ width of 10 μm at $\theta = -45°$ into the silicon slab via a 1D grating. (b) Grating spacing, a_s, that optimizes in-coupling transmission ($\theta = -45°$), as a function of the slot width, w_s, for a uniform grating. The line of best fit for a linear function is shown (red dashed). (c) FDTD simulation layout for out-coupling light from the silicon slab mode to free-space above the grating. (d) Out-coupling radiation profile measured 1 μm above the uniform grating coupler with w_s = 100 nm and a_s = 474 nm (blue), when the silicon slab mode is launched. The best fit exponential decay curve (dash-dotted yellow line), and the profile of the input Gaussian beam (dashed red) are also included. (e) Decay rates as a function of w_s, for uniform gratings with a_s found from the line of best fit in (b). (f) Out-coupling radiation profile measured 1 μm above the apodized grating coupler (blue), when the silicon slab mode is excited. The predicted decay profile (yellow dash dotted) and the excitation Gaussian beam for in-coupling profile (red dashed), as also plotted.

$a_\mathrm{s}(w_\mathrm{s})$. The decay intensity pattern predicted for this grating apodization scheme is plotted in Fig. C.1(f), along with the simulated profile and the excitation Gaussian. The reflection is estimated to be 0.072 and is reduced to 0.041 when the first grating slot is replaced by one with w_s = 80 nm.

A schematic of the final apodized grating design, extended to two-dimensions, is shown in Fig. 3.13(a). As described in Section 3.2.2, the transmission efficiencies between free-space and the single-mode waveguide (via the parabolic waveguide), plotted in Fig. 3.13(c) and (f) are estimated using a combination of FDTD and MODE eigen-mode expansion (EME) simulations, which are now described.

The in-coupling efficiency, from free-space to the single-mode channel waveguide is found by first simulating the coupling of light into the opening of the parabolic using FDTD simulation, then that light is propagated in the parabolic waveguide to the channel waveguide using the MODE eigenmode solver[80]. In the in-coupling FDTD simulation, the beam is centred 4 μm from the front slot, and the field profile at the entrance to the parabolic waveguide is saved, along with the transmission through the planar monitor. The field profile is then launched as a source in an EME simulation of the parabolic waveguide and finally the transmission into the mode of the 500 nm wide channel waveguide is found, and is plotted in Fig. 3.13(c). The transmission of light through the parabolic waveguide is found to be ~ 0.85, while the reflection is found to be 0.0062 for the grating studied here. In EME simulation, the parabolic waveguide is divided into 90 cells, and the modes supported by waveguide cross-section at each cell interface are calculated. The transmission through the full waveguide is calculated based on scattering matrices found by considering the boundary conditions at each interface such that a bi-direction (transmission and reflection) estimate for light propagation is achieved. This method is not exact, like the FDTD method, however it yields almost identical results and requires significantly less computational resources.

For out-coupling simulations, the fundamental mode is launched in the single-mode channel waveguide, and the field profile at the end of the parabolic waveguide is calculated with the EME solver and is saved, along with the transmission efficiency. It is then used in an FDTD simulation as a source directed toward the grating, and transmission of light through a monitor lying 1 μm above the grating surface is monitored, as is plotted in Fig.3.13(c).

The collection efficiency of the elliptical mirror is accounted for by considering the distribution of light in the far field, as illustrated in Figs. 3.13(d) and (e). The far field is calculated using Lumerical FDTD's "farfield3d" function, which calculates the Fraunhofer diffraction pattern. The collection efficiency of the mirror is calculated by dividing the integrated field intensity within the mirror surface area by the total integrated field intensity, both found using the "farfield3dintegrate" function. The total out-coupling efficiency is found by multiplying the collection efficiency by the free-space out-coupling transmission efficiency.

Appendix D

Transmission efficiencies

The analyses of experimental data in this thesis require knowledge of the optical powers in the input and output PC waveguides. These powers are calculated by considering the raw powers measured in the experiment, and the transmission efficiencies of components along the optical path.

D.1 Linear and nonlinear transmission

In transmission measurements, the power coupled into the output PC waveguide is,

$$T(\lambda) = \frac{T_{\mathrm{raw}}(\lambda)}{\eta_{\mathrm{tot}}^{\mathrm{out}}(\lambda)}, \tag{D.1}$$

where $\eta_{\mathrm{tot}}(\lambda)$ is the total transmission efficiency of all free-space and integrated components on the optical path between the output PC waveguide and the photodetector, where the raw transmission $T_{\mathrm{raw}}(\lambda)$ is measured. The power in the input PC waveguide is,

$$P^{\mathrm{in}}(\lambda) = \frac{P_{\mathrm{raw}}^{\mathrm{in}}(\lambda)\eta_{\mathrm{tot}}^{\mathrm{in}}(\lambda)}{\eta_{\mathrm{m2}}^{\mathrm{in}}}, \tag{D.2}$$

where $\eta_{\mathrm{tot}}^{\mathrm{in}}(\lambda)$ is the total transmission efficiency of all integrated components on the optical path between the input PC waveguide and free-space directly off the chip surface, and $\eta_{\mathrm{m2}}^{\mathrm{in}}$ is the transmission efficiency of the mirror ("Mirror 2") that is placed directly before the chip to redirect light towards a photodetector that measures the raw input power $P_{\mathrm{raw}}^{\mathrm{in}}(\lambda)$. The relative transmission is,

$$\overline{T}(\lambda) = \frac{T(\lambda)}{P^{\mathrm{in}}(\lambda)}. \tag{D.3}$$

The free-space and integrated component transmission efficiencies that compose $\eta_{\mathrm{tot}}^{\mathrm{out}}$ and $\eta_{\mathrm{tot}}^{\mathrm{in}}$ are described the following, and are summarized in Table D.1.

Table D.1: Summary of the transmission efficiencies for components in the transmission and four-wave mixing (FWM) set-ups illustrated in Fig. 2.5 and Fig. 2.11

Set-up	Component	Transmission efficiency
Transmission Set-up	Elliptical mirror + Mirror 1	$\eta_{\mathrm{em}}\eta_{\mathrm{m1}} = 0.864 \pm 0.007$
	Output Polarizer	$\eta_{\mathrm{op}} = 0.529 \pm 0.005$
	Mirror 2	$\eta_{\mathrm{m2}} = 0.922 \pm 0.01$
FWM Set-up	Fibre coupling	$\eta_{\mathrm{fibre}} = 0.27 \pm 0.02$
	Filter	$\max[\eta_{\mathrm{filter}}(\lambda)] = 0.355 \pm 0.010$
	SPD	$\eta_{\mathrm{D}} = 0.116 \pm 0.005$
Integrated Components	Input grating coupling	$\eta_{\mathrm{GC}}^{\mathrm{in}}(\lambda)$
	Output grating coupling	$\eta_{\mathrm{GC}}^{\mathrm{out}}(\lambda)$
	Input parabolic waveguide	$\eta_{\mathrm{par}}^{\mathrm{in}}(\lambda)$
	Output parabolic waveguide	$\eta_{\mathrm{par}}^{\mathrm{out}}(\lambda)$
	Input PC waveguide	$\eta_{\mathrm{PCwg}}^{\mathrm{in}}(\lambda)$
	Output PC waveguide	$\eta_{\mathrm{PCwg}}^{\mathrm{out}}(\lambda)$

The total transmission efficiency along the collection path is,

$$\eta_{\mathrm{tot}}^{\mathrm{out}}(\lambda) = \eta_{\mathrm{em}}\eta_{\mathrm{m1}}\eta_{\mathrm{op}}g_{\mathrm{out}}(\lambda), \tag{D.4}$$

where η_{em}, η_{m1} and η_{op} are the measured transmission efficiencies of the elliptical mirror, Mirror 1 and the output polarizer, respectively, along free-space collection path of the transmission set-up in Fig. 2.5. The $g_{\mathrm{out}}(\lambda)$ function contains the transmission efficiencies of the integrated components,

$$g_{\mathrm{out}}(\lambda) = \eta_{\mathrm{GC}}^{\mathrm{out}}(\lambda)\eta_{\mathrm{par}}^{\mathrm{out}}(\lambda)\eta_{\mathrm{PCwg}}^{\mathrm{out}}(\lambda), \tag{D.5}$$

where $\eta_{\mathrm{GC}}^{\mathrm{out}}(\lambda)$, $\eta_{\mathrm{par}}^{\mathrm{out}}(\lambda)$ and $\eta_{\mathrm{PCwg}}^{\mathrm{out}}(\lambda)$ are the transmission efficiencies for the output grating coupler, parabolic waveguide and the channel waveguide-to-PC waveguide transition region, respectively. Similarly, the total transmission efficiency along the input path, which includes only the input integrated components, is,

$$\eta_{\text{tot}}^{\text{in}}(\lambda) = g_{\text{in}}(\lambda) = \eta_{\text{GC}}^{\text{in}}(\lambda)\eta_{\text{par}}^{\text{in}}(\lambda)\eta_{\text{PCwg}}^{\text{in}}(\lambda). \tag{D.6}$$

The free-space component efficiencies, η_{em}, η_{m1} and η_{op}, have only very weak wavelength dependencies over the tuning range of the lasers and are taken to be constants. Here, the elliptical mirror transmission efficiency accounts for loss and scattering from the mirror surface, and does not account for the geometrical collection efficiency (this is considered part of the grating coupler characterization, discussed shortly). The polarizer transmission efficiency is reported here for incident light polarized along the transmission axis, which is normal to the plane of Fig. 2.3 to be consistent with the s-polarized grating modes of interest.

The relative uncertainty in the relative microcavity transmission, $\delta\overline{T}/\overline{T}$, is estimated to be 4%. This is based on the uncertainties in the optical component transmission efficiencies (see Table D.1), and fluctuations in the transmitted powers measured for the reference devices and the microcavity device.

D.2 Four-wave mixing idler power calibration

In four-wave mixing measurements, fibre-based components are added to the transmission set-up, including spectral filters and a single photon detector (shown in Fig. 2.11), with transmission efficiencies $\eta_{\text{filter}}(\lambda)$ and η_{D} respectively. The values for these efficiencies are reported in Table D.1, along with the coupling efficiency of free-space light to the single mode fibre, η_{fibre}. Fibre components are also added to the excitation path, including a spectral filter and a 50/50 splitter, however these do not affect the input power calculation, as the power is measured downstream of their locations.

The idler power in the output PC waveguide, P_{idler} is calculated from the raw idler power, $P_{\text{idler}}^{\text{raw}}$, measured by the detector (after accounting for the dead-time, as described in Appendix D), using,

$$P_{\text{idler}} = \frac{P_{\text{idler}}^{\text{raw}}}{\eta_{\text{tot}}^{\text{out}}(\lambda_{\text{idler}}, \phi_{\text{out}})\eta_{\text{fibre}} \max[\eta_{\text{filter}}(\lambda)]\eta_{\text{D}}}. \tag{D.7}$$

The input pump and signal ("p/s") powers in the input PC waveguide are calculated as,

$$P^{\mathrm{in}}_{\mathrm{p/s}} = \frac{P^{\mathrm{in}}_{\mathrm{raw,p/s}}(\lambda)\eta^{\mathrm{in}}_{\mathrm{tot}}(\lambda_{\mathrm{p/s}}, \phi_{\mathrm{in}})}{\eta^{\mathrm{in}}_{\mathrm{m2}}}, \tag{D.8}$$

The relative uncertainty in the idler power $\delta P_{\mathrm{idler}}/P_{\mathrm{idler}}$, is estimated based on two contributions that are added in quadrature: 1) the uncertainty arising from the transmission efficiency calculations, which includes the optical components transmission efficiency uncertainties (see Table D.1), and fluctuations in the transmitted powers measured for the reference devices, and 2) the uncertainty due to fluctuations in the count rate measured by the single photon detector. The former is estimated to be 5%, while the former is estimated for each measurement individually.

D.3 Integrated component transmission efficiencies

The transmission efficiencies of the integrated components in the microcavity devices are addressed here. To calculate the power in the input PC waveguide, the transmission of the Gaussian beam excitation through to the PC waveguide, $g_{\mathrm{in}}(\lambda)$, must be found. This transmission efficiency captures the passage of light through the input grating coupler, the parabolic waveguide, and finally, into the PC waveguide. Similarly, to calculate the power in the output PC waveguide, the transmission efficiency $g_{\mathrm{out}}(\lambda)$, must be found, that captures passage of light from the output PC waveguide, through the parabolic waveguide and output grating coupler, and finally the collection by the elliptical mirror. The $g_{\mathrm{in}}(\lambda)$ and $g_{\mathrm{out}}(\lambda)$ have two main differences: 1) the input and output PC waveguides have different structures in the microcavity device, and 2) the spectrum associated with coupling the Gaussian beam excitation into the input channel waveguide via the input grating coupler, is different from the spectrum associated with the elliptical mirror collection of light leaving output channel waveguide via the output grating coupler. These two points are considered in the following.

To address the first point, $g_{\mathrm{in}}(\lambda)$, is estimated by analyzing the transmission spectrum of reference device $\mathrm{PCWG_{in}}$, which has the PC waveguide structure that matches that of the microcavity input waveguide, as described in Section 3.3.1. Meanwhile, $g_{\mathrm{out}}(\lambda)$ is estimated by analyzing the transmission spectrum of $\mathrm{PCWG_{out}}$, whose PC waveguide structure matches that out the microcavity output waveguide.

The second point is less straight-forward to deal with. If input and output coupling efficiencies were the same, then it would be possible to find the efficiencies by taking the square roots of the $\mathrm{PCWG_{in}}$ and $\mathrm{PCWG_{out}}$ transmission spectra. For example, this would be an appropriate approach to take if the transmission measurements involved direct coupling of light between the grating couplers and optical fibres. In the free-space transmission measurements taken in this thesis, with non-symmetric excitation and collection optics, there is no way of knowing the individual contributions from input and output coupling spectra. As a result, simulation results are used to estimate the ratio between the two.

Finally, one added challenge in determining $g_{\mathrm{in}}(\lambda)$ and $g_{\mathrm{out}}(\lambda)$ is that oscillations appear in the transmission spectra due to effective Fabry-Perot cavities formed in the parabolic waveguides. The peaks of these oscillations are shifted from device to device, which makes the reference device transmission spectrum unreliable in this regard.

D.3.1 Calculations of transmission efficiencies $g_{\mathrm{in}}(\lambda)$ and $g_{\mathrm{out}}(\lambda)$

The relative transmission spectra, taken from directly before the input grating coupler to directly after the elliptical mirror collection, $\widetilde{T}(\lambda)$, are shown in Fig. D.1 for the four reference devices in the $s_{\mathrm{gc}} = 0.97$ set of Group 3 on Chip A, measured with $\theta = -41°$. Here, the raw transmission spectra measured by the photodetector, $T_{\mathrm{raw}}(\lambda)$, are used to calculate $\widetilde{T}(\lambda)$ using the following,

$$\widetilde{T}(\lambda) = \frac{T(\lambda)}{P^{\mathrm{in}}(\lambda)} = \frac{T_{\mathrm{raw}}(\lambda)}{P^{\mathrm{in}}_{\mathrm{raw}}(\lambda)} \frac{\eta_{\mathrm{m2}}}{\eta_{\mathrm{em}}\eta_{\mathrm{m1}}\eta_{\mathrm{op}}}, \tag{D.9}$$

where $T(\lambda) = T_{\mathrm{raw}}(\lambda)/(\eta_{\mathrm{em}}\eta_{\mathrm{m1}}\eta_{\mathrm{op}})$ is the transmitted power estimated after collection by the elliptical mirror (however with non-geometrical mirror losses removed), and $P^{\mathrm{in}}(\lambda) = P^{\mathrm{in}}_{\mathrm{raw}}(\lambda)/\eta_{\mathrm{m2}}$ is the input power estimated at the chip surface. The transmission spectra peaks are centred near $\lambda = 1542$ nm, with bandwidths $\simeq 30$ nm. The spectral lineshapes agree well with the product of the simulated input and output grating coupling spectra for $s_{\mathrm{gc}} = 0.92$ and $\theta = -41°$, where the simulated peak wavelength is 1540 nm and the bandwidth is 34 nm. The difference in experimental and simulated s_{gc} implies that the actual grating slots are likely smaller than intended (in the

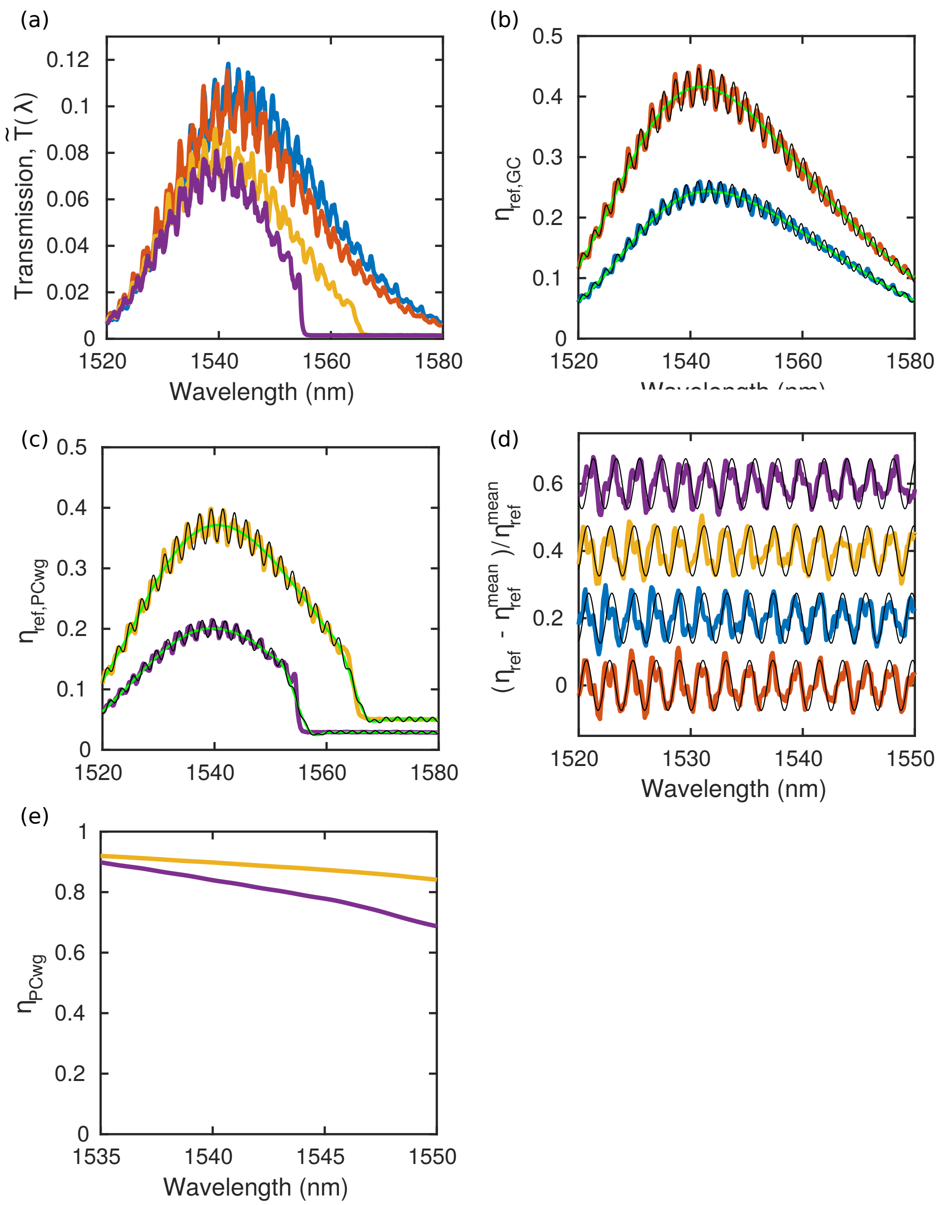

Figure D.1: Transmission spectra for reference devices in Group 3 of Chip A, with $s_{\mathrm{ms}} = 0.97$. (a) Transmission from directly before the input grating coupler to directly after collection by the elliptical mirror, for the G2G$_{\mathrm{out}}$ (blue), G2G$_{\mathrm{in}}$ (red), PCWG$_{\mathrm{out}}$ (purple) and PCWG$_{\mathrm{in}}$ (yellow) devices. (b) Transmission efficiencies, $\eta^{\mathrm{out}}_{\mathrm{ref,GC}}$ (blue) and $\eta^{\mathrm{in}}_{\mathrm{ref,GC}}$ (red) from found transmission measurements of G2G$_{\mathrm{out}}$ and G2G$_{\mathrm{in}}$ respectively. (c) Transmission efficiencies, $\eta^{\mathrm{out}}_{\mathrm{ref,PCwg}}$ (purple) and $\eta^{\mathrm{in}}_{\mathrm{ref,PCwg}}$ (yellow) from found transmission measurements of PCWG$_{\mathrm{out}}$ and PCWG$_{\mathrm{in}}$, respectively. (d). The green lines in (b) and (c) are $\eta^{\mathrm{mean}}_{\mathrm{ref,X}}(\lambda)$, found by filtering $\eta_{\mathrm{ref,X}}(\lambda)$ spectra to remove the fast oscillations. The black lines are the best fit $g(\lambda, \phi)$ functions. (d) The scaled coupling efficiencies for (bottom to top) G2G$_{\mathrm{in}}$ (blue), G2G$_{\mathrm{out}}$ and PCWG$_{\mathrm{in}}$ (blue), PCWG$_{\mathrm{out}}$. (e) The input (yellow) and output (purple) PC waveguide coupling efficiencies. Black lines plot the best fit sinusoidal functions.

layout). In addition, the simulated transmission efficiency is 1.9 times greater than that found experimentally. It is unclear why this large difference exists, but is possibly due to fabrication imperfections in the grating couplers or the long parabolic waveguides.

From the reference device transmission spectra in Fig. D.1(a), it is possible to estimate the following transmission efficiencies,

$$\eta^{\text{in}}_{\text{ref,GC}}(\lambda) = \eta^{\text{in}}_{\text{GC}}(\lambda)\eta^{\text{in}}_{\text{par}}(\lambda) = \sqrt{f_{\text{GC}}\widetilde{T}^{\text{in}}_{\text{G2G}}(\lambda)}, \tag{D.10}$$

$$\eta^{\text{out}}_{\text{ref,GC}}(\lambda) = \eta^{\text{out}}_{\text{GC}}(\lambda)\eta^{\text{out}}_{\text{par}}(\lambda) = \sqrt{\frac{\widetilde{T}^{\text{out}}_{\text{G2G}}(\lambda)}{f_{\text{GC}}}}, \tag{D.11}$$

$$\eta^{\text{in}}_{\text{ref,PCwg}}(\lambda) = \eta^{\text{in}}_{\text{GC}}(\lambda)\eta^{\text{in}}_{\text{par}}(\lambda)\eta^{\text{in}}_{\text{PCwg}}(\lambda) = \sqrt{f_{\text{GC}}\widetilde{T}^{\text{in}}_{\text{PCwg}}(\lambda)}, \tag{D.12}$$

and

$$\eta^{\text{out}}_{\text{ref,PCwg}}(\lambda) = \eta^{\text{out}}_{\text{GC}}(\lambda)\eta^{\text{out}}_{\text{par}}(\lambda)\eta^{\text{out}}_{\text{PCwg}}(\lambda) = \sqrt{\frac{\widetilde{T}^{\text{out}}_{\text{PCwg}}(\lambda)}{f_{\text{GC}}}}, \tag{D.13}$$

where $\widetilde{T}^{\text{in}}_{\text{G2G}}(\lambda)$ and $\widetilde{T}^{\text{out}}_{\text{G2G}}(\lambda)$ are the transmission spectra for G2G_{in} and G2G_{out} devices, and $\widetilde{T}^{\text{in}}_{\text{PCwg}}(\lambda)$ and $\widetilde{T}^{\text{out}}_{\text{PCwg}}(\lambda)$ are those for PCWG_{in} and PCWG_{out} devices, respectively. Here $f_{\text{GC}} = \eta^{\text{in}}_{\text{GC}}/\eta^{\text{out}}_{\text{GC}}$, is the ratio between input and output coupling, as found using simulations (see Section 3.2.2). For the grating coupler structure studied here, and this coupling angle of $\theta = -41°$, f_{GC} is estimated to be 1.75. The $\eta_{\text{ref,GC}}(\lambda)$ [Eqns. (D.10) and (D.11)] are plotted in Fig. D.1(b) and $\eta_{\text{ref,PCwg}}(\lambda)$ [Eqns. (D.12) and (D.13)] are plotted in Fig. D.1(c).

The $g_{\text{in}}(\lambda)$ and $g_{\text{out}}(\lambda)$ transmission efficiency spectra are essentially given by $\eta^{\text{in}}_{\text{ref,PCwg}}(\lambda)$ and $\eta^{\text{out}}_{\text{ref,PCwg}}(\lambda)$. These spectra capture the slow underlying peak, associated with grating coupling [i.e. $\eta_{\text{GC}}(\lambda)$] and coupling between the PC and channel waveguides [i.e. $\eta_{\text{PCwg}}(\lambda)$], in addition to the fast oscillations that arise to due an effective Fabry-Perot cavity formed inside each parabolic waveguide as a result of reflections off the grating coupler on one end, and off the waveguide transition to a narrow single mode waveguide on the other. The fast oscillations are problematic because, from device to device, the oscillations peaks occur at different wavelengths due to small differences in the roundtrip phase for light propagating in the long parabolic waveguide. This means that reference measurements can't reliably capture the phase of the sinusoid, and as a result the ϕ_{in} and ϕ_{out} parameters are introduced to the transmission efficiency functions as unknowns, that are ultimately fit parameters in the nonlinear analysis. This parameterization is important because the oscillation amplitude is large enough that phase errors in the efficiency functions could potentially result in an unphysical resonant mode relative transmission. For example, modes with near unity relative transmission may be found to have $\overline{T}^{\text{max}} > 1$.

Here $g(\lambda)$ function associated with the reference device X (any one of the four) are given by,

$$g_{\text{X}}(\lambda) = \eta^{\text{mean}}_{\text{ref,X}}(\lambda)\left[1 + A\cos\left(\frac{2\pi}{\Delta\lambda_{\text{FSR}}}\lambda + \phi\right)\right], \tag{D.14}$$

where $\eta^{\text{mean}}_{\text{ref,X}}(\lambda)$ is the slowly varying spectrum that results when the fast oscillations are filtered out of $\eta_{\text{ref,X}}(\lambda)$ calculated by Eqns. (D.10) to (D.13). The $\eta^{\text{mean}}_{\text{ref,X}}(\lambda)$ are plotted for each spectrum in D.1(b) and (c) as a green centerline. To find oscillation amplitude, A, and the period, $\Delta\lambda_{\text{FSR}}$, the experimental data in D.1(b) and (c) are replotted in Figure D.1(d) as $[\eta_{\text{ref,X}}(\lambda) - \eta^{\text{mean}}_{\text{ref,X}}(\lambda)]/\eta^{\text{mean}}_{\text{ref,X}}(\lambda)$, and are fit with the function $A\cos\left(\frac{2\pi}{\Delta\lambda_{\text{FSR}}}\lambda + \phi\right)$. The amplitudes are found to be $A \simeq 0.075$ and the periods are $\Delta\lambda_{\text{FSR}} \simeq 2.06$ nm, while the phase shifts varying between 0 to 2π. The best fit cosine functions are plotted as black lines in Figure D.1(d), and the $g(\lambda, \phi)$ functions are plotted as solid black lines in D.1(b) and (c).

It is important to note that the $g_{\text{in}}(\lambda)$ and $g_{\text{out}}(\lambda)$ functions, determined from $\eta^{\text{in}}_{\text{ref,PCwg}}(\lambda)$ and $\eta^{\text{out}}_{\text{ref,PCwg}}(\lambda)$ respectively, must be found for each set of devices studied with different s_{gc} and s_{h} pairs, as the grating coupling spectral features depend on s_{gc}, and the PC waveguide spectral features depend on s_{h}.

D.3.2 Fabry-Perot model comparison

The relationship between the $A, \Delta\lambda_{\text{FSR}}$ and ϕ parameters, and the properties of the parabolic waveguide Fabry-Perot cavity, are now discussed. The transmission of light through a general Fabry-Perot cavity has the following form [85],

$$T_{\text{FP}}(\lambda) = \frac{T_{\text{max}}(\lambda)}{1 + \left(\frac{2\mathscr{F}}{\pi}\right)^2 \sin^2\left(\frac{2\pi n_{\text{g}} L}{\lambda}\right)} \tag{D.15}$$

where $\mathscr{F} = \pi(R_1R_2)^{1/4}/(1-\sqrt{R_1R_2})$ is the finesse for the weak cavity, and $T_{\max}(\lambda) = T_1T_2/(1-\sqrt{R_1R_2})$ is the maximum transmission. This is used as an approximate model for the Fabry-Perot cavity formed by the parabolic waveguide. The grating coupler is taken to be the first reflector, with transmission $T_1 = T_{\text{GC}}$ and $R_1 = R_{\text{GC}}$, and other end of the parabolic waveguide, where the constriction is fastest, is considered to be the other reflector with $T_2 = T_{\text{par}}$ and $R_2 = R_{\text{par}}$. The phase shifts accumulated on reflection are ignored here. The group index is taken to be constant within the parabolic waveguide, which is an oversimplification, as multiple different modes are excited throughout the waveguide as it expands. Despite these approximations, this model provides a foundation to study some of the basic physics of this effective cavity. In the limit of low finesse, the cavity transmission is,

$$
\begin{aligned}
T_{\text{FP}}(\lambda) \simeq & T_{\max}(\lambda)\left[1-\left(\frac{2\mathscr{F}}{\pi}\right)^2 \sin^2\left(\frac{2\pi n_{\text{g}}L}{\lambda}\right)\right] && \text{(D.16)}\\
= & T_{\max}(\lambda)\left[1-B+B\cos\left(\frac{4\pi n_{\text{g}}L}{\lambda}\right)\right], && \text{(D.17)}
\end{aligned}
$$

where $B = 2(\mathscr{F}/\pi)^2$. Using a Taylor Series expansion for $1/\lambda$ around $\lambda_0 = 1545$ nm, it is approximated as,

$$
T_{\text{FP}}(\lambda) \simeq T_{\max}(\lambda)\left[1-B+B\cos\left(\frac{2\pi}{\Delta\lambda_{\text{FSR}}}\lambda+\phi(\lambda_0)\right)\right], \tag{D.18}
$$

where $\Delta\lambda_{\text{FSR}} = \lambda_0^2/(2n_{\text{g}}L)$ is the free spectral range [5], and $\phi(\lambda_0)$ is a phase shift. The form of the model function $g(\lambda,\phi)$ presented above in Eqn. (4.4), is matched to $T_{\text{FP}}(\lambda)$ by setting $\eta_{\text{ref,X}}^{\text{mean}}(\lambda) = T_{\max}(\lambda)(1-B)$ and $A = B/(1-B)$.

Finite-difference time-domain simulations predict that the parabolic waveguide reflection is approximately independent of wavelength, with $R_{\text{par}} \simeq 0.0008$, while the grating reflection (from inside the parabolic waveguide) varies between $R_{\text{GC}} \simeq 0.02$ to 0.03 over $\lambda = 1530$ nm to 1580 nm. The group index for the fundamental mode of the 500 nm wide channel waveguide is $n_{\text{g}} = 4.22$ near $\lambda = 1545$ nm, while that for the 20 μm on the other end of the parabolic waveguide is $n_{\text{g}} = 3.59$. These simulated parameters result in an estimated $A \simeq 0.01$, which is within an order of magnitude from that found experimentally, and $\Delta\lambda_{\text{FSR}} \simeq 1.9 - 2.2$ nm, which is very close to experiment.

[5]This FSR is consistent with that found in Eqn. 2.1 in Section 2.1.1, where $\text{FSR}/\omega_0 \simeq \Delta\lambda_{\text{FSR}}/\lambda_0$.

The locations of the sinusoidal peak wavelengths in the experimental Fabry-Perot spectra in Fig. D.1 are similar for three of the four devices in the set studied here, while one is shifted by $\sim \Delta\lambda_{\mathrm{FSR}}/3$. In general, there can be variation in the peak locations across a set of devices due to fabrication imperfections in the relatively long parabolic waveguides ($L \simeq 100\lambda$). For example, Fabry-Perot peaks near $\lambda = 1545$ nm shift by approximately one $\Delta\lambda_{\mathrm{FSR}}$ if the group index changes by 0.5%.

D.3.3 Channel-to-photonic crystal waveguide transmission

Finally, the coupling efficiencies between the channel waveguides and the input/output PC waveguides are found by taking $\eta_{\mathrm{PCwg}}(\lambda) = \eta^{\mathrm{mean}}_{\mathrm{ref,PCwg}}(\lambda)/\eta^{\mathrm{mean}}_{\mathrm{ref,GC}}(\lambda)$, where the appropriate "in"/"out" superscripts are applied across the efficiencies. The PC waveguide coupling efficiencies are plotted in Figure D.1(e). Near $\lambda = 1545$ nm, $\eta^{\mathrm{in}}_{\mathrm{PCwg}}(\lambda) = 0.86$ and $\eta^{\mathrm{out}}_{\mathrm{PCwg}}(\lambda) = 0.78$, which are lower than those simulated, $\eta^{\mathrm{sim,in}}_{\mathrm{PCwg}}(\lambda) = 0.93$ and $\eta^{\mathrm{sim,out}}_{\mathrm{PCwg}}(\lambda) = 0.92$. The efficiencies here are plotted only over the range of wavelengths where microcavity modes appear, however by inspecting Fig. D.1(a) and (e), there appears to be a large drop in the PC waveguide coupling efficiencies at long wavelengths, near $\lambda = 1564$, and $\lambda = 1554$, for input and output PC waveguides, respectively. This is due to the presence of the low-energy waveguide mode band edge. The efficiency drops observed in simulations of the waveguide coupling region occur at $\lambda = 1587$ nm, and $\lambda \simeq 1576$ nm, respectively. This large ~ 24 nm difference between the experimental and simulated results is surprising given that the cavity resonant modes compare quite closely (within several nanometers), and might also be related to the difference between the experimental and simulated coupling efficiencies.

D.4 Filter transmission efficiency

Three fibre-coupled spectral filters (JDSU TB9 Tunable Grating Filter) are included in the optical set-up for four-wave mixing. Two of which are placed before single photon detector, allowing idler photons to pass while rejecting pump and signal photons, while the third is placed after the high power tunable laser (Venturi TLB 6600-H-CL) to suppress noise. The transmission efficiency spectrum for each grating filter, plotted in Figs. D.2(a) and (b) on linear and log scales respectively, is measured by sweeping the wavelength of the low power laser (Venturi TLB 6600-L-CL) while the filter centre wavelength is held fixed at $\lambda = 1545$ nm [6]. The peak transmission efficiencies are 0.63, 0.56 and 0.65 for filters A, B and C, respectively and the FWHM widths are 0.235 nm, 0.243 nm and 0.231 nm, which are close to the specifications (peak transmission > 0.4, and bandwidth 0.25 ± 0.15 nm). The wavelength calibration is slightly varied between different filters and the laser, as shown by the small offsets in the peak wavelengths from 1545 nm. Each filter has > 40 dB rejection for wavelengths > 1 nm away from the center, as seen in the log scale plot in Fig. D.2(b).

The transmission efficiency spectrum for filters A and B paired together is plotted in Figs. D.2(c) and (d) on linear and log scales, respectively. Here the center wavelengths for filter B are offset such that the peak transmission for A and B are aligned. The peak transmission efficiency is $\eta_{\text{filter}} = 0.355 \pm 0.010$, the bandwidth is 0.166 nm. The uncertainty in η_{filter} is primarily due to the uncertainty in the filter wavelength alignment during FWM measurements ($\sim \pm 0.02$ nm). The rejection at approximately one mode spacing (~ 2.4 nm) away from the peak is ~ 100 dB.

The filter C is placed at the output of the high power laser suppresses the noise from -43 dB down to ~ -90 dB, which is sufficient for practical four-wave mixing measurements, as described in Section 2.3.1.

D.5 Single photon detector efficiency and dead-time

The single photon detector is implemented in "free-running mode", where the avalanche photodiode is biased above the breakdown voltage threshold, such that the absorption a photon triggers an avalanche that produces effectively an infinite gain, resulting in sufficient amplification to detect the single photon. The avalanche is quenched after a detection event (i.e. the diode is biased below the breakdown voltage) for the duration of the "dead time". The efficiency of the detector is improved by increasing the bias voltage above the breakdown, however, this comes at the cost decreasing the signal to noise, due to carriers generated in the diode junction that also trigger the avalanche response, resulting in dark counts. Unwanted counts are also generated by an effect called "after pulsing", when carriers generated and trapped during an avalanche are released and retrigger

[6] This measurement is easier to implement than holding the laser wavelength fixed and scanning the filter center wavelength. Both approaches give very close to the same results.

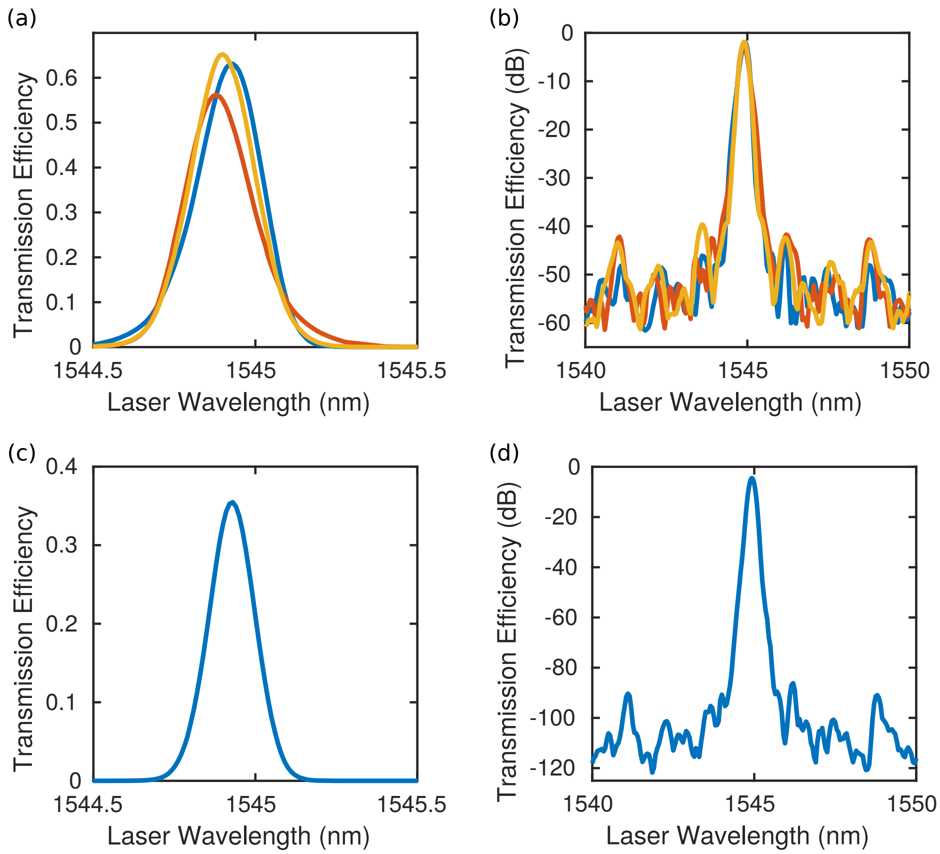

Figure D.2: Spectral filter transmission efficiencies measured by fixing the filter center wavelength at $\lambda_{\text{filter}} =$ 1545 nm and sweeping the laser wavelength. (a) Transmission efficiencies of filters A (blue), B (red) and C (yellow) on a linear scale. (b) Same as (a) but on a log scale. (c) Product of the transmission efficiencies for filters A and B, when their peak wavelengths are aligned, plotted on a linear scale. (d) Same as (c) but on a log scale.

the avalanche. After-pulsing effects are reduced by using a longer dead time. The efficiency and deadtime settings used in this thesis are 0.10 and 100 μs.

To determine the *actual* average rate of photons incident on the detector (R_{ph}) based on the total count rate (R_{tot}) measured, the detector efficiency (η_{D}), dead-time (τ_{DT}), and dark count rate (R_{DC}) must all be considered. The dark count rate, R_{DC}, is measured by blocking the light that enters the detector. The raw count rates R_{tot} and R_{DC} reported by the detector represent the average number of counts per time, where this "per time" includes when the detector is blanked (during the dead-time). The true detection rate, which represents the number of counts per active detector time, are calculated by,

$$R_{\text{active}}(R, \tau_{\text{DT}}) = (R^{-1} - \tau_{\text{DT}})^{-1}, \tag{D.19}$$

where $R = R_{\text{tot}}$ or R_{DC}. The average rate of photons incident on the detector is,

$$R_{\text{ph}} = \frac{R_{\text{active}}(R_{\text{tot}}, \tau_{\text{DT}}) - R_{\text{active}}(R_{\text{DC}}, \tau_{\text{DT}})}{\eta_{\text{D}}}. \tag{D.20}$$

To enable accurate calculations of R_{ph}, η_{D} and τ_{DT} are measured by strongly attenuating light from a laser and sending it into the detector. Figure D.3(a) is a plot of the detected power as a function of input power for measurements with two different attenuation schemes. The detected power is calculated as $P_{\text{D}} = \hbar\omega_0[R_{\text{active}}(R_{\text{tot}}, \tau_{\text{DT}}) - R_{\text{active}}(R_{\text{DC}}, \tau_{\text{DT}})]$, where ω_0 is the laser frequency. The gray circles show the calculated detected power when $\tau_{\text{DT}} = 100$ μs is applied. A linear relationship is expected between the input and detected power (i.e. constant detection efficiency), away from the detector saturation, however this is not observed with $\tau_{\text{DT}} = 100$ μs (see the black line for reference). The nonlinear trend is arises due to the deviation of the *actual* dead-time from the detector setting value. Even a small deviation causes a large error for high count rates, when R_{tot}^{-1} approaches τ_{DT}. The actual dead-time is estimated using a least squares calculation that involves minimizing the squared difference between the calculated $P_{\text{D}}(P_{\text{in}}, \tau_{\text{DT}})$ and the linear best fit to $P_{\text{D}}(P_{\text{in}}, \tau_{\text{DT}})$. The X^2 for this calculation is given by

$$X^2(\tau_{\text{DT}}) = \sum_{P_{\text{in}}} \frac{[P_{\text{D}}(P_{\text{in}}, \tau_{\text{DT}}) - h_{\text{DT}}(P_{\text{in}}, \tau_{\text{DT}})]^2}{\sigma_P^2} \tag{D.21}$$

where P_{in} is the input power, σ_P is the measurement uncertainty in $P_{\text{D}}(P_{\text{in}}, \tau_{\text{DT}})$, and $h_{\text{DT}}(P_{\text{in}}, \tau_{\text{DT}})$ is the best linear fit to $P_{\text{D}}(P_{\text{in}}, \tau_{\text{DT}})$. The X^2 is plotted as a function of τ_{DT} in Fig. D.3(b), and is clearly minimized for $\tau_{\text{DT}} = 99.9788$ μs. The detected power, calculated with the best fit $\tau_{\text{DT}} = 99.9788$ μs, is plotted for the two data sets (blue circles and orange triangles) in Fig. D.3(a), along with the best linear fit trend (black line referred to earlier). For the highest input power tested here, $P_{\text{in}} = 13.3$ pW, there is a 25% difference between $P_{\text{D}}(13.3\ \text{pW}, 100\ \mu\text{s})$ and $P_{\text{D}}(13.3\ \text{pW}, 99.9788\ \mu\text{s})$, which is substantial given the small difference in the τ_{DT} applied. Based on the slope of the line of best fit, the detector efficiency is $\eta_{\mathrm{D}} = 0.116 \pm 0.005$. The detector efficiencies, $P_{\mathrm{D}}(P_{\mathrm{in}}, 99.9788\ \mu\mathrm{s})/P_{\mathrm{in}}$, are plotted in Fig. D.3(c), where the error bars show the uncertainty in the measurement. Based on the detector specifications, the efficiency is expected to be vary by less than 0.003 over the wavelength range of interest.

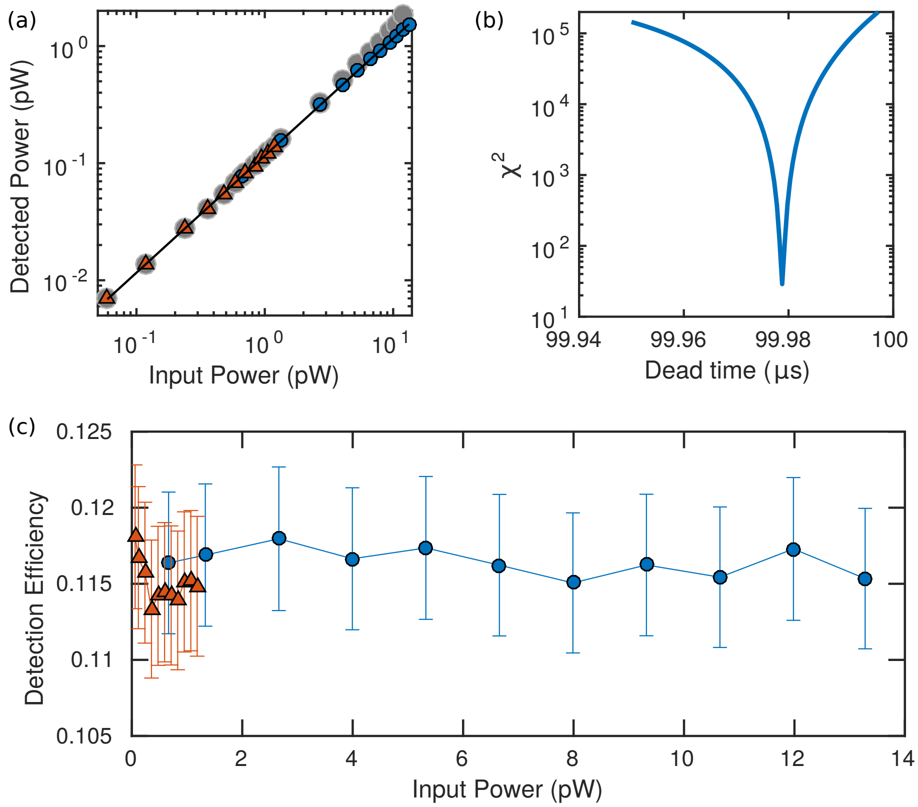

Figure D.3: Single photon detector characterization, when set with a dead time of 100 μs and efficiency 10 %. (a) Detected power calculated with a dead-time $\tau_{\mathrm{DT}} = 99.9788\ \mu$s for high-power (blue circles) and low-power (orange triangles) measurements, and calculated with the detector setting $\tau_{\mathrm{DT}} = 100\ \mu$s is also plotted (large gray circles). The line of best fit for $\tau_{\mathrm{DT}} = 99.9788\ \mu$s is plotted (black line), with the slope giving detection efficiency $\eta_D = 0.116$. (b) Chi squared based on the square differences between the calculated detected power (dependent on τ_{DT}) and the linear best fit to the data. The X^2 is minimized for $\tau_{\mathrm{DT}} = 99.9788\ \mu$s. (c) The detection efficiencies calculated with $\tau_{\mathrm{DT}} = 99.9788\ \mu$s for high-power (blue circles) and low-power (orange triangles) measurements. Error bars show uncertainty in the measurement.

The stimulated FWM idler power is ultimately found by subtracting off the background photon counts, measured when the signal laser is turned off, while the pump laser remains active. The idler power is calculated as,

$$P_{\text{idler}} = \frac{\hbar\omega_0}{\eta_{\text{tot}}^{\text{out}}\eta_{\text{fibre}}\max[\eta_{\text{filter}}(\lambda)]\eta_D}\Big(R_{\text{active}}(R_{\text{tot}}^{\text{FWM}}, \tau_{\text{DT}}) - R_{\text{active}}(R_{\text{DC}}^{\text{FWM}}, \tau_{\text{DT}}) - [R_{\text{active}}(R_{\text{tot}}^{\text{BG}}, \tau_{\text{DT}}) - R_{\text{active}}(R_{\text{DC}}^{\text{BG}}, \tau_{\text{DT}})]\Big), \tag{D.22}$$

where “BG” indicates the background count rate.

Appendix E

Nonlinear model function derivations

In this Appendix, the perturbative approach used to introduce nonlinearities to the coupled mode equations presented in Chapter 5 is reviewed. The nonlinear frequency shifts and lifetimes in Table 5.2 are derived, along with the nonlinear coefficients in Table 5.3.

E.1 Perturbation theory

As discussed in Chapter 5, the nonlinearity is introduced to the coupled mode equations through weak complex-valued changes in the mode resonance frequencies, $\omega_m \rightarrow \omega_m + \delta\omega_m^{\mathrm{NL}}$, due to perturbations of the dielectric constant $\delta\varepsilon_m^{\mathrm{NL}}(\mathbf{r})$, where [39],

$$\frac{\delta\omega_m^{\mathrm{NL}}}{\omega_m} = -\frac{1}{2}\frac{\int d^3\mathbf{x}\delta\varepsilon_m^{\mathrm{NL}}(\mathbf{r})|\mathbf{E}_m(\mathbf{r})|^2}{\int d^3\mathbf{x}\varepsilon(\mathbf{r})|\mathbf{E}_m(\mathbf{r})|^2} \tag{E.1}$$

and $\mathbf{E}_m(\mathbf{r}) = a_m\breve{\mathbf{E}}_m(\mathbf{r})/\sqrt{\int d^3\mathbf{x}\frac{1}{2}\varepsilon(\mathbf{r})|\breve{\mathbf{E}}_m(\mathbf{r})|^2}$ is the m^{th} steady-state mode field. There are a number of contributions to $\delta\omega_m^{\mathrm{NL}}$:

$$\delta\omega_m^{\mathrm{NL}} = \delta\omega_m^{\mathrm{Kerr}} + \delta\omega_m^{\mathrm{FWM}} + \delta\omega_m^{\mathrm{TPA}} + \delta\omega_m^{\mathrm{FCA}} + \delta\omega_m^{\mathrm{FCD}} + \delta\omega_m^{\mathrm{thermal}}, \tag{E.2}$$

which are associated with the Kerr effect, four-wave mixing, two-photon absorption, free-carrier absorption, free-carrier dispersion, and thermal dispersion. The first three contributions, $\delta\omega_m^{(3)} = \delta\omega_m^{\mathrm{Kerr}} + \delta\omega_m^{\mathrm{FWM}} + \delta\omega_m^{\mathrm{TPA}}$, are directly a result of the third order nonlinear susceptibility $\boldsymbol{\chi}^{(3)}$ of silicon, while other effects are indirectly associated with these nonlinearities.

The perturbation due to the third order nonlinearity is rewritten in terms of the third order polarization, $\mathbf{P}_m^{(3)}(\mathbf{r}) = \delta\varepsilon_m^{(3)}(\mathbf{r})\mathbf{E}_m(\mathbf{r})$, to give [71],

$$\frac{\delta\omega_m^{(3)}}{\omega_m} = -\frac{1}{2}\frac{\int d^3\mathbf{x}\mathbf{P}_m^{(3)}(\mathbf{r})\cdot\mathbf{E}_m^*(\mathbf{r})}{\int d^3\mathbf{x}\varepsilon(\mathbf{r})|\mathbf{E}_m(\mathbf{r})|^2}. \tag{E.3}$$

In this model for FWM, it is assumed that the electric field is composed of monochromatic waves at the frequencies $\{\omega_i'\} = \{\pm\omega_m\}$ $(m = 1, 2, 3)$ such that [16],

$$\mathbf{E}(\mathbf{r}, t) = \frac{1}{2}\sum_{\omega_i'\geq 0}\left[\mathbf{E}_{\omega_i'}(\mathbf{r})e^{-i\omega_i' t} + \mathbf{E}_{-\omega_i'}(\mathbf{r})e^{i\omega_i' t}\right] \tag{E.4}$$

where $\mathbf{E}_{-\omega_i'}(\mathbf{r}) = \mathbf{E}^*_{\omega_i'}(\mathbf{r})$ and $\mathbf{E}_{\omega_m}(\mathbf{r}) = \mathbf{E}_m(\mathbf{r})$ above. Similarly,

$$\mathbf{P}^{(3)}(\mathbf{r}, t) = \frac{1}{2}\sum_{\omega_i'\geq 0}\left[\mathbf{P}^{(3)}_{\omega_i'}(\mathbf{r})e^{-i\omega_i' t} + \mathbf{P}^{(3)}_{-\omega_i'}(\mathbf{r})e^{i\omega_i' t}\right]. \tag{E.5}$$

The frequency dependent electric field and polarization are found by taking the fourier transforms of (E.4) and (E.5) respectively, resulting in,

$$\mathbf{E}(\mathbf{r}, \omega) = \frac{1}{2}\sum_{\omega_i'\geq 0}\left[\mathbf{E}_{\omega_i'}(\mathbf{r})\delta(\omega - \omega_i') + \mathbf{E}_{-\omega_i'}(\mathbf{r})\delta(\omega + \omega_i')\right] \tag{E.6}$$

$$\mathbf{P}^{(3)}(\mathbf{r}, \omega) = \frac{1}{2}\sum_{\omega_i'\geq 0}\left[\mathbf{P}^{(3)}_{\omega_i'}(\mathbf{r})\delta(\omega - \omega_i') + \mathbf{P}^{(3)}_{-\omega_i'}(\mathbf{r})\delta(\omega + \omega_i')\right]. \tag{E.7}$$

In general, the nonlinear polarization is given by,

$$\mathbf{P}^{(3)}(\mathbf{r}, \omega) = \varepsilon_0\int d\omega_1\int d\omega_2\int d\omega_3\boldsymbol{\chi}^{(3)}\cdots\mathbf{E}(\mathbf{r}, \omega_1)\mathbf{E}(\mathbf{r}, \omega_2)\mathbf{E}(\mathbf{r}, \omega_3)\delta(\omega - \omega_1 - \omega_2 - \omega_3) \tag{E.8}$$

where "$\cdots$" indicates multiplication over three tensor dimensions. This is alternatively written as,

$$(P^{(3)}(\mathbf{r}, \omega))_\alpha = \varepsilon_0\sum_{ijk}\int d\omega_1\int d\omega_2\int d\omega_3\chi^{(3)}_{\alpha ijk}E_i(\mathbf{r}, \omega_1)E_j(\mathbf{r}, \omega_2)E_k(\mathbf{r}, \omega_3)\delta(\omega - \omega_1 - \omega_2 - \omega_3) \tag{E.9}$$

to explicitly show the tensor multiplication, where i, j and k are each summed over $\{x, y, z\}$.

Substituting (E.6) into (E.8) yields $(3 \times 2)^3$ terms inside of the summation, although not all of which are unique. For example, consider a set of three frequencies, $\omega_x : \{\omega_x^1, \omega_x^2, \omega_x^3\}$ where $\omega_x = \omega_x^1 + \omega_x^2 + \omega_x^3$ and each ω_x^i is one of the $\pm\omega_i'$ terms. The polarization amplitude for ω_x will have terms that look like,

$$(P^{(3)}_{\omega_x})_\alpha = 2\varepsilon_0 \sum_{ijk} \bigg[\chi^{(3)}_{\alpha ijk}(-\omega_x; \omega_x^1, \omega_x^2, \omega_x^3) \frac{1}{2}(E_{\omega_x^1})_i \frac{1}{2}(E_{\omega_x^2})_j \frac{1}{2}(E_{\omega_x^3})_k \tag{E.10}$$

$$+\chi^{(3)}_{\alpha ijk}(-\omega_x; \omega_x^2, \omega_x^1, \omega_x^3) \frac{1}{2}(E_{\omega_x^2})_i \frac{1}{2}(E_{\omega_x^1})_j \frac{1}{2}(E_{\omega_x^3})_k \tag{E.11}$$

$$+ \ldots \bigg].$$

Here the **r**-dependence has be dropped for convenience. The terms in (E.10) and (E.11) are identical, as is found by relabelling dummy indices (i, j) in (E.11) to (j, i), then applying permutation symmetry $\chi^{(3)}_{\alpha,i,j.k}(-\omega_x; \omega_x^1, \omega_x^2, \omega_x^3) = \chi^{(3)}_{\alpha,j,i,k}(-\omega_x; \omega_x^2, \omega_x^1, \omega_x^3))$. The number of identical terms that appear depends how many distinguishable frequencies ω_x^i there are in the ω_x set, as sets with two or more identical ω_x^i will result in fewer identical terms. The polarization is written as,

$$(P^{(3)}_{\omega_x})_\alpha = \varepsilon_0 \sum_{ijk} K(-\omega_x; \omega_x^1, \omega_x^2, \omega_x^3) \chi^{(3)}_{\alpha ijk}(-\omega_x; \omega_x^1, \omega_x^2, \omega_x^3)(E_{\omega_x^1})_i (E_{\omega_x^2})_j (E_{\omega_x^3})_k \tag{E.12}$$

where

$$K(-\omega_x; \omega_x^1, \omega_x^2, \omega_x^3) = \left(\frac{1}{4}\right) \frac{3!}{N_x^a! N_x^b! N_x^c!}. \tag{E.13}$$

The right-most fraction in $K(-\omega_x; \omega_x^1, \omega_x^2, \omega_x^3)$ is the number of permutations of $\{\omega_x^i\}$, where N_x^a, N_x^b, N_x^c are the number of times each *unique* ω_x^i (labelled $a, b, c..$) appear in $\{\omega_x^i\}$.

In general, the same ω_x can be achieved with distinct sets. For example, when ω_1, ω_2 and ω_3 are equally spaced (as is the case for FWM), then two possible distinct sets are $\omega_1 : \{\omega_2, \omega_2, -\omega_3\}$ and $\omega_1 : \{\omega_1, \omega_2, -\omega_2\}$. The polarization amplitude in (E.12) is generalized to sum of distinct sets of ω_x,

$$(P^{(3)}_{\omega_x})_\alpha = \varepsilon_0 \sum_{\text{distinct } \{-\omega_x;\omega_x^1,\omega_x^2,\omega_x^3\}} \sum_{ijk} K(-\omega_x;\omega_x^1,\omega_x^2,\omega_x^3)\chi^{(3)}_{\alpha ijk}(-\omega_x;\omega_x^1,\omega_x^2,\omega_x^3)(E_{\omega_x^1})_i(E_{\omega_x^2})_j(E_{\omega_x^3})_k. \tag{E.14}$$

In evaluating the sum over i, j, k, it is useful to consider the crystalline properties of the nonlinear material. In this study, the device layer is silicon, which is a centrosymmetric $3m3$ crystal with non-zero $\boldsymbol{\chi}^{(3)}$ tensor terms [14]:

$$\begin{aligned}
&\chi^{(3)}_{xxxx} = \chi^{(3)}_{yyyy} = \chi^{(3)}_{zzzz}\\
&\chi^{(3)}_{xyxy} = \chi^{(3)}_{yxyx} = \chi^{(3)}_{xzxz} = \chi^{(3)}_{zxzx} = \chi^{(3)}_{yzyz} = \chi^{(3)}_{zyzy}\\
&\chi^{(3)}_{xxyy} = \chi^{(3)}_{yyxx} = \chi^{(3)}_{xxzz} = \chi^{(3)}_{zzxx} = \chi^{(3)}_{yyzz} = \chi^{(3)}_{zzyy}\\
&\chi^{(3)}_{xyyx} = \chi^{(3)}_{yxxy} = \chi^{(3)}_{xzzx} = \chi^{(3)}_{zxxz} = \chi^{(3)}_{yzzy} = \chi^{(3)}_{zyyz}
\end{aligned} \tag{E.15}$$

and $\chi^{(3)}_{xxxx} = 3\chi^{(3)}_{xyxy} = 3\chi^{(3)}_{xxyy} = 3\chi^{(3)}_{xyyx}$. In the following, the notation for $\chi^{(3)}_{iiii}$ is simplified to $\chi^{(3)}_{\text{Si}}$ for silicon, as is typical in the literature.

The non-zero $\boldsymbol{\chi}^{(3)}$ tensor terms are evaluated in (E.14), and applied to $\mathbf{P}^{(3)}_m(\mathbf{r}) \cdot \mathbf{E}^*_m(\mathbf{r})$ in the perturbation equation (E.3), to give,

$$\begin{aligned}
\mathbf{P}^{(3)}_{\omega_m} \cdot \mathbf{E}_{-\omega_m} = \frac{\varepsilon_0}{3} \sum_{\text{distinct } \{-\omega_m;\omega_m^1,\omega_m^2,\omega_m^3\}} & K(-\omega_m;\omega_m^1,\omega_m^2,\omega_m^3)\chi^{(3)}_{\text{Si}}(-\omega_m;\omega_m^1,\omega_m^2,\omega_m^3)\\
&\Big[(\mathbf{E}_{\omega_m^1}\cdot\mathbf{E}_{\omega_m^2})(\mathbf{E}_{\omega_m^3}\cdot\mathbf{E}_{-\omega_m}) + (\mathbf{E}_{\omega_m^1}\cdot\mathbf{E}_{\omega_m^3})(\mathbf{E}_{\omega_m^2}\cdot\mathbf{E}_{-\omega_m})\\
&+(\mathbf{E}_{\omega_m^1}\cdot\mathbf{E}_{-\omega_m})(\mathbf{E}_{\omega_m^2}\cdot\mathbf{E}_{\omega_m^3})\Big]
\end{aligned} \tag{E.16}$$

A summary of the $K(-\omega_m;\omega_m^1,\omega_m^2,\omega_m^3)$ values and the electric field terms for each distinct set at each of the mode frequencies is listed in Table E.1. The simplified notation for the electric field profile, $\mathbf{E}_m(\mathbf{r}) = \mathbf{E}_{\omega_m}(\mathbf{r})$, is used in this table and in the following.

The perturbed mode frequencies are found by using the terms in Table E.1 to insert (E.16) into (E.3), and by substituting, $\mathbf{E}_m(\mathbf{r}) = a_m\breve{\mathbf{E}}_m(\mathbf{r})/\sqrt{\int d^3\mathbf{x}\frac{1}{2}\varepsilon(\mathbf{r})|\breve{\mathbf{E}}_m(\mathbf{r})|^2}$,

Table E.1: Polarization terms for four-wave mixing. For each mode, m, $K(-\omega_m;\omega_m^1,\omega_m^2,\omega_m^3)$ and electric field terms are listed for each distinct set for ω_m.

m	Distinct sets for ω_m	K	Electric field terms
1	$\{\omega_2,\omega_2,-\omega_3\}$	$\frac{3}{4}$	$(\mathbf{E}_2\cdot\mathbf{E}_2)(\mathbf{E}_1^*\cdot\mathbf{E}_3^*)+2(\mathbf{E}_2\cdot\mathbf{E}_1^*)(\mathbf{E}_2\cdot\mathbf{E}_3^*)$
	$\{\omega_1,\omega_1,-\omega_1\}$	$\frac{3}{4}$	$(\mathbf{E}_1\cdot\mathbf{E}_1)(\mathbf{E}_1^*\cdot\mathbf{E}_1^*)+2\lvert\mathbf{E}_1\rvert^4$
	$\{\omega_1,\omega_2,-\omega_2\}$	$\frac{3}{2}$	$(\mathbf{E}_1\cdot\mathbf{E}_2)(\mathbf{E}_1^*\cdot\mathbf{E}_2^*)+(\mathbf{E}_1\cdot\mathbf{E}_2^*)(\mathbf{E}_1^*\cdot\mathbf{E}_2)+\lvert\mathbf{E}_1\rvert^2\lvert\mathbf{E}_2\rvert^2$
	$\{\omega_1,\omega_3,-\omega_3\}$	$\frac{3}{2}$	$(\mathbf{E}_1\cdot\mathbf{E}_3)(\mathbf{E}_1^*\cdot\mathbf{E}_3^*)+(\mathbf{E}_1\cdot\mathbf{E}_3^*)(\mathbf{E}_1^*\cdot\mathbf{E}_3)+\lvert\mathbf{E}_1\rvert^2\lvert\mathbf{E}_3\rvert^2$
2	$\{\omega_1,\omega_3,-\omega_2\}$	$\frac{3}{2}$	$(\mathbf{E}_2^*\cdot\mathbf{E}_2^*)(\mathbf{E}_1\cdot\mathbf{E}_3)+2(\mathbf{E}_2^*\cdot\mathbf{E}_1)(\mathbf{E}_2^*\cdot\mathbf{E}_3)$
	$\{\omega_2,\omega_1,-\omega_1\}$	$\frac{3}{2}$	$(\mathbf{E}_2\cdot\mathbf{E}_1)(\mathbf{E}_2^*\cdot\mathbf{E}_1^*)+(\mathbf{E}_2\cdot\mathbf{E}_1^*)(\mathbf{E}_2^*\cdot\mathbf{E}_1)+\lvert\mathbf{E}_2\rvert^2\lvert\mathbf{E}_1\rvert^2$
	$\{\omega_2,\omega_2,-\omega_2\}$	$\frac{3}{4}$	$(\mathbf{E}_2\cdot\mathbf{E}_2)(\mathbf{E}_2^*\cdot\mathbf{E}_2^*)+2\lvert\mathbf{E}_2\rvert^4$
	$\{\omega_2,\omega_3,-\omega_3\}$	$\frac{3}{2}$	$(\mathbf{E}_2\cdot\mathbf{E}_3)(\mathbf{E}_2^*\cdot\mathbf{E}_3^*)+(\mathbf{E}_2\cdot\mathbf{E}_3^*)(\mathbf{E}_2^*\cdot\mathbf{E}_3)+\lvert\mathbf{E}_2\rvert^2\lvert\mathbf{E}_3\rvert^2$
3	$\{\omega_2,\omega_2,-\omega_1\}$	$\frac{3}{4}$	$(\mathbf{E}_2\cdot\mathbf{E}_2)(\mathbf{E}_1^*\cdot\mathbf{E}_3^*)+2(\mathbf{E}_2\cdot\mathbf{E}_1^*)(\mathbf{E}_2\cdot\mathbf{E}_3^*)$
	$\{\omega_3,\omega_1,-\omega_1\}$	$\frac{3}{2}$	$(\mathbf{E}_3\cdot\mathbf{E}_1)(\mathbf{E}_3^*\cdot\mathbf{E}_1^*)+(\mathbf{E}_3\cdot\mathbf{E}_1^*)(\mathbf{E}_3^*\cdot\mathbf{E}_1)+\lvert\mathbf{E}_3\rvert^2\lvert\mathbf{E}_1\rvert^2$
	$\{\omega_3,\omega_2,-\omega_2\}$	$\frac{3}{2}$	$(\mathbf{E}_3\cdot\mathbf{E}_2)(\mathbf{E}_3^*\cdot\mathbf{E}_2^*)+(\mathbf{E}_3\cdot\mathbf{E}_2^*)(\mathbf{E}_3^*\cdot\mathbf{E}_2)+\lvert\mathbf{E}_3\rvert^2\lvert\mathbf{E}_2\rvert^2$
	$\{\omega_3,\omega_3,-\omega_3\}$	$\frac{3}{4}$	$(\mathbf{E}_3\cdot\mathbf{E}_3)(\mathbf{E}_3^*\cdot\mathbf{E}_3^*)+2\lvert\mathbf{E}_3\rvert^4$

$$\begin{aligned}
\frac{\delta\omega_1^{(3)}}{\omega_1} &= -\beta_1(a_2)^2(a_3)^*/a_1-(\alpha_0+i\rho_0)(\alpha_{11}|a_1|^2+\alpha_{12}|a_2|^2+\alpha_{13}|a_3|^2) \\
\frac{\delta\omega_2^{(3)}}{\omega_2} &= -\beta_2 a_1 a_3(a_2)^*/a_2-(\alpha_0+i\rho_0)(\alpha_{22}|a_2|^2+\alpha_{21}|a_1|^2+\alpha_{23}|a_3|^2) \\
\frac{\delta\omega_3^{(3)}}{\omega_3} &= -\beta_3(a_2)^2(a_1)^*/a_3-(\alpha_0+i\rho_0)(\alpha_{33}|a_3|^2+\alpha_{32}|a_2|^2+\alpha_{31}|a_1|^2)
\end{aligned} \tag{E.17}$$

where

$$\beta_2=\frac{1}{2}\frac{\int_{\mathrm{Si}}d^3\mathbf{x}\varepsilon_0\,\mathrm{Re}(\chi_{\mathrm{Si}}^{(3)})\left[(\breve{\mathbf{E}}_2^*\cdot\breve{\mathbf{E}}_2^*)(\breve{\mathbf{E}}_1\cdot\breve{\mathbf{E}}_3)+2(\breve{\mathbf{E}}_2^*\cdot\breve{\mathbf{E}}_1)(\breve{\mathbf{E}}_2^*\cdot\breve{\mathbf{E}}_3)\right]}{(\int d^3\mathbf{x}\varepsilon(\mathbf{r})|\breve{\mathbf{E}}_2|^2)(\int d^3\mathbf{x}\varepsilon(\mathbf{r})|\breve{\mathbf{E}}_1|^2)^{1/2}(\int d^3\mathbf{x}\varepsilon(\mathbf{r})|\breve{\mathbf{E}}_3|^2)^{1/2}}, \tag{E.18}$$

$$\beta_1=\beta_3=\beta_2^*/2, \tag{E.19}$$

$$\alpha_{m,m} = \frac{\int_{\mathrm{Si}} d^3\mathbf{x}\left[(\breve{\mathbf{E}}_m^* \cdot \breve{\mathbf{E}}_m^*)(\breve{\mathbf{E}}_m \cdot \breve{\mathbf{E}}_m) + 2|\breve{\mathbf{E}}_m|^4\right]}{(\int d^3\mathbf{x}\varepsilon(\mathbf{r})|\breve{\mathbf{E}}_m|^2)^2}, \tag{E.20}$$

$$\alpha_{m,m'} = 2\frac{\int_{\mathrm{Si}} d^3\mathbf{x}\left[(\breve{\mathbf{E}}_m \cdot \breve{\mathbf{E}}_{m'})(\breve{\mathbf{E}}_m^* \cdot \breve{\mathbf{E}}_{m'}^*) + (\breve{\mathbf{E}}_m \cdot \breve{\mathbf{E}}_{m'}^*)(\breve{\mathbf{E}}_m^* \cdot \breve{\mathbf{E}}_{m'}) + |\breve{\mathbf{E}}_m|^2|\breve{\mathbf{E}}_{m'}|^2\right]}{(\int d^3\mathbf{x}\varepsilon(\mathbf{r})|\breve{\mathbf{E}}_m|^2)(\int d^3\mathbf{x}\varepsilon(\mathbf{r})|\breve{\mathbf{E}}_{m'}|^2)}, \tag{E.21}$$

$$\alpha_0 = \frac{\omega_m}{4}\varepsilon_0 \,\mathrm{Re}\left(\chi_{\mathrm{Si}}^{(3)}\right), \tag{E.22}$$

and

$$\rho_0 = \frac{\omega_m}{4}\varepsilon_0 \,\mathrm{Im}\left(\chi_{\mathrm{Si}}^{(3)}\right). \tag{E.23}$$

Here $\int_{\mathrm{Si}}$ indicates integration over the volume occupied by silicon, and $\chi_{\mathrm{Si}}^{(3)}$ is the complex diagonal element of the third order nonlinear susceptibility tensor, with units [$\mathrm{m}^2/\mathrm{V}^2$], where the explicit frequency dependence of $\chi_{\mathrm{Si}}^{(3)}$ is removed. This is appropriate for the nonlinear processes considered, as $\omega_1 \simeq \omega_2 \simeq \omega_3$ thus the same $\chi_{\mathrm{Si}}^{(3)}(-\omega; \pm\omega, \pm\omega, \pm\omega)$ is applied for the mixing processes studied. The explicit dependence of $\breve{\mathbf{E}}_m$ on position $\mathbf{r}$ in the nonlinear coefficients is removed to simplify notation.

The individual contributions to Eqn. (E.17) are identified as,

$$\frac{\delta\omega_1^{\mathrm{FWM}}}{\omega_1} = -\beta_1(a_2)^2(a_3)^*/a_1 \tag{E.24}$$

$$\frac{\delta\omega_2^{\mathrm{FWM}}}{\omega_2} = -\beta_2 a_1 a_3 (a_2)^*/a_2 \tag{E.25}$$

$$\frac{\delta\omega_3^{\mathrm{FWM}}}{\omega_3} = -\beta_3(a_2)^2(a_1)^*/a_3 \tag{E.26}$$

$$\frac{\delta\omega_m^{\mathrm{Kerr}}}{\omega_m} = \alpha_0 \sum_{m'} \alpha_{mm'}|a_{m'}|^2 \tag{E.27}$$

$$\frac{\delta\omega_m^{\mathrm{TPA}}}{\omega_m} = i\rho_0 \sum_{m'} \alpha_{mm'}|a_{m'}|^2 \tag{E.28}$$

where $m' = \{1, 2, 3\}$. The first three terms contribute nonlinear photon generation ($\beta_{\mathrm{FWM}} = \beta_1$ in Chapter 2). Equations (E.27) and (E.28) result in a frequency shift due to the nonlinear Kerr effect $\Delta\omega_m^{\mathrm{Kerr}}$, two photon absorption lifetime τ_m^{TPA}, respectively.

E.2 Nonlinear lifetimes and frequency shifts

In this section, the effects of two-photon absorption (TPA), free-carrier absorption (FCA) and thermal absorption on the cavity mode lifetimes and resonant frequencies are derived, building off of the perturbative approach presented above.

E.2.1 Cavity lifetime

With the inclusion of nonlinear losses, the total cavity lifetime for each mode m, is given by,

$$\tau_m(U_1,U_2,U_3)^{-1} = {\tau_m^{\text{in}}}^{-1} + {\tau_m^{\text{out}}}^{-1} + {\tau_m^{\text{scatt}}}^{-1} + {\tau_m^{\text{abs}}}^{-1} + \tau_m^{\text{TPA}}(U_1,U_2,U_3)^{-1} + \tau_m^{\text{FCA}}(U_1,U_2,U_3)^{-1}, \tag{E.29}$$

where $\tau_m^{\text{TPA}}(U_1,U_2,U_3)$ and $\tau_m^{\text{FCA}}(U_1,U_2,U_3)$ are derived below.

Two-photon absorption (TPA) Two-photon absorption introduces an imaginary part to the $\chi^{(3)}_{\text{Si}}$ tensor, such that $\text{Im}(\chi^{(3)}_{\text{Si}}) = 2\beta^{\text{TPA}}\epsilon_0 c^2 {n_{\text{Si}}}^2/(3\omega_m)$, where β^{TPA} is the TPA coefficient with units [mW^{-1}], and n_{Si} is the index of refraction of the nonlinear material for a single frequency, in this case silicon [51], both found in Table 5.4. The perturbation equation is,

$$\frac{\delta\omega_m^{\text{TPA}}}{\omega_m} = -i\rho_0 \sum_{m'} \alpha_{m,m'}|a_{m'}|^2 \equiv -\frac{i}{\omega_m}\frac{1}{\tau_m^{\text{TPA}}} \tag{E.30}$$

such that the TPA lifetime is,

$$\frac{1}{\tau_m^{\text{TPA}}} = \rho_0 \sum_{m'} \alpha^{\text{TPA}}_{m,m'} U_{m'} \tag{E.31}$$

The $m' = m$ contribution to the TPA lifetime arises from the absorption of two ω_m photons, whereas the $m' \neq m$ contributions arise from absorption of one ω_m photon and one $\omega_{m'}$ photon. The latter process is often referred to as “cross TPA”, or XTPA.

Free-carrier absorption The free-carriers excited in the TPA process present an additional loss mechanism. The Drude model predicts that light propagating in a bulk material, in the presence of free-carriers, is attenuated with loss per unit length,

$$\alpha^{\mathrm{FCA}} = \sigma^{\mathrm{FCA}} N(\mathbf{r}), \tag{E.32}$$

where $N(\mathbf{r})$ is the density of electron hole pairs, and $\sigma^{\mathrm{FCA}} = \sigma_{\mathrm{e}}^{\mathrm{FCA}} + \sigma_{\mathrm{h}}^{\mathrm{FCA}}$ is the free-carrier cross-section with units of [m^2], taken to be the sum of the electron and hole cross-sections, and is found in Table 5.4. The loss per unit length is related to the local absorption rate of the energy density through the group velocity v_g, such that

$$\gamma_m^{\mathrm{FCA}}(\mathbf{r}) = \sigma^{\mathrm{FCA}} v_g N(\mathbf{r}). \tag{E.33}$$

The material dispersion is typically small in bulk measurements, so the group index $n_g \simeq n_{\mathrm{Si}}$, as will be used in the following.

The time dependence of $N(\mathbf{r}, t)$ follows [11, 51],

$$\frac{dN(\mathbf{r}, t)}{dt} = G(\mathbf{r}) - \frac{N(\mathbf{r}, t)}{\tau_{\mathrm{carrier}}(N(\mathbf{r}, t))}, \tag{E.34}$$

where $G(\mathbf{r})$ is the local carrier generation rate, and $\tau_{\mathrm{carrier}}(N(\mathbf{r}, t))$ is the effective free-carrier lifetime, including recombination, diffusion and drift effects. The temperature dependence of τ_{carrier} is neglected here, as the temperature changes due to nonlinear absorption are relatively small. While the local free-carrier lifetime depends on the proximity to surfaces, the $\tau_{\mathrm{carrier}}(N(\mathbf{r}, t))$ considered here represents a mean lifetime for the carrier distribution.

In steady-state,

$$N(\mathbf{r}) = \tau_{\mathrm{carrier}}(N(\mathbf{r})) G(\mathbf{r}). \tag{E.35}$$

The local generation rate is approximated to be,

$$G(\mathbf{r}) = \frac{p_{\mathrm{TPA}}(\mathbf{r})}{2\hbar\omega_m}, \tag{E.36}$$

where $p_{\mathrm{TPA}}(\mathbf{r})$ is time-averaged the power absorbed through TPA given by,

$$p_{\mathrm{TPA}}(\mathbf{r}) = -\frac{1}{2}\,\mathrm{Re}(i\omega_m \mathbf{P}^{(3)}_{m,\mathrm{TPA}}(\mathbf{r})\cdot\mathbf{E}^*_m(\mathbf{r})) \tag{E.37}$$

The lifetime τ_m^{FCA} is expressed through,

$$\frac{-i}{\omega_m}\frac{1}{\tau_m^{\mathrm{FCA}}} = \frac{\delta\omega_m^{\mathrm{FCA}}}{\omega_m} = \frac{-i}{2\omega_m}\frac{\int_{\mathrm{Si}} d^3\mathbf{x}\gamma_m^{\mathrm{FCA}}(\mathbf{r})\varepsilon(\mathbf{r})|\mathbf{E}_m(\mathbf{r})|^2}{\int d^3\mathbf{x}\varepsilon(\mathbf{r})|\mathbf{E}_m(\mathbf{r})|^2}, \tag{E.38}$$

with

$$\gamma_m^{\mathrm{FCA}}(\mathbf{r}) = -\frac{\sigma^{\mathrm{FCA}} v_g \tau_{\mathrm{carrier}}(N(\mathbf{r}))}{4\hbar\omega_m}\,\mathrm{Re}(i\omega_m\mathbf{P}^{(3)}_{m,\mathrm{TPA}}(\mathbf{r})\cdot\mathbf{E}^*_m(\mathbf{r})). \tag{E.39}$$

The effective energy absorption rate, $\gamma^{\mathrm{FCA}}_{\mathrm{carrier},m} = 2/\tau_m^{\mathrm{FCA}}$, is essentially a weighted average of the local absorption rate $\gamma_m^{\mathrm{FCA}}(\mathbf{r})$. This is derived from perturbation theory by setting $\delta\varepsilon^{\mathrm{FCA}} = 2n\varepsilon_0\delta n^{\mathrm{FCA}}(\mathbf{r}) = i\gamma_m^{\mathrm{FCA}}(\mathbf{r})n^2\varepsilon_0/(\omega_m)$ in Eqn. (E.3). The dot product is evaluated using Eqn. (E.16), where only the imaginary part of $\chi^{(3)}_{\mathrm{Si}}$ is applied, $i\,\mathrm{Im}(\chi^{(3)}_{\mathrm{Si}})$. The fields are normalized by setting $\mathbf{E}_m(\mathbf{r}) = a_m\breve{\mathbf{E}}_m(\mathbf{r})/\sqrt{\int d^3\mathbf{x}\frac{1}{2}\varepsilon(\mathbf{r})|\breve{\mathbf{E}}_m(\mathbf{r})|^2}$ to give,

$$\frac{1}{\tau_m^{\mathrm{FCA}}} = \kappa_0\sum_{l,l'}\kappa^{\mathrm{FCA}}_{m,l,l'}U_lU_{l'} \tag{E.40}$$

where for $l = l'$,

$$\kappa^{\mathrm{FCA}}_{m,l,l} = \frac{\int_{\mathrm{Si}} d^3\mathbf{x}\left[(\breve{\mathbf{E}}^*_l\cdot\breve{\mathbf{E}}^*_l)(\breve{\mathbf{E}}_l\cdot\breve{\mathbf{E}}_l) + 2|\breve{\mathbf{E}}_l|^4\right]\varepsilon|\breve{\mathbf{E}}_m|^2}{(\int d^3\mathbf{x}\varepsilon|\breve{\mathbf{E}}_m|^2)(\int d^3\mathbf{x}\varepsilon|\breve{\mathbf{E}}_l|^2)^2}, \tag{E.41}$$

and for $l' \neq l$,

$$\kappa^{\mathrm{FCA}}_{m,l,l'} = 2\frac{\int_{\mathrm{Si}} d^3\mathbf{x}\left[(\breve{\mathbf{E}}_l\cdot\breve{\mathbf{E}}_{l'})(\breve{\mathbf{E}}^*_l\cdot\breve{\mathbf{E}}^*_{l'}) + (\breve{\mathbf{E}}_l\cdot\breve{\mathbf{E}}^*_{l'})(\breve{\mathbf{E}}^*_l\cdot\breve{\mathbf{E}}_{l'}) + |\breve{\mathbf{E}}_l|^2|\breve{\mathbf{E}}_{l'}|^2\right]\varepsilon|\breve{\mathbf{E}}_m|^2}{(\int d^3\mathbf{x}\varepsilon|\breve{\mathbf{E}}_m|^2)(\int d^3\mathbf{x}\varepsilon|\breve{\mathbf{E}}_l|^2)(\int d^3\mathbf{x}\varepsilon|\breve{\mathbf{E}}_{l'}|^2)}. \tag{E.42}$$

with

$$\kappa_0 = \frac{\sigma^{\mathrm{FCA}}\tau_{\mathrm{carrier}}\,\mathrm{Im}(\chi^{(3)}_{\mathrm{Si}})\varepsilon_0 c}{8\hbar n_{\mathrm{Si}}} \tag{E.43}$$

E.2.2 Nonlinear frequency shift

The total nonlinear resonance frequency shift is

$$\Delta\omega_m^{\mathrm{NL}} = \Delta\omega_m^{\mathrm{Kerr}} + \Delta\omega_m^{\mathrm{FCD}} + \Delta\omega_m^{\mathrm{thermal}}, \tag{E.44}$$

where $\Delta\omega_m^{\mathrm{Kerr}}$ is the shift due to the Kerr effect, which has already been considered for the model, $\Delta\omega_m^{\mathrm{FCD}}$ is the shift due to free-carrier dispersion, and $\Delta\omega_m^{\mathrm{thermal}}$ is the thermal shift resulting from the energy absorbed that heats the nonlinear material and changes its refractive index.

Kerr nonlinearity The frequency shift due to the Kerr nonlinearity is given as

$$\Delta\omega_m^{\mathrm{Kerr}} = \delta\omega_m^{\mathrm{Kerr}} = -\alpha_0 \sum_{m'} \alpha_{m,m'} U_{m'} \tag{E.45}$$

Free-carrier dispersion The local index of refraction changed induced by free-carriers predicted by a Drude model is,

$$\delta n_{\mathrm{FCD}}(\mathbf{r}) = -\zeta N(\mathbf{r}) \tag{E.46}$$

where $\zeta = \zeta^e + \zeta^h$ is a free-carrier dispersion nonlinear material parameter with units [m^3], which includes both electron and hole effects. Based on experimental results [82], the Drude model is modified for silicon:

$$\delta n_{\mathrm{FCD}}(\mathbf{r}) = -\left[\zeta_{\mathrm{Si}}^e N^e(\mathbf{r}) + \left(\zeta_{\mathrm{Si}}^h N^h(\mathbf{r})\right)^{0.8}\right] \tag{E.47}$$

The frequency shift predicted by perturbation theory is

$$\frac{\Delta\omega_m^{\mathrm{FCD}}}{\omega_m} = \frac{\delta\omega_m^{\mathrm{FCD}}}{\omega_m} = -\frac{\int d^3\mathbf{x} \frac{\delta n_{\mathrm{FCD}}(\mathbf{r})}{n_{\mathrm{Si}}(\mathbf{r})} \varepsilon(\mathbf{r}) |\mathbf{E}_m(\mathbf{r})|^2}{\int d^3\mathbf{x} \varepsilon(\mathbf{r}) |\mathbf{E}_m(\mathbf{r})|^2}. \tag{E.48}$$

where $\Delta\omega_m^{\mathrm{FCD}} = \Delta\omega_m^{\mathrm{FCD,e}} + \Delta\omega_m^{\mathrm{FCD,h}}$. Assuming electrons and holes are generated in pairs, such that $N^e = N^h = N$, the frequency shift due to electron free-carriers has the same form as Eqn.

(E.38), except with $\gamma_m^{\mathrm{FCA}}(\mathbf{r})/2 = \sigma^{\mathrm{FCA}} v_g N(\mathbf{r})/2$ replaced by $-\delta n_m^{\mathrm{FCD}}/n_{\mathrm{Si}} = \zeta_{\mathrm{Si}}^{\mathrm{e}} N(\mathbf{r})/n_{\mathrm{Si}}$ to yield,

$$\Delta\omega_m^{\mathrm{FCD,e}} = \frac{2\omega_m \zeta_{\mathrm{Si}}}{\sigma^{\mathrm{FCA}} c} \kappa_0 \sum_{l,l'} \kappa_{m,l,l'}^{\mathrm{FCA}} U_l U_{l'}. \tag{E.49}$$

The shift due to hole-carriers requires revisions to the integrals to account for the power of 0.8 in the modified Drude model. The total resulting FCD shift is given by,

$$\Delta\omega_m^{\mathrm{FCD}} = \nu_0^{\mathrm{FCD,e}} \sum_{l,l'} \kappa_{m,l,l'}^{\mathrm{FCA}} U_l U_{l'} + \nu_0^{\mathrm{FCD,h}} \sum_{l,l'} \kappa_{m,l,l'}^{\mathrm{FCD,h}} \Big(U_l U_{l'} \Big)^{0.8}, \tag{E.50}$$

where for $l = l'$,

$$\kappa_{m,l,l}^{\mathrm{FCD,h}} = \frac{\int_{\mathrm{Si}} d^3\mathbf{x} \Big[(\breve{\mathbf{E}}_l^* \cdot \breve{\mathbf{E}}_l^*)(\breve{\mathbf{E}}_l \cdot \breve{\mathbf{E}}_l) + 2|\breve{\mathbf{E}}_l|^4 \Big]^{0.8} \varepsilon |\breve{\mathbf{E}}_m|^2}{(\int d^3\mathbf{x} \varepsilon |\breve{\mathbf{E}}_m|^2)(\int d^3\mathbf{x} \varepsilon |\breve{\mathbf{E}}_l|^2)^{1.6}}, \tag{E.51}$$

and for $l' \neq l$,

$$\kappa_{m,l,l'}^{\mathrm{FCD,h}} = 2^{0.8} \frac{\int_{\mathrm{Si}} d^3\mathbf{x} \Big[(\breve{\mathbf{E}}_l \cdot \breve{\mathbf{E}}_{l'})(\breve{\mathbf{E}}_l^* \cdot \breve{\mathbf{E}}_{l'}^*) + (\breve{\mathbf{E}}_l \cdot \breve{\mathbf{E}}_{l'}^*)(\breve{\mathbf{E}}_l^* \cdot \breve{\mathbf{E}}_{l'}) + |\breve{\mathbf{E}}_l|^2 |\breve{\mathbf{E}}_{l'}|^2 \Big]^{0.8} \varepsilon |\breve{\mathbf{E}}_m|^2}{(\int d^3\mathbf{x} \varepsilon |\breve{\mathbf{E}}_m|^2)(\int d^3\mathbf{x} \varepsilon |\breve{\mathbf{E}}_l|^2)^{0.8} (\int d^3\mathbf{x} \varepsilon |\breve{\mathbf{E}}_{l'}|^2)^{0.8}}, \tag{E.52}$$

with

$$\nu_0^{\mathrm{FCD,e}} = \frac{\omega_m \zeta_{\mathrm{Si}}^{\mathrm{e}} \tau_{\mathrm{carrier}} \varepsilon_0 \,\mathrm{Im}(\chi_{\mathrm{Si}}^{(3)})}{4\hbar n_{\mathrm{Si}}}, \tag{E.53}$$

and

$$\nu_0^{\mathrm{FCD,h}} = \frac{\omega_m}{n_{\mathrm{Si}}} \left(\frac{\zeta_{\mathrm{Si}}^{\mathrm{h}} \tau_{\mathrm{carrier}} \varepsilon_0 \,\mathrm{Im}(\chi_{\mathrm{Si}}^{(3)})}{4\hbar} \right)^{0.8}. \tag{E.54}$$

Thermal effect The mean index change based on a thermal shift is,

$$\delta n_{\mathrm{thermal}} = \frac{dn}{dT} \Delta T = \frac{dn}{dT} R_{\mathrm{th}} P_{\mathrm{abs}} \tag{E.55}$$

where ΔT is the mean temperature change of the nonlinear material due to the power absorbed by nonlinear processes, P_{abs}. The thermo-optic coefficient, dn/dT, is known a priori for the nonlinear material, while the thermal resistance, $R_{\mathrm{th}} = dT/dP_{\mathrm{abs}}$, is unknown. Assuming that the temperature is evenly distributed [11], then the thermal frequency shift is given by,

$$\frac{\Delta\omega_m^{\text{thermal}}}{\omega_m} = \frac{\delta\omega_m^{\text{thermal}}}{\omega_m} = -\frac{\Gamma_m^{\text{th}}}{n_{\text{Si}}}\frac{dn}{dT}\frac{dT}{dP_{\text{abs}}}P_{\text{abs}} \tag{E.56}$$

where

$$P_{\text{abs}} = \sum_{m'}\left(\frac{2}{\tau_{m'}^{\text{abs}}} + \frac{2}{\tau_{m'}^{\text{TPA}}} + \frac{2}{\tau_{m'}^{\text{FCA}}}\right)U_{m'} \tag{E.57}$$

and

$$\Gamma_m^{\text{th}} = \frac{\int_{\text{Si}} d^3\mathbf{x}\varepsilon(\mathbf{r})|\mathbf{E}_m(\mathbf{r})|^2}{\int d^3\mathbf{x}\varepsilon(\mathbf{r})|\mathbf{E}_m(\mathbf{r})|^2}. \tag{E.58}$$

Appendix F

Nonlinear coefficients

The integral nonlinear coefficients in Table 5.3 are calculated based on FDTD simulation results. A subset of the nonlinear coefficient values are reported in Table F.1.

Table F.1: Nonlinear coefficients calculated from FDTD simulations.

Coefficient	Units	Device 1	Device 2	Devices 3 & 4
$\lvert\beta_2\rvert$	$[1/J]$	1.29×10^8	1.21×10^8	1.19×10^8
Γ_1^{th}		0.936	0.936	0.936
Γ_2^{th}		0.939	0.939	0.939
Γ_3^{th}		0.939	0.938	0.938
Γ_1^{TPA}		0.983	0.982	0.981
Γ_2^{TPA}		0.983	0.983	0.983
Γ_3^{TPA}		0.982	0.982	0.982
Γ_1^{FCA}		0.991	0.991	0.990
Γ_2^{FCA}		0.991	0.991	0.991
Γ_3^{FCA}		0.990	0.990	0.990
V_1^{TPA}	$(\lambda_1/n_{\mathrm{Si}})^3$	7.95	7.48	7.80
V_2^{TPA}	$(\lambda_2/n_{\mathrm{Si}})^3$	6.83	6.83	6.84
V_3^{TPA}	$(\lambda_3/n_{\mathrm{Si}})^3$	9.51	9.75	9.16
V_1^{FCA}	$(\lambda_1/n_{\mathrm{Si}})^3$	5.57	5.20	5.44
V_2^{FCA}	$(\lambda_2/n_{\mathrm{Si}})^3$	5.39	5.39	5.40
V_3^{FCA}	$(\lambda_3/n_{\mathrm{Si}})^3$	7.14	7.33	6.75
V_1^{eff}	$(\lambda_1/n_{\mathrm{Si}})^3$	1.69	1.60	1.66
V_2^{eff}	$(\lambda_2/n_{\mathrm{Si}})^3$	2.08	2.06	2.09
V_3^{eff}	$(\lambda_3/n_{\mathrm{Si}})^3$	2.33	2.34	2.10

In Table F.1, $\beta_2, \Gamma_m^{\mathrm{th}}$ and V_m^{eff} are reported and are given by,

$$\beta_2 = 2\beta_1^* = 2\beta_3^* = \frac{1}{2}\frac{\int_{\mathrm{Si}} d^3\mathbf{x}\varepsilon_0\,\mathrm{Re}(\chi_{\mathrm{Si}}^{(3)})\left[(\breve{\mathbf{E}}_2^*\cdot\breve{\mathbf{E}}_2^*)(\breve{\mathbf{E}}_1\cdot\breve{\mathbf{E}}_3)+2(\breve{\mathbf{E}}_2^*\cdot\breve{\mathbf{E}}_1)(\breve{\mathbf{E}}_2^*\cdot\breve{\mathbf{E}}_3)\right]}{(\int d^3\mathbf{x}\varepsilon(\mathbf{r})|\breve{\mathbf{E}}_2|^2)(\int d^3\mathbf{x}\varepsilon(\mathbf{r})|\breve{\mathbf{E}}_1|^2)^{1/2}(\int d^3\mathbf{x}\varepsilon(\mathbf{r})|\breve{\mathbf{E}}_3|^2)^{1/2}} \tag{F.1}$$

and

$$\Gamma_m^{\mathrm{th}} = \frac{\int_{\mathrm{Si}} d^3\mathbf{x}\varepsilon(\mathbf{r})|\mathbf{E}_m(\mathbf{r})|^2}{\int d^3\mathbf{x}\varepsilon(\mathbf{r})|\mathbf{E}_m(\mathbf{r})|^2}, \tag{F.2}$$

and

$$V_m^{\mathrm{eff}} = \frac{\int d^3\mathbf{x}\varepsilon(\mathbf{r})|\breve{\mathbf{E}}_m|^2}{\max\left[\varepsilon(\mathbf{r})|\breve{\mathbf{E}}_m|^2\right]}. \tag{F.3}$$

The coefficients $\alpha_{m,m}$ and $\kappa_{m,m,m}^{\mathrm{FCA}}$ are indirectly reported through Γ_m^{TPA}, Γ_m^{FCA}, V_m^{TPA}, and V_m^{FCA}, where,

$$\alpha_{m,m} = \frac{\int_{\mathrm{Si}} d^3\mathbf{x}\left[(\breve{\mathbf{E}}_m^*\cdot\breve{\mathbf{E}}_m^*)(\breve{\mathbf{E}}_m\cdot\breve{\mathbf{E}}_m)+2|\breve{\mathbf{E}}_m|^4\right]}{(\int d^3\mathbf{x}\varepsilon(\mathbf{r})|\breve{\mathbf{E}}_m|^2)^2} = \frac{3\Gamma_m^{\mathrm{TPA}}}{V_m^{\mathrm{TPA}}(\varepsilon_{\mathrm{Si}})^2}, \tag{F.4}$$

and

$$\kappa_{m,m,m}^{\mathrm{FCA}} = \frac{\int_{\mathrm{Si}} d^3\mathbf{x}\varepsilon(\mathbf{r})|\breve{\mathbf{E}}_m|^2\left[(\breve{\mathbf{E}}_m^*\cdot\breve{\mathbf{E}}_m^*)(\breve{\mathbf{E}}_m\cdot\breve{\mathbf{E}}_m)+2|\breve{\mathbf{E}}_m|^4\right]}{(\int d^3\mathbf{x}\varepsilon(\mathbf{r})|\breve{\mathbf{E}}_m|^2)^3} = \frac{3\Gamma_m^{\mathrm{FCA}}}{(V_m^{\mathrm{FCA}})^2(\varepsilon_{\mathrm{Si}})^2}. \tag{F.5}$$

The reported coefficients Γ_m^{TPA}, Γ_m^{FCA}, V_m^{TPA} and V_m^{FCA} are commonly quoted in the literature for various PC microcavity structures [11, 94, 106, 111]. They are given by,

$$\Gamma_m^{\mathrm{TPA}} = \frac{1}{3}\frac{\int_{\mathrm{Si}} d^3\mathbf{x}\varepsilon(\mathbf{r})^2\left[(\breve{\mathbf{E}}_m^*\cdot\breve{\mathbf{E}}_m^*)(\breve{\mathbf{E}}_m\cdot\breve{\mathbf{E}}_m)+2|\breve{\mathbf{E}}_m|^4\right]}{\int d^3\mathbf{x}\varepsilon(\mathbf{r})^2|\breve{\mathbf{E}}_m|^4}, \tag{F.6}$$

$$V_m^{\mathrm{TPA}} = \frac{(\int d^3\mathbf{x}\varepsilon(\mathbf{r})|\breve{\mathbf{E}}_m|^2)^2}{\int d^3\mathbf{x}\varepsilon(\mathbf{r})^2|\breve{\mathbf{E}}_m|^4}, \tag{F.7}$$

$$\Gamma_m^{\mathrm{FCA}} = \frac{1}{3}\frac{\int_{\mathrm{Si}} d^3\mathbf{x}\varepsilon(\mathbf{r})^3|\breve{\mathbf{E}}_m|^2\left[(\breve{\mathbf{E}}_m^*\cdot\breve{\mathbf{E}}_m^*)(\breve{\mathbf{E}}_m\cdot\breve{\mathbf{E}}_m)+2|\breve{\mathbf{E}}_m|^4\right]}{\int d^3\mathbf{x}\varepsilon(\mathbf{r})^3|\breve{\mathbf{E}}_m|^6}, \tag{F.8}$$

and

$$\left(V_m^{\mathrm{FCA}}\right)^2 = \frac{(\int d^3\mathbf{x}\varepsilon(\mathbf{r})|\breve{\mathbf{E}}_m|^2)^3}{\int d^3\mathbf{x}\varepsilon(\mathbf{r})^3|\breve{\mathbf{E}}_m|^6}. \tag{F.9}$$

Appendix G

X^2 minimization plots

In this appendix, the X^2 minimizations are plotted as a function of the 8 fit parameters found from the nonlinear transmission analysis. Figures G.1 to G.4 are plots for the independent characterizations of Devices 1 to 4, while Figs. G.5 to G.8 are for the minimizations calculated with R_{th}, τ_{carrier} and Q_{abs} held fixed at the mean values.

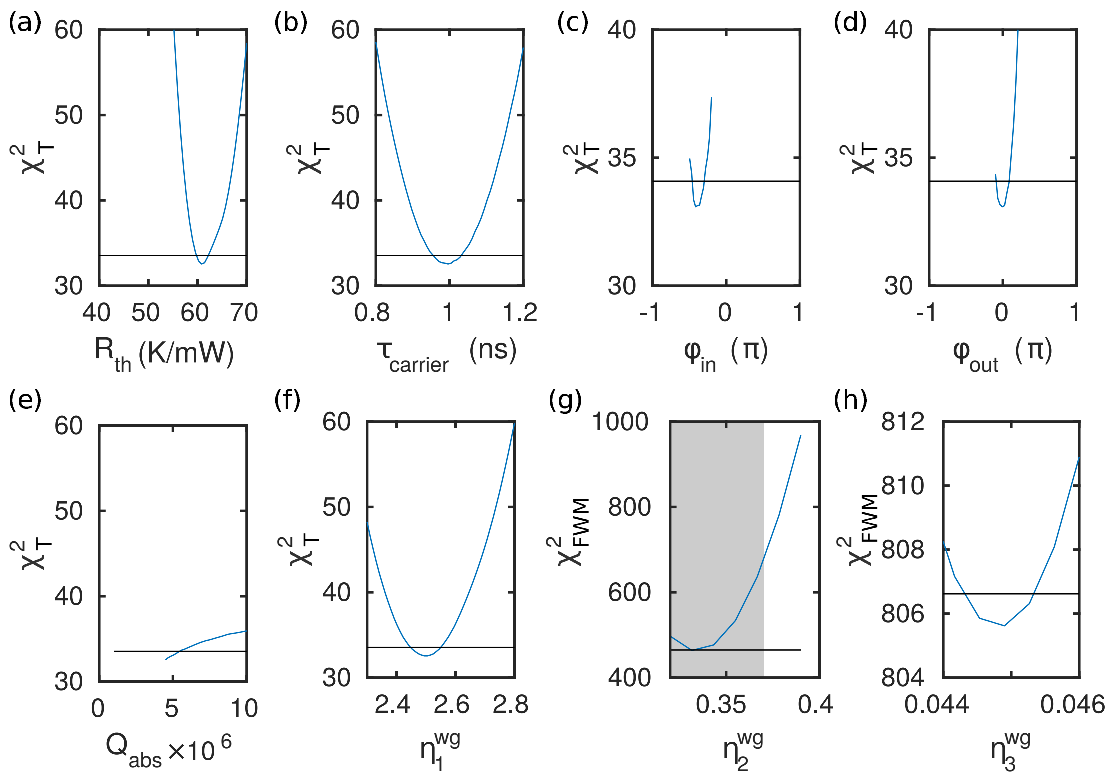

Figure G.1: Device 1 X^2 minimization plots. The parameter on each x axis is fixed and the minimum X^2 over all other parameters is shown. The straight black lines show the $\min(X^2) + 1$. The shaded region in (g) indicates η_2^{wg} values outside of the range of possible values.

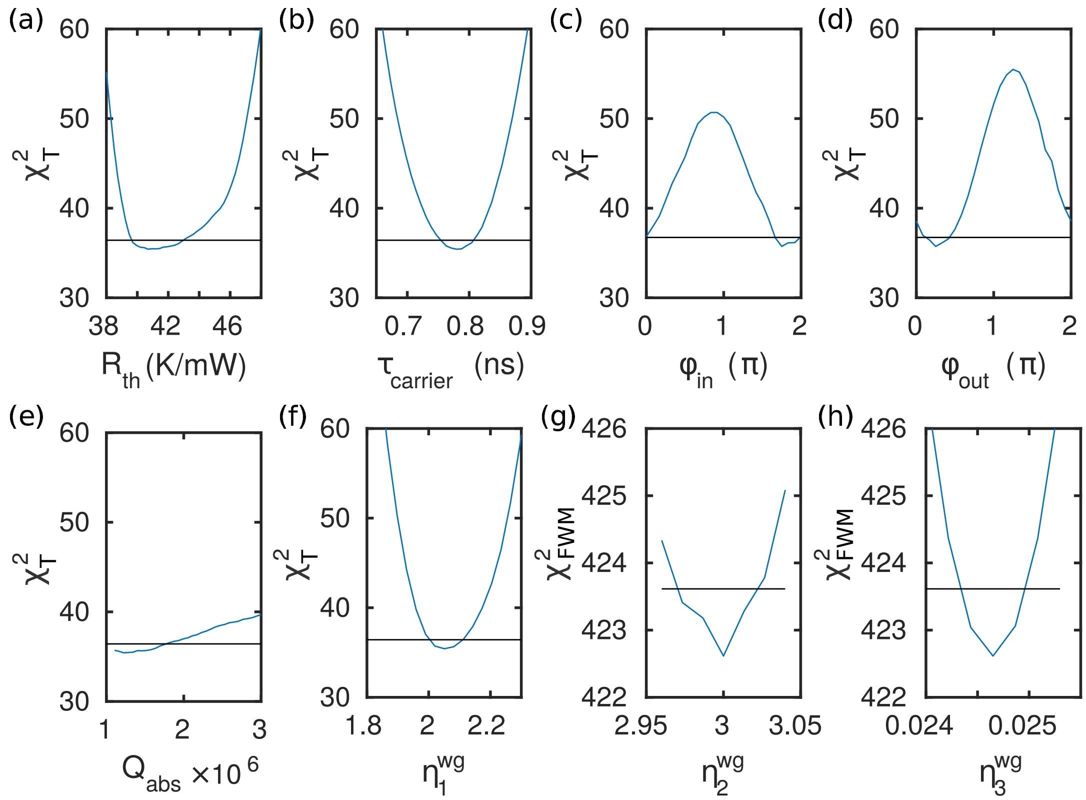

Figure G.2: Device 2 X^2 minimization plots. The parameter on each x axis is fixed and the minimum X^2 over all other parameters is shown. The straight black lines show the $\min(X^2) + 1$.

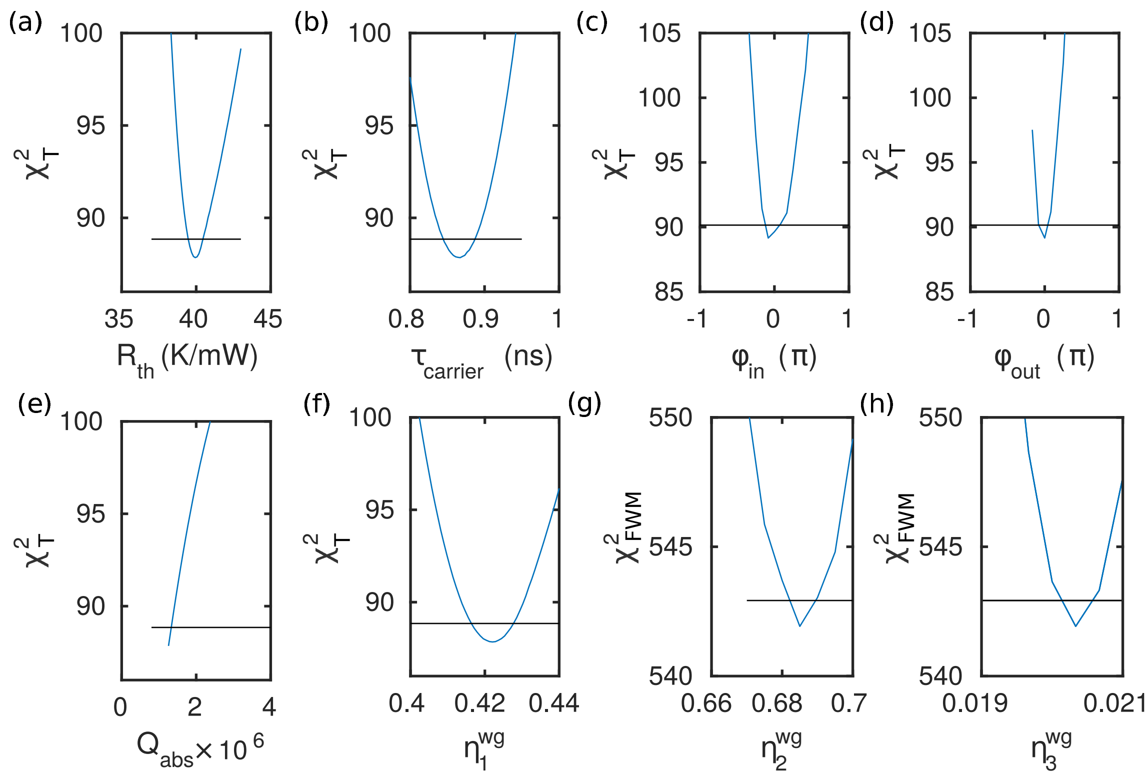

Figure G.3: Device 3 X^2 minimization plots. The parameter on each x axis is fixed and the minimum X^2 over all other parameters is shown. The straight black lines show the $\min(X^2) + 1$.

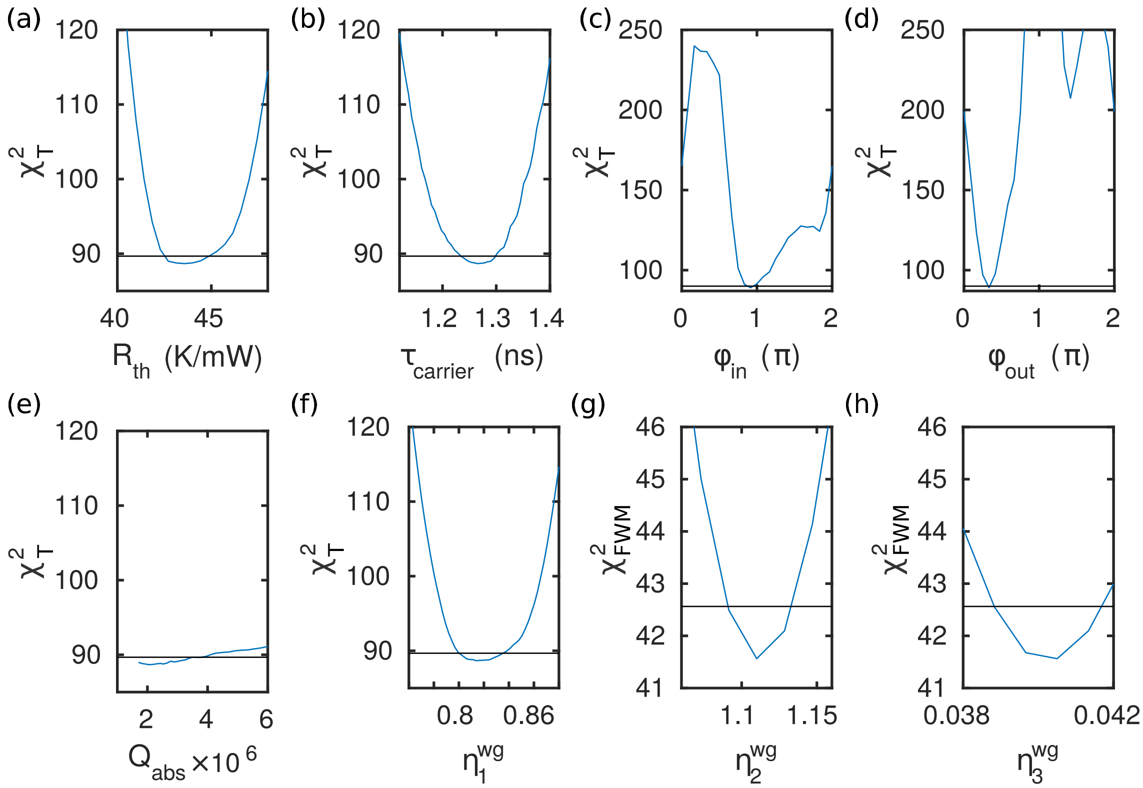

Figure G.4: Device 4 X^2 minimization plots. The parameter on each x axis is fixed and the minimum X^2 over all other parameters is shown. The straight black lines show the $\min(X^2) + 1$.

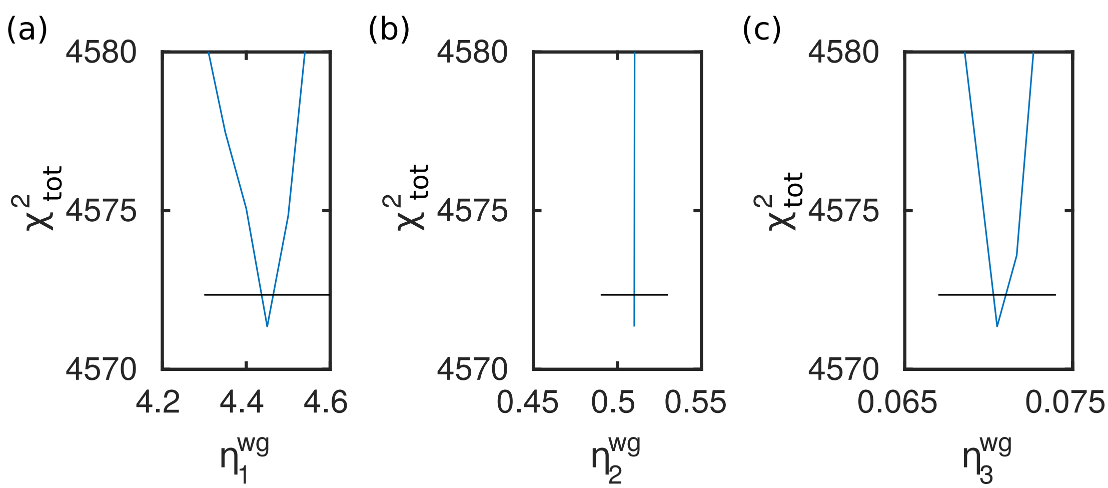

Figure G.5: Device 1 X^2 minimization plots, when $R_{\rm th}, Q_{\rm abs}$ and $\tau_{\rm carrier}$ are fixed to the average values in the model functions. The parameter on each x axis is fixed and the minimum X^2 over all other free parameters is shown. The straight black lines show the $\min(X^2) + 1$.

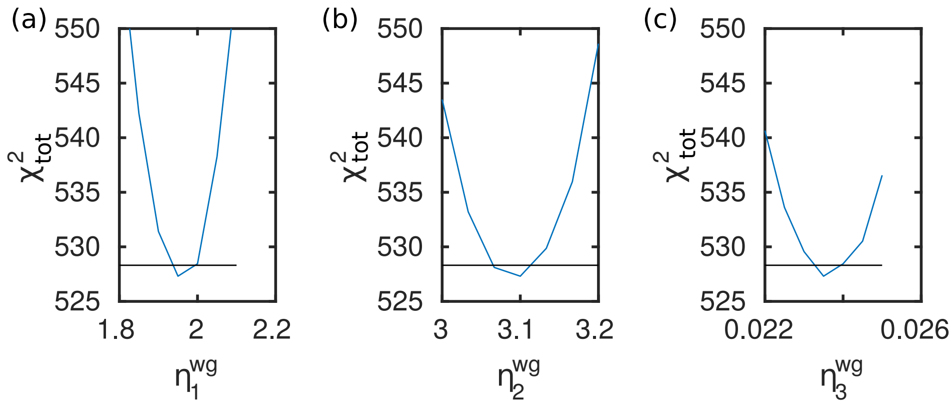

Figure G.6: Device 2 X^2 minimization plots, when $R_{\mathrm{th}}, Q_{\mathrm{abs}}$ and τ_{carrier} are fixed to the average values in the model functions. The parameter on each x axis is fixed and the minimum X^2 over all other parameters is shown. The straight black lines show the $\min(X^2) + 1$.

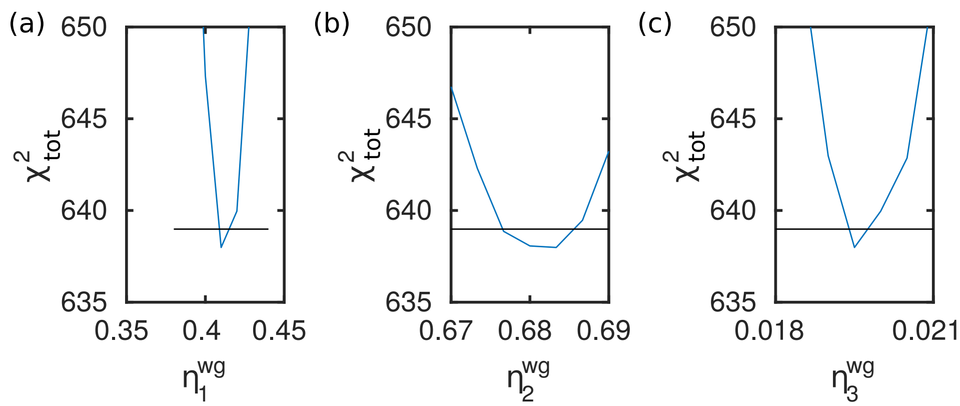

Figure G.7: Device 3 X^2 minimization plots, when $R_{\mathrm{th}}, Q_{\mathrm{abs}}$ and τ_{carrier} are fixed to the average values in the model functions. The parameter on each x axis is fixed and the minimum X^2 over all other parameters is shown. The straight black lines show the $\min(X^2) + 1$.

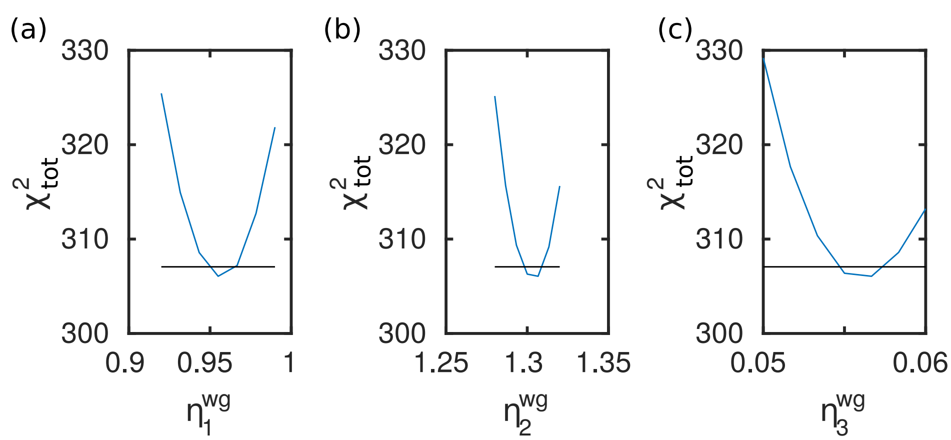

Figure G.8: Device 4 X^2 minimization plots, when $R_{\mathrm{th}}, Q_{\mathrm{abs}}$ and τ_{carrier} are fixed to the average values in the model functions. The parameter on each x axis is fixed and the minimum X^2 over all other parameters is shown. The straight black lines show the $\min(X^2) + 1$.